BIMETALLIC THERMAL RESISTS FOR PHOTOMASK, MICROMACHINING AND MICROFABRICATION

by

Richard Yuqiang Tu
B.A.Sc., Shanghai Jiao Tong University, China, 1988
M.Sc., Shanghai University of Science and Technology, China, 1991
M.Sc., Nanyang Technological University, Singapore, 1995

THESIS SUBMITTED IN PARTIAL FULFILMENT OF
THE REQUIREMENTS FOR THE DEGREE OF

DOCTOR OF PHILOSOPHY

In the School
of
Engineering Science

SIMON FRASER UNIVERSITY
Dec 2004

APPROVAL

Name: Yuqiang Tu (Richard)

Degree: Doctor of Philosophy

Title of Thesis: Bimetallic Thermal Resists for Photomask, Micromachining and Microfabrication

Examining Committee:

Chair: Dr. Albert Leung
Prof., School of Engineering Science, SFU

Senior Supervisor: _____
Dr. Glenn Chapman
Senior Supervisor
Prof., School of Engineering Science, SFU

Supervisor: _____
Dr. Bonnie Gray
Supervisor
Prof., School of Engineering Science, SFU

Supervisor: _____
Dr. Karim Karim
Supervisor
Prof., School of Engineering Science, SFU

Internal Examiner: _____
Dr. Karen Kavanagh
Prof., Physics Department, SFU

External Examiner: _____
Dr. Franklin Kalk
Chief Technology Officer, DuPont Photomasks, Inc.

Date Approved: Dec 06, 2004

SIMON FRASER UNIVERSITY

PARTIAL COPYRIGHT LICENCE

ABSTRACT

Photoresists and photomasks are two of the most critical materials in microfabrication and micromachining industries. As the shift towards shorter wavelength exposure continues, conventional organic photoresists and chrome/quartz photomasks start to encounter problems.

This thesis investigates and presents an alternative to organic photoresists and chromium photomasks which overcomes their intrinsic problems. A bimetallic thin film, such as Bi/In and Sn/In, creates an inorganic thermal resist with many interesting properties. Both experiments and simulations demonstrate that this class of thermal resists can be converted by laser exposure with wavelengths from 213 nm to 830 nm, showing wavelength invariance. Simulations of the projected wavelength response show that Bi/In thermal resist works down to the 1 nm X-ray range. Exposed bimetallic thermal resists can be developed in two different acid solutions with excellent selectivity. A standard etch (RCA2) can strip the unexposed bimetallic film when photoresist rework is needed. Exposed bimetallic films are resistant to Si anisotropic wet etching and fluorine, O_2 and chlorine plasma etching. The Bi/In thermal resist is the first reported resist that works for both wet chemical anisotropic Si etching and dry plasma etching. All these features make the bimetallic film a complete thermal resist. Another very important property of bimetallic thin films is the largest change in the optical absorption ever reported in the literature (3.0 OD before exposure and 0.22 OD after exposure, 365 nm), with the exposed areas becoming nearly transparent. The transmission of the exposed films depends on the laser writing power. Thus, Bi/In resist and its class can be utilized as a direct-write photomask material for both binary and grayscale photomasks. Binary photomasks and grayscale photomasks were successfully created. 2D and 3D structures were successfully generated in Shipley organic photoresists using a mercury lamp mask aligner with exposure conditions identical to those for conventional chrome masks. Material analyses show that the transformation after laser exposure of bimetallic thermal resists is an oxidation process. Laser-converted Bi/In and Sn/In oxides have a structure similar to that of indium tin oxide films.

To My Wife
Lijun

Many men and women have done excellently,
but you surpass them all.

To The Two Little Engineers
Edward and Daniel

Can we fix it? Yes, we can!

献给我父母和岳父岳母
感谢您们的理解与支持

ACKNOWLEDGEMENTS

The author would like to thank Professor Glenn Chapman of Simon Fraser University for his encouragement and support during this project. Special thanks are extended to Mr. Bill Woods, whose help in the lab made valuable contributions to the research presented in this document. Also I would like to thank Prof. John Jones, Prof. Karen Kavanagh and Dr. Eva Czyzewska for their helpful suggestions. This work was supported in part by CREO Products Inc. and the British Columbia Advanced Systems Institute.

TABLE OF CONTENTS

LIST OF TABLES

LIST OF FIGURES

LIST OF ABBREVIATIONS AND ACRONYMS

MEMS	Microelectromechanical system
OD	Optical density
HMDS	hexamethyldisilazane
$D°$	Bond strength in diatomic molecules
$E°$	Reduction potential
PVD	Physical vapour deposition
CVD	Chemical vapour deposition
CMOS	Complementary Metal Oxide Semiconductor
DUV	Deep ultraviolet
EUV	Extreme ultraviolet
IC	Integrated circuit
NA	Numerical aperture
PAC	Photo-active compound
RIE	Reactive ion etch
UV	Ultraviolet
TMAH	Tetramethyl ammonium hydroxide
EDP	ethylene diamine pyrocatechol
JCPDF	Joint Committee for Powder Diffraction Files
Ra	Average roughness
LIGA	*LIthographie Galvanoformung Abformung* (German), or Lithography Electroforming Moulding

Chapter 1
Introduction

1.1 General

This thesis presents a novel class of inorganic, bimetallic, thin-film, thermal resists, including Bi/In and Sn/In, as alternatives to conventional organic photoresists and photomask materials for micromachining and microfabrication.

Bi/In is the first reported inorganic, thermal resist that can be exposed by laser/light sources with a wide range of wavelengths, that can be developed by acid solutions, and that can act as both a wet chemical, anisotropic, Si etch masking layer, and a dry CF_4/CHF_3 plasma Si and SiO_2 etch masking layer. Simulations of Airy Summation optical modelling and experimental results showed that this resist can operate from X-ray (1 nm) to infrared (IR 830 nm) wavelengths. Thermal modelling and experimental results indicate that a 15/15 nm Bi/In bilayer has a sensitivity of $7mJ/cm^2$ with 4 ns pulses at the Nd:YAG (Neodymium-doped Yttrium Aluminium Garnet) 266nm wavelength, the same sensitivity as current organic photoresists.

An extremely large optical absorption change was also observed in Sn/In and Bi/In bilayer films, with the exposed areas becoming nearly transparent over the 900 nm to 365 nm wavelength range. This suggests that Sn/In, Bi/In and others of this type can be used as a direct-write photomask material. Tests showed that Sn/In and Bi/In are two excellent direct-write materials in terms of optical absorption change: from 3 OD (optical density, refer to Section 1.2.2.1 for OD ~ transmission rate conversion equation) before laser exposure to 0.22 OD after laser exposure [1,2]. Some other unique features have also been explored.

This chapter introduces the issues that current lithography has with organic photoresists and photomasks, and the reason why Bi/In and its class are promising alternatives. Subsequent chapters will discuss these subjects in detail.

1.2 Background

The revenue of the global semiconductor industry (microfabrication) reached US$140.7 billion for 2002, making it one of the largest manufacturing industries in the world. Its revenue has increased by ~ 20% per annum for two decades [3]. The cost of materials used in chip fabrication is high. The 2002 global semiconductor materials market reached US$23 billion according to Semiconductor Equipment and Materials International (SEMI) [4]. The value of fabrication (wafer fab) materials is US$14 billion. Among them, microlithography formed 30% of the total materials expenses: photoresists cost US$1.5 billion and photomasks US$2.7 billion. An upward trend is also seen in the MEMS (Microelectro-Mechanical System, or micromachining) industry, where worldwide MEMS revenue is forecast to grow from $3.9 billion in 2001 to $9.6 billion in 2006 [5].

1.2.1 Microlithography

Microlithography, also called photolithography or just photo by engineers in wafer fabs, is a critical process which transfers integrated circuit or micro-mechanical patterns onto wafers for micromachining and microfabrication. Conventional microlithography includes three important parts: a) photomasks which have the patterns for various circuit or mechanical levels; b) photoresists that are sensitive to a certain kind of radiation, such as laser, X-ray, electron, ion, etc., that can faithfully replicate the photomask patterns and act as etching masks in subsequent

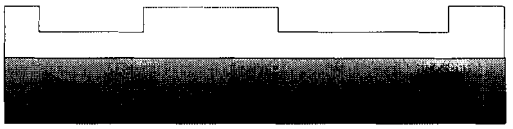

● *Device layer*

← *Silicon wafer*

(a) Si wafer with devices made from previous processes.

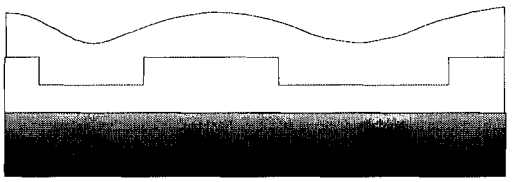

● *Spun-on photoresist*

(b) Photoresist is spin-coated on the wafer.

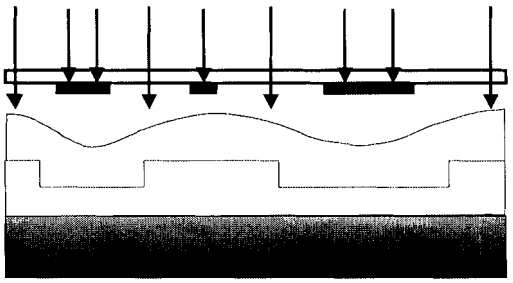

● *Laser Exposure*

● *Photomask with Chromium patterns*

(c) Photoresist is exposed with UV illumination through the photomask.

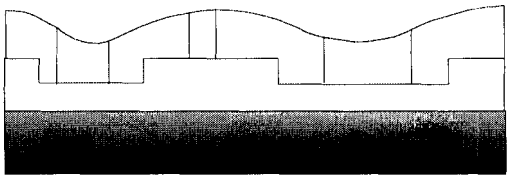

(d) Chemical properties of resist change in exposed area.

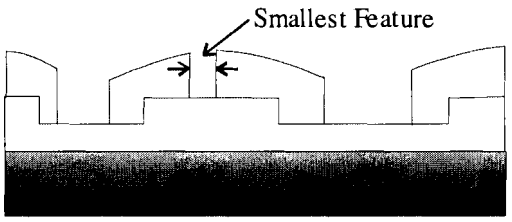

(e) For a negative photoresist, exposed areas are retained after development. The pattern is transferred to the resist. The arrows show the smallest feature patterned.

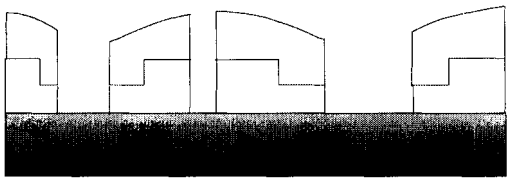

(f) Dry or wet etch transfers the pattern from resist to the device layer underneath.

(g) The last step is photoresist removal where the photo-resist remain is chemically or plasma-etched.

Figure 1.1 Microlithographic and etching processes of negative photoresists for micromachining and microfabrication.

etching processes; and c) exposure tools, such as steppers and mask aligners. This thesis investigates and proposes an alternative to the first two parts. Microlithography is the key technology in micromachining and microfabrication, because it is repeated in a process sequence that depends on the IC and MEMS designs. It determines the device dimensions, the production yield and the manufacturing cost.

Figure 1.1 shows the typical microlithographic and etching techniques that are currently used during micromachining and microfabrication manufacturing. The silicon wafer, with devices made from previous processes, is prepared for photoresist coating, as shown in Figure 1.1 (a). In order to enhance the adhesion of the photoresist to the layer underneath, special precursor chemicals (priming agents such as HMDS: hexamethyldisilazane) are often dispensed onto the wafer before photoresist coating. Liquid organic photoresist is applied to the wafer, and spun off to form a thin layer, typically 0.7 μm to 1 μm thick depending on the process integration requirements, as shown in Figure 1.1 (b). The resist is soft-baked at 80 – 110 °C for 1 – 20 minutes to remove the resist solvent and relax stress [6]. The photoresist layer is then patterned with an image illuminated by a UV light (Hg vapour or Excimer laser) through a photomask (Figure 1.1 (c)). Chromium-on-fused silica has been the choice of photomask material for the industry for many years. The exposure systems that are commonly used in the industry are steppers, which project the pattern images on the photomasks to the wafer with a 4 to 10× reduction. After exposure, a photolysis process causes a change in the chemical properties of the exposed area (Figure 1.1 (d)). It is chemically different enough that the exposed and unexposed areas of the resist have different dissolution rates in aqueous, alkaline-base developers. For a negative photoresist, the unexposed area dissolves quickly in the developer, and the exposed area is insoluble (shown in Figure 1.1 (e)). Figure 1.1 (a) to (e) illustrate the basic microlithography process steps employed in the industry.

After the patterns have been transferred from the photomasks to the photoresists on the wafer, dry (plasma) or wet chemical etching is carried out to transfer the patterns into the device layer underneath. As shown in Figure 1.1 (f), the area covered by the photoresist is protected from being etched away because the photoresist is resistant to the etching chemicals or plasma (hence the generic name "resists"), while the "open" area not covered by the resist is etched away by the chemicals or plasma. The whole microlithography / etching cycle ends with the stripping of the photoresist, as shown in Figure 1.1 (g). Dry O_2 plasma ashing or wet solvent stripping is usually used to remove the resist residue. To make a typical 64 MB DRAM chip, the microlithographic and etching process cycle is repeated 20 to 30 times.

The smallest feature (also called geometry size, technology node or critical dimension - CD, as shown in Figure 1.1 (e)) that can be patterned by the microlithographic process determines the device density, speed and power consumption of a chip. As the need for high-speed, low-power and high-density ULSI (Ultra-large Scale Integrated) devices from multimedia, communication and computer systems grows, the feature size keeps shrinking. Current technology (Year 2003 – 2004) has reached a 0.09 μm geometry size using an ArF excimer, 193 nm laser exposure source [7,8]. The geometry size is controlled by many factors in the microlithographic process. Among them, laser sources and photoresists play major roles.

The minimum Line Width (*LW*) of a feature printed in a photoresist by a projection system is given by the famous Rayleigh equation:

$$LW = \frac{k_1 \lambda}{NA} \tag{1.1}$$

where k_1 is a constant related to the mask and resist process, λ is the laser source wavelength, and *NA* is the numerical aperture of the optical system [9]. As one can see from Equation (1.1), in addition to increasing the *NA* value, using a shorter-wavelength laser source and improving

photoresist performance can reduce the feature size. Looking for advanced photoresists for shorter wavelengths is always a grand challenge to the semiconductor industry [10].

Although organic photoresists and chromium / quartz photomasks have been the workhorses for micromachining and microfabrication for decades, more and more problems are appearing as the lithography technology moves from 248 nm deep ultraviolet (DUV) to 193 nm and 157 nm extreme ultraviolet (EUV) nodes, and in future, to 13.4 nm soft X-ray wavelength. This will be discussed in the next sections.

1.2.2 Issues with Organic Photoresists

Organic photoresists consist of three components: resin, photoactive compound (PAC) and solvent [27]. For example, almost all of the positive photoresists for near-UV, g-line (435 nm) and I-line (365 nm) lithography in the micromachining and microfabrication industries are DNQ (diazonaphthoquinone) / Novolac resists. Novolac is the resin and DNQ is the PAC. As shown in Figure 1.2, when DNQ is exposed to light, it produces an unstable intermediate, a ketene, through the Wolf rearrangement [28]. The ketene (indene shown here in Figure 1.2) immediately reacts with a water molecule in the resist matrix to form indenecarboxylic acid (ICA) [11]. The Novolac resin is soluble in the alkaline developer. However, DNQ prevents it from dissolving. This inhibition is removed after DNQ is exposed to light and converted into ICA, which is highly soluble in alkali developers. Due to the high solubility of ICA in alkali, the fully exposed resist dissolves even faster than the unexposed resin.

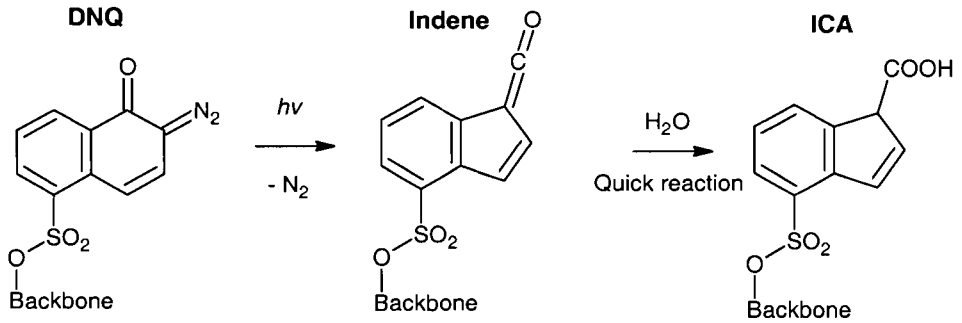

Figure 1.2 Photochemical reaction of organic photoresists: the DNQ / Novolac group [11].

Generally, organic photoresists should have the following four technical features. (1) *High transparency*: to obtain a high-resolution resist pattern with a steep profile; one has to use a resist film that is nearly transparent to the illumination light source. (2) *High sensitivity*: resists with high sensitivity are desirable due to the power limit of laser sources and the production throughput requirement. (3) *High dry-etching resistance*: this is essential in order to transfer the photoresist patterns to the substrates. And (4) *Aqueous developable*: Aqueous-developers are safe and easy to handle [11].

With some modifications of the composition, the DNQ/Novolac resist has been improved significantly in its resolution capability and has met the requirements of g-line and I-line exposure applications. However, with the trend towards shorter wavelengths (DUV 248 nm), as shown in the wavelength spectrum in Figure 1.3, DNQ/Novolac resist encounters a problem: the polymer transparency decreases sharply at shorter wavelengths. The transmission rate of DNQ/Novolac resist drops to around 10% at 248 nm [11]. As shown in Figure 1.4, when the transparency of the resist is low, the exposure dose at the top of the film is higher than that at the bottom. The resist profiles after development no longer have steep sidewalls. They are narrower at the top for positive resists and wider at the top for negative resists. This will no doubt cause problems for line width control on the substrate. To solve this problem, a new generation of photoresists was developed. Research shows that polymethylmethacrylate (PMMA), polydimethylglutarimide

(PMGI) and polyhydroxystyrene (PHS) have over 30% transmissivity at 248 nm wavelength and exhibit good resist profiles [11]. However, PHS and PMGI do not work for the 193 nm node as they have extremely low transmissivity at this wavelength.

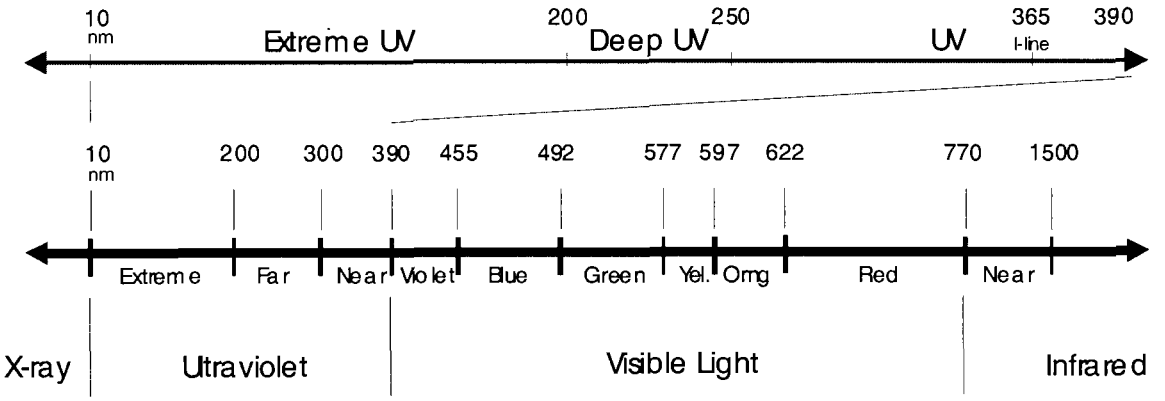

Figure 1.3 The spectrum of electromagnetic field suitable for microlithography.

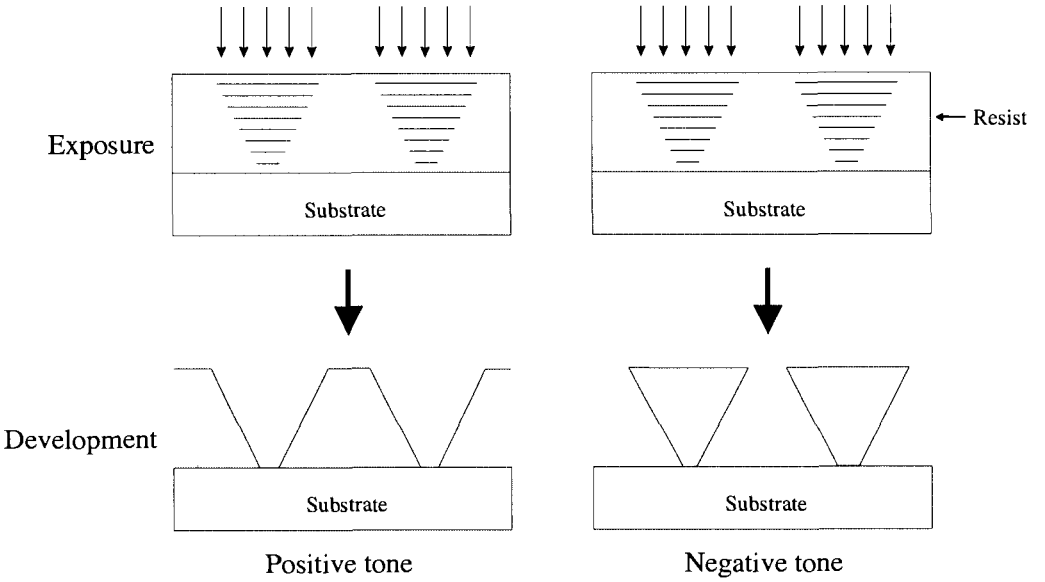

Figure 1.4 The influence of the transparency of a resist film on the resist profile after development.

As the wavelength moves to next generation 157 and 13.4 nm nodes, one of the biggest challenges in microlithography is the photoresist. Because many organic compounds are opaque

at 157 nm, designing transparent photoresists at this wavelength has become a difficult task. It is reported that the incorporation of fluorine in polymers is very effective at reducing the optical absorbance at 157 nm [29]. The organo-silicon related "Top Surface Imaging" process, which converts the top silicon-containing organic layer into silicon dioxide, which in turn has its pattern transferred to a thicker protective layer underneath, uses a top layer with an entirely different chemistry [30]. Although a large number of researchers are working on developing new resists and great progress has been made, recent tests carried out at Intel shows that there is still a lot of work that needs to be done before a 157 nm photoresist can be used in manufacturing [31].

Conventional organic photoresists only cater to a limited number of etching processes. They work well with dry plasma etches using different chemistries, but they cannot withstand the heated silicon anisotropic wet chemical etchants, such as KOH, TMAH and EDP, which are classic etchants for bulk silicon micromachining. Masking layers such as SiO_2 or Si_3N_4 must be deposited on top of the silicon wafer for such etching processes. Literature indicates that no photo or thermal resists withstand heated KOH, TMAH and EDP; and no resists work for both dry plasma etching and wet chemical silicon anisotropic etching.

Organic photoresists are also sources of organic contaminants in wafer processing. Fab experiences show that photoresist residues can cause furnace contamination, and particle issues. Hence, thorough wet cleans, including acid baths, solvent cleaning and long DI water rinse, are needed before subsequent process steps. Since they are all in liquid form, and are applied to wafers by spin-coating, organic photoresists are not compatible with an all-dry manufacturing process. Fabrication facilities, such as a space fab, where the wafers are handled and processed completely in vacuum in order to maintain an even cleaner microfabrication environment, have been proposed by Professor Glenn Chapman at Simon Fraser University [32].

The exposed image on the photoresist, also called the latent image, is not visible before development. Thus, the CD (critical dimension) and overlay registration checks can only be done

after development. It would shorten lithographic process time if the image could be seen right after the exposure. Thus, photo rework could be done without development in the case where metrology inspection fails.

So far, none of the photo or thermal resists in use are electrically conductive. This is not a serious issue. However, a resist with fair conductivity may open doors to some new applications, such as using the resist as a seed layer for electroplating.

In summary, organic photoresists are facing three major issues. Firstly, they are wavelength sensitive, that is, one type of photoresist works only for a light source of one specific wavelength. A brand new series of resists needs to be developed for each new generation, shorter wavelength light source. This is always costly and time-consuming. Inadequacies in resist performance and supply have already led to a slowdown in the pace of advances in lithography [33]. Secondly, no organic photoresist can withstand both dry plasma etching and wet alkaline-based silicon anisotropic etching. Thirdly, organic photoresists are sources of wafer contamination; hence extensive cleaning is needed before the next process step. Finally, they are incompatible with an all-dry process, a promising future microfabrication environment [32]. With such intrinsic issues in organic resists, it is worth investigating an alternative approach: an inorganic thermal resist which is activated by optically-driven, thermal processes.

1.2.3 Alternative to Organic Resists: Inorganic Resists

In order to avoid these organic resist problems, people have looked into inorganic resists as alternatives. There have been studies and reports in the literature for decades. The main advantages of inorganic resists are listed in Table 1.1. However, these are not the only ones. This thesis will, in coming sections, present some new features unique to inorganic resists. According

to the activation mechanism, inorganic resists can be generally categorized into two groups: inorganic photo resists and inorganic thermal resists.

Table 1.1 Comparison between inorganic resists and organic resists.

	Inorganic resists	**Organic resists**
Deposition process	Dry (CVD, Sputter, Evaporation in vacuum)	Wet (spin-coating)
Baking	Not needed	Pre- and post-baking needed
Fire / Toxicity	No, fireproof and non-toxic	Yes, solvent is used
Thickness of resist	Thin layer used in process (< 200 nm)	Thick (0.2 μm – 1.5 μm)
Shelf life of exposed / unexposed material	Months, even years (Bi/In, Sn/In)	Days
Source of contamination	To be evaluated (Chapter 10)	Yes

1.2.3.1 Inorganic Photo Resists

Just like silver iodide (AgI) in films for black and white photography, there are many inorganic resists that are photosensitive. The most widely used among them are chalcogenides, such as $GeSe_y$ and As_2S_3. The imaging abilities of chalcogenide layers and chalcogenide-metal structures were first reported in two primary publications [34,35] in the mid-1960's. Both effects result in substantial changes in the chalcogenide layer solubility, which make the production of relief images possible. Numerous publications and patents that followed have shown ways for their practical application in microlithography for micromachining and microfabrication [36-41]. With the addition of silver, Ag-chalcogenide inorganic resists, such as Ag_2Te/As_2S_3, and $Ag_2Se/GeSe_2$, can have very high exposure sensitivity: 3 – 10 mJ/cm^2 at 248 nm [38]. Conventional organic resists at 248 nm require 10 – 50 mJ/cm^2 [33]. However, it is well-known that Ag is poisonous to silicon devices, as it creates traps and kills carrier lifetime. Thus, it is suitable for micromachining and data storage [42], but not for microfabrication applications [43].

1.2.3.2 Inorganic Thermal Resists

Instead of being photochemically sensitive to light, inorganic thermal resists are activated by heat from a light, electrons (e-beam), ions (ion-beam) or X-ray that is absorbed by the resist films. Since the conversion process requires simply a temperature change, thermal resists are more wavelength invariant than organic or inorganic photoresists.

One of the first proposed inorganic thermal resist was an amorphous, iron oxide film deposited by chemical vapour deposition (CVD) [44]. When irradiated, the film crystallized if the temperature exceeded 820°C. The area where the temperature was less than 820°C remained amorphous. The unexposed amorphous area of the iron oxide film dissolved in acid solutions much faster than the crystallized area. Thus, this thermal resist could be developed as conventional organic photoresists. However, the high conversion temperature of the iron oxide film required over 100 J/cm^2 of energy, much higher than conventional organic photoresists 10 – 50 mJ/cm^2, thus making it impractical for microfabrication and micromachining applications.

Bozler reported another metal-oxide, thermal resist: Al/O [45,46]. The Al/O thermal resist is prepared with vacuum evaporation methods, such as evaporation of Al in an O_2 atmosphere. The as-deposited film is a mixture of metallic Al and oxide Al_2O_3, about 30 nm thick. It is shiny, smooth and electrically conductive. When exposed to a single 20 ns UV laser pulse with 40-100 mJ/cm^2 energy, the exposed area absorbs a portion of the laser energy and heats the film above a threshold temperature, where the film transforms from an electrically conducting metallic phase to an electrically insulating "black" phase. The converted regions are much more insoluble in phosphoric acid / H_2O etchants than the unexposed area. Thus, the exposed film can be developed in such acid solutions, and then used as a masking layer for RIE plasma etching in CHF_3 chemistry. Although Al/O thermal resist was claimed to be more sensitive than the iron oxide film, it still requires about 100 mJ/cm^2 for film conversion, several times higher than conventional organic photoresists. This is obviously due to the high melting

point of Al, which is 660°C. It is also noted that the high reflectance of the as-deposited film makes the film less absorbing. The film also has high thermal conductivity (237 W/mK), which is 3 times that of indium and 30 times that of bismuth. The conversion temperature can still be close to 800°C [45].

Despite all these shortcomings, Fe/O and Al/O thermal resists, based on an oxidation mechanism, gave us three very clear guidelines for choosing a more sensitive inorganic metallic thermal resist system. First, the metal or metals in the thermal resist system should have as low a melting / reaction temperature as possible. Compared to Al, Fe has too high a melting point (1535°C). That is the reason why Fe/O has much lower sensitivity than Al/O, although Fe has a much lower thermal conductivity (73W/mK), giving it less heat dissipation. To obtain an even lower melting point, we can choose a binary metal system with a local minimum eutectic point. Second, the material system should have a low thermal conductivity, which causes less heat loss during the irradiation process. Finally, the single or bilayer metallic film should be highly absorbing.

Gelbart has proposed a microlithography process called TREOL: the Thermal Resist Enhanced Optical Lithography process which utilizes the threshold property of thermal resists to reduce the minimum geometry of a microlithographic system [47,56]. The TREOL process proposes that multiple sub-field masks should be used, each of which exposes only small sections of the total mask so that diffracted light from neighbouring features does not interfere. No resolution improvement should be observed in photoresists using the TREOL method, as organic photoresists are reciprocal: the exposure results are the same whether the exposure was carried out in many steps or in one single step, with the same total dosage. The diffraction effect in the area between neighbouring features will affect the image resolution. However, thermal resists are non-reciprocal or partially non-reciprocal. When a small section is exposed, the resist is heated up by the laser and converts in the area where the temperature exceeds the conversion threshold. The

resist in the diffraction region whose light intensity is lower does not convert, and the heat dissipates away. When the neighbouring section is then exposed, the same diffraction area will not convert either, due to the lower exposure intensity. No heat can be accumulated in the diffraction region due to the heat dissipation. Thus, geometry enhancement can be achieved with the TREOL process by using current exposure systems with slight modification and a thermal resist.

1.2.4 Photomasks

Photomasks are integral components in the lithographic process of semiconductor and MEMS manufacturing. Conventional photomasks are made of high-purity quartz or glass plates containing precision images of integrated circuits or MEMS parts. They are used as masters to optically transfer these images onto substrates coated with photoresists. IC chips and MEMS devices are manufactured layer by layer, and each layer requires a unique photomask. The current generation of semiconductor devices has 25 or more layers; thus a chip needs 25 or more masks. According to the type of image transferred to the substrate, photomasks can be categorized into two groups: binary and grayscale photomasks. The image transferred from a binary mask to the substrate is a 2-dimensional (2D) structure, while the image from a grayscale mask is 3-dimensional (3D).

1.2.4.1 Binary Photomasks

Binary photomasks consist of two types of image regions: opaque and nearly completely transparent areas. Both the opaque and the transparent areas have spatially constant transmission so that the light intensity does not change after shining through them: light is either completely blocked or transmitted. Binary photomasks are normally used to expose substrates which are in

focus. This kind of photomask has been and will still be widely used in micromachining and microfabrication, and the importance of photomasks in both industries is growing. For example, binary photomasks have been widely used together with mask aligners for the past four decades to produce features larger than 1 μm on substrates. Steppers typically reduce the mask image by 10 or 5×, thus mask feature sizes are 5× larger than those on the wafers. As exposure wavelength has been reduced: from I-line (365 nm) to deep-UV KrF-excimer laser (248 nm), ArF-excimer laser (193 nm) and F_2 laser (157 nm); mask magnification has been reduced from 5× to 4× to cope with increasing chip size. Six-inch-square, 0.25-inch-thick quartz plates are commonly used in steppers for both I-line and KrF exposure. The use of nine-inch-square plates has also been considered for future scanner applications [10,11].

While photomasks used for micromachining and microfabrication industries are less than ten-inch-square plates, a large area binary photomask has been attracting attention recently. That is the photomask for liquid crystal display (LCD) patterning. LCDs play a crucial role in our daily lives as the interface between people and digital technology. High resolution, various sizes of LCDs have been widely used as cell phone panels, laptop and desktop screens, camera monitors, and even large TV displays. Manufacturing of LCD displays requires large size photomasks. Currently, companies like SK-Electronics are developing photomasks with less than 1 μm resolution on 2 metre square masks [12].

A mask blank consists of an opaque film on a substrate. Quartz is usually used as a substrate material due to its high transmission at wavelengths shorter than UV (Newport Crystal Quartz® has 85% transmission at 175 nm wavelength [13]), its low thermal expansion coefficient (0.52×10^{-6}/K), and its chemical stability. The opaque film should have an optical density OD > 3 (less than 0.1% transmission). Equation 1.2 shows the formula to calculate optical density from transmission:

$$OD = -\log_{10}(T) \tag{1.2}$$

where T is the transmission of the material. An optical density larger than 3 means that the transmittance of the light must be less than 0.1%. The opaque film should also have the following properties [11]:

1) High chemical stability,

2) High durability against irradiation,

3) Strong adhesion to the substrate,

4) Moderate electrical conductivity, and

5) Ease of preparation and patterning.

Of all the materials with these properties, chromium and its compounds are those most widely used [11,14,15,16]. Pure Cr has high reflectance on both the film side and the glass side of a photomask, which causes trouble due to stray light. To solve the problem an anti-reflection coating (such as CrO_xN_y) is used on one side or both sides of the Cr film, as shown in Figure 1.5.

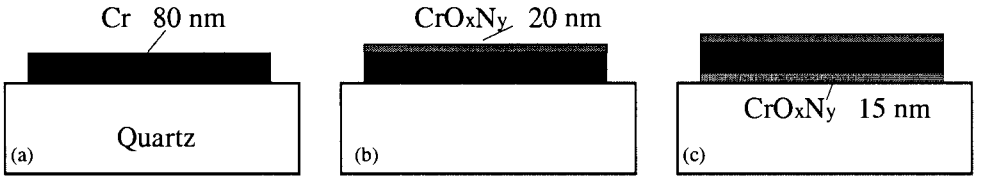

Figure 1.5 Structure of binary-intensity photomasks. (a) single-layer, (b) bi-layer, and (c) tri-layer.

The manufacturing process of conventional photomasks is similar to that of the microlithography and etching of silicon wafers shown in Figure 1.1, which involves many of the same steps such as resist coating, resist patterning, development, etching, etc. Figure 1.6 shows a typical process flow for the preparation of a photomask [11]. The details of the main steps which are different from those for wafer processing are described as follows.

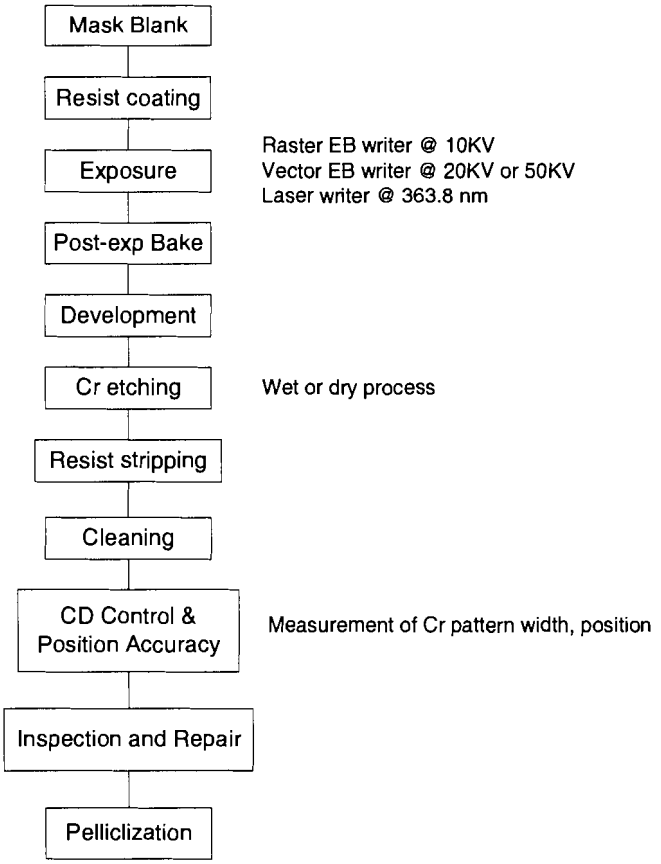

Figure 1.6 Process flow chart of mask manufacturing.

Resist coating: Photo resist with a target thickness of 300 – 500 nm is spun on the blanks with an accuracy of 3 – 5 nm, except within 5 mm of the edges [11].

Resist patterning: Patterning is done with a raster or vector scan beam exposure system that converts a CAD design file into the structures for that layer. Electron beam (EB) writers are mainly used in production. However, laser writers have also taken up an important role both historically and recently. As the device geometry gets smaller, the EB diameter must shrink, lowering the throughput of the system. For example, one study has shown that, to make a 4 Mb DRAM mask (0.7μm technology), a 0.5 μm beam diameter is needed and the throughput is 1.3 mask/hour; but for a 256 Mb DRAM mask (0.25 μm technology), a 0.05 μm beam diameter and the throughput drops to 0.0125 mask/hour [11].

Etching: Wet-etching is commonly used. An aqueous acid solution of ceric ammonium nitrate, $(NH_4)_2Ce(NO_3)_6$, and perchloric acid, HClO, is used as the etchant. However, the use of dry etching has increased [11].

CD-control, position accuracy, inspection and pelliclization: CD-control is to ensure the accuracy of the feature sizes in the pattern. Position accuracy, also called placement or registration accuracy, is the correctness of the pattern placement in a single mask and among a set of masks for a device. Mask inspection detects defects created during the mask making process. Each type of mask has a minimum intolerable defect size, flaws larger than which should either be removed or repaired. Pelliclization involves the mounting of a pellicle on the Cr film side of the mask to prevent foreign materials from adhering to it. All these post-patterning steps are to ensure the quality of the mask, which will influence the microlithographic process in production.

In summary, the making of conventional Cr binary photomasks requires 5 – 9 process steps. The EB writing systems are expensive and will have lower throughput as design rules become smaller.

1.2.4.2 Greyscale Photomasks

Different from binary masks, grayscale photomasks generate spatially variable transmission with many transmission values (grayscales). Greyscale photomasks have attracted much attention recently for the application of making three dimensional micromachined mechanical, electrical and optical devices, using a modification of conventional IC manufacturing photolithography and reactive ion etching (RIE). There are two main categories of grayscale photomasks: binary (or digital) grayscale masks, and analogue grayscale masks.

Halftone grayscale masks are the typical digital grayscale masks, and are manufactured like typical binary Cr masks, and have been utilized by the industry for many years [17,18,19,20]. The masks use photographic emulsions or chrome as the light absorbing / blocking material, and

are made with conventional photomask making processes, which include chrome deposition, photolithography, etching of patterns and photoresist strip. As shown in Figure 1.7, a state-of-the-art halftone chrome mask consists of a mixture of 0.5 μm chrome square or round equal size spots which are totally opaque (light blocked by Cr film) and spots which are completely transparent (area not covered by Cr film) on the glass photomask substrate. The grayscale in a halftone chrome mask is determined by the ratio of the number of opaque spots to transparent spots within a grayscale resolution unit. For a grayscale chrome mask having 4 grayscale levels, a grayscale resolution unit must have 4 spots (or a square of 4 binary spots). When all 4 binary spots in a grayscale resolution unit are opaque, the grayscale resolution unit is totally opaque (0% transmission). When one spot is transparent, the transmission is 25% or (1/4). With the increase of the number of transparent spots, the transmittance increases linearly in steps of 25%. Thus, a 2-bit, 4 level grayscale photomask is obtained. It is noticed that the dimension of each unit increases as the grey level increases. For example, as shown in Figure 1.7, a 2-bit, 4 level grayscale resolution unit is 1 μm × 1 μm, a unit of 4-bit, 16 grayscale levels is 2 μm × 2 μm, and a unit of 8-bit, 256 grayscale levels will be 4 μm × 4 μm. The exposed resist surface is placed at a certain defocused position, where the scattering and the diffraction of the spots can be ignored, and the dots merge to create an exposure intensity that replicates the corresponding grayscale image.

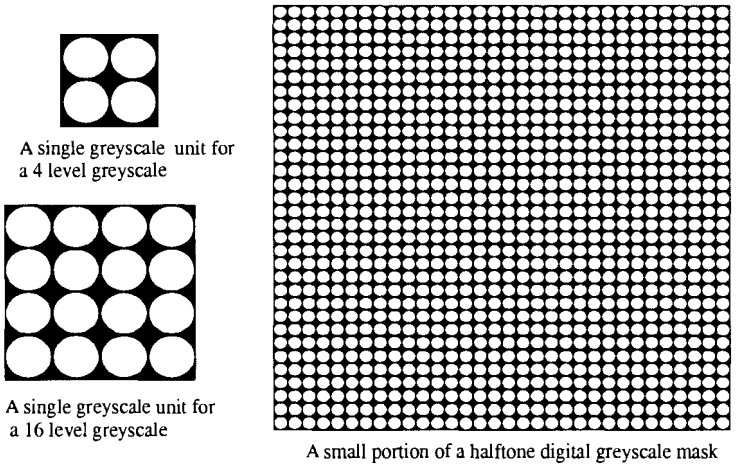

Figure 1.7 Halftone grayscale photomask.

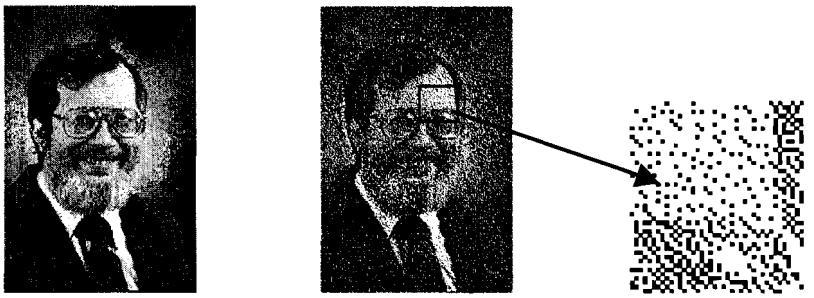

Figure 1.8 Example of a halftone grayscale picture.

Figure 1.8 is an example showing how halftone grayscale works. The left picture is an original 8-bit grayscale bitmap image. The middle is the binary halftone grayscale image. The right is the enlarged detail of the halftone picture, with the tiny square as the single unit. As mentioned earlier in this section, it is necessary to blur the mask image on the photoresist surface during exposure. The defocus distance is about 80 μm in the example cited [21]. More defocus gives a smoother resist surface, but also causes lower lateral resolution. On the other hand, the original binary pattern will appear if enough defocus is not used. It is always time-consuming to find the best exposure position. High laser power is another problem with halftone grayscale masks, which will be discussed later.

In comparison, analogue grayscale masks have a continuous tone of grey level, as shown in Figure 1.9 (a). Instead of being either fully transparent or completely opaque as in a digital grayscale mask, each grayscale unit in an analogue grayscale mask can be at any grey level. The total number of grayscale levels is dependent on the analogue grayscale mask material. So far, some special glass materials have been developed [2,22]. Wu proposed HEBS (High Energy Beam Sensitive) glasses [2] whose optical density changes with the electron beam dosage and acceleration voltage. He claimed that more than 1000 grey levels can be assigned to each spot. Since HEBS glass is a direct-write material, this simplifies the grayscale mask manufacturing process. Defocusing of the substrate is not necessary as the light intensity is directly modulated

by the mask material (Figure 1.9 (b)). Figure 1.9 (c) shows a slope is created on a positive photoresist after being exposed with the grayscale mask in (b).

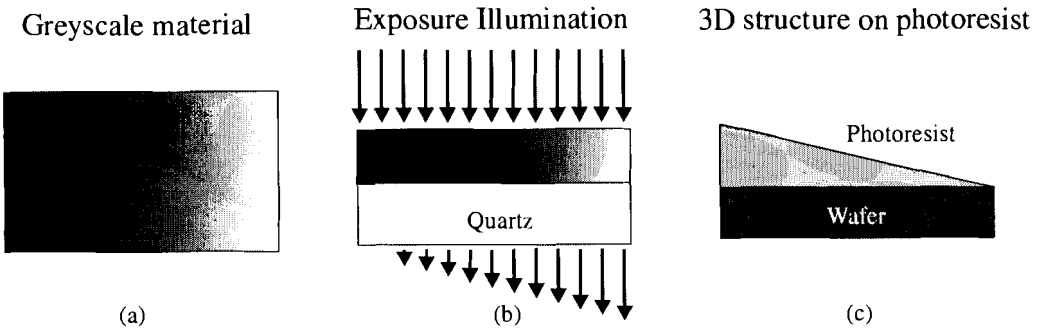

Figure 1.9 Analogue grayscale photomask: (a) an analogue grayscale mask material has continuous grey tone; (b) during exposure, defocusing of substrate is not needed; and (c) a 3D slope made on a positive photoresist.

1.2.4.3 Direct-Write Photomask

Direct-write photomask refers to a new mask making process where an e-beam or laser beam is used to directly write the mask pattern in a material whose transparency can be varied with exposure. In the previous two sections, two types of photomasks (binary and grayscale masks) were discussed. Chrome binary and grayscale mask patterning requires several multi-step processes that include direct e-beam or CW laser scanning of resist layers, followed by resist development and sample etching to form the desired pattern. To simplify the mask making process, people have looked into different processes and materials that allow direct image formation on quartz substrates.

Laser ablation is one of the direct-write approaches that can potentially shape high-resolution structures in a single processing step. Direct writing of thin chrome layers for photomasks has been studied by Venkatakrishnan using a Ti:sapphire chirped-pulse amplified ultra fast laser [23]. As a matter of fact, ultra fast lasers are currently used at IBM for photomask repair [24,25], taking the advantage of the short-pulse interactions to avoid damage to the underlying quartz substrate. However, an expensive short-pulse laser system is needed for this

technique. Furthermore, the damage thresholds, debris control, ablations rates, and incubation processes are still major unsolved issues preventing this direct-write method from being used widely.

Using materials whose optical density changes after exposure to certain radiation, is another way of direct-writing photomasks. Drexler [26] heated up an exposed silver-halide emulsion to 250°C, and the emulsion became visually transmissive to yellow-orange light in both silver and non-silver clear areas, but opaque to ultraviolet wavelengths in the silver areas. However, due to the low transmission at < 500 nm, this emulsion material cannot be used for current UV exposure systems.

1.2.5 Issues with Conventional Photomasks

As described earlier, the typical Cr binary photomask manufacturing process involves the blank mask preparation: Cr and Cr oxide deposition, photoresist coating, resist baking, laser or e-beam direct-writing, resist development, metal layer dry or wet etching, resist stripping and cleaning. There are many issues with the current photomask and its preparation processes. Firstly, it is difficult to minimize defects, as there are 5 – 9 operation steps involved in making a photomask and each step can introduce process defects and particles. Secondly, mask damage from ESD (Electro-Static Discharge) has long been a concern. Although effort has been spent in making the photomask and the pellicle set conductive by adding conductive films, conductive frames, conductive dust pellicles, etc.[48,49], ESD damage can be more problematic due to the shrinkage of feature size. Furthermore, masks for 157nm lithography will be kept in ambient atmospheres nearly free of water, which will increase the risk of ESD damage [50]. Thirdly, although Cr dry etching has become a standard mask-making process step, the loading effect is still a serious problem. The chrome etch rate changes with the ratio of clear area to opaque area

on the mask, which can seriously affect Critical Dimension (CD) control [51]. Fourthly, the cost of mask-making is escalating. A 0.18 μm binary photomask for critical layers costs $8000 – $22,000, and those for non-critical layers cost $18,000 - $20,000. OPC (Optical Proximity Correction) and PSM (Phase Shift Mask) add substantially to these prices[52]. In order to solve all these issues, people in the semiconductor industry must explore new processes and new materials. For example, Takaoka, et al[53], proposed a sol-gel combined with a DTR (diffusion transfer) process. A liquid containing metal oxide is applied to the substrate, and this dried and heated coating acts as a physical development nucleus layer into which a silver complex compound is diffused to form a silver film at the unexposed area. Plasma etching is not necessary. However, it still involves more than 5 steps.

Gray-scale photomasks, especially the digital type, have problems similar to those of binary Cr photomasks. Furthermore, the out-of-focus process requires increased illumination levels, and mask deterioration is observed when the laser intensity is greater than 200 mJ/cm^2 [54]. HEBS is one of the most popular analogue grayscale mask materials. However, specific CAD tools are required for the generation of mask data of the e-beam drawing system. The e-beam conversion process takes an extremely long time and requires very powerful e-beams [2], hence it is very costly. Also the best working wavelength of the mask is around 500 nm, at which HEBS glasses give the largest optical density difference before and after the electron beam irradiation. This is incompatible with current deep UV lithography systems. These two drawbacks prevent HEBS glasses from being widely used in the industry.

1.2.6 An Alternative to Conventional Photomasks

To solve all the problems mentioned in previous section, this thesis will present a novel single step direct-write photomask made from bimetallic thermal resists, including Bi/In and

Sn/In. Unlike lithographic steps for patterning conventional photomasks, bimetallic thermal resists themselves are thermally activated optical materials. Hence, patterns can be directly written onto the films, causing the exposed area to become more transparent. The optical density of the films substantially decreases with laser exposure, going from highly absorbing (3 OD) to nearly transparent (0.26 OD). Mask defects can be drastically reduced since many fewer steps are needed in the preparation process. Moreover, because both the exposed and unexposed Bi/In are conductive, there is inherently no ESD problem with this type of photomask. Obviously the manufacturing cost of bimetallic thermal resist photomasks will be much lower than conventional masks. This mask material is targeted at I-line or mask aligner applications.

Since the optical density of the bimetallic films decreases nearly linearly with the laser power, both Sn/In and Bi/In films can be used as direct-write analogue grayscale photomask materials which have much better features than HEBS and any of the other grayscale mask materials available on the market.

1.3 Thesis Objectives

This thesis will present a new class of bimetallic thermal resist that is compliant with an all dry process and requires exposure energy doses comparable to current organic photoresist. Because the conversion process is thermally activated, the bimetallic resist maintains the wavelength invariance characteristic of other inorganic thermal resists while increasing the exposure sensitivity. Three different bimetallic resists will be studied: Bi/In, Sn/In and single metal In. Features unique to each one of them will be shown. Excellent results will be presented to demonstrate that these bimetallic thermal resists are promising resist and photomask materials for micromachining and microfabrication.

Chapter 2 introduces the concept of bimetallic thermal resists and describes the concept and initial development of a Bi/In thermal resist. This builds on the work done previously by Prof. Glenn Chapman and his graduate student Mr. Marinko Sarunic. It will be extended with some new supporting data and analysis in this thesis.

Chapter 3 models the optical interaction of an incident light with bimetallic films using the Airy Summation method and presents the wavelength invariance theory for these new resists. Prof. Chapman and Mr. Sarunic set up a two-metal-layer optical model in 1999. They explored the film optical performance only down to 193 nm. In this research, the wavelength invariance will be explored over a wider range from IR to X-ray using this model. Also, an extended three-layer optical model will be investigated.

Chapter 4 describes the preparation of the bimetallic thermal resists and the experimental setup, which include the laser exposure system, the plasma etch system and the analysis tools.

Chapter 5 demonstrates that a bimetallic thin film is a completely functional thermal resist that can be exposed, developed and stripped.

Chapter 6 studies the material structures of the thermal resist films before and after the laser exposure, and presents a structural mechanism of the laser conversion.

Chapter 7 continues to show that, after development, a bimetallic thermal resist can act as an etching mask layer for both wet and dry etching, which is not possible for conventional resists. Other unique features are also presented.

Chapter 8 explores the applications of bimetallic thermal resists as direct-write photomask materials for both binary and grayscale masks.

Chapter 9 models the thermal conversion process of the bimetallic films when exposed to laser radiation.

Chapter 10 discusses the contamination compatibility of bimetallic films with silicon processes.

Chapter 11 presents conclusions and discusses future work that should be done to improve the performance of bimetallic thermal resists.

Chapter 2
Creating Sensitive Bimetallic Thermal Resists

2.1 Introduction

This chapter introduces the underlying strategies behind bimetallic thermal resists and their applications in micromachining and microfabrication. As discussed in the preceding chapter, previously investigated inorganic metallic thermal resists are too insensitive to be exposed by conventional laser exposure systems and thus have no practical value. A thermal resist should have five basic characteristics:

1) It should be sensitive to and fully converted by sufficient illumination;

2) The conversion caused by irradiation should produce significant chemical changes in the resist film so that it can be developed by wet or dry methods with good selectivity; and

3) The developed resist should be resistant to wet and/or dry etching. No resists are currently known to be resistant to both Si anisotropic wet etching and dry plasma etching.

4) The resist should be removed easily (stripped) when dry or wet etching is done or when photolithography rework is needed.

5) The resist should be compatible with silicon processes and not poisonous to silicon devices.

In this chapter, the prerequisites for a sensitive, inorganic, metallic thermal resist will be investigated, including the melting point, the thermal conductivity of the material, the optical properties of the deposited film, the energy of the metal-oxygen chemical bonds $D°$, and the reduction potential $E°$ of the metal. The latter two are mentioned because, as found in Chapter 6,

the laser conversion is an oxidation process, and the film's chemical stability before and after laser exposure is important. Based on these requirements, a material selection is then conducted to locate the best material or material combination. Finally, the thermal resist film structure is discussed (i.e., should it be a single layer, bilayer or multilayer structure).

2.2 Requirements for a Sensitive Metallic Thermal Resist

2.2.1 Exposure: Sensitive to Irradiation

Since a thermal resist is sensitive to and converted by heat, two questions are asked when it is exposed to a laser beam: how much heat is needed to fully convert the resist; and how efficiently does the resist film absorb the light energy and convert it into heat.

It is obvious that the less heat required the more sensitive the thermal resist. The experience with previous metallic oxide thermal resists Fe/O and Al/O tells us that a lower melting point metal gives us better sensitivity, since the conversion can start at a lower temperature. Since the melting point of a eutectic phase of a binary alloy is lower than either of the two metals, higher sensitivity is expected by using eutectic bimetallic systems. Thus, both low melting point single metal and bi-metal systems can be our choices. Figure 2.1 shows a typical binary phase diagram of A and B metals, with one eutectic point. One can see, the eutectic point at E is lower that the melting points M_A and M_B of A and B, respectively.

An additional possible advantage of using a bilayer eutectic systems is that when an area is exposed to radiation and undergoing eutectic thermal conversion, it is surrounded by single metals with higher melting points. This could help enhance the image resolution.

However, even with a significantly low melting point, the thin film resist cannot be converted if it does not absorb laser light efficiently. Thus, materials with a high optical absorption coefficient are desired. The optical absorbance of a thin film is determined by its n and

k values, film thickness, film structure (single layer or multilayer) and the light wavelength. Chapter 3 will discuss this issue in detail with an optical model.

Heat dissipation is associated with the thermal resist conversion process. A much higher energy density is needed to expose thermal resists with conventional CW lasers (I-line and longer wavelength sources) compared to pulsed lasers, since the heat dissipation rate is close to or comparable with the energy input rate. This means that a significant portion of the energy is wasted, making thermal resists less applicable for industrial applications. With the UV and DUV pulsed laser sources now being used in the industry, thermal resists become a feasible process since the energy input rate is now much faster than the heat dissipation rate. Hence, much less energy density is needed for the exposure of thermal resists, making it nearly as sensitive as organic photoresists.

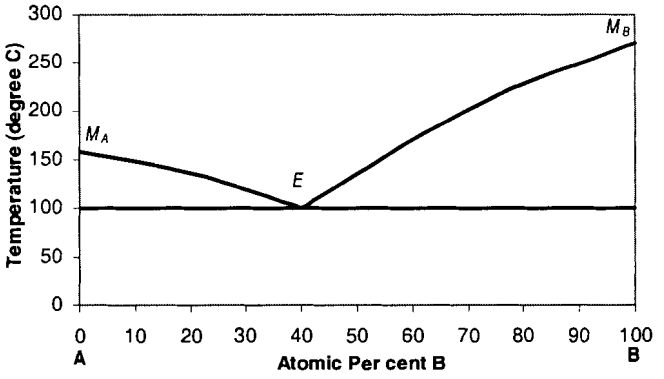

Figure 2.1 Typical binary phase diagram with one eutectic point.

The thermal conductivity of metals tends to be much higher than that of organic or semiconductor materials. This could be a problem for metallic thermal resists, since too much heat dissipation will not only lower the sensitivity, but also reduce the image resolution. Lower thermal conductivity is preferred when we search for thermal resist candidates [47].

In order to create an all-dry inorganic thermal resist, the selected material should also be compatible with PVD (Physical Vapour Deposition) and / or CVD (Chemical Vapour Deposition) processes. The deposited film should not have any physical or chemical changes under the typical storage conditions in a manufacturing environment for an acceptable period of time before the next process step. For example, conventional organic photoresists are stable for dozens of hours after soft bake and before exposure. Hence, metals with melting points close to room temperature are not suitable for a thermal resist application, as it is difficult to prepare thin films of these materials before they melt in normal environment.

2.2.2 Development: High Dissolution Ratio of Exposed and Unexposed Regions

When organic photoresists are exposed to a light of certain wavelength, photochemical reactions cause the rearrangement of chemical bonds, and hence the significant difference in chemical properties of the resists between the exposed and unexposed areas. This results in a modification of dissolution properties in alkaline solutions, enabling the development of a relief image. While an etch rate ratio (often called dissolution ratio in organic photoresists) of 10 is just sufficient to get a decent exposed pattern, the resolution of the lithography increases with the ratio [11].

An inorganic metallic thermal resist must exhibit a larger than 10 development selectivity. To achieve this ratio, laser conversion should induce substantial physical and chemical changes in the exposed areas. For a single metal resist film, phase change of the material and / or chemical reaction with the atmosphere is expected after exposure. For a bimetallic film, besides the above two transformations, alloying is also possible. A special solution (developer) should accordingly be made available for wet development, which preferentially removes the exposed area (or the unexposed), and retains the unexposed area (or

the exposed). Most of the conventional organic and inorganic resists (photo and thermal) are developed by wet acid or alkaline solutions. In order to have an all-dry process, it is desirable that the exposed inorganic metallic thermal resists could also be developed with dry plasma etching.

2.2.3 Etching: Good Resistance to Dry and / or Wet Etching

The essential function of an exposed and developed resist pattern is to allow the transfer of the pattern into the layer underneath, and at the same time provide a protection layer to the covered areas. The underneath substrates / layers that need patterning in the micromachining and microfabrication industries are silicon, silicon dioxide, silicon nitride, titanium nitride, copper, aluminium, tungsten, etc.. In order to ensure proper pattern transfer from the resist to these substrates, the etch rate of the resist should meet the requirement of the process. For 2D patterning, the etch rate of the resist should be sufficiently lower than that of the substrate; while for 3D structure transferring, the resist etch rate can be equal to that of the substrate, or tuned to meet the process specification. This thesis will focus on metallic thermal resists for 2D applications.

The required etch selectivity for semiconductor manufacturing is dependent on the thickness of the underlying layer that the resist pattern will be transferred onto, and also the thickness of the coated resist. Although, the selectivity varies with different layers, a selectivity larger than 1:3 is preferred by the process engineer [6]. Nevertheless, much higher selectivity is requested by micromachining, as much deeper and longer etching is necessary to make bulk-machined structures. Deep reactive ion etching (RIE) requires selectivity as high as 1:80, in order to make power electronics and harsh environment MEMS with an etch depth of 100 μm [55].

It was discussed in the previous chapter that none of the current organic photoresists are compatible with silicon anisotropic etching, since most organics are eroded away quickly in

heated alkaline solutions. However, it is desirable to have an inorganic thermal resist that works with both wet and dry etching. This "almighty" resist, together with a process combination of wet etch and dry etch, can enable one to create some special structures that are not possible by other processes.

2.2.4 Resist Removal

Resist removal or stripping is the last step of the lithography process, after dry or wet etching is completed. Before the next functional layer can be deposited onto the silicon wafer, the resist residues must be removed, as they are a source of contamination to semiconductor devices and subsequent processes. Conventional organic photoresists are removed either by solvent or O_2 plasma etching. After stripping, thorough cleaning, such as an RCA clean, is required. When CD or overlay registration check fails after exposure, photolithography rework is inevitable. In the rework process the resist, together with the developed image (relief pattern), is removed either by solvent or O_2 plasma etching. A new inorganic metallic thermal resist should also have the property of being easily stripped off.

CD and overlay check is done after development, because the latent image (the exposed pattern in a resist before development) in conventional organic photoresists is not visible. Thus, whether photo-rework is needed is only known after the resist is developed. Several process step and considerable cycle time could be saved, if the latent image is visible. This thesis will show that our new bimetallic thermal resist exhibits this advantageous feature.

2.2.5 Compatibility with Silicon Processing

Sub-micron device technologies are highly susceptible to contamination, such as particles and chemical impurities which are present during the silicon process. Among the most well-

known contaminants, metallic impurities are a major source of performance failure in IC devices including increased p-n junction leakage, degradation of gate oxide breakdown voltage and reduced carrier lifetime. As critical device geometries continue to shrink below 0.13 μm, strict control of contaminants in the whole process cycle has become mandatory. Thus, metals including Ag, Au, Cu, Na, and K, should not be considered for metallic thermal resists.

Reactions with silicon substrates, such as alloying and the formation of inter-metallic compounds should be avoid, as these changes will also poison the silicon devices. However, a thick amorphous carbon film can be used as an intermediate protection layer between the metallic thermal resist and the substrate to solve this problem. Marinco Sarunic discussed this carbon protection layer process in his thesis [56].

2.3 Materials Selection

2.3.1 Metals with Lower Melting Points

The initial exploration of materials for potential bimetallic thermal resists was pretty much done by Mr. Sarunic and Professor Chapman in 1999. Details can be found in Sarunic's master thesis [56]. In this thesis we extend that work with newer experimental and theoretical understanding of the resist process. Figure 2.2 is a comparison of melting points of some of the widely used metals. Fe has a very high melting point, hence a high Fe/O resist conversion temperature. Al melting point is less than half of that of Fe. Thus, one can see a sensitivity improvement for Al/O resist. There are three metals (excluding Hg) whose melting points are lower than that of In and are very close to room temperature: Rb, Ga and Cs. Actually Rb and Cs are in liquid state at room temperature. Li has a melting point slightly higher than In. However, these four metals are not suitable for metallic thermal resists applications. Li, Rb and Cs are chemically unstable (the metals with * in Figure 2.2), as they all react fiercely with water at room

temperature. Thus, the three metals that most likely meet the requirements for a sensitive metallic thermal resist are In, Bi and Sn.

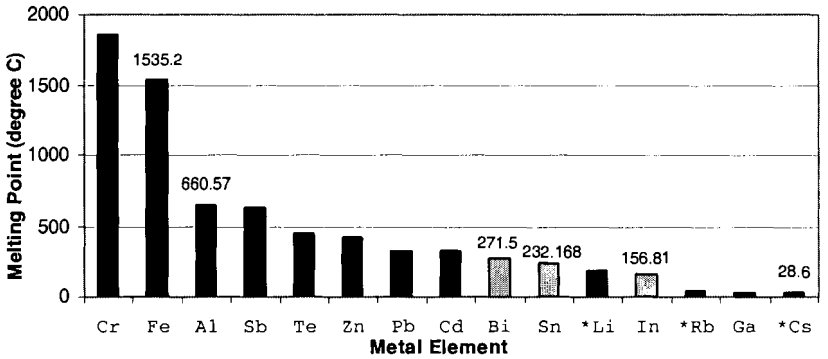

Figure 2.2 Comparison of melting points of some metals. (Data from [58])

It is worth mentioning here that alloying of two metals was first speculated to be the bimetallic thermal resist exposure conversion mechanism, and much of the effort was focused on searching for suitable two metal systems. However, as will be discussed later in Chapter 6, oxidation is essentially what happens during the laser exposure. Therefore, both single metal and bimetal systems can be metallic thermal resist candidates, as long as they meet the requirements stated in Section 2.2.

Bismuth is the most attractive metal as it has a low melting point, the lowest thermal conductivity (as shown in Figure 2.3) and also a low reflectivity. Unfortunately, as will be discussed in Chapter 6, Bi does not form a continuous film after laser exposure, thus, it is not a good single metal resist candidate. Nevertheless, it is still suitable to be the top layer for a bimetallic thermal resist. Indium is clearly the best choice as a single metal thermal resist, with the lowest compatible melting point and moderate thermal conductivity. Indium is also the best option as the bottom layer of a Bi/In bimetallic thermal resist, as Bi and In form three low temperature eutectics, as shown in Bi-In phase diagram in Figure 2.4. Bi is a Group V element and In is a Group III element. If there is any unwanted doping effect with Bi/In resist, the p-type In doping can be cancelled by the n-type Bi doping [56]. Besides Bi and In, Sn also shows

promising properties including a low melting point, low thermal conductivity, and forming eutectics with In, as shown in the Sn-In binary phase diagram, Figure 2.5.

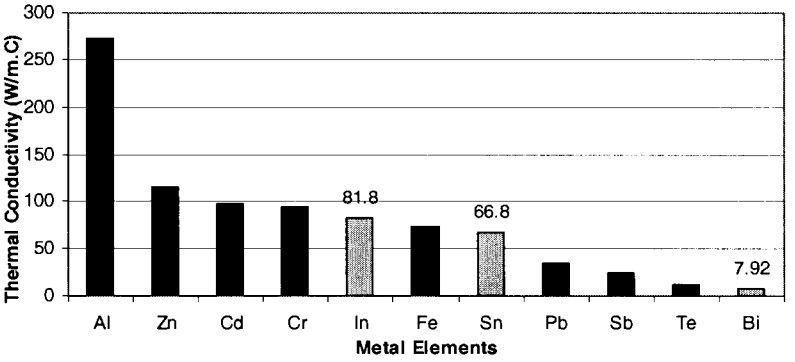

Figure 2.3 Comparison of thermal conductivity of metals. (Data from [58])

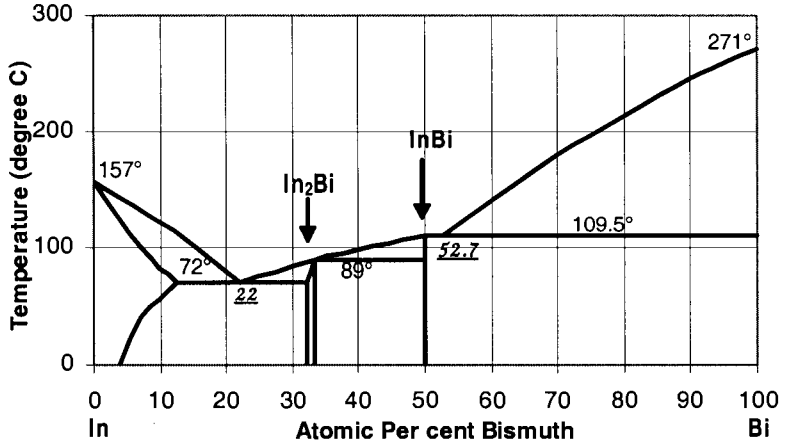

Figure 2.4 Bi-In binary phase diagram [57].

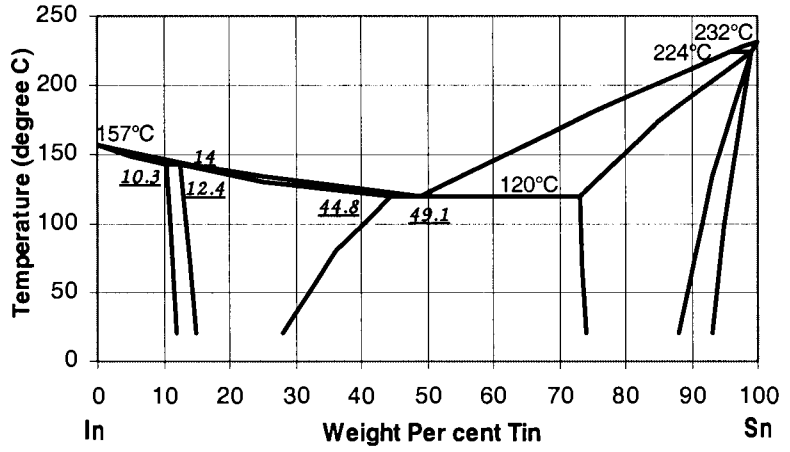

Figure 2.5 Sn-In binary phase diagram [57].

Table 2.1 Comparison of reduction potentials $E°$ (Volts) of important reactions [58].

Reduction Reaction	Reduction Potential (V)
$Li^+ + e = Li$	-3.0
$Al^{3+} + 3e = Al$	-1.7
$Fe^{2+} + 2e = Fe$	-0.45
$In^{2+} + e = In^+$	-0.40
$In^{3+} + 3e = In$	-0.34
$Ni^{2+} + 2e = Ni$	-0.26
$In^+ + e = In$	-0.14
$Sn^{2+} + 2e = Sn$	-0.14
$2H^+ + 2e = H2$	0
$Bi^{3+} + 3e = Bi$	0.31
$Cu^{2+} + 2e = Cu$	0.34
$Bi^+ + e = Bi$	0.50
$Au^+ + e = Au$	1.7
$F_2 + 2e = 2F^-$	2.9

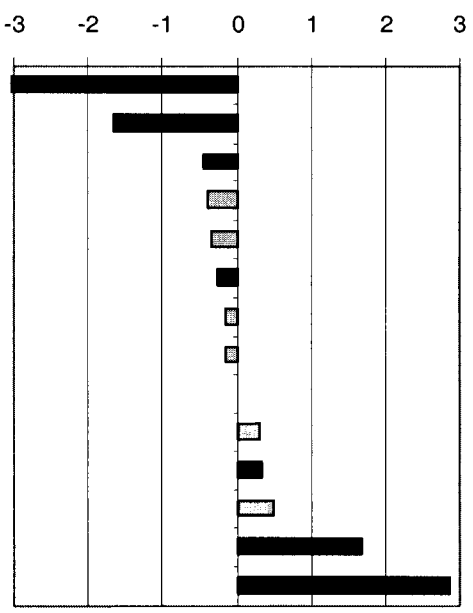

2.3.2 Chemical Properties of Metals

One point not understood at the time of Sarunic's thesis was that, which will be discussed in Chapter 6, the laser conversion is not only a process of melting the metal or metals, but also a chemical reaction. Thus, chemical stability of the metals before laser exposure is critical. Bi, In and Sn must be very stable under normal environment: they should not oxidize, or react with water. Table 2.1 lists the reduction potential $E°$ of some metal reduction reactions at 25°C and 1 atmosphere. The reduction potential is the quantitative tendency for a half reaction to occur in the reduction direction, or the tendency of a half reaction to accept electrons. A reaction will be exergonic if the half reaction acting in the electron accepting direction has a reduction potential that is more positive than the one acting in the oxidation direction. It is the inherent tendency of a compound or element to act as an electron donor or an electron acceptor. Measured in volts, the more negative the reduction potential, the easier the element will lose electrons, and thus oxidize. $Li^+ + e = Li$ has a reduction potential of -3.04 V, indicating that Li is very active, unstable and likely to oxidize. On the other hand, the element has a stronger tendency to accept electrons if it

has a more positive reduction potential value. The reduction potential of $F_2 + 2e = 2F^-$ indicates that F_2 is also a very active and unstable gas. Reduction potential is a good meter to determine the stability of an element: the lower the absolute value the more stable the element. Bi, In and Sn have absolute value reduction potentials ≤ 0.5 V, showing that these metals are very stable under normal conditions. Shelf tests of as-deposited Bi, In and Sn discussed in Chapter 5 confirms this prediction.

Chemical stability of the converted material after laser exposure is also vital to a lithography process, as it ensures that the exposed pattern will not deform due to chemical reactions in the subsequent processes. Chapter 6 reveals that laser conversion is actually an oxidation process. Metal oxides, such as In_2O_3, Bi_2O_3 and SnO are generated after laser exposure. The stability of a metal oxide is, to some extent, reflected in the metal-oxygen bond strength, which measures how much energy or enthalpy is needed to break a chemical bond. Figure 2.6 is a comparison of metal-oxygen bond strengths. Bi-O and In-O have similar, medium bond strength, higher than Cu-O and lower than Al-O. This implies that In_2O_3 and Bi_2O_3 could be more stable than CuO, although not as stable as Al_2O_3. Sn-O has a bond strength even higher than Al-O. In summary, metal-oxygen bond strength data indicate that laser converted material: Bi, In and Sn oxides are chemically stable. Shelf test experiments of laser converted Bi, In and Sn presented in Chapter 5 are consistent with these predictions.

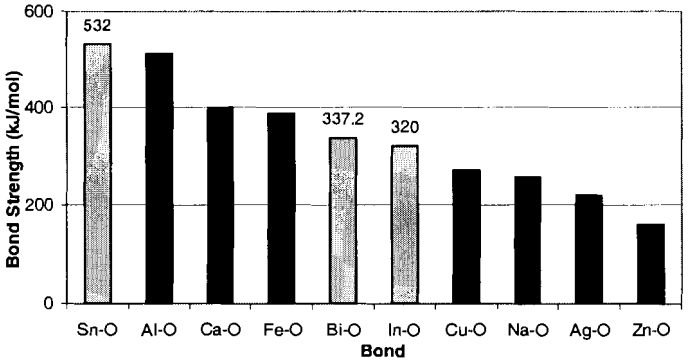

Figure 2.6 Comparison of metal-oxygen bond strength [58].

2.4 Thermal Resist Film Structure

Section 2.3 discussed the three metals that likely meet the criteria for a sensitive thermal resist. How will the material be arranged in a film? It is easy for a single metal thermal resist: a single layer of the metal will be deposited on a substrate. How about a bimetallic thermal resist such as Bi/In or Sn/In? Should the resist be prepared as a bilayer structure or a single mixed metal layer, as shown in Figure 2.7? How thick should the thermal resist be?

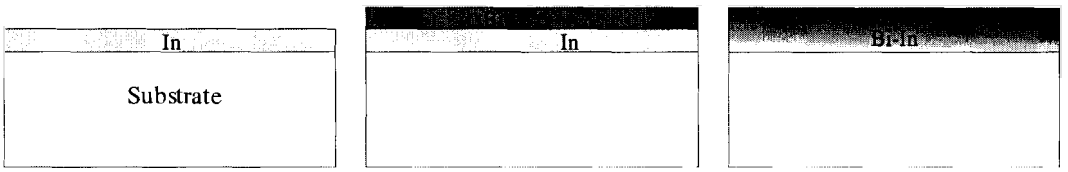

Figure 2.7 Metallic thermal resist film structure.

From the point of view of film preparation, a bilayer structure is preferred. DC- or RF-sputtering, which will be used to put metal films onto a substrate, will be more efficient to deposit two layers of different metal films onto the substrate from two separate targets than to co-sputter two targets to get one mixed metal layer. One can have a much more accurate control over the composition of the bimetallic films with a bilayer structure than with a single mixed layer. It is also easier to vary the composition. Optical modelling of light absorption by as-deposited film, which will be discussed in Chapter 3, reveals that a two-layer structure has better light absorption. Thus, it is more thermal-sensitive than a single layer structure. And this is in agreement with experimental results shown in Chapter 5.

The sensitivity of the thermal resist and the influence of thickness on the vertical profile are the two major issues that should be considered when we choose the resist film thickness. Modelling using a 2D finite element, linear heat conduction analysis, discussed in detail in Chapter 9, reveals that thinner thermal resist is more sensitive than thicker resist. Thinner resist

has also better sidewall profile than thicker ones, and that the CD control should also be more accurate for thinner film. It is obvious that the metal films should be very thin, on the order of 10 (to form continuous metal film) to 100 nm, in order to be exposed at a low laser energy level and to have a good profile.

Will such thin thermal resist provide enough protection during wet or dry etching process? This question will be answered positively in Chapter 7. Even if the answer were no, we still could use a carbon protection layer process proposed by Chapman and Sarunic [56] after Bozler [45], as shown in Figure 2.8 to solve this problem.

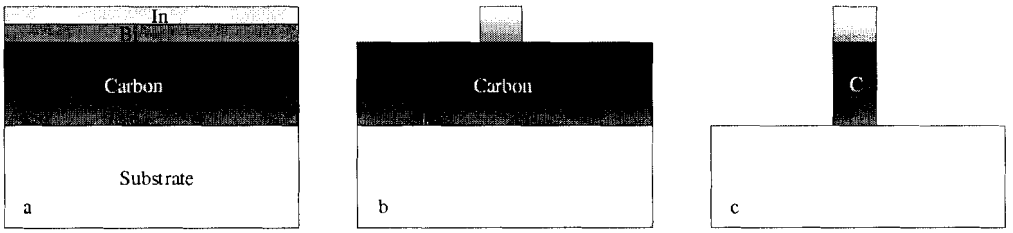

Figure 2.8 Thick carbon film as a protection layer in a thin inorganic thermal resist process.

The first layer deposited on the substrate is an a-C:H film, which can be prepared by PVD method in a hydrogen atmosphere, as shown in Figure 2.8 (a). The thickness of the carbon protection layer can range typically from 0.5 to 2.5 microns [59], according to the process requirement. If Bi/In thermal resist is used, the two metal films are then deposited on top of the carbon layer. The metallic thermal resist is first patterned and developed, as shown in (b). The pattern on Bi/In film is then transferred to the carbon protection layer through oxygen plasma etching, as shown in (c). As it is known to be resistive to many reactive ion plasma and wet chemical etching [59], carbon film can be used as a plasma etching protection layer for longer etching. (Refer to Chapter 7 for further discussion)

2.5 Summary

This chapter introduced the criteria for a sensitive metallic thermal resist: low melting point, optically absorbing and low thermal conductivity. Eutectic alloying is a good way to further bring down the melting point. To be a complete thermal resist, physical and chemical properties should change enough after laser exposure, so that the exposed pattern can be developed by wet dissolution or dry plasma etching. The laser converted material should also be resistant to wet and / or dry etching for pattern transfer from the resist to the underneath substrate. Material search based on these requirements gives promising results. Bi, In and Sn are three of the best metals suitable for thermal resist applications. Oxygen bond strength and reduction potential data indicate that these three metals are chemically stable before and after laser conversion. Bi/In and Sn/In are good candidates for bimetallic thermal resists with lower eutectic points than each of the single metal. Primary analysis shows that a bimetallic thermal resist with thin bilayer structure is preferred. The next chapter will investigate the optical model of the bimetallic films.

Chapter 3
Optical Modelling and Wavelength Invariance

3.1 Introduction

Since thermal resists are converted by heat during laser exposure, it is important to understand how an incident laser beam interacts with the thermal resists, how much of the laser energy is absorbed to heat the sample, and how the energy absorption changes with film thickness, laser wavelength, film structure or different types of material. In this chapter, an optical model will be used to compute the light transmitted (T) through, reflected (R) and absorbed (A) by the as-deposited thermal resist during the laser exposure. The main purpose here is to use the model to investigate and explore the main advantage of inorganic bimetallic thermal resists: wavelength invariance from X-ray to IR. The influence of film structure on the sensitivity of thermal resists will also be calculated.

3.2 Optical Modelling: Laser Interaction with As-deposited Resists

This work extends a computer model developed by Sarunic [56]. Since he gave a complete description in his master's thesis, the optical model will only be discussed briefly. The significant difference between most other optical models and this bimetallic optical model is that the materials are highly absorbing. The refractive index of an absorbing material is defined in a complex number $\underline{n}$:

$$\underline{n} = n - ik \tag{3.1}$$

where n is the real part of the refractive index and k is the absorption index, which is the imaginary part of the complex refractive index [60]. For a completely transparent (non-absorbing) medium, k is zero, and for an absorbing medium, k is larger than zero.

The light absorption in a medium is governed by Beer's law. The light intensity has following relationship with the thickness of the film, light wavelength and the material property:

$$I_f = I_0 e^{-\frac{4\pi kd}{\lambda}} = I_0 e^{-(\alpha_l d)} \tag{3.2}$$

where I_f is the light intensity after the light travels through a distance of d in the film, I_0 is the incident light intensity, λ is the wavelength of the light, k is the absorption index, and $\alpha_l = \frac{4\pi k}{\lambda}$ is called the absorption coefficient. This equation can be rewritten in the following format to represent the attenuation rate of the electric field amplitude of light inside the medium:

$$a = \frac{E_f}{E_0} = e^{-\frac{2\pi kd}{\lambda}} \tag{3.3}$$

where E_f is the amplitude of electric field of the light after it travels through a distance of d in the film, E_0 is the amplitude of electric field of the incident light, and a the electric field attenuation rate.

Note that when metal films are exposed to laser illumination under a chemically active environment, such as oxygen or air, two additional effects may need to be considered: the modification of the optical properties of the exposed area, and the additional heat release due to exothermic reactions. These two effects can influence, sometimes even totally control the reaction process. In this section, as we are only interested in the heat conversion right before the chemical reaction, these two effects are ignored to simplify the optical model. It is further assumed that the metal films are optically uniform in thickness and have sharp interfaces with each other and with the substrate. Three interactions will be taken into account when light shines on a bimetallic thermal resist film: absorption when laser travels through the film, reflection and refraction at the film interfaces.

Sarunic compared two widely used methods for the calculation of the electric field magnitude in a film: the matrix method and the Airy summation. He found that only Airy summation can give reflection and transmission at each film interface, and also the energy deposited as a function of film thickness [56]. Airy summation adds up all the electric field vectors reflected and refracted at each interface of a multilayer film. Although it requires more calculation, the Airy summation has the advantage of giving light intensity at any point inside the film. As shown in Figure 3.1, the laser beam reflects and refracts at each of the interfaces inside the bilayer film on a glass substrate. Each reflected and refracted beam will further reflect and refract at the interfaces. The Airy summation adds the refracted electric fields on the air side, and together with the first reflection, it becomes the total reflection R. The sum of the refracted electric fields on the glass side becomes the total transmission T. The absorption A can be easily obtained by the following:

$$A = 1 - R - T \tag{3.4}$$

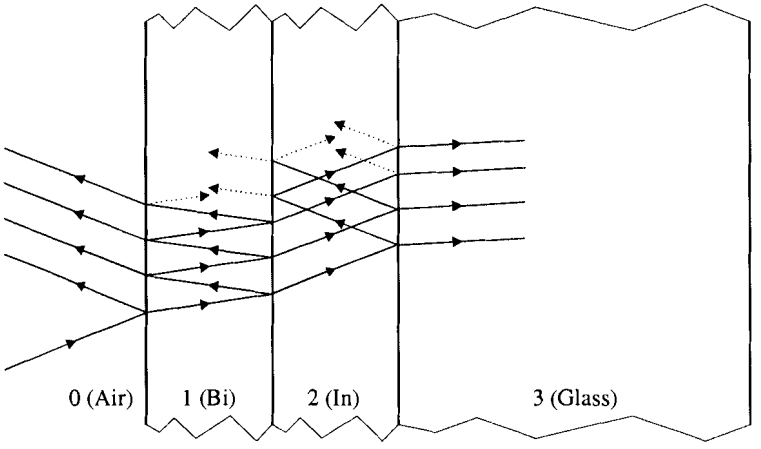

Figure 3.1 Laser beam reflects and refracts at each of the interfaces in a bilayer structure deposited on glass substrate. (After Sarunic's thesis Figure 2.4 [56])

If we assume a light beam perpendicular to the film surface, the reflection and refraction of the electric field at the film interfaces between two different films of refractive complex indices $\underline{n}_0$ and $\underline{n}_1$, are expressed by the Fresnel coefficients:

$$r_{01} = \frac{\underline{n}_1 - \underline{n}_0}{\underline{n}_0 + \underline{n}_1} \tag{3.5}$$

$$t_{01} = \frac{2\underline{n}_0}{\underline{n}_0 + \underline{n}_1} \tag{3.6}$$

where r_{01} is the reflection when light travels from medium *0* to film *1*, t_{01} is the refraction when light travels from medium *0* to film *1*[61]. The Fresnel coefficients r and t describe the behaviour of the electric field. The actual light intensity Fresnel coefficient is the coefficient times its conjugate. The light reflection R and transmission T are as follows:

$$R = r_{01}r_{01}^*; \text{ for media } n_0 \text{ and } n_1, \quad R = \frac{(n_1 - n_0)^2}{(n_0 + n_1)^2} \tag{3.7}$$

$$T = t_{01}t_{01}^*; \text{ for media } n_0 \text{ and } n_1, \quad T = \frac{4n_0^2}{(n_0 + n_1)^2} \tag{3.8}$$

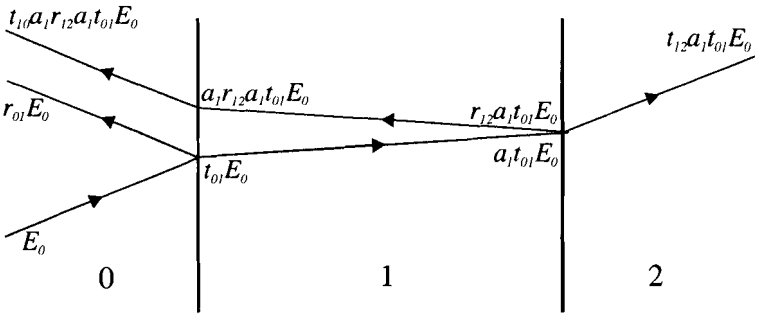

Figure 3.2 Airy Summation: Electric field E_0 splits into reflection $r_{01}E_0$ and refraction $t_{01}E_0$ at the interface when it travels from medium 0 to 1. E field $t_{01}E_0$ attenuates when it travels in medium 1 and further splits at interface 1 / 2.

Knowing the Fresnel coefficients and attenuation rate, one can easily calculate the electric field after each interaction with the medium or media. Figure 3.2 demonstrates the first few rounds of reflection and refraction, and how the electric field changes at each interface. The light starts with the incident electric field E_0. It splits into a reflected $r_{01}E_0$ and a refracted $t_{01}E_0$ beam, with the modifications of electric fields by the Fresnel coefficients. The first refracted E

field, $t_{01}E_0$, attenuates when it travels inside medium 1. It becomes $a_1t_{01}E_0$ after reaching interface 1 / 2. Reflection and refraction take place again at the 1 / 2 interface: $r_{12}a_1t_{01}E_0$ is the reflected part, and $t_{12}a_1t_{01}E_0$ is the refracted part of $a_1t_{01}E_0$. $r_{12}a_1t_{01}E_0$ attenuates and becomes $a_1r_{12}a_1t_{01}E_0$ after it reaches interface 0 / 1. The refracted component of $a_1r_{12}a_1t_{01}E_0$ is $t_{10}a_1r_{12}a_1t_{01}E_0$. The total reflected electric field E_R and refracted electric field E_T are as follows:

$$E_R = r_{01}E_0 + t_{10}a_1r_{12}a_1t_{01}E_0 + \text{.....}(\textit{all E fields travelling into medium 0}) \quad (3.9)$$

$$E_T = t_{12}a_1t_{01}E_0 + t_{12}a_1r_{10}a_1r_{12}a_1t_{01}E_0 + \text{.....} (\textit{all E fields travelling into medium 2}) \quad (3.10)$$

It is the light energy or intensity that interests us, rather than the amplitude or phase of the electric field. Interference in the films is expected to modify the energy fluxes in addition to the electric field wave fronts. Thus, we should convert the electric field into energy flux. Electromagnetic theory defines the energy flux as the Poynting's vector:

$$\mathbf{S} = \mathbf{E} \times \mathbf{H} \quad (3.11)$$

where **E** and **H** are the electric and magnetic vectors. Applying boundary conditions to the solutions of Maxwell's equations, one can get the following expressions for **E** and **H** [61]:

$$\mathbf{E} = \mathbf{u}\, E_0\, e^{\,i(\omega t - \mathbf{kz})} \quad (3.12)$$

$$\mathbf{H} = 1/(\omega\mu_0)\,[\mathbf{k} \times \mathbf{E}] \quad (3.12)$$

where **u** is a unit vector along the x direction, E_0 is the amplitude, $\omega = 2\pi f$ (f is the frequency), μ_0 is the permeability of vacuum, z is the distance along the z direction, and **k** is the propagation vector, along the wave propagation direction.

Substituting the **E** and **H** in Equation (3.11) with the Equation (3.12) and (3.13), one obtains the Poynting's vector for a non-magnetic material, when light travels into air as follows, with $\underline{n} = 1$:

$$\mathbf{S} = \frac{\mathbf{k}}{\omega\mu_0} E^2 \cos^2(\omega t - \mathbf{kz}) \tag{3.14}$$

The time averaged Poynting's vector can be written as:

$$\overline{S} = I = \frac{n}{2c\mu_0} E^2 \tag{3.15}$$

which we can also take as the intensity of the reflected or transmitted light. Here n is the refractive index of the film.

Assuming I_0, I_R, I_T and I_A are the incident light intensity, the reflected light intensity, the transmitted light intensity and the absorbed light intensity, respectively, we have the following *RAT* (reflection, absorption and transmission) definition satisfying the law of conservation of energy:

$$R = \frac{I_R}{I_0}, \quad A = \frac{I_A}{I_0}, \quad T = \frac{I_T}{I_0} \tag{3.16}$$

$$R + T + A = 1 \tag{3.17}$$

Sarunic compared the Airy summation simulation results of a multilayer optical film MgF_2/Ge/glass with some published results. They gave a perfect match, demonstrating that this model works fine.

3.3 Influence of Thermal Resist Film Structure on Absorption

In a previous chapter, a question was raised as to how thermal resist film structures would affect resist sensitivity. With the Airy summation optical model, one can easily calculate and compare the absorption of films with a single metal, single mixed (co-sputtered) and 2-layer structures. When Chapman and Sarunic first developed the optical model [62], we jointly used

that to explore the bimetallic film optical behaviour from 1064 to 248 nm. This thesis extends that work considerably. In this section, *RAT* curves are calculated for different wavelengths: 830 nm (GaAs IR laser diode), 514 nm (argon ion laser), 248 nm (DUV), 157 nm (EUV), 13.4 nm (Soft X-Ray) and 1 nm (X-ray). The 1064 nm RAT curves will not be re-plotted here (refer to Sarunic's thesis [56]). There are four plots in each of the following wavelength figure group. The first plot at each wavelength is a 50*at.%* / 50*at.%* Bi/In, 2-layer structure. The film thickness is chosen such that the atomic compositions of the elements are equal. It is found that equal thickness of Bi and In layers gives almost equal atomic compositions of the two elements. The Bi is on the top of the In film. The x-axis is the thickness of each metal layer. The y-axis is the light intensity. The second and the third plots are for single In and Bi layers, respectively. The fourth is a single mixed (50*at.%* - 50*at.%* co-sputtered) Bi-In film. All the optical properties n and k are from published literature [63,64]. For the n and k values for the mixed alloy (50% - 50% co-sputtered Bi-In film), we assumed we could use an average of the n and k values of single Bi and In films. As the x-axis of the first plot is the thickness of each metal layer, and the x-axis in the other plots is the total thickness of the single layer, the *RAT* readings in the first plot should be compared with those at twice the thickness of the second, third and fourth plots.

Figure 3.3 shows the results for 830 nm [65], the wavelength of a GaAs IR laser diode, which is widely used in the industry [66]. The absorption of a 2-layer Bi/In (Bi on the top of In and In on substrates) is ~ 29% at 20 / 20 nm, less than that of Bi, but greater than a single 40 nm thick In film ~ 12%, and the mixed Bi-In single film ~ 20%. This clearly shows that a 2-layer Bi/In structure with the same total thickness has better absorption than single In or mixed Bi/In films.

It is noted that Bi has ~ 34% absorption at 40 nm. As Bi has a very low thermal conductivity, theoretically, Bi should be a very optically sensitive material. However, we will show from materials analysis, discussed in Chapter 6, that Bi films melt and agglomerate to form

round shaped dots after laser exposure. Also exposed Bi patterns cannot be developed by simple acid solutions (discussed in Chapter 5), and converted Bi film is not resistant to dry and wet etching (discussed in Chapter 7).

All these drawbacks prevent Bi from being a thermal resist candidate. When the film total thickness reaches 80 nm, the absorption of a 2-layer Bi/In film is ~ 37%, similar to single Bi ~ 38%, while single In is ~ 12%, and single mixed Bi-In 20%.

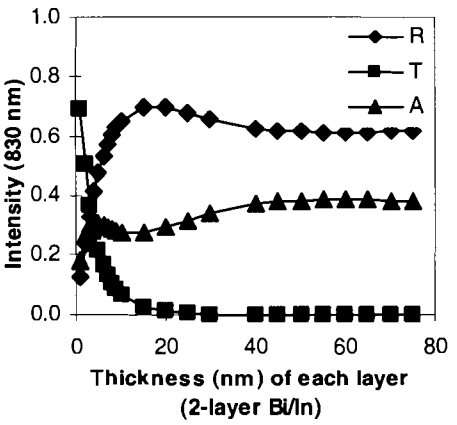

Figure 3.3 (a)

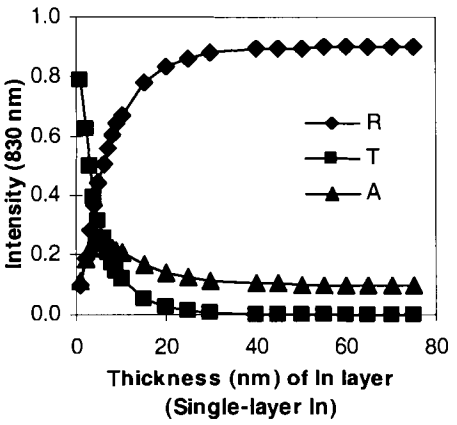

Figure 3.3 (b)

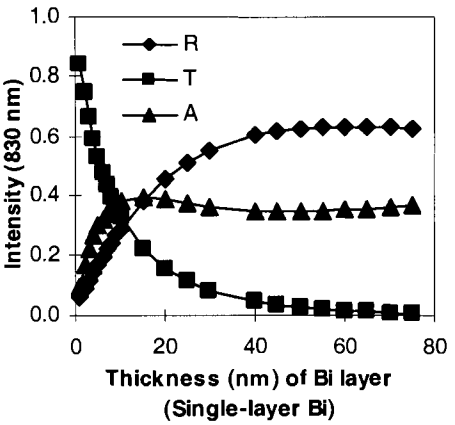

Figure 3.3 (c)

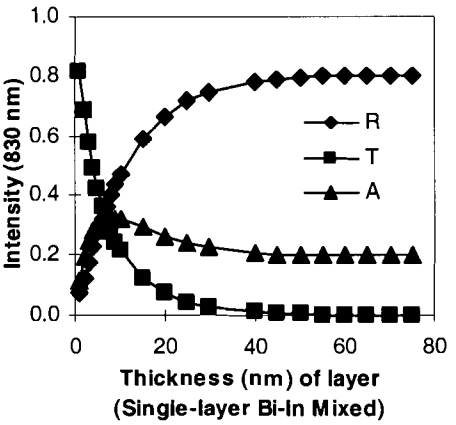

Figure 3.3 (d)

Figure 3.3 ***RAT*** **curves at wavelength 830 nm of (a) 2-layer Bi/In, (b) single In and (c) Bi film, and (d) single layer co-sputtered Bi-In (50% mixed) film.**

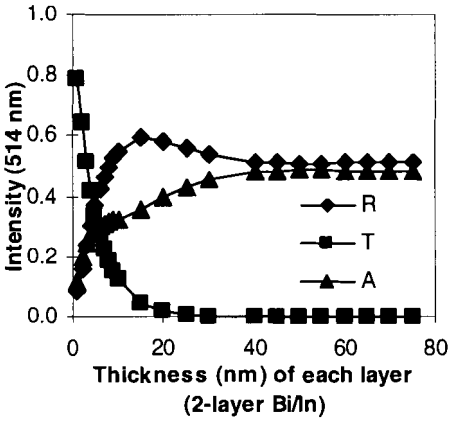

Figure 3.4 (a)

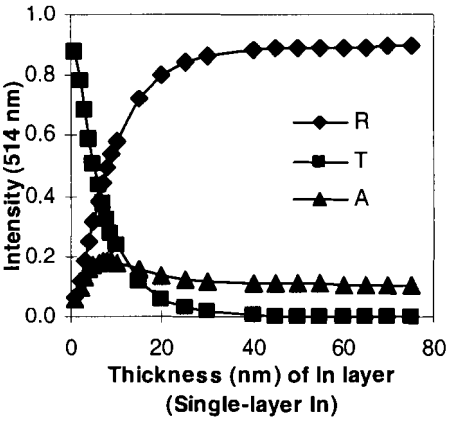

Figure 3.4 (b)

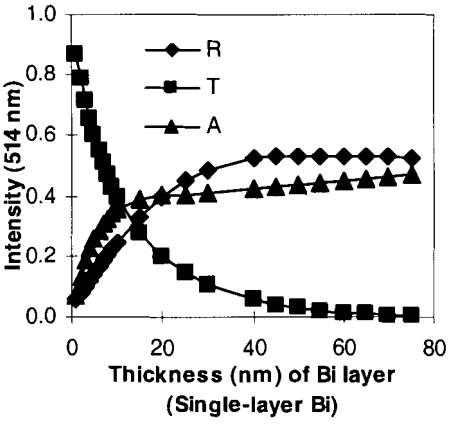

Figure 3.4 (c)

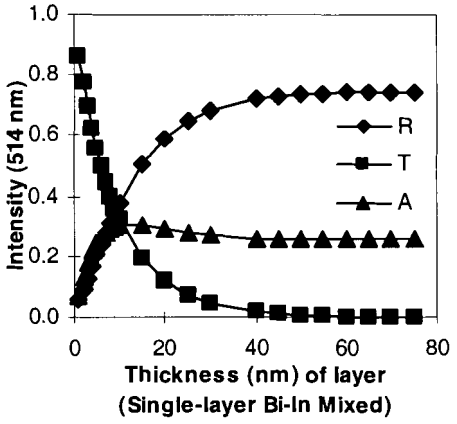

Figure 3.4 (d)

Figure 3.4 ***RAT*** **curves at wavelength 514 nm of (a) 2-layer Bi/In, (b) single In and (c) Bi film, and (d) single layer co-sputtered Bi-In (50% mixed) film.**

Similar results were obtained for 514 nm (Figure 3.4), the argon laser wavelength, which is used mainly in our lab, and for 248 nm and 157 nm [65,67]. Bilayer Bi/In has a higher absorption than that of single In and single Bi-In mixed film. For the 514 nm wavelength, at 40 nm total film thickness, bilayer Bi/In is ~ 39%, mixed Bi-In ~27%, and single In only ~ 12%. At 80 nm total film thickness, bilayer Bi/In is ~ 45%, mixed Bi-In still ~ 27%, and single In still ~ 12%. Absorption becomes comparable between bilayer Bi/In and single Bi film when the total thickness reaches 40 nm.

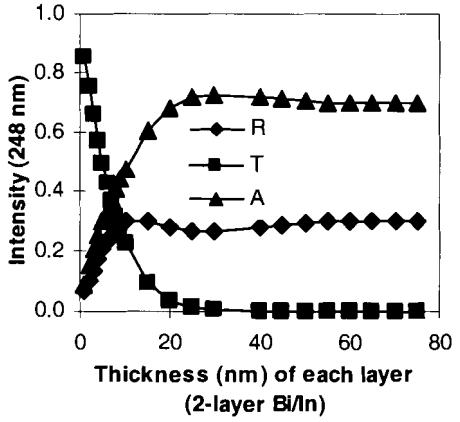

Figure 3.5 (a)

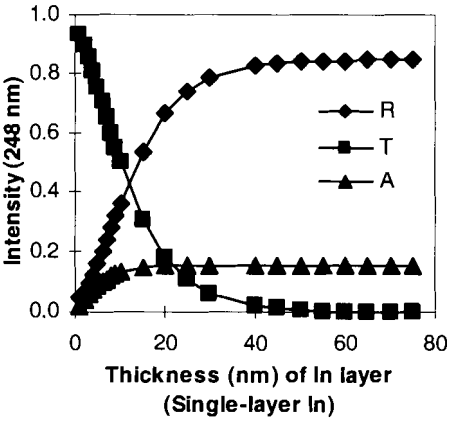

Figure 3.5 (b)

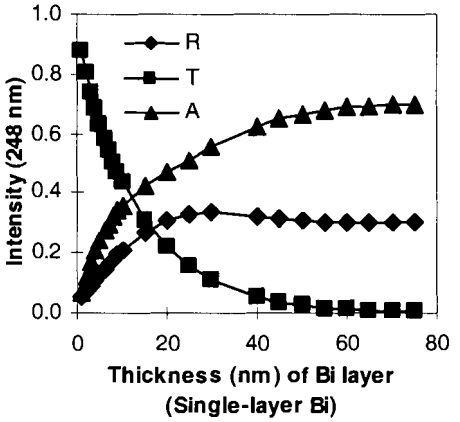

Figure 3.5 (c)

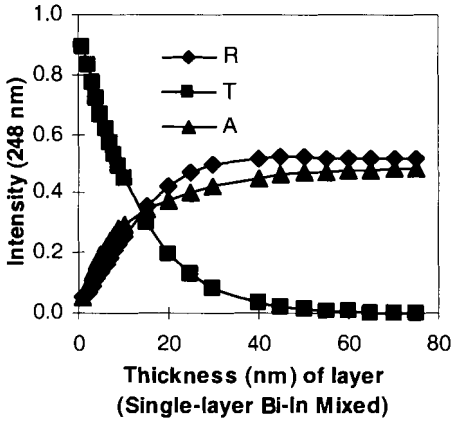

Figure 3.5 (d)

Figure 3.5 ***RAT*** **curves at wavelength 248 nm of (a) 2-layer Bi/In, (b) single In and (c) Bi film, and (d) single layer co-sputtered Bi-In (50% mixed) film.**

For 248 nm, the common KrF excimer exposure tool wavelength, at 40 nm total film thickness, bilayer Bi/In is ~ 66%, mixed Bi-In ~41%, and single In only ~ 15%. At 80 nm total film thickness, bilayer Bi/In is ~ 70%, mixed Bi-In still ~ 41%, and single In still ~ 15%. Absorption becomes comparable between bilayer Bi/In and single Bi film when total thickness reaches 20 nm.

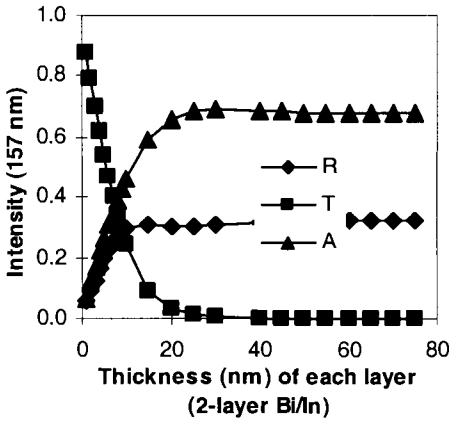

Figure 3.6 (a)

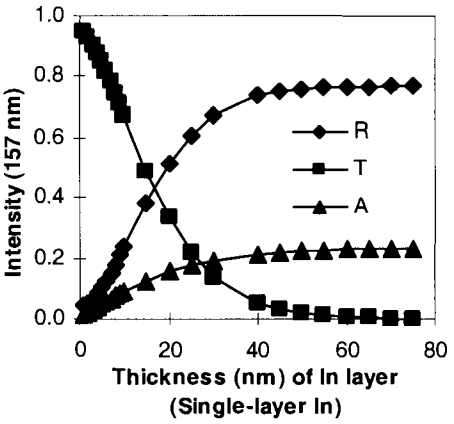

Figure 3.6 (b)

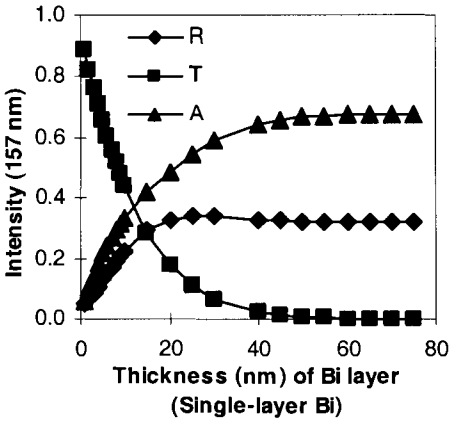

Figure 3.6 (c)

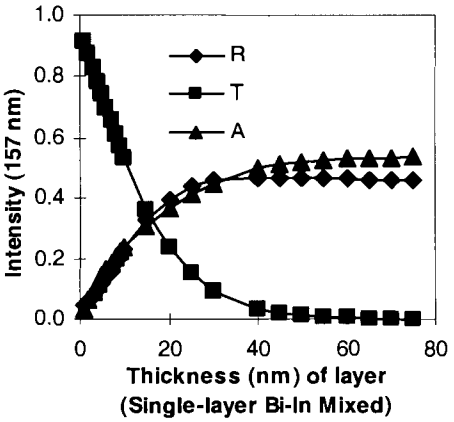

Figure 3.6 (d)

Figure 3.6 ***RAT*** **curves at wavelength 157 nm of (a) 2-layer Bi/In, (b) single In and (c) Bi film, and (d) single layer co-sputtered Bi-In (50% mixed) film.**

Extending this work deeper into the UV range, let us consider the 157 nm wavelength, the proposed F_2 laser exposure tool wavelength. At 40 nm total film thickness, bilayer Bi/In is ~ 64%, mixed Bi-In ~50%, and single In only ~ 20%. At 80 nm total film thickness, bilayer Bi/In is ~ 65%, mixed Bi-In still ~ 51%, and single In still ~ 20%. Absorption becomes comparable between bilayer Bi/In and single Bi film when total thickness reaches 30 nm.

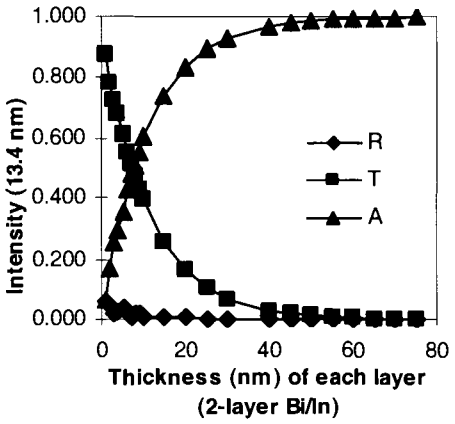

Figure 3.7 (a)

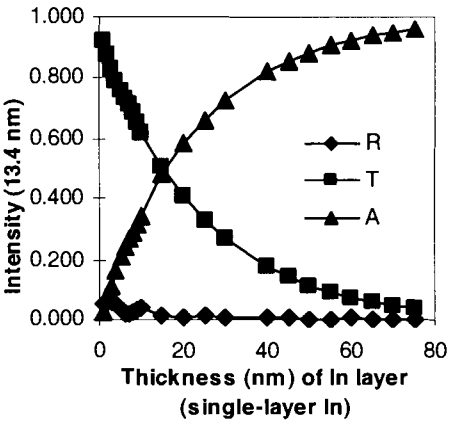

Figure 3.7 (b)

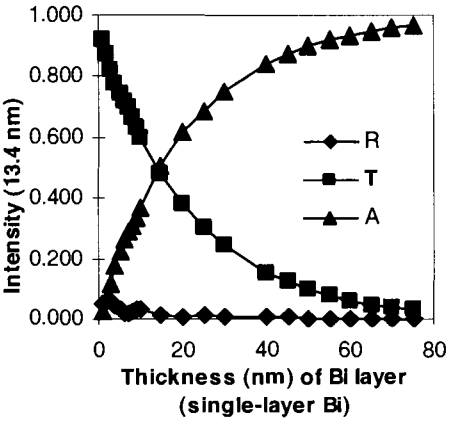

Figure 3.7 (c)

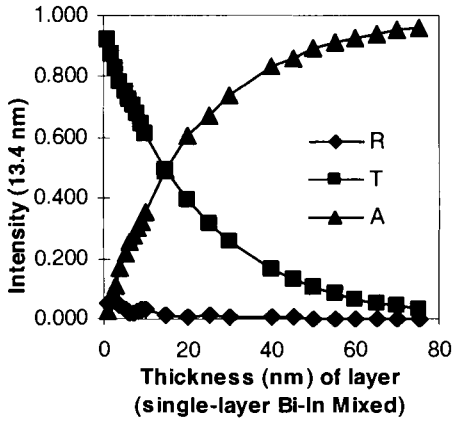

Figure 3.7 (d)

Figure 3.7 ***RAT*** **curves at wavelength 13.4 nm of (a) 2-layer Bi/In, (b) single In and (c) Bi film, and (d) single layer co-sputtered Bi-In (50% mixed) film.**

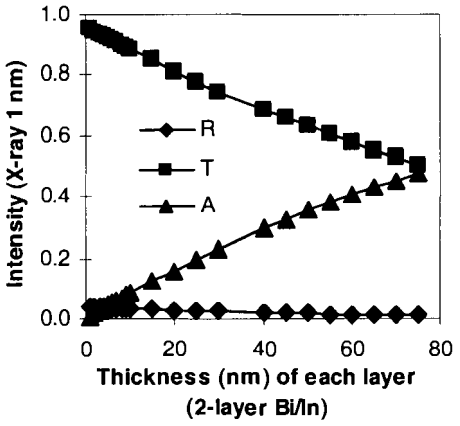

Figure 3.8 (a)

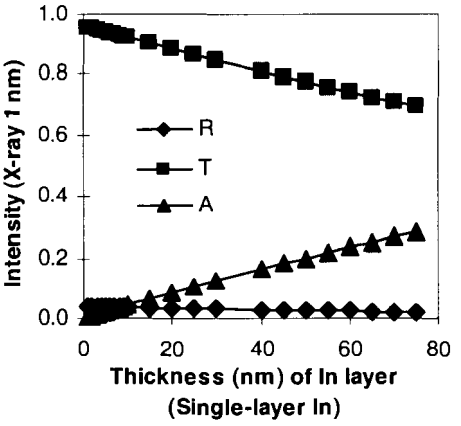

Figure 3.8 (b)

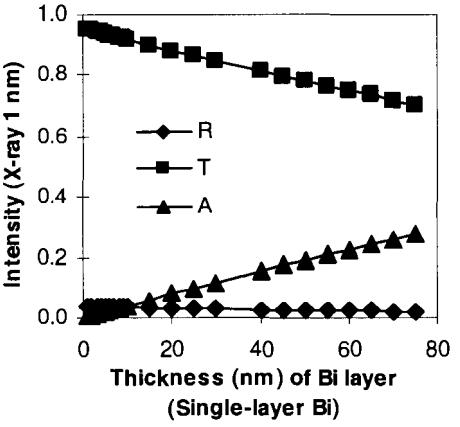

Figure 3.8 (c)

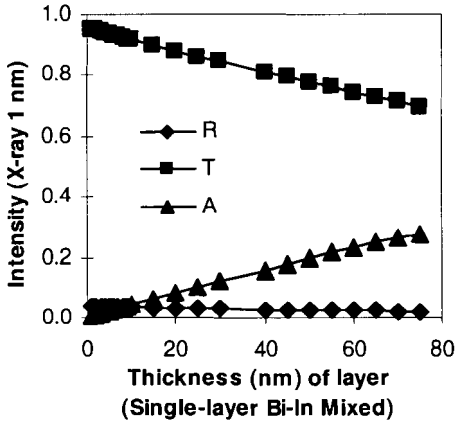

Figure 3.8 (d)

Figure 3.8 ***RAT*** **curves at wavelength 1 nm of (a) 2-layer Bi/In, (b) single In and (c) Bi film, and (d) single layer co-sputtered Bi-In (50% mixed) film.**

As the wavelength moves further into the extreme UV and the X-ray range, the absorption difference between different film structures gets smaller [68]. At 13.4 nm, the proposed EUV exposure system wavelength, bilayer Bi/In has ~ 60% absorption when the total film thickness is 20 nm, while single In is ~ 59%, Bi-In mixed ~ 60% and single Bi ~ 61%. When the total thickness is 40 nm, all of the four structures absorb ~ 81% of the incident light, a 25% increase over the absorption at 248 nm. At 1 nm, as the n and k values of Bi and In films are almost identical, there is actually no absorption difference between the four structures. A film with 40 nm total thickness absorbs ~ 18% of the incident X-ray.

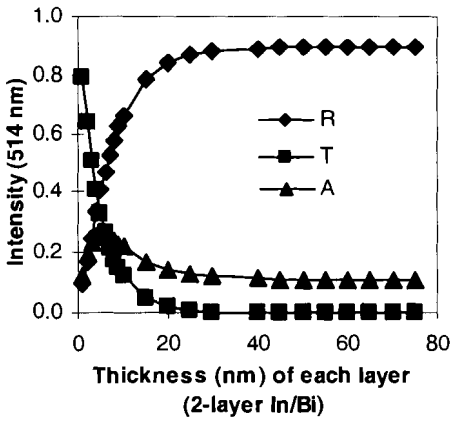

Figure 3.9 (a)

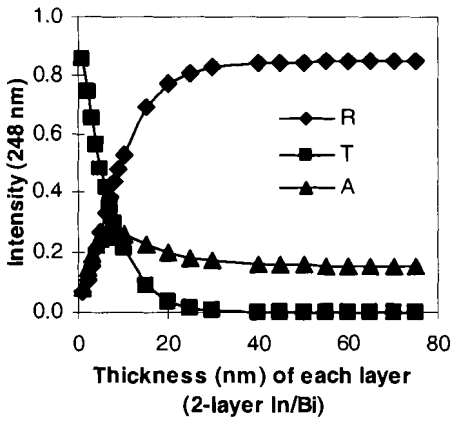

Figure 3.9 (b)

Figure 3.9 ***RAT*** **curves of 2-layer In/Bi at wavelength (a) 514 nm and (b) 248 nm, respectively.**

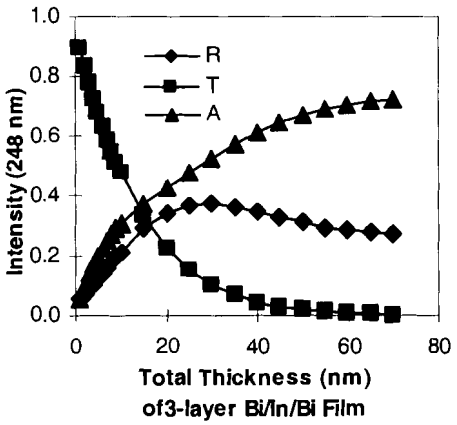

Figure 3.10 (a)

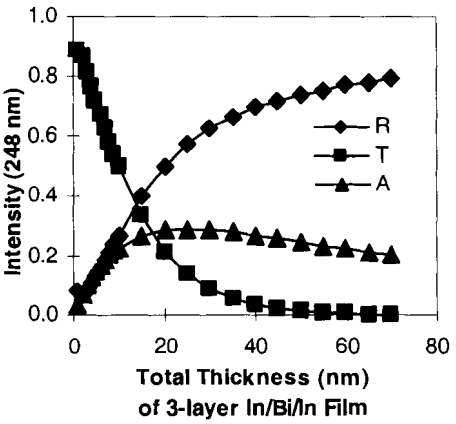

Figure 3.10 (b)

Figure 3.10 ***RAT*** **curves at wavelength 248 nm of (a) 3-layer Bi/In/Bi, and (b) 3-layer In/Bi/In films.**

All of the 2-layer simulation results presented so far are with Bi on top of In and In on the substrate (Bi/In/substrate). How about an In/Bi/substrate structure? Unfortunately, due to In's high reflectivity, an In-on-top 2-layer structure (In/Bi/substrate) has a much lower absorption than does a Bi-on-top structure (Bi/In/substrate). The two RAT plots in Figure 3.9 showed that absorption for 40 and 80 nm total thick films are lower than 20% for both 514 nm and 248 nm wavelengths, while reflection is more than 80 %.

Simulations were also carried out on 3-layer structure films to search for thermal resists with a higher sensitivity. The two RAT curves in Figure 3.10 illustrate the optical performance of

two kinds of 3-layer structures: Bi/In/Bi/substrate and In/Bi/In/substrate, at 248 nm. Compared to a 248 nm 2-layer Bi/In, Bi/In/Bi 3-layer film has a 60% absorption at a 40 nm total film thickness, 6% lower. The difference between the absorption of the two film structures decreases as the film thickness increases. When the total film thickness reaches 80 nm, absorption is 70% for both structures. Meanwhile, an In/Bi/In 3-layer film has a much lower absorption than a 2-layer Bi/In films, indicating that it is not suitable for practical applications.

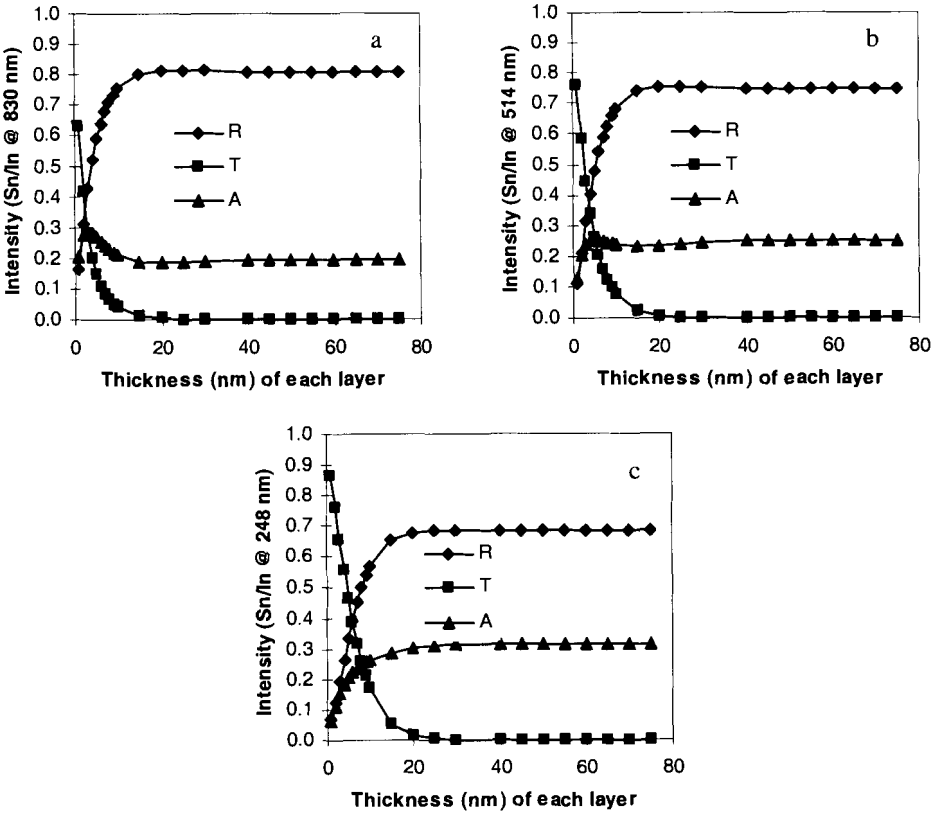

Figure 3.11 The simulation results of Sn/In from the optical model. The three plots are the reflection, transmission and absorption curves versus film thickness at wavelength (a) 830 nm, (b) 514 nm and (c) 248 nm.

Similarly, the absorption of Sn/In does not change very much from 830 nm to 514 nm and from 514 nm to 248 nm, as shown in Figure 3.11 [65]. It is noticed that Sn/In has only half of the Bi/In absorption. As will be shown in Chapter 8, this is confirmed by the experimental results,

which show that in order to get to the saturated optical density, twice as much laser power for Bi/In is needed to expose Sn/In.

In summary, bilayer Bi/In thermal resist does show better absorption, hence higher sensitivity, than single mixed (co-sputtered) Bi-In film and single In film. As 2-layer Bi/In films are easier to deposit than mixed Bi-In, bilayer metallic Bi/In, and later Sn/In films, are prepared and used in this thesis.

3.4 Wavelength Invariance: Simulation Results

As discussed in Chapter 1, organic photoresists currently used in the semiconductor industry operate by photochemical processes, and they are wavelength sensitive, which means that photoresists that work under current 248 nm exposure systems will not work under 157 nm. This is always true for photo resists as the chemical reaction rate and film optical absorption is highly wavelength sensitive. However, bimetallic thermal resists are activated by the heat that the resist films generate by the absorption of the laser exposure. This has lead us to propose an important new characteristic of bimetallic thermal resists: near wavelength invariance for exposure values.

What is important is that since the optical parameters (*RAT*) change slowly with the laser wavelength, and a thermal resist Bi/In depends only on the energy deposited in the films, it shows near wavelength invariance in the exposure energies. Plots (a) in Figure 3.3 to Figure 3.8 demonstrate this with simulated Reflection, Transmission and Absorption (*RAT*) curves versus film thickness at wavelengths 830 nm, 517 nm, 248 nm (current microfabrication exposure systems), 157 nm, 13.4 nm and 1 nm (X-ray). Optical simulations suggest that Bi/In absorption varies little from 514 nm to 248 nm. Simulation suggests exposure is almost unchanged from 248 nm down to 157 nm (in Figure 3.12), the proposed next generation exposure tools, with

absorption varying less than 3.5% over all thickness. When these simulations are extended from 248 nm to 13.4 nm the absorption increases by 24% (as shown in Figure 3.13) at the thickness 20 nm of each layer (from 65% at 248 nm to 81% at 13.4 nm), and reflectivity becomes very small (<1%), indicating an even better sensitivity. This is important as no organic resist successfully works over this range.

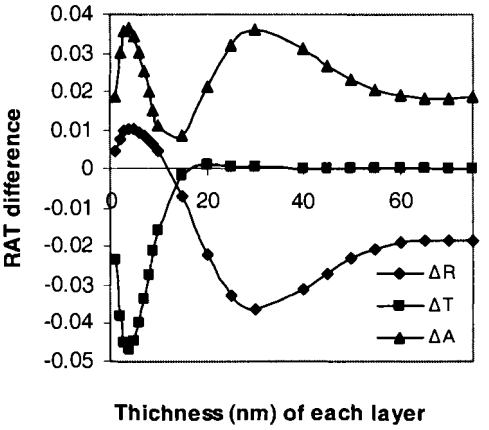

Figure 3.12 ***RAT*** **difference between 157 nm and 248 nm for a bilayer Bi/In film. The difference between these two wavelengths is very small (<±5%).**

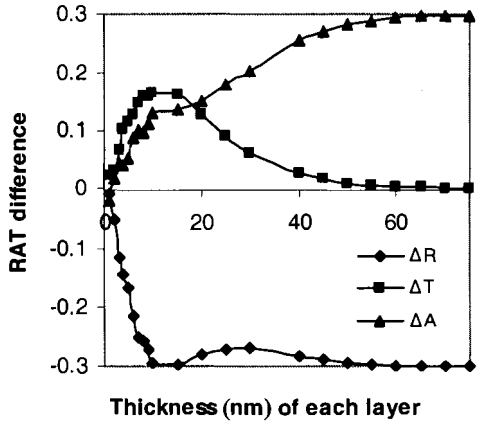

Figure 3.13 ***RAT*** **difference between 13.4 nm and 248 nm for a bilayer Bi/In film. The absorption improves when the laser wavelength moves from 248 nm to 13.4 nm.**

There is very little change in the 50 nm to 10 nm exposure range. Newer X-ray exposure systems are using laser-generated plasmas that produce X-ray of 1 nm with pulse durations of about 1nsec. Wavelength response simulation (Figure 3.8 (a)) projected into the 1 nm X-ray range

shows that there is still 15% absorption for 20 nm per layer films and this absorption increases nearly linearly with thickness until ~100 nm. Using the previous measured sensitivity at 266 nm and extrapolating the absorption to 1 nm this suggests an X-ray sensitivity of ~35 mJ/cm^2 using a 15/15 nm Bi/In thermal resist [68]. Compared to one of the most sensitive X-ray photoresists reported [69], which is 100 mJ/cm^2 for 200 nm thick films, our bimetallic film is expected to be much better. This high sensitivity could definitely improve the X-ray photolithography throughput and make X-ray litho-process practical.

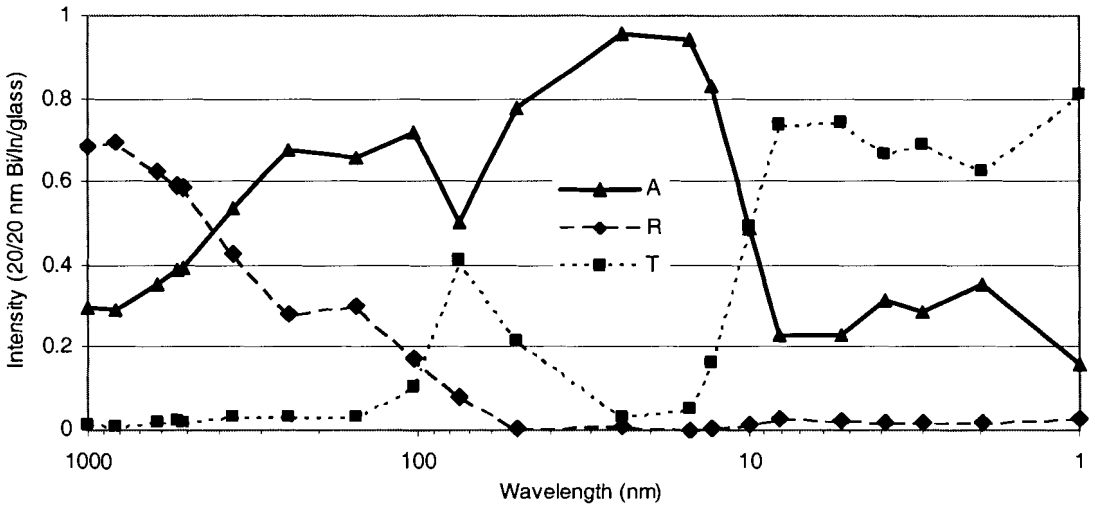

Figure 3.14 ***RAT*** **versus wavelengths of the incident beam in 20/20 nm Bi/In film deposited on glass.**

Figure 3.14 shows the *RAT* performance at different wavelengths from IR (1066 nm) to X-ray (1 nm) for a 20/20 nm Bi/In film deposited on a glass substrate. From 1066 nm (IR) to 250 nm (DUV), the absorption slowly increases. Then from 250 nm to 100 nm the absorption remains nearly constant. Below 150 nm the reflection drops significantly. From 100 nm to 10 nm, the absorption first drops at around 80 – 70 nm, and then increases and peaks at ~ 24 nm (95.5%). The reflection drops until 50 nm when it reaches 0.3%, and stays at that level into X-ray range. From 10 nm to 1 nm (X-ray range), the absorption varies from 15% to 35%, while the transmission is high (>60%) and the reflection very low (0.2% ~ 3.0%). This plot demonstrates

again that Bi/In (20/20 nm) maintains >15% absorption over this wide wavelength range, showing its wavelength invariance. However, the exposure sensitivity (determined by the absorption) of the film does vary slowly with the wavelengths. The optical model predicts that a Bi/In (20/20 nm) film maintains >50% absorption within the 400 nm to 10 nm range, higher than that of the rest of the wavelengths. Thus, it should be more sensitive in this wavelength region.

Bi/In experimental results (will be presented in Chapter 5) confirm that Bi/In thermal resists can be exposed by 830 nm solid state IR laser (Chapter 8), 533 nm Nd:YAG 2^{nd} harmonic laser, 514 nm argon laser, and 266 nm Nd:YAG 4^{th} harmonic laser. There are also indications that X-ray radiation can cause changes in the Bi/In bimetallic films.

3.5 Summary

This chapter described an optical model that is used to calculate the reflected, transmitted and absorbed light intensity. Based on Airy summation, the model sums all the electric fields that leave the medium and travel along the opposite direction of the incident beam into a reflected electric field. And, it adds all the electric fields leaving the medium and travelling in the same direction as the incident beam as the transmitted electric field. With the Poynting vector, one can easily calculate light intensity from the electric field. The sum of the light intensity of reflection, transmission and absorption should be 1. Comparison between the simulation results and published results shows that the optical model is accurate. Using this optical model, we calculated and plotted the *RAT* curves versus film thickness and light wavelength (from 830 nm to 1 nm), and compared results for different film structures. This introduces the concept of the bimetallic thermal resists showing something very new: near wavelength invariance. For the first time, the investigation of bimetallic films was extended into the EUV and X-ray range. It was found that 2-layer Bi/In film has a better absorption than other film structures, indicating that bilayer metallic

thermal resists are more sensitive than co-sputtered single layer Bi-In films. Simulation results also showed that the film absorption changes slowly as light wavelength gets shorter, showing the property of wavelength invariance. The next chapter discusses the resist experimental preparation and equipment.

Chapter 4
Resist Preparation and Experimental Setup

4.1 Introduction

Materials selection in Chapter 2 identifies that Bi, In and Sn are the best candidates for sensitive inorganic metallic thermal resists. The simulation results of the Airy summation optical model discussed in the previous chapter show that bimetallic thermal resists have a higher sensitivity than other film structures, and exhibit a wavelength invariance attribute. In this chapter, the preparation processes will be described for the bimetallic thermal resists on different kinds of substrates: the standard RCA cleaning, and the DC- and RF-sputter deposition. Two kinds of laser systems will be described that were used to expose the bimetallic films: argon laser and Nd:YAG laser. The important equipment for patterning, the computer-controlled X-Y-Z table, will also be introduced. As lots of applications in wet and dry etching will be explored, the wet bench system used for KOH, EDP and TMAH anisotropic etching, and the dry plasma Axic PECVD/RIE dual chamber etcher with CF_4/CHF_3 will be described. Different pieces of analysis equipment were used in the thesis work, including a profilometer, UV spectrometer, X-ray diffractometer, scanning electron microscope and transmission electron microscope.

4.2 Resist Preparation and Sputtering System

Bimetallic thermal resist coating is a completely dry process using PVD (physical vapour deposition) method. In this thesis work, DC- and RF-sputtering are used to deposit thin films from target materials onto substrates.

4.2.1 Characterization of As-Deposited Single Film

As discussed in Chapter 2, a bimetallic thermal resist at a eutectic composition has a much lower melting point than do single metals, and hence potentially a higher sensitivity. Thus, film deposition with accurately controlled film thickness is key to making the best bimetallic thermal resist. This section will investigate the deposition rate of each metal, and the relationship between thickness ratio and the atomic ratio of the bimetallic films.

The thin film DC-/RF-sputtering system in our laboratory is made by Corona Vacuum Coaters (as shown in Figure 4.1). The system is equipped with a 24" deposition chamber with multiple sample holders, a Varian 6-inch oil-diffusion pump combined with a 2-stage mechanical roughing pump. The sputter system rack holds the vacuum gauges, DC power supply (Advanced Energy MDX-1K), RF power supply (Advanced Energy RFX-600 with an ATX-600 matching system), substrate heating element controller, the computer control interface box and also the switches for pumps. A butterfly throttle valve and mass flow controller are used to control the chamber pressure during the deposition.

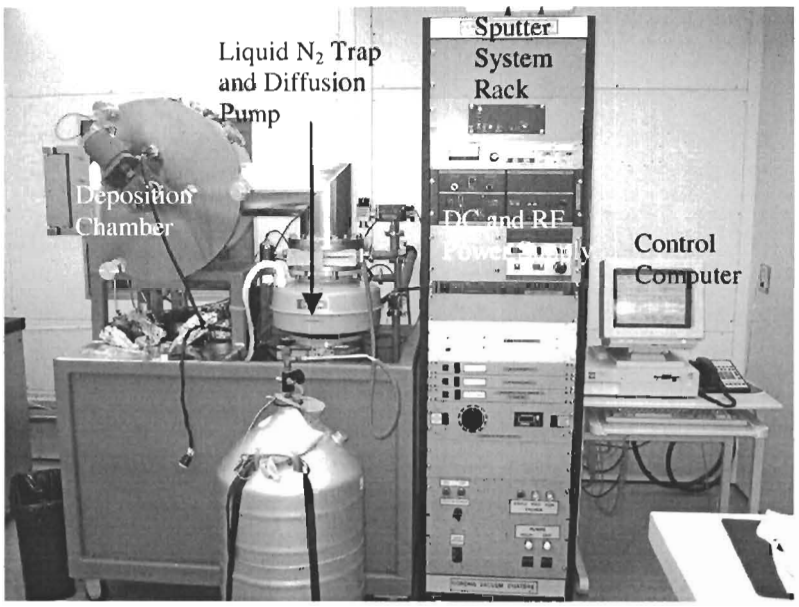

Figure 4.1 Corona thin film sputtering system.

The deposition chamber can accommodate 5 targets: four 2" in diameter round targets and one 4"× 6" rectangular target. This allows the deposition of multilayers without an air break. The metal Bi, and In targets used in film deposition were 2 inch in diameter and 1/8 inch thick, 99.99% purity powder pressed targets. A Sn target was 99.85% purity. Deposition starts after sample substrates are loaded and the base pressure reaches 0.8 ~ 1×10^{-6} Torr. Argon is used as the sputtering gas, and the chamber pressure is usually kept at 4 mTorr during sputtering.

Glass slides, quartz and silicon wafers are used as substrates to deposit thermal resist for various purposes. Before being loaded into the deposition chamber, all the substrates have to go through a standard cleaning process in order to remove organic and metallic contaminants. Table 4.1 lists the process steps and four solutions used in our lab for substrate cleaning.

Table 4.1 Solutions used to clean substrates before film deposition.

Process Step	Solution/Name	Chemical Content	Temperature	Duration
1	Piranha	H_2SO_4 : H_2O_2 = 4:1	100°C	15 min
2	HF dip	HF : H_2O = 1:10	25°C	30 sec
3	RCA1	NH_3OH : H_2O_2 : DI-H_2O = 1:1:5	80°C	10 min
4	RCA2	HCl : H_2O_2 : DI-H_2O = 1:1:6	80°C	10 min
5	DI water rinse	H_2O	25°C	5 min
6	Oven Baking	-	120°C	20 min

Substrates are usually cleaned with RCA1 and RCA2 (see Table 4.1), followed by 5 minutes of DI water rinse and then baked in a 120°C oven for 20 min to remove moisture. When the process requires it, the Piranha and HF dip steps are carried out before RCA cleaning, especially for silicon wafers. Piranha removes organic contaminants and also creates a thin oxide layer. It is normally followed by an HF dip which then removes the oxide layer, together with contaminants. The RCA1 cleaning also removes organic contaminants and the RCA2 cleaning removes metallic contaminants.

In order to determine the film deposition rate (in unit of Å/w·m), glass slides were used as the substrates. Film thickness was measured with a Tencor AlphaStep 500 profiler after each deposition. Table 4.2 lists the DC- and RF-sputtering rates of each of the metal films.

It is known that most deposition techniques produce films with densities that deviate from the bulk density [70-72]. Gas inclusion and / or crystalline disorder may produce pores in the films, and an increased concentration of vacancies in the crystals reduces the film density. Low film densities have been reported to influence film properties such as the refractive index, the film adhesion, and the crystallization behaviour. However, thin-film density is difficult to measure directly, primarily due to the small amount of material involved. Although X-ray reflectivity has been reported to be the most accurate method [73], in practice, thin-film density is often determined indirectly by making separate measurements of mass, film area and thickness. To calculate the film density, the glass slide was weighed before and after film deposition. Then the area and the thickness of the deposited film were measured. The film density can be obtained easily by the following formula:

$$d_f = \frac{m_f}{V_f} = \frac{m_2 - m_1}{A_f t_f} \tag{4.1}$$

where d_f is the film density, m_f is the mass of the film, V_f is the volume of the film, m_2 and m_1 are the glass slide masses after and before film deposition, A_f is the area and t_f is the thickness of the film.

Shown in Table 4.3 are the measurement and calculation results. Note that 80 w·min of Bi and 240 w·min of In were sputtered on glass slides separately. According to the deposition rates in Table 4.2, sputtering should deposit equal thickness films of around 960 ± 160 Å of Bi and 960 ± 144 Å of In, respectively. The actual thicknesses of Bi and In films are higher than calculated. Besides the sputtering current / voltage fluctuation, the spreading of sputtered materials to the neighbour substrates could also be the reason for thicker deposited films. The measured film densities of Bi and In are lower than their bulk values: 82.84% of bulk for Bi and 74.13% for In. The entry "Mol of metal / cm^2" is how many moles of Bi or In exist in 1 cm^2, the ratio of which indicates the atomic ratio of the equal thickness Bi/In films. The measurements

show that an equal thickness Bi/In thermal resist has 46.53at.% Bi and 53.47at.% In, and the atomic ratio is therefore 1:1.15. For more accurate film thickness and atomic ratio control during the deposition, cross deposition over neighbouring substrates should be taken into account and it is recommended that one sample holder be used for each pump-down. Table 4.4 lists the single film density of Bi, In and Sn, compared to their bulk density values.

Table 4.2 Single metal film sputter rates (Å/w·min)

Film	DC rate	RF rate
Bi	12.0 ± 2.0	7.2 ± 1.2
In	4.0 ± 0.6	2.3 ± 0.4
Sn	6.4 ± 1.0	3.8 ± 0.6

Table 4.3 Bi and In film density and atomic ratio for equal thickness Bi/In film.

	Bi	In
Sputter amount (w.min)	80	240
m_1 - Pre-sputter weight (g)	5.02920	5.05489
m_2 - Post-sputter weight (g)	5.03124	5.05617
m_f - Film mass (g)	0.00204	0.00128
t_f - Average film thickness (Å)	1258	1190
A_f - Total area in cm^2	19.97196	19.85017
V_f - Total volume cm^3	2.51297E-04	2.36217E-04
d_f - Film density g/cm^3	8.11788	5.41875
% of bulk density	82.84%	74.13%
Mol of metal / cm^2	4.88770E-07	5.61601E-07
Equal thick Bi/In atomic %	46.53%	53.47%
Atomic ratio =	1:1.15	

Table 4.4 Single metal film density, compared to its bulk value.

Element	Bulk Density (g/cm^3)	Atomic Weight	Film Density (g/cm^3)	% of Bulk Density
Bi	9.80	208.98	8.12	82.84%
In	7.31	114.82	5.42	74.13%
Sn	7.30	118.69	6.42	87.95%

4.2.2 Bimetallic Film Preparation

Since the sputter system used in our laboratory has multiple targets, Bi/In two-layer thermal resists can be deposited in the vacuum without an air-break by sequential sputtering of In then Bi (only one pump down is needed). This reduced the level of contamination or oxidation at

the interface of the two metal films. The two-layer Bi/In thin film thermal resists were of Bi/In/substrate structure (Bi on top), unless otherwise specified. The sputter process is simple: let the substrate face the In target for a pre-set period of time, and then change the position of the substrate and let it face the Bi target for sputtering. The nominal thickness of each layer was calculated and set using the sputter rates listed in Table 4.2. When sputter power was fixed, sputter duration was used to control the film thickness, and also the atomic ratio.

In order to deposit single layer, Bi-In mixed thin films, two-target co-sputtering was used. During co-sputtering, Bi and In targets were fired up and the substrate was arranged to move over each one of the targets alternately. The faster the movement was, the more even the film would be, yet also the slower the deposition rate. The sputter power ratio, in this case, determined the atomic ratio of the film, and sputter time influenced the total film thickness.

4.3 Inorganic Thermal Resist Exposure System

After the bimetallic thermal resist was prepared, the sample was then transferred to the thermal resist exposure system. The exposure system includes mainly three sections of equipment: X-Y-Z table, control computer and laser sources, as shown in Figure 4.2.

4.3.1 X-Y-Z Table and Control Computer

The X-Y-Z table is used to position the samples under the laser beam. The X-Y-Z table, as shown in Figure 4.3, is mounted on an air vibration isolated 2.5 ton granite base to minimize vibration. The table positioning was controlled by 633 nm laser interferometry using an HP 5517B Laser Head, together with an Anorad laser controller. The positioning accuracy of this table is $\pm 0.05\mu m$ over a 25 × 25 cm area. The moving speed of the table along the X and Y

direction can be set from 1 μm/s to 25 cm/s. A video camera, which is connected to a microscope, sends the laser exposure live video to the control computer screen. The thermal resist coated sample is placed on an aluminium sample holder, which is mounted on a Z-axis stage. The Z-axis stage offers the great convenience of focusing the laser beam on the sample.

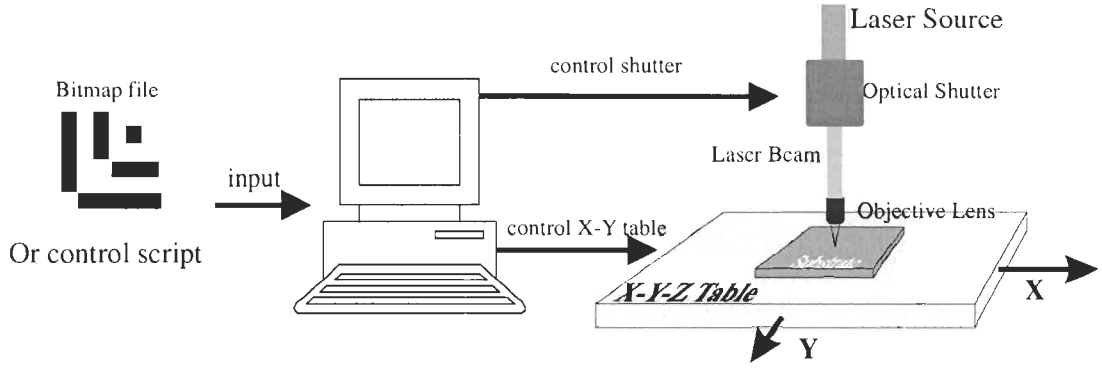

Figure 4.2 Thermal resist exposure system: X-Y-Z table, control computer and laser sources.

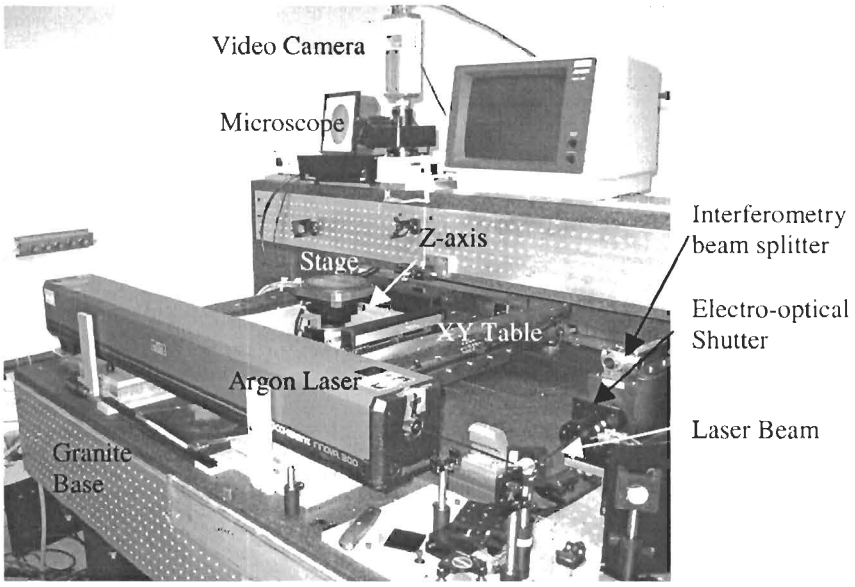

Figure 4.3 X-Y-Z table and part of the argon laser system.

The control computer is the central part of the whole system. It runs Microsoft Windows 2000 as the operating system and proprietary laser table control software written by Professor Glenn Chapman and his group (refer to James Dykes' and Andrew McPherson's [74] theses). The computer communicates with the laser sources, X-Y-Z table, the electro-optical shutter and

mechanical shutters through a multiple-port PCI card. As the diameter of the laser beam is small, a raster-scan was often used to expose large areas and make patterns on the thermal resists. The control computer can take either command scripts or an 8-bit, bitmap image file as the input. The X-Y-Z table movement is controlled by the computer during the raster-scanning, while the laser beam stays stationary, as shown in Figure 4.2.

4.3.2 Laser Sources

Two laser systems were used as our light sources: a Coherent Innova 300 CW Argon Ion Laser and a Coherent Infinity Nd:YAG laser.

4.3.2.1 Argon Laser

The Coherent Innova 300 argon ion laser normally runs at 488 or 514 nm wavelengths, and the laser power can be continuously tuned from 0.06 W to over 6 W. Figure 4.4 shows the setup of the exposure optics using the argon laser. The laser beam was first reflected by a dielectric mirror into an electro-optical shutter. The shutter can not only operate at On (at which state the shutter lets over 85% laser go through) and Off (at which state the shutter lets only less than 1% laser go through) states, but also adjust the laser through rate smoothly from 1 ~ 85% according to the input from the function generator. This allows a continuous control of laser power, which is critical for grayscale mask preparation, discussed in Chapter 8. The shutter can also turn on and off at a very fast rate, controlling the laser exposure duration from minimum 2 μs to an arbitrary period of time. After passing through the shutter, the laser beam was focused by a converging lens (either a 50 mm lens, a 5× objective lens, or a 50× objective lens) before it hit the surface of a resist-coated sample.

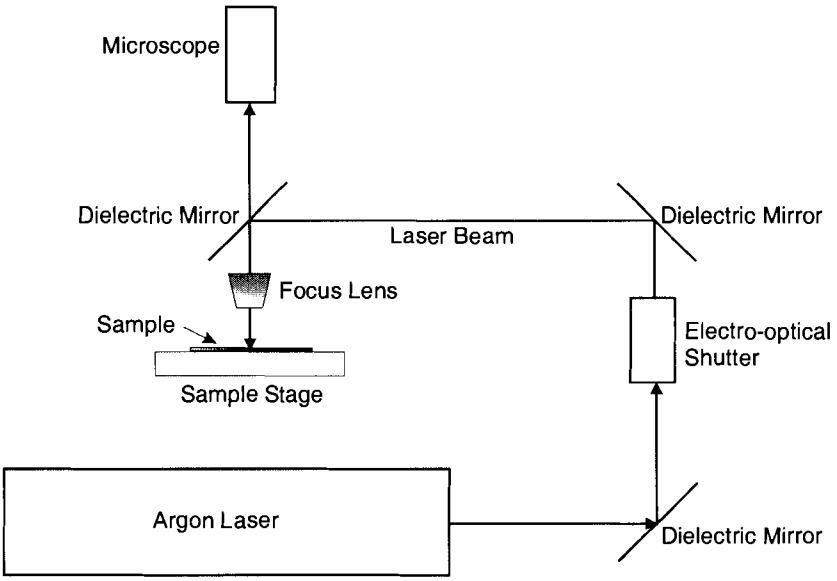

Figure 4.4 Coherent Innova 300 CW argon laser and its exposure optics.

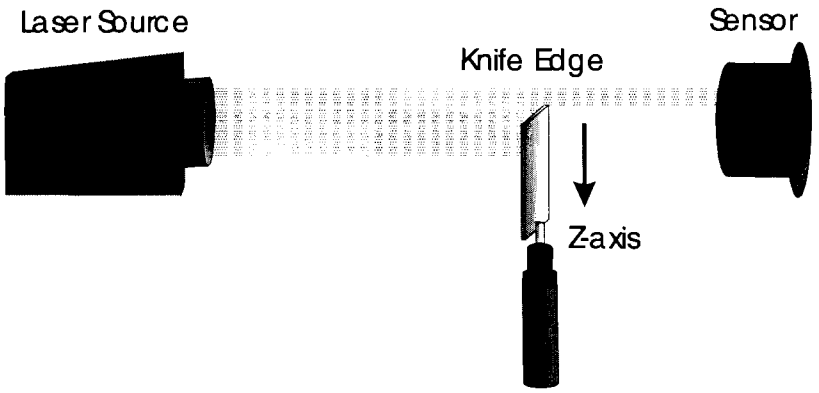

Figure 4.5 Knife edge test set up.

Laser beam profile tests were carried out using a knife edge method to check the laser beam shape and size, as they are important to the exposure of thermal resists. Figure 4.5 shows the test setup. A blade was placed on a micro-movement stage, and the stage moved along the direction perpendicular to the laser beam. The test started with the blade either blocking the whole beam, so that the sensor read 0 W, or the reverse. The stage moved a fix step along one direction. The laser power was measured by a sensor, which was connected to a meter, at each point.

In an ideal TEM_{00} mode, a laser beam has a simplified one dimension Gaussian intensity distribution of the following:

$$f(x)=\frac{1}{A\sqrt{2\pi\sigma^2}}e^{\frac{-(x-u)^2}{2\sigma^2}} \tag{4.2}$$

where, A is a constant related to the peak intensity $I_0=\frac{1}{A\sqrt{2\pi\sigma^2}}$, u is the centre position of the beam and σ is the standard deviation and also half of the beam radius at $1/e^2$ of the peak intensity. The beam radius is commonly defined as the point where the beam intensity drops to $1/e^2$ of its peak value. Integrating $f(x)$ gives the error function as follows, and $P(x)$ is the measurement from the knife edge test. Note that this is a simplified one dimension model, depicting the cross-section of a laser beam.

$$\begin{aligned} P(r)&=\frac{1}{A\sqrt{2\pi\sigma^2}}\int_{\infty}^{x}e^{\left(\frac{-(r-u)^2}{2\sigma^2}\right)}dr+P_B \\ erfc(x)&=\frac{2}{\sqrt{\pi}}\int_{\infty}^{x}e^{-s^2}ds \\ s&=\frac{(x-u)}{\sqrt{2}\sigma} \\ dr&=\sqrt{2}\sigma ds \\ P(x)&=\frac{1}{2A}erfc\left(\frac{(x-u)}{\sqrt{2}\sigma}\right)+P_B \end{aligned} \tag{4.3}$$

In this test, the argon laser power was set to 0.08 W on the console, and the laser was further attenuated to 0.0127 W by a neutral density filter of 0.8 OD. The micro-movement stage moved 50 steps and each step was 48 μm. Figure 4.6 shows the measured laser power vs. the error function fitted curve, with u = 1143.2 μm, σ = 394.4 μm, and A = 76.8 W/m. The beam $1/e^2$ diameter is 4σ = 1.6 mm. Figure 4.7 is the argon laser Gaussian profile with the error function fitting parameters.

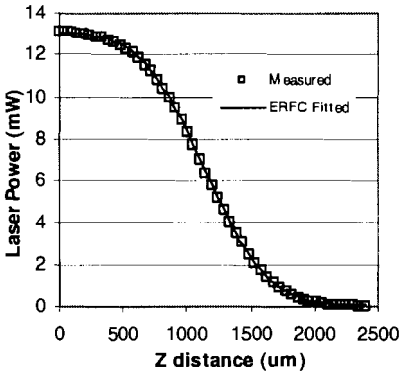

Figure 4.6 The knife edge test: power measurements of the argon laser vs. Z distance with an error function fitted curve.

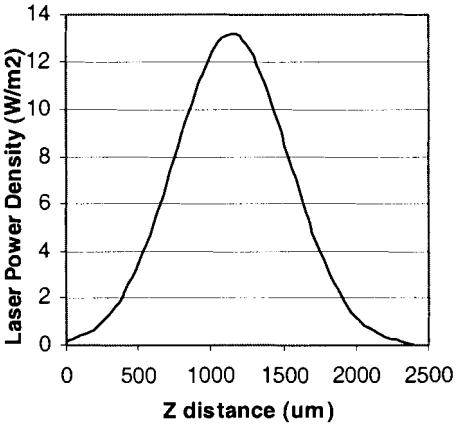

Figure 4.7 The argon laser Gaussian profile curve using the error function fitting parameters: u=1143.2 μm, σ=394.4 μm, and A=76.8 W/m.

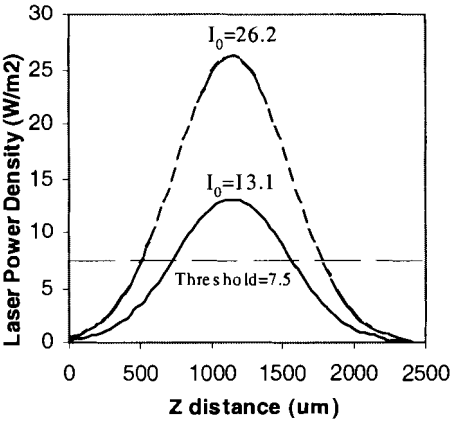

Figure 4.8 The influence of argon laser beam intensity on the size of exposure on the thermal resist.

It is noticed that the laser beam diameter is not defined according to the absolute power intensity value, but an intensity ratio. Shown in Figure 4.8, the two Gaussian beams have

different peak power density, but they have the same beam size. However, as thermal resists are sensitive to absolute power density (the total amount of heat absorbed per area), laser beams with different power densities will create exposure areas of different sizes. Figure 4.8 reveals that, assuming the sensitivity threshold of a thermal resist is 7.5 W/m^2, a laser beam with I_0 = $26.2W/m^2$ creates spots 50% larger than a laser beam with I_0 = $13.1W/m^2$. The relationship between the laser power and the laser exposure size on a resist is important when laser direct-writing is used to expose thermal resists, and is critical when fine features need to be created.

4.3.2.2 Nd:YAG Laser

As most of the modern exposure systems used in wafer fabs are now steppers equipped with pulsed laser sources at wavelengths 248 nm or 193 nm, a special Nd:YAG (Neodymium doped Yttrium Aluminium Garnet) laser was used in our lab to make pulsed exposures on Bi/In and its class of bimetallic thermal resists. Figure 4.9 shows the structure inside the Nd:YAG laser system. It is equipped with three harmonic crystals: 2^{nd}, 4^{th} and 5^{th} HG. The system is rotated 90° counter-clock-wise with reference to Figure 4.10. The major difference between CW lasers and ultrafast (pulsed) lasers is that the latter can deliver laser of much higher power density. As the power density influences the heat flow in the resist thin film, thermal resist performance can be quite different under pulse laser exposure than under CW lasers. Figure 4.10 shows the optical system of the Coherent Infinity™ Nd:YAG laser in our lab. The laser has a diode pumped Nd:YAG unit (or DPMO: diode pumped master oscillator), and an IR (1064 nm) flash lamp pulsed amplifier. The collimating lens, thin film polarizer, spatial filter, vacuum cell, etc., are used to modify the laser beam wave form and shape.

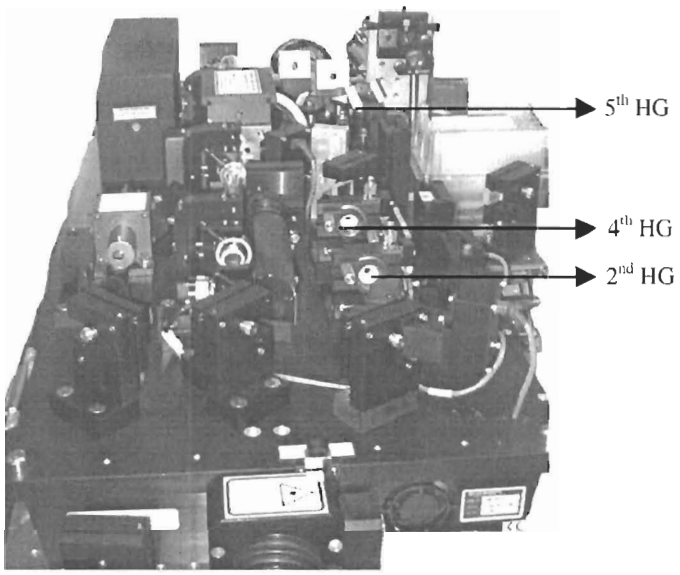

Figure 4.9 Inside the Nd:YAG laser box.

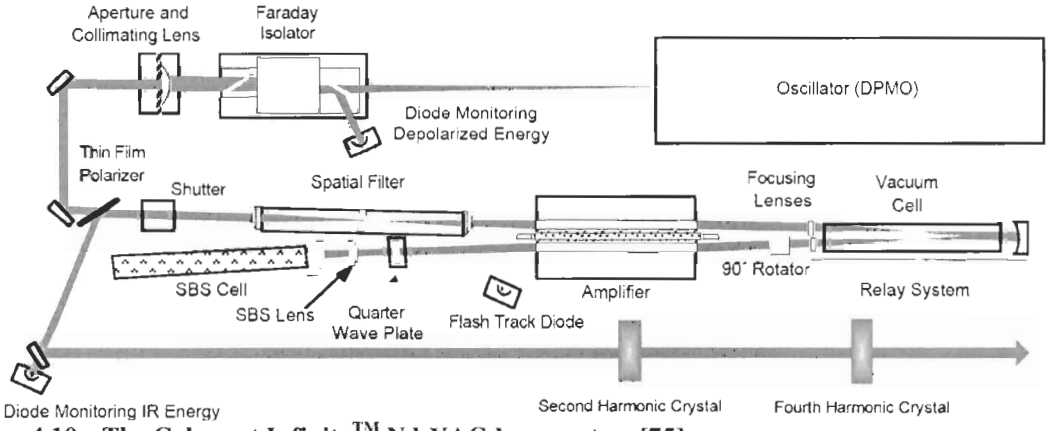

Figure 4.10 The Coherent Infinity™ Nd:YAG laser system [75].

The fundamental laser wavelength of this Nd:YAG system is 1064 nm. After the second harmonic crystal, as shown in Figure 4.10, the laser frequency is doubled and laser wavelength is halved to 533 nm. If a fourth harmonic crystal is added after the second harmonic the laser wavelength will be further halved to 266 nm. Similarly, a fifth harmonic crystal will reduce the laser wavelength to 213 nm. Table 4.5 lists the wavelengths available on our Nd:YAG laser system with the corresponding harmonic crystals, pulse duration and maximum power. The pulse repetition rate can be changed from 0.1 ~ 30 Hz. The optical table system inside the Nd:YAG

laser box is designed to permit rapid changes between these wavelengths. The Nd:YAG laser beam was reflected and sent to the sample stage by dielectric mirrors of corresponding wavelengths.

Table 4.5 Coherent Infinity Nd:YAG laser output wavelength and power.

Crystal	Wavelength (nm)	Max Power (mJ/pulse)	Pulse Duration (ns)
None	1064	640	4
2nd Harmonic	533	500	4
4th Harmonic	266	100	4
5th Harmonic	213	25	4

A knife-edge test was also carried out to study the Nd:YAG laser beam profile and beam spot size. The test result would help understand the source of a distortion in the direct-pattern or projected image. The experiment setup was the same as in Figure 4.5. Figure 4.11 is a plot of the measured laser power from the sensor versus distance across the laser beam.

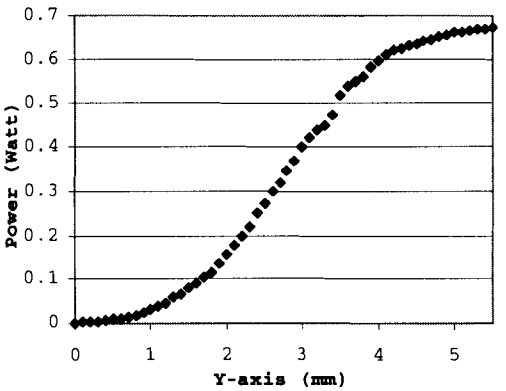

Figure 4.11 Laser power measured from the thermal sensor versus distance across the Nd:YAG 533nm laser beam along the Y direction.

An error function curve fitting was carried out, and the result showed that the best fit was when A = 7.05 W/mm, u = 2.81 mm, σ = 1.29 mm. Figure 4.12 shows the fitting curve versus the measurement. From the fitting result one can see that the laser power intensity has a normal distribution. The corresponding Gaussian distribution is shown in Figure 4.13. The beam $1/e^2$

diameter was $4\sigma = 5.16$ mm, and the centre was at 2.81 mm. The knife edge test result shows that the highest intensity is at the centre of the beam, showing no skew.

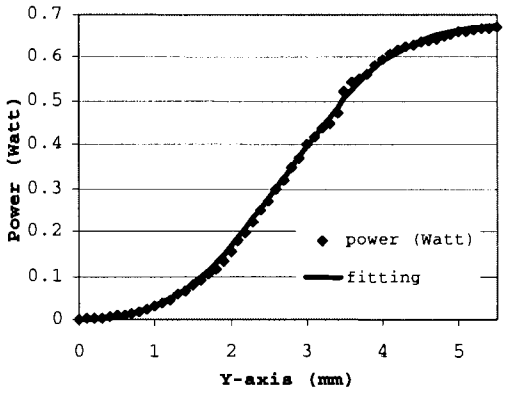

Figure 4.12 Nd:YAG 533 nm laser spot: Gaussian distribution curve fitting of laser power versus the Y position measurement.

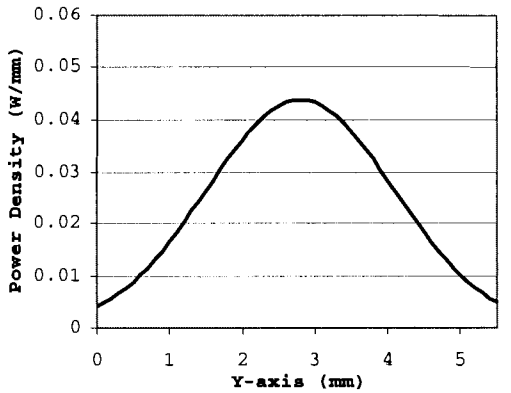

Figure 4.13 The Gaussian distribution curve of Nd:YAG 533 nm laser spot that corresponds to the fitting parameters: A = 7.05W/mm, u = 2.81 mm, σ = 1.29 mm.

4.4 Regular Photoresist Exposure Tool: Mask Aligner

The Quintel 4 Inch Mask Aligner is a top and bottom side contact lithography exposure tool for fine lines down to 1 micron or better. It uses a mercury arc lamp, and is capable of processing 4 inch substrates. The mask aligner, as shown in Figure 4.14 consists of several coordinated, inter-related systems including:

1. Substrate loading, holding and unloading system.

2. The mask supporting system.

3. The substrate/mask/align system.

4. The viewing system (microscope and illuminators).

5. The exposing system.

The exposure power is approximately 10.0 to 12.5 mW/cm^2 for I-line (365 nm). Exposure time can be set to 0.1 ~ 99.9 sec in 0.1 sec increment.

Figure 4.14 Quintel 4 inch mask aligner with a Hg arc lamp as light source is used to expose regular organic photoresists.

4.5 Wet Chemical Benches

Wet chemical benches (as shown in Figure 4.15) were used extensively in this research for four processes: RCA cleaning before deposition, oxidation and diffusion, thermal resist development after exposure (discussed in Chapter 5), electroplating using bimetallic thermal resists as seed layers, and alkaline-based silicon anisotropic wet etching (both discussed in Chapter 7). All wet processes were carried out in fume hoods with negative pressure (-0.2 Water inch) so that no chemical fumes would spread out.

Figure 4.15 Wet chemical bench.

The equipment used for RCA cleaning was quite simple: two 2-litre beakers which could clean eight four-inch wafers at one time, and a hot plate for heating up the RCA chemicals. As the wet development of exposed thermal resist and electroplating were done at room temperature, hot plate was not needed.

Silicon anisotropic etching was carried out in heated (80 ~ 95°C) KOH, TMAH or EDP solutions. A stirring hot plate with the agitation from a magnetic stirring bar, a water cooling vapour condenser and a 2-litre beaker were used for the etching process, as shown in Figure 4.16.

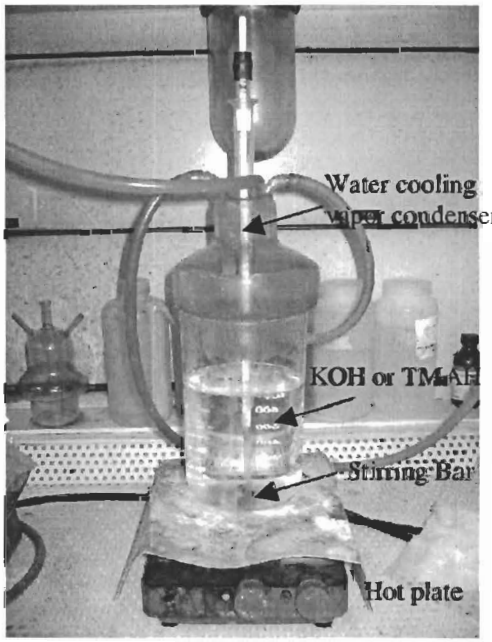

Figure 4.16 The setup for silicon anisotropic etching.

4.6 Plasma Etching Tool

As will be discussed in Chapter 7, bimetallic thermal resists were found to be resistant to fluorine-based dry plasma etching, and O_2 plasma etching. Extensive plasma etching experiments were also carried out using the Axic Benchmark-II PECVD/RIE dual chamber system, as shown in Figure 4.17. Basic components in the Benchmark 800-II® system include a Windows-based PC controller with recipe storage, two process chambers: one for PECVD deposition and the other for RIE (reactive ion etching). The RIE process chamber is made of aluminium. The upper portion contains the top electrode and is available with in-situ variable electrode spacing. The lower portion contains the substrate electrode without a heating element. Both electrodes are made of stainless steel. The upper electrode contains the "showerhead" gas delivery system and the spacing between the upper and lower electrodes can be continuously varied between 1" and 3.5". The RIE cathode is supplied with a dark space shield, confining the plasma between the two electrodes. An automatic hoist raises the upper portion of the chamber for easy access to the lower electrode for sample loading. The plasma sources are solid state and air cooled. The RF frequency is 13.56 MHz and the maximum power is 600 watts, with auto matching networks. Three channels of gases, CF_4, CHF_3 and O_2, are connected to the chamber and controlled by mass flow controllers.

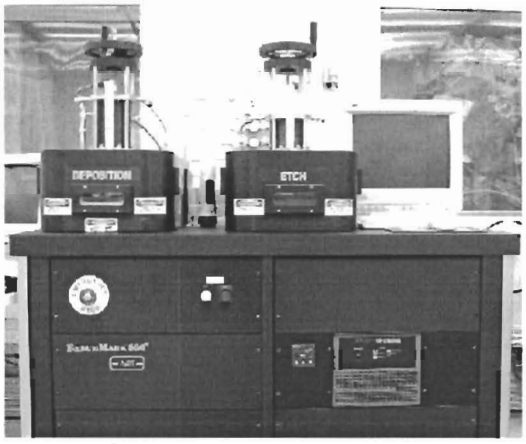

Figure 4.17 Axic Benchmark-II PECVD/RIE Dual Chamber System.

4.7 Film Analysis Tools

In order to investigate the basic materials characteristics of bimetallic thermal resists before and after the laser exposure, different kinds of analysis tools have been employed in this thesis work.

A Varian Cary 3E UV-Vis spectrometer, at the Chemistry Department in Simon Fraser University, was used to test the optical transmission of as-deposited and laser exposed thermal resist films. It has a built-in dual beam system which can eliminate the influence of the substrates. The scanned wavelength range is from 190 nm to 900 nm.

Film thickness measurement was one of the most important tests in the lab, as it was closely connected to the resist sensitivity and optical transparency. A Tencor Alpha-Step 500 Profiler was used for this purpose. The profiler is a computerized, high-sensitivity surface profiler that measures roughness, waviness, and stop height in a variety of applications. It uses a moving stylus and features the ability to measure vertical structures ranging from 100 Å to ~ 0.3 mm, with a vertical resolution of 1 or 25 Å. It can also measure micro-roughness with up to 1Å resolution over short distances as well as waviness over a full 10 mm scan.

4.8 Structural Analysis Tools

Material analyses tools at the Physics Department in Simon Fraser University have been heavily used throughout this research to understand what had happened during each of the processes. X-ray diffraction θ–2θ scan (XRD, Cu $K\alpha_1$) analysis has been frequently used in this research to evaluate the thin film compositional and micro-structural characteristics. Transmission electron microscopy (TEM, Hitachi 8000, 200 kev) was used to investigate the grain size and the film crystal structure. Scanning electron microscopy (SEM, FEI 235 Dualbeam

with Focused Ion Beam) was used to study the film surface morphology, and various thermal resist application results. AFM (atomic force microscopy) was used to test the thermal resist surface roughness. SAM (scanning Auger microscopy), RBS (Rutherford Back Scattering, at Western Ontario University) and XPS (X-ray photoemission spectrometer) analyses played important roles in understanding the laser conversion mechanism

4.9 Summary

This chapter described the preparation procedure of bimetallic thermal resist, using DC- and RF-sputtering. Single metal films were studied to determine the sputtering speed and the film density. Bi had the fastest sputter rate (12.0 Å/w.min) and In the slowest (4.0 Å/w.m). Film density was over 80% of bulk material for Bi and Sn and ~ 74% for In. The laser exposure system included mainly three components: X-Y-Z table, laser sources and control computer. The control computer could take either 8-bit bitmap file or command script text file as an input for pattern writing. Argon and Nd:YAG lasers were used as the laser sources, which offered a wide range of wavelengths from 213 nm to 533 nm. The wet bench tools and the dry plasma etcher were also introduced, as many wet and dry etching experiments were conducted on bimetallic thermal resists. Analysis tools were also briefly presented. A Varian Cary 3E UV-Vis Spectrometer, Tencor thin film profiler and an X-ray diffraction system were the three major analysis tools used throughout the thesis. The next chapter uses the deposited samples and measurement tools of this chapter to investigate the behaviour of the bimetallic thermal resists.

Chapter 5
Bimetallic Thin Film as a Thermal Resist

5.1 Introduction

For a complete photo or thermal resist, the material should be successfully exposed by sufficient irradiation, developed by dry plasma or wet solutions, able to protect underneath layer during etching, and stripped off easily when rework is required or lithography process is done. This chapter examines the attributes of the bimetallic thin films as thermal resists. The exposure process will be studied using several sources, starting with pulsed and CW argon laser. Nd:YAG laser, with different wavelengths, have also been used to make pulsed exposures on the bimetallic thin films. While direct-writing is the common method for pattern creation on the thermal resists in the lab, image projection has also been tried out. Development is an important step in photolithography to complete the pattern transfer from the mask to the resist. Two simple acid solutions will be introduced to develop the exposed thermal resists with high selectivity. Shelf tests will also be carried out to determine the film stability under extreme conditions.

5.2 Thermal Resist Exposure

Bi/In and its class of thermal resists have been exposed by several types of laser sources at 5 different wavelengths, and with different exposure methods. This section investigates the changes of physical property after exposure. The exposures described here were made on thermal resists deposited on glass slides, as described in Chapter 4.

5.2.1 Pulsed Argon Laser Exposure

The first experiment on any new film combination is to create a matrix of spots to establish the resist exposure condition. The experimental setup for argon laser pulsed and continuous exposure is shown in Figure 4.4. The laser beam was focused by a 50 mm converging lens. Exposing the thermal resists with single argon laser pulses was extensively investigated by J. Dhaliwal [76] and M. Sarunic [56] on Bi/In and Bi/Sn. As Innova 300 argon laser is a continuous laser, so the pulse was created by an electro-optical shutter. The shutter gives the fastest on and off cycle down to 10μs, and the pulse can be adjusted to any longer duration, including CW. Working in conjunction with the X-Y-Z table, the exposure system made an array of exposure spots on a Bi/In (50% Bi, 300 nm thick) film, with power ranging from 0.1W to 1.25W and pulse duration ranging from 10 μs to 20 ms. Figure 5.1 shows two pictures, front-lit and back-lit, of the same spots exposed by pulsed argon laser with different pulse duration, from left to right, 100 μs, 30 μs and 10 μs, and with different power, from top to bottom, 1.25 W, 1.0 W and 0.9 W. No surface reflectivity or colour change was observed when using 10 μs and 0.08W exposure parameters. However, with the increase of the laser power and pulse duration, black spots were observed. The spot sizes increased with the laser power and pulse duration. It is very interesting to notice that the exposed area became more transparent than the unexposed area, as checked by a back-lit illumination. This indicated obvious physical characteristics changes, and suggested even chemical property changes were incurred by the laser exposure.

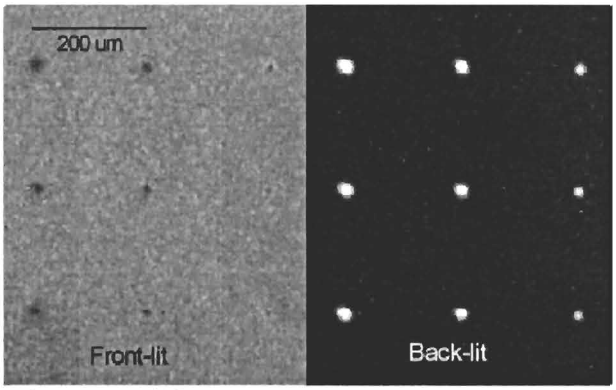

Figure 5.1 The array of spots on Bi/In, made by pulsed exposures using argon laser with electro-optic shutter. Front-lit picture shows reflectivity changes on the exposed spots, and back-lit shows the exposed spots are transparent [56].

5.2.2 CW Argon Laser Exposure

In order to create continuous exposed lines, large exposed areas and designed patterns for various applications and analyses, raster-scan exposure using continuous argon laser and X-Y-Z table was employed in this research. The setup is shown in Figure 4.2. A 48/48 nm Bi/In on glass substrate was place on the X-Y-Z table. The X-Y-Z table moved back and forth along X direction, and took a small increment step along Y direction after each X swipe. The laser beam was kept stationary during the raster-scanning and focused by a 50 mm converging lens onto the sample surface. The table moving velocity along the X-direction was usually set at 10 mm/s unless otherwise specified. In order to ensure that the raster-scan process would create an even exposure on the thermal resists, the Y-direction incremental step (Y-step) was set according to the laser spot size and the laser power. When using a 50 mm converging lens, the Y-step was set to 10 μm, as the exposed area on the resist was measured to be 16 μm wide for a single X swipe. When using a 50× objective lens, as the laser spot size was reduced, the Y-step was set to < 2 μm.

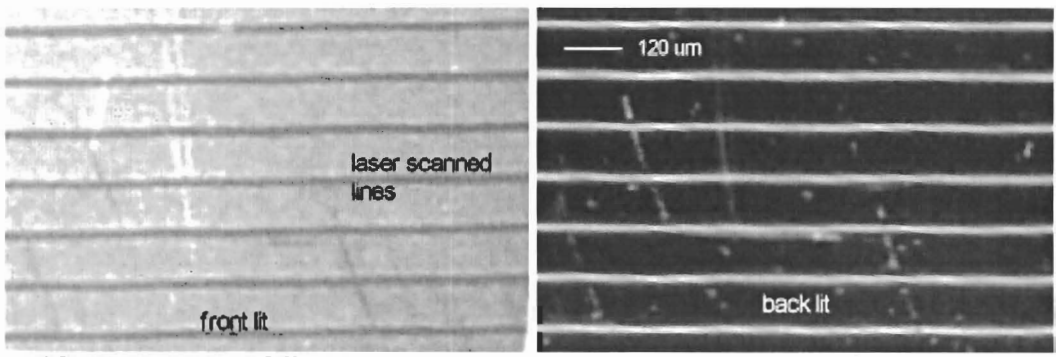

Figure 5.2 Laser exposed lines on Bi/In film made with continuous argon laser raster scanning. (glass substrate, 0.2 W laser focused by 50 mm lens)

Figure 5.2 shows a front lit picture of a group of parallel, single-scan lines exposed with 0.2 W laser beam focused by a 50 mm focal length converging lens. The thermal resist was a 48/48 nm Bi/In film deposited on glass. The correspondent back lit picture shows that the lines turned out to be transparent, as were the single pulse exposed spots in Figure 5.1. The line width was about 18 μm.

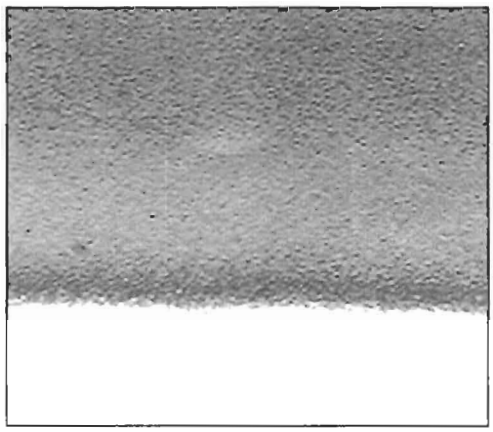

Figure 5.3 40/40 nm Bi/In: an argon laser raster-scanned area (the upper grey part), exposed with 0.5 W beam, focused by a 50 mm focal length converging lens. The lower part is the unexposed shiny bimetal film. (800 × optical micrograph)

Shown in Figure 5.3 is part of a large raster-scanned area (0.3 inch × 1 inch) made on a 40/40 nm Bi/In film, using a 0.5 W laser beam focused by a 50 mm focal length converging lens before hitting the film surface. The 800× optical image shows a continuous laser exposed film (the upper portion of the picture), a smooth interface line, and the shiny, unexposed bimetallic

film (the lower portion of the picture). The scanning speeds along X and Y directions were set to 10 mm/sec, and the lateral step size was 10 μm. The picture clearly shows that there were no obvious stripes caused by the raster-scan process.

It is noticed that the bimetallic films, such as Bi/In and Sn/In, and the single metal Bi, In and Sn films, are very soft. Scratches can be easily made on the unexposed films by finger nails. Thus, surface protection is critical to this bimetallic thermal resist process.

5.2.3 Exposure with Pulsed Nd:YAG Laser

In order to meet the high throughput requirements, laser sources of high power are needed in the micromachining and microfabrication industry. It is easy to calculate how much light power is needed from the sensitivity of a photoresist and the exposure time of a required throughput [6]. A typical I-line (365 nm) photoresist requires an optical energy density of 100 mJ/cm^2 for its exposure. A minimum optical power density of 200 mW/cm^2 is necessary if the exposure is set to 0.5 second. Usually light sources (e.g. mercury vapour lamps) with 2.5 to 5 times the requested minimum power are supplied. Taking the total illuminated area as 8 cm^2, which is common for stepper systems, a total power of 4 to 8 W is required. This is a significant amount of laser power.

The photo exposure systems that are most widely used in modern microlithography are steppers with high power (2 – 20 W) pulsed excimer lasers, with the wavelength ranging from 248 nm to 195 nm (may be extended to 157 nm in the future), and pulse duration from 4 ns to 50 ns depending on the laser type. Photoresists for these wavelengths are exposed at the level of 5 – 50 mJ/cm^2. Another laser light source, Nd:YAG laser, has the great potential applications in the lithography: the two useful wavelengths are 4th harmonic 266 nm and 5th harmonic 213 nm, with very good optical characteristics and a similar pulse duration. However, the successful

introduction of 248 nm and the great progress made in development of 193 nm excimer laser lithography has attracted much of the attention away from the Nd:YAG laser [6]. Nevertheless, Nd:YAG laser is similar to an excimer: both are pulsed lasers and with comparable wavelengths. As excimer lasers require complex optical systems to correct their poor optical characteristics, Nd:YAG is the ideal alternative to an industrial level exposure system. The Nd:YAG system used in our lab was described in Chapter 4. Since it can provide laser beams with four different wavelengths (while excimers have only one), the Nd:YAG system gives the research wavelength flexibility to investigate wavelength invariance characteristics of the bimetallic thermal resists, and the minimum energy needed to convert the bimetallic thermal resists at different wavelengths.

Two kinds of exposure methods were employed in the Nd:YAG pulse experiment: proximity and projection exposure. In the proximity exposure test, the beam from the Nd:YAG laser, with a diameter of approximately 5 mm, was used without any additional lenses to focus the beam. A series of tests were done with nested L type exposure structures (see Figure 5.4) at various laser powers for several film thicknesses. A 150/150 nm thick Bi/In imaging layer converted to the low absorbing material with a minimum energy pulse of approximately 40mJ/cm^2 with 533 nm light (very close to the wavelength of the argon laser). SEM and optical microscope inspection showed that the imaging layers exposed with the short pulse were identical in appearance to exposures with the CW argon laser. For a thinner Bi/In sample, 15nm/15nm thick, deposited on glass, the minimum exposure energy at 533 nm was measured at about 7 mJ/cm^2. The diameter of the 266 nm laser remained at about 5 mm and no lenses were used to focus the light. Again using a sample of the 15 nm/15 nm thick Bi/In imaging layer deposited on glass, the 266 nm exposure converted the resist to the low absorbing material at a power density of about 6 ~ 7 mJ/cm^2, similar to the 533 nm light, illustrating the wavelength invariance property of the resist, that is, the exposure condition varies little with the wavelength.

In addition to just exposing the thermal resist with the Nd:YAG laser spots, images have also been made on 35/35 nm Bi/In films as shown in Figure 5.4. A normal chrome mask with fine structures of various sizes was placed 0.5 mm above the Bi/In film. 2nd harmonic 533 nm was used as an illuminating source, with a power density of 2.5 mJ/cm^2, and repetition rate of 2 pulses/sec. One to ten pulses were used to make an image.

This result also shows that the conversion reaction time is < 4 nsec. Hence, the necessary exposure time is set by the laser heating rate of the film (i.e., the time needed to reach the threshold temperature), not the reaction rate.

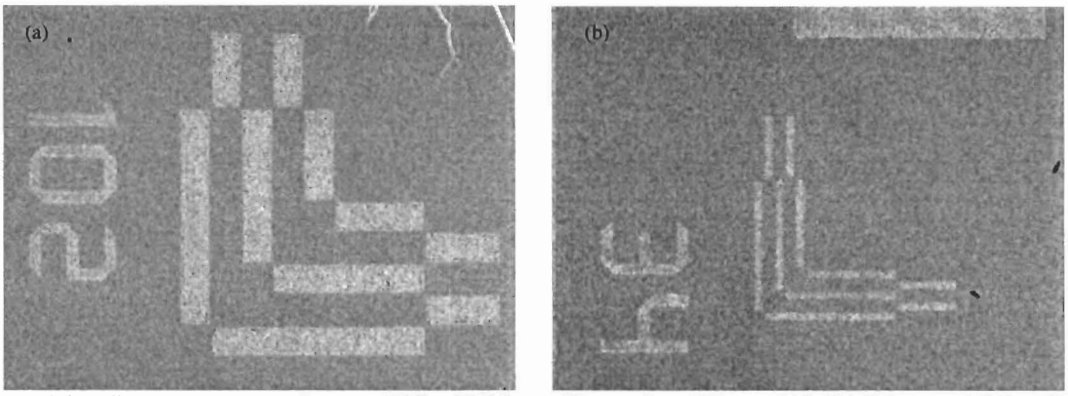

Figure 5.4 Images were made on a Bi/In 35/35 nm film, using 533 nm Nd:YAG laser at 2.5 mJ/cm^2, 3.5 ns/pulse. The line width is 150 μm in (a) and 30 μm in (b) (50 × optical micrograph).

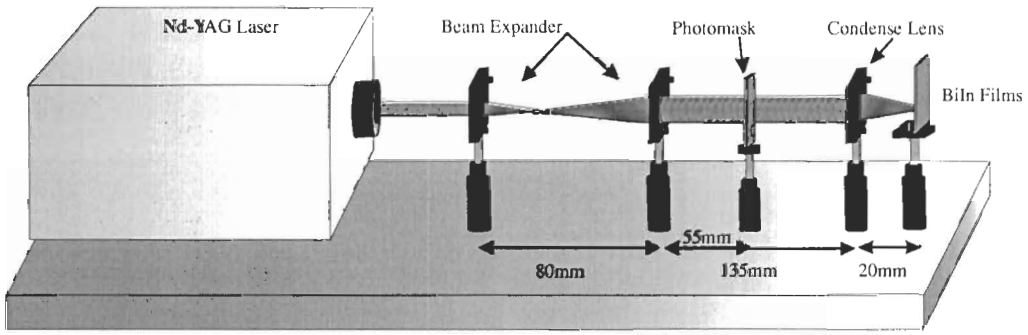

Figure 5.5 The optical setup for Nd:YAG to make a projected image on the Bi/In thermal resist.

Figure 5.6 One of the patterns on the Al photomask used for the projection. The width of the rectangular lines is from 50 to 150 μm.

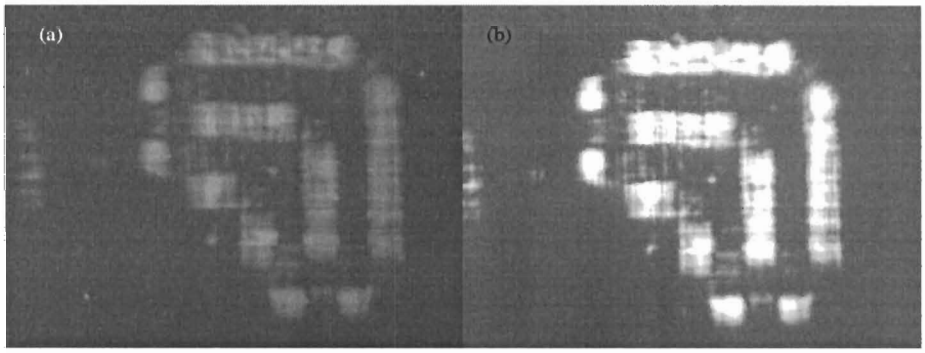

Figure 5.7 An image made on a 45/45 nm Bi/In film. (a) is a front-lit microscopic view of a projected pattern, and (b) is the back-lit view of the same image. The line width is 20 μm.

The optical setup for projection exposure is shown in Figure 5.5. It consisted of a beam expander, a condensing lens and a photo mask in between. The Nd:YAG lasers running at the 2nd harmonic (533 nm green), 4th (266 nm UV) and 5th (213 nm UV) were used as the projecting light source. The photomask was full of the pattern shown in Figure 5.6, with feature widths from 50 to 150 μm. Figure 5.7 (a) and (b) are the front and back-lit microscopic pictures of the projected images projected on a 45/45 nm Bi/In film. It was noted that the projected image had some unwanted exposures between the patterned lines. This was caused by the poor uniformity of the Nd:YAG laser beam.

It is important to notice that the laser exposed areas on the thermal resist, either exposed by argon laser or Nd:YAG lasers of different wavelengths, show a substantial change in optical

characteristics: the exposed areas are more transparent than the unexposed films, so that the projected pattern is visible. This demonstrates an important advantage of these thermal resists: the exposed pattern is directly seen after imaging. It is known that the latent images made on conventional photoresist after exposure are not visible, and the inspections such as CD measurement, overlay registration, can only be done after development, when the relief images are generated. Photo re-work has to be done if serious defects are found. With the unique feature that the latent images patterned on the thermal resists are visible, bimetallic films will save process cycle time, as inspections can be carried out before development. For our experimental design, this visibility was extremely important. As will be discussed in Section 5.3, when a visible pattern appeared on the film, it could be successfully produced as a developed structure (relief image). Thus, it was only necessary to visibly inspect the films after exposure to determine whether the exposure levels required were obtained. In comparison, no organic photoresists can be inspected before development.

Unlike conventional organic photoresists, which should be handled only under the standard photolithography yellow safelights, the bimetallic films do not show exposure under regular illumination for any given period of time. It is only when the laser energy is delivered in a short enough pulse and exceeds the thermal threshold are these films exposed. This makes thermal resists more flexible in the environment of expensive fabs.

5.2.4 Wavelength Invariance: Experimental Results

RAT simulations presented previously in Chapter 3 suggest that exposure sensitivity (absorption) changes slowly from 514 nm, 248 nm, 157 nm to 13.4 nm and 1nm. Experimental results in the previous section show that single pulse exposures of ~7 mJ/cm^2 can successfully create exposed images on Bi/In films of 15/15 nm to 45/45 nm thick at 213 nm, 266 nm and 533

nm. Argon lasers with 514 nm and 488 nm wavelengths have also successfully exposed the bimetallic films. This confirms the optical calculations predicting wavelength invariance.

It is also worth noting that simulation suggests that Bi/In films of 15/15 nm thickness still absorb ~12% of the total exposure light in the X-ray range (1nm) (refer to Chapter 3). Compared with about 60% of the light absorption at 248 nm. Based on the measured 266 nm Nd:YAG exposure sensitivity, which is 7 mJ/cm^2, this projects that Bi/In resist could have a single pulse exposure sensitivity of ~35 mJ/cm^2 at the X-ray range.

Given the fact that it can be exposed by IR 830 nm GaAs diode laser beam, which will be discussed in Chapter 8, both theoretical modelling and experimental results demonstrate that bimetallic thermal resists operate from IR to the EUV, and even into X-ray range, showing the wavelength invariance property.

5.3 Thermal Resist Stripping and Development

5.3.1 Resist Stripping

Being able to be stripped from the substrate is one of the fundamental requirements of a good photoresist. Organic photoresists are usually stripped by solvents such as acetone and O_2 plasma. But organic contamination is always a problem. Hence, chemical cleans (e.g. RCA) are often done between layers. For inorganic metallic thermal resists, RCA2 ($HCl:H_2O_2:H_2O$ = 1:1:6) at 80°C has been chosen as the stripper after the patterning is done with defects or there is a need for reworking. The reason that RCA2 is used is that it has been the classic cleaning solution to remove metallic contaminants in the microfabrication industry for decades. It is silicon process compatible.

To test the effectiveness of RCA2 stripping, a silicon wafer was first deposited with 120/120 nm Bi/In film. Laser raster-scanning (0.15 W argon laser focused by 50× objective lens,

y direction increment 0.4 μm) was then carried out to created a 1 × 1 cm^2 exposed area. The whole wafer was subsequently processed with an RCA2 clean (1:1:6 at 80°C). It was observed that the unexposed area dissolved in RCA2 in less than 10 seconds. The exposed area dissolved in about 4 minutes. After a full cycle of RCA2 cleaning for 10 minutes, the wafer was rinsed thoroughly with DI water. Auger test was carried out to analyse the wafer surface before and after the cleaning on both exposed and unexposed areas. As shown in Figure 5.8, Bi and In peaks were seen on as-deposited film. An oxygen peak appeared after laser exposure. After RCA2 stripping, only Si and O peaks showed up, indicating that Bi and In had dropped below the Auger test detectable limit.

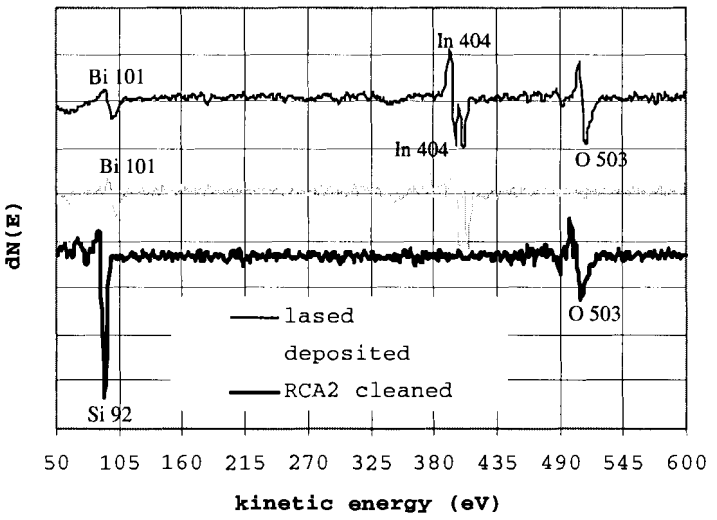

Figure 5.8 Auger analysis shows that RCA2 can strip exposed (0.15W, 50× objective lens) and unexposed Bi/In film effectively. Lased and RCA2 cleaned curves was shifted by +4000 and -2800 counts, respectively, for display purpose.

It was also noted that RCA2 cleaning could not remove the exposed film effectively when it had been exposed with very high laser power (> 0.35W 50× objective lens on the same silicon wafer). HF dip was needed in order to completely remove the layer. Refer to Chapter 7 and 10 for the discussion of the possible cause of this phenomenon.

5.3.2 Resist Development

Resist development is an essential process for modern microlithography, in which either the laser exposed area (positive resists) or the unexposed area (negative resists) should be selectively removed so that the retained will form a lithographic mask for subsequent processes. The development selectivity results from the change of the chemical and physical properties of the resist after exposure. It was noted that Bi/In deposited on glass and quartz substrates was converted to a significantly less optically-absorbing material when exposed to laser irradiation. Such considerable optical change suggested that the converted materials have significantly different physical and chemical characteristics than the unconverted materials. In wafer fabrication industry, an etch selectivity ratio > 20:1 (the ratio between the etch rate of the unexposed and exposed layers) is preferred when developing hard masks.

Two types of developer can be examined: one is to selectively eliminate the unexposed area of the metallic resist, making it a negative resist; the other is to selectively remove the exposed area, making it a positive resist. A Bi/In film deposited on SiO_2 (100 mm diameter wet oxidized wafer) with equal thickness of 45/45 nm was used in this test. A series of lines with different widths were first made by argon CW laser raster-scanning (0.2 W focused by 50× objective lens). The sample (for good comparison, one wafer was cut into pieces and each time a small piece was tested.) was then dipped in the developing solution for 5 sec to over 15 min and rinsed thoroughly with DI water. A profiler was used to measure the film thickness at the exposed and unexposed areas before and after the development. Different acid solutions with different concentrations and acid combinations were tried out, including nitric acid, hydrochloric acid, acetic acid, sulphuric acid, phosphoric acid, mixtures of nitric acid and hydrochloric acid, nitric and acetic acid, sulphuric and hydrochloric acid, and phosphoric and acetic acid.

Most of the acid solutions and acid mixtures did not meet the developer requirement. However, it was found that a solution of DI water, nitric acid and acetic acid with the ratio of

HNO_3:CH_3COOH:H_2O = 1:3:6 at room temperature removes the unexposed area much faster than the exposed, thus making the resist a negative one. It gave a good etch selectivity of exposed to unexposed area of larger than 65:1 (refer to Table 5.1). The etch rate of unexposed area is about 26 Å/sec. However, nitric acid solution has a scum problem: it cannot remove the trace metal residue in the unexposed area within the nominal development time according to the etch rate, as shown in Figure 5.9. To solve this problem, usually longer development is applied and followed by a dilute RCA2 clean up for 10 to 30 seconds.

The chemical reactions during the development are not fully understood at this moment. It is speculated that HNO_3 is the major etchant. The role of acetic acid (CH_3COOH) in the developer is complex. It is frequently substituted for water as the dilutent. It has a lower dielectric constant than water (6.15 for CH_3COOH versus 81 for H_2O), which produces less dissociation of the HNO_3 and yields a higher oxidation power of HNO_3. Also acetic acid is less polar than water and can help in achieving proper wetting of the metal surface [77]. With the increase of nitric acid concentration, the etch speed of both exposed and unexposed films increases. But the develop selectivity decreases. Figure 5.10 shows the relation between the develop selectivity and the nitric acid : acetic acid : DI water ratio. The x-axis is the number of parts of nitric acid in the solution, y-axis is that of acetic acid, where the total of nitric acid, acetic acid and DI water should be 10. It shows that the 1:3:6 ratio yields the highest selectivity.

The RCA2 stripping process lead to the finding that the solution of HCl:H_2O_2:H_2O = 1:1:48 at room temperature is an even better developer for Bi/In resist. Instead of using the HCl:H_2O_2:H_2O solution at a much higher concentration and at the temperature of 80°C for stripping, the exposed films were developed in a much dilute formula and at room temperature. From the slope of these lines, the selectivity is above 60:1, and the etch rate is 65 Å/sec, which is faster than nitric acid solution (Table 5.1). It also has good descumming capability, and no remnant material was left behind after the development, as shown in Figure 5.11. Figure 5.12

shows the result from an etch comparison experiment. One can notice that the thickness of the unexposed area of the film reduces rapidly, while that of the exposed area changes slowly with time.

Table 5.1 Development solutions

Solution	Chemical Ratio	pH Value	Etching Selectivity	Etch Rate
Nitric Acid Solution @25°C	HNO_3:CH_3COOH: H_2O = 1:3:6	2	> 65:1	26 Å/sec
HCl:H_2O_2: H_2O @25°C	HCl:H_2O_2: H_2O = 1:1:48	2	> 60:1	30 Å/sec

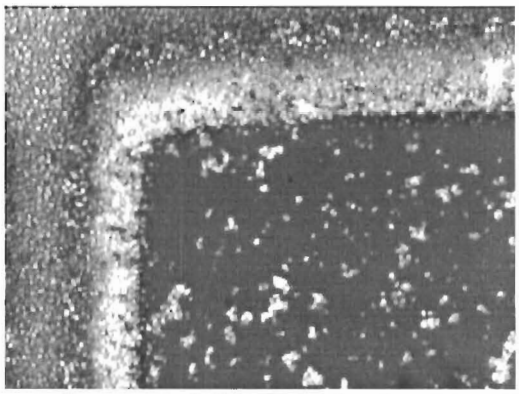

Figure 5.9 Residue was seen after exposed Bi/In was developed by nitric acid solution. (30/30 nm film exposed by 0.2 W argon laser focused by 50 mm lens, developed for 1 minute)

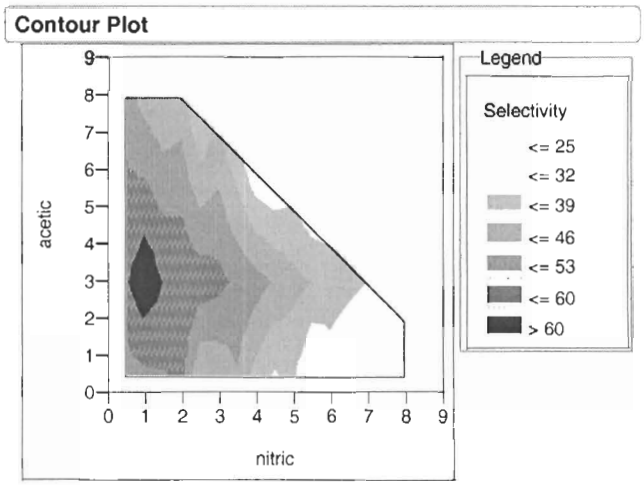

Figure 5.10 Develop selectivity vs. nitric acid : acetic acid : DI water ratio.

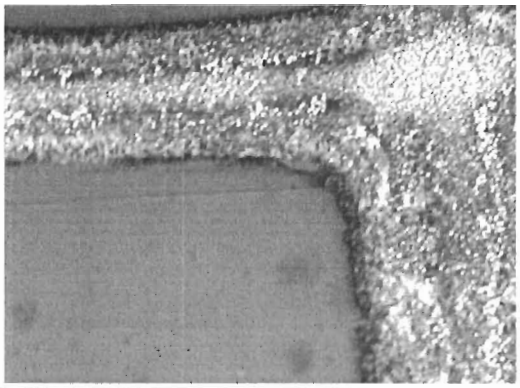

Figure 5.11 Developed with dilute RCA2 solution, no residue was seen on the sample.

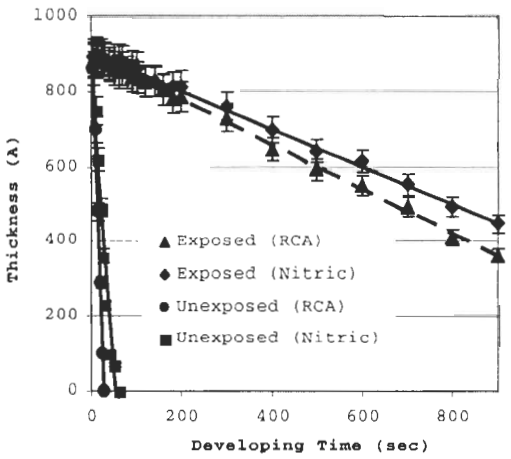

Figure 5.12 Development rate comparison between nitric acid solution and $HCl:H_2O_2:H_2O$ solution. The thickness of Bi/In films reduces as the etching time increases.

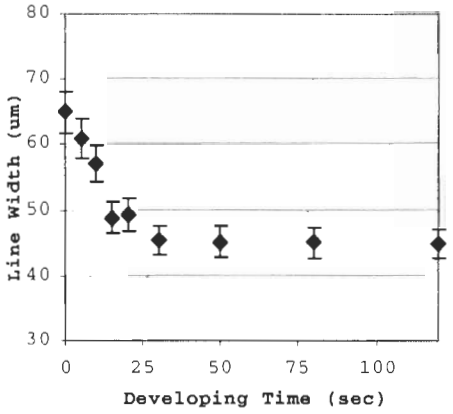

Figure 5.13 Line width reduces with the developing (dilute RCA2) time. It saturates at 45 μm.

As a wet development process is not anisotropic etching, the width of the exposed lines is expected to decrease with the development time. A 45/45 nm Bi/In film was exposed with 65 μm

wide lines using CW argon laser raster-scanning (0.2 W and 50 mm lens). The sample was developed in a $HCl:H_2O_2:H_2O$ solution for different durations (5-150 seconds). The width of the lines was measured using an optical microscope line width system. As shown in Figure 5.13, the line width dropped quite fast for the first 20 seconds, and then saturated at 45 μm. There are many possible causes to this line width reduction phenomenon. One of the most likely reasons is that since the argon laser intensity across the laser beam follows a Gaussian distribution, the thermal resist exposed to the beam edge is not converted as completely as is the centre of the beam. Also the heat dissipation along the lateral directions in the resist film could partly convert the film to the exposed state when the film thickness is greater than 30 nm [78]. This is due to the long duration (~ 1 msec) argon laser pulse, and would not occur in the shorter 20 nsec excimer laser pulses of current DSW (direct-step-on-wafer) exposure tools, since the exposure is too short for the heat to flow more than 1 nm. (See Chapter 9 thermal modelling)

In order to make an anisotropic development, plasma etching of the bimetallic thermal resist is a viable method as ions in the plasma can be guided in one direction. Also, successful plasma development will make Bi/In thermal resist a completely dry lithographic process material.

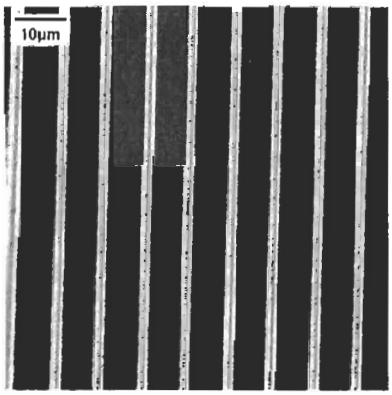

Figure 5.14 SEM picture of the developed 2 μm wide Bi/In lines with 10 μm spacing.

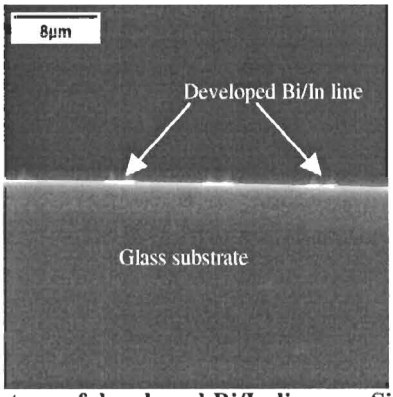

Figure 5.15 A 45° tilted SEM picture of developed Bi/In lines on SiO_2/Si wafer.

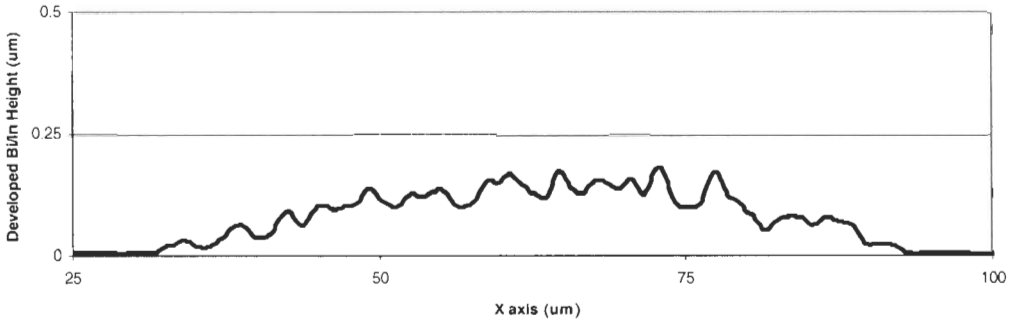

Figure 5.16 Profile of a developed Bi/In line.

Figure 5.14 is an SEM picture of a developed Bi/In line pattern on a SiO_2 layer on a silicon wafer. These are 2 μm wide lines with 10 μm spacing made by CW argon laser (514 nm at 0.05 W, 50× objective lens) raster scanning on a 45/45 nm Bi/In film. The sample was developed in a $HCl:H_2O_2:H_2O$ solution for 60 sec. Figure 5.15 shows a 45° tilted SEM picture of the developed Bi/In lines. Figure 5.16 shows the profile of a developed Bi/In line on the same sample. The total thickness of the film was ~0.12 μm.

5.4 Stability of As-deposited Bimetallic Thermal Resists

A shelf lifetime test was conducted to investigate the stability of the as-deposited Bi/In films. A Bi/In 50/50 nm film was deposited on a glass slide. Then the slide was cut into 4 pieces. XRD analysis and UV spectrum were carried out on each of the slide pieces before the shelf test.

A multi-purpose stainless steel oven was used for the shelf test. The oven temperature was kept at 50±1°C , >90% humidity for 10 days (Table 5.2).

The four samples were taken out of the oven separately according to the time schedule in Table 5.2, and then XRD and UV spectrum tests were immediately conducted. Figure 5.17 is the combined result of pre and post oven test XRD (Refer to Chapter 6 for more discussion of XRD analysis). The film properties do not change after around 10 days in the humid, hot environment. UV-Spectrometer result shows the same result, as in Figure 5.18. As a matter of fact, the Bi/In films can still be exposed and developed even after being stored on our lab shelf for 3 years. Sn/In films exhibit the same stability characteristics. Bimetallic thermal resists are extremely stable under normal environment conditions. By comparison, the life time of a typical organic photoresist is about 7 days if it is to operate properly as a resist. Older photoresists are also much harder to strip.

Table 5.2 Shelf test conditions.

Sample	#1	#2	#3	#4
BiIn film structure	50 nm / 50 nm	50 nm / 50 nm	50 nm / 50 nm	50 nm / 50 nm
Shelf Test Temperature	50±1°C	50±1°C	50±1°C	50±1°C
Shelf Test Humidity	>90%	>90%	>90%	>90%
Shelf Test Duration	66 hours	117 hours	158 hours	233 hours

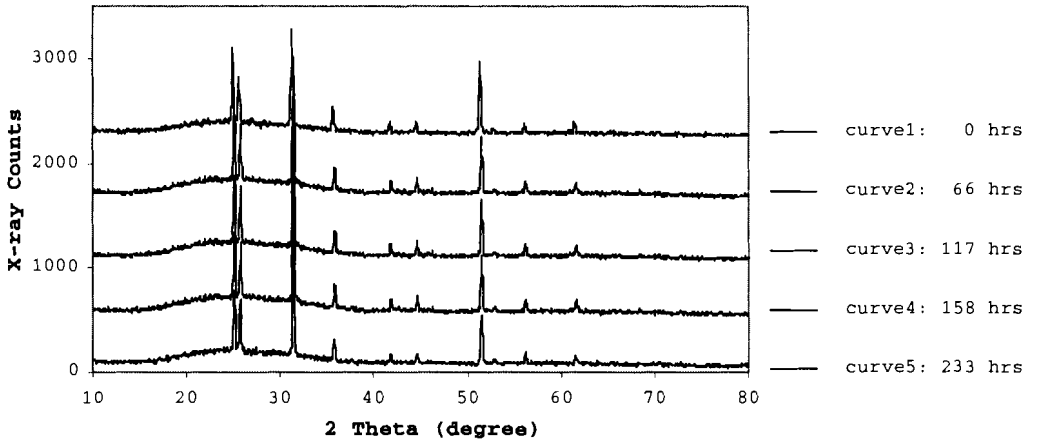

Figure 5.17 XRD spectra for shelf test on the same 50/50 Bi/In film. From the bottom to the top are curves of 1) as-deposited, 2) after 66 hours, 3) 117 hours, 4) 158 hours and 5) 233 hours of oven time. No detectable changes were observed.

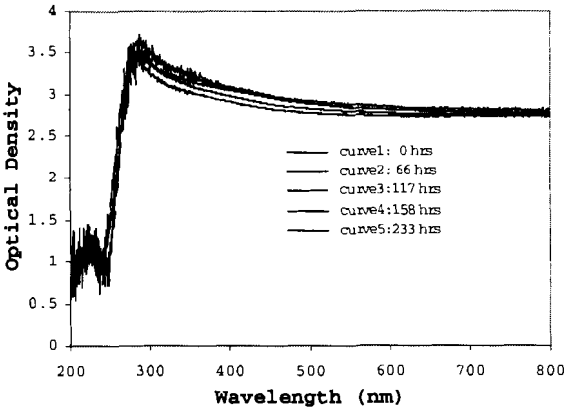

Figure 5.18 UV-Spectrometer results of shelf test. From bottom to top are 1) after 0 hours, 2) 66 hours, 3) after 117 hours, 4) after 158 hours and 5) after 233 hours of shelf test.

The experiments on Bi/In films first started in 1999. We have samples of unexposed and exposed bimetallic resists which are over 4 years old. No notable changes in these films are found. Since stripping is a chemical etch process, it is also unaffected by age. This long lifetime is another advantage to Bi/In and its class of thermal resists.

5.5 Electrical Properties of Exposed Bimetallic Resists

Relative to organic resists Bi/In has the unusual property of being electrically conductive instead of insulating both before and after exposure. This in turn opens the possibility of several interesting applications which will be discussed in Chapter 7 and 8.

Organic photoresist layers, from the process point of view, are sacrificial layers, which must be removed after the patterns are transferred to the structural layers below. Bimetallic thermal resists are totally different. Not only can it be used as a lithographic layer for patterning, but also as a structural film for subsequent processes. Another significant difference, which can be explored, is that the bimetallic thin film thermal resist is conductive both before and after exposure. This electrical conductivity opens the door to many potential applications. The sheet

resistance of exposed and unexposed samples was measured using an MP0705A four-point probe from Wentworth Labs, which was connected to an HP 3478A multimeter. The 4 probes are arranged in a line with 1 mm spacing between each another. Electric current flows between the outer two probes, and the voltage drop across the film is measured by the inner two probes. To ensure the accuracy of the measurement, it is required that the conducting film thickness be less than 40% of the spacing, and that the edges of the film be more than 4 times the spacing distance away from the measurement points. The sheet resistance measurement was carried out on a series of single and bilayer thin films deposited on glass substrates. The Bi/In bilayer film was 30/30nm. It was first measured on the unexposed Bi/In film (Bi/In 30/30 U in Table 5.3), and then on the argon laser raster-exposed film (Bi/In 30/30 E in Table 5.3). The laser power was 0.20 W. The exposed sample was dipped in $HCl:H_2O_2:H_2O$ solution for 40 sec for development, and its sheet resistance was measured after a N_2 blow-dry (Bi/In 30/30 D in Table 5.3). The resistances of single layer Bi and In films of thickness 15 nm, 30 nm, and 45 nm were also measured. It is noticed that the resistivity of the thinner Bi and In films was higher than that of bulk materials, dropping significantly as the films got thicker. This can be attributed to the fact that the oxidized part of the film is likely more significant in thinner films than in thicker films. It is noticed that the exposed films were slightly more conductive than unexposed films. A surprising finding is that the developed resist is conductive. It is known that ITO (indium tin oxide) is a conductive and transparent oxide, and it has been widely used as a conductive optical film for decades. Indium bismuth oxide is clearly a new type of conductive and transparent oxide. This indicates that the Bi/In thermal resist can not only be used as a patterning material, but also as an electroplating seeding layer (refer to Chapter 7 for the electroplating application). This has the potential to simplify the manufacturing process since separate resist removal and seeding processes are not required. The developed film is more conductive than most of the current barrier layer films and silicide films. For example, the resistivity of the most conductive silicide

$TiSi_2$ is about 1.6×10^{-2} Ωcm, and TaN, the barrier layer used for copper plating, is about 2.5×10^{-1} Ωcm [79].

Table 5.3 Sheet resistance/resistivity of as-deposited and exposed Bi/In films (0.2 W, 50 mm lens).

	Bi (15nm)	Bi (30nm)	Bi (45nm)	In (15nm)	In (30nm)	In (45nm)	Bi/In 30/30 U	Bi/In 30/30 E	Bi/In 30/30 D
Sheet resistance (Ω/sq)	484.7±39	171.0±13	79.6±5	32±3	9.3±0.9	3.5±0.2	82.8±6	80.8±5	97.5±7
Film resistivity (Ωcm)	7.27×10^{-4}	5.13×10^{-4}	3.58×10^{-4}	4.91×10^{-5}	2.79×10^{-5}	1.56×10^{-5}	4.97×10^{-4}	4.85×10^{-4}	5.03×10^{-4}
Bulk resistivity (Ω cm)	1.3×10^{-4}			8.0×10^{-6}			-	-	-

5.6 Summary

The main focus of this chapter was to reveal that bimetallic thermal resists are complete resists: they can be exposed, developed and stripped, just like conventional organic photoresists. Experimental results confirmed that bimetallic thermal resists are wavelength insensitive, as predicted by the optical model. Different laser sources (argon and various Nd:YAG lasers) and different exposure methods (proximity and projection exposures) were applied to convert the bimetallic thermal resists. Shelf life tests demonstrated that as-deposited bimetallic films are very stable under normal environments. An interesting finding was that exposed bimetallic films are still conductive, which could open the door to some new applications. Although Bi/In was mainly reported here, Sn/In and single In metal films have identical exposure and development characteristics. The next chapter will discuss the structural analysis of the bimetallic thermal resists before and after laser exposure.

Chapter 6
Structural Analysis of Bimetallic Resists

6.1 Introduction

Bimetallic thermal resists have shown, in previous chapter, unique features and promising applications in micromachining and microfabrication industry. They can be laser exposed, wet developed, are resistant to wet and dry etching, and more transparent after laser exposure, which makes them potentially a commercially viable direct-write photomask material. But why the bilayer thin film becomes etch-resistant and transparent after laser exposure? To understand the laser conversion mechanism of bimetallic thermal resists, extensive material analyses will be carried out in this chapter. First, single metal films will be studied by XRD and surface profiler before and after the laser exposure. The test results will give one some idea of intrinsic behaviour of each metal film under laser exposure. Then Auger, XPS, RBS, XRD analyses will be carried out to investigate the structural changes in bimetallic films. It is well-known that microfabrication is extremely susceptible to contaminants. An important question on bimetallic thermal resist process is: is the thermal resist poisonous to silicon devices? The successful manufacturing of solar cells with bimetallic thermal resist process gives a positive sign. In this chapter, this issue will be further inspected from a different angle: material analysis.

6.2 Analyses of Single Film Laser Exposure

6.2.1 Bismuth Films

It is advantageous to look into the laser exposure of single film system as it is much simpler than that of a bilayer system. Single layer Bi and In 40-48 nm films were DC-sputtered separately on glass slides. These experiments used the same Argon laser system with the beam focused by a 50 mm lens.

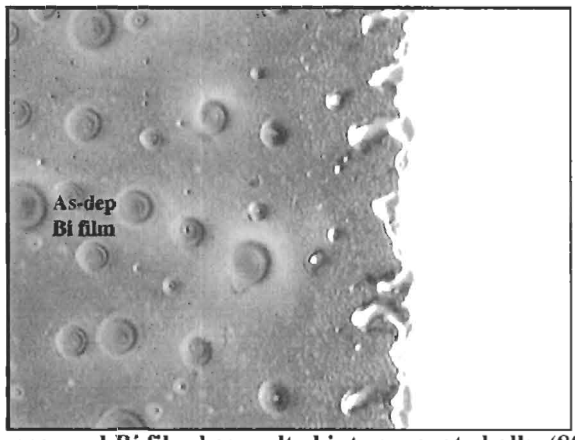

Figure 6.1 Laser raster-scanned Bi film has melted into separate balls. (800× optical)

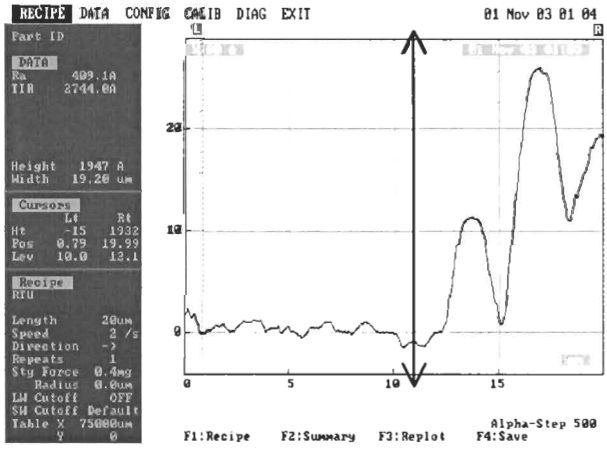

Figure 6.2 Profile test shows comparatively smooth as-deposited Bi area on the left of the plot and balling up on the exposed Bi area on the right of the plot.

The exposed Bi film started to show "transparency" at very low laser powers (75 mW). This is in agreement with the fact that the Bi thermal conductivity is lower than any metal, except

mercury, and is also in agreement with our optical modelling, indicating that Bi film absorbs more energy from the incident light, although Bi has higher melting point than In. However, it was found that the Bi film melted and agglomerated to form round shape dots. It was not continuous, as shown in Figure 6.1. Profilometry confirmed this discontinuous characteristic (Figure 6.2). This is totally unlike the single In films which remain contiguous.

6.2.2 Indium Films

More interestingly, it was found that In film turned transparent at 225 mW, twice as much power needed to make Bi/In bilayer transparent. Since there is no other metal in this single In system, alloying is not likely the main process in bimetallic thermal resist laser conversion. Under the microscope it was found that converted In film was even and continuous (Figure 6.3). Profilometry test showed that as-deposited In film was rough, as in Figure 6.4 (a). The film became even rougher as the film thickness increased. The roughness remained pretty much the same after In film is laser exposed, and the film is still continuous and even. However, significant growth in film thickness was observed, as in Figure 6.4 (b). Film thickness increase (from 48 nm to 148 nm) indicates a possible reaction process, and this was confirmed by XRD analysis.

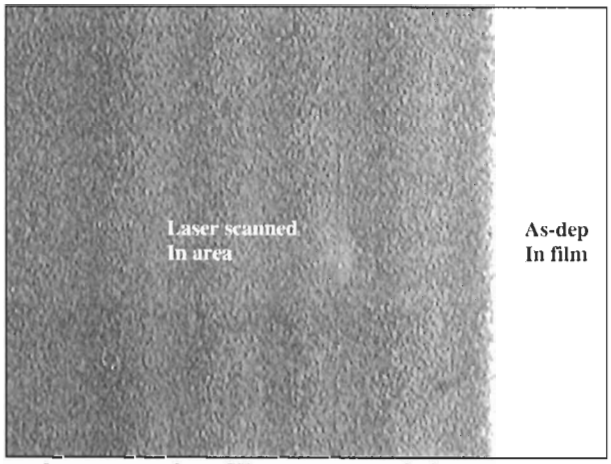

Figure 6.3 In film after laser scanning. The grey area is laser raster-scanned. It is transparent, even and continuous. The white area is as-deposited 48 nm thick In. (800× optical)

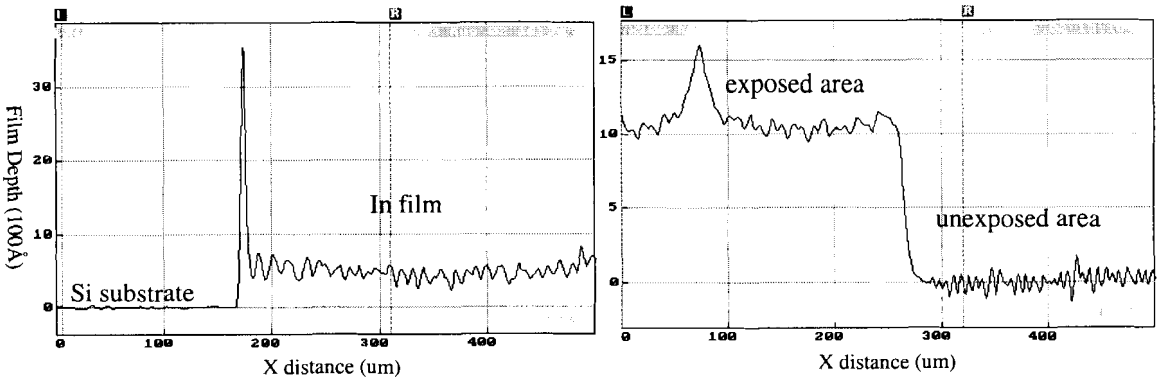

Figure 6.4 (a) Profilometry result of 48 nm thick, as-deposited, single layer In on silicon substrate. On the left side of the high peak is the Si substrate and the right side is the In film, Ra = 218 Å. (b) A profile across the exposed and unexposed area of 48 nm In film. Area on the left side of the high step is exposed, while the right is unexposed.

6.2.3 X-ray Diffraction of Bi and In films

X-ray diffraction analysis was carried out on the Bi and In laser-exposed films to investigate how single film structure changes with laser power. In order to get strong XRD peaks from the single metal films, thick films (120 nm) of Bi and In were DC-sputtered on glass slides. The argon laser was used to raster-scan the samples to make large laser-converted area. As per Sections 6.2.1 and 6.2.2, XRD was performed on areas scanned with different laser power. The XRD peaks were indexed by calculating the crystal plane distance d from the diffraction angle of the peak θ using Bragg's Law equation, and checking against the JCPDF (Joint Committee for Powder Diffraction Files) cards 5-519, 5-642, 14-699 and 6-416 [80]. The Bragg's Law shows that

$$n\lambda = 2d \sin\theta \tag{6.1}$$

where d is the crystal plane distance, θ is the diffraction angle, λ is the wavelength of the X-ray, and n is an integer.

Although Bi thin film melted to form round shape dots, XRD analysis showed that Bi was actually also oxidized after laser exposure. As shown in Figure 6.5, no oxidation was

observed in as-deposited film. With lower power laser exposure, Bi_2O_3 started to grow. With exposure of 0.9 W laser power, all Bi peaks disappeared and only one Bi_2O_3 peak was seen, indicating that laser conversion of Bi film is an oxidation process, and that the exposed Bi film was arranged along a preferred orientation <121>. The hump from 15° to 35° in the XRD curve was caused by the glass substrate.

Figure 6.6 shows three XRD curves of In samples: as-deposited film (0 W), scanned with 0.4 W and with 0.9 W laser. As expected, the as-deposited film displays typical diffraction peaks of powder indium. All the major peaks show up. From left to right, the peaks are (101) (002) (110) (112) (103) and (211), respectively. No preferred orientation is observed. With the increase of laser power to 0.4 W, In was oxidized and two In_2O_3 peaks appeared. When In film was laser-scanned with 0.9 W laser power, all the In peaks disappeared, indicating that the film was completely converted into a non-metal structure. It is interesting to notice that even indium oxide peaks no longer existed. This may be due to an orientation change of the converted film, or, most likely, its conversion to an amorphous material. Powder diffraction analysis on the high power laser converted film will be carried out to confirm whether the film is crystalline or amorphous.

6.2.4 Single Metal Process

These single metal film results give an important clue to the process of bimetallic thermal resists. The X-ray results are very clear because these peaks are well known in the literature. It is noted that as there is only one metal laser exposed, there can be no metal alloying reaction. The clear presence of metal oxide peaks demonstrates that oxidation is an important part of the metallic thermal resist process. By extension, this helps us understand the probable behaviour of the bimetallic films as Bi-In alloy oxide X-ray data are not available in the literature.

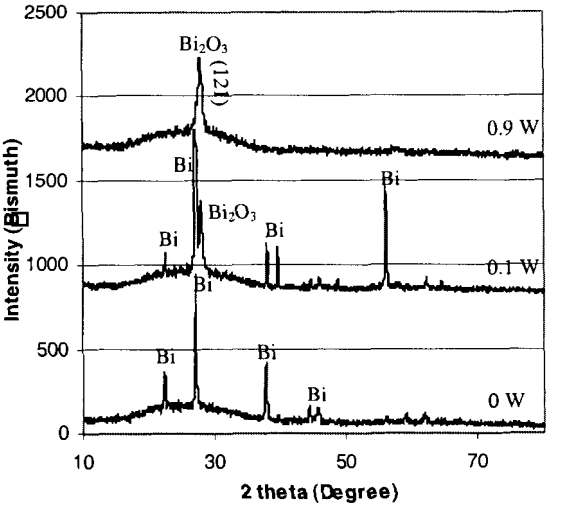

Figure 6.5 X-ray diffraction of Bi films: as-deposited (0 W), 0.1 W and 0.9 W laser exposed. The laser conversion is an oxidation process.

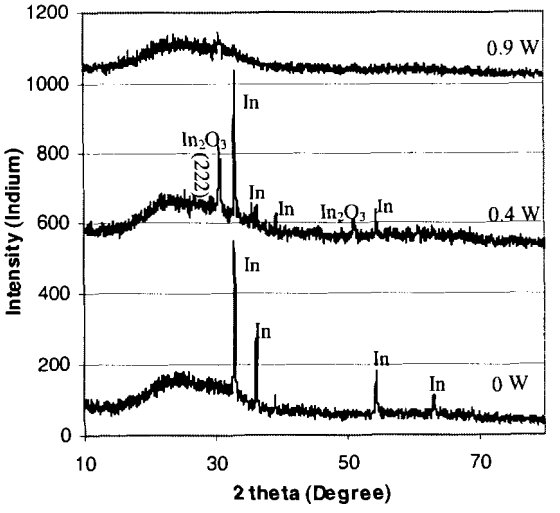

Figure 6.6 X-ray diffraction of In films: as-deposited (0 W), 0.4 W and 0.9 W laser exposed. With the increase of laser power, In is oxidized and becomes amorphous.

6.3 Analyses of Bilayer Film Laser Exposure

Single metal film tests showed that oxidation and film re-orientation are the two major structural modifications due to laser exposure. With the addition of another metal layer, the situation becomes a little more complicated.

6.3.1 Analysis of Bi/In Laser Conversion

6.3.1.1 Profile Test

Single film analysis showed that Bi film was smooth with Ra = 20 Å (Ra is the average roughness), while single In layer was very rough with Ra = 218 Å. Figure 6.7 shows a profile test across the exposed and unexposed area of a 40/40 nm Bi/In film (raster-scan laser power = 1.5 W with 5× objective lens, scan speed = 1cm/sec, and Y direction increment = 5 μm). Due to the roughness of In, Bi/In was much rougher than Bi, yet smoother than an In layer, with Ra = 100 Å. The laser scanned Bi/In film on the left became rougher than the unexposed film on the right, with Ra = 200 Å. A slight film thickness increase (~300 Å) was observed on the exposed side, which is unlike the In film that showed a significant film volume increase after laser exposure.

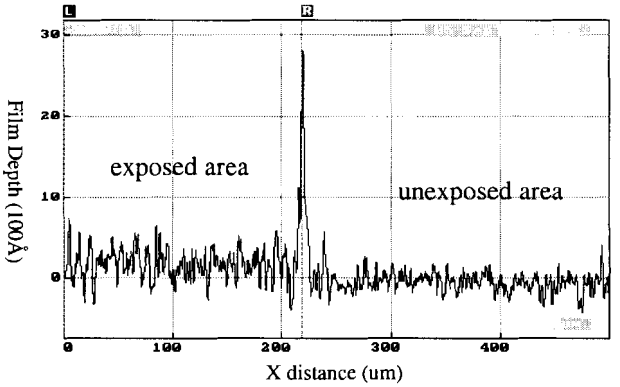

Figure 6.7 A profile of 40/40 nm Bi/In film across the exposed and unexposed areas. Area on the left side of the high peak is exposed, while the right is unexposed.

6.3.1.2 XRD Analysis

X-ray diffraction (Cu, $K\alpha_1$) was used to identify the structural components in the Bi/In bimetallic films before and after the laser exposure. Bilayer Bi/In films of different thickness were deposited on glass substrates. Figure 6.8 shows the XRD results of the as-deposited and 0.5W laser scanned 15/15 nm Bi/In. It was surprising to find that the Bi-In alloy InBi was the major component in the as-deposited film. There was one weak Bi peak, showing the existence of single Bi metal, but no single metal In peaks were observed, indicating that most of In had

alloyed with Bi. From the 15/15 nm Bi/In XRD result, one can see that there is slightly more Bi than In in the film. This may be due to the fact that the sputter rate of Bi is faster than that of In, and it is not constant through out the sputter process. However, quantitative analysis with X-ray data is difficult as this can only be taken as an indication, not a measurement of the ratio difference.

It is important to point out that indexing the peaks of the XRD scan of Bi/In films is difficult, because the 2θ / d spacing values of many of the peaks from different phases are close to each other (see examples in Table 6.1). This is even more obvious when indexing laser scanned Bi/In films. After the 15/15 nm Bi/In was laser exposed, all the InBi alloy peaks disappeared, and some new peaks appeared. It is hard to tell whether the strong peak of the 0.5W exposure is Bi or Bi_2O_3. Referring back to the findings in the previous section on single metal analysis, one could infer that it could be an oxide peak. The same problem occurs to most of the other peaks in the 0.5 W curve.

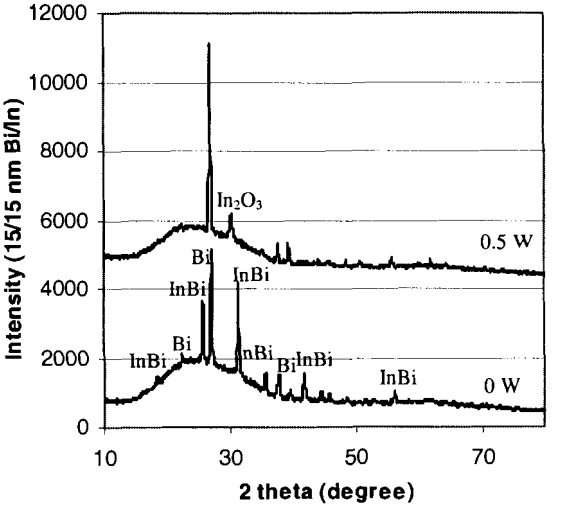

Figure 6.8 X-ray diffraction results of 15/15 nm Bi/In films on glass substrates: as-deposited and 0.5 W laser scanned.

Figure 6.9 shows the XRD curves of a thicker, 90/90 nm Bi/In when it was as-deposited, scanned with 0.8 W, and 1.0 W laser powers. Similar to the thinner sample, 90/90 nm Bi/In had

mostly InBi alloy peaks in the curve, but In and Bi peaks were also spotted. After laser exposure, most of the peaks disappeared and new peaks appeared. Checking against the JCPDF (Joint Committee for Powder Diffraction Files) cards, one can see In_2O_3 peaks, and also note that not all of the new peaks can be indexed. It is rational to assume that some new material, possibly ternary alloy oxides were formed after laser exposure.

Table 6.1 Examples of pairs of XRD peaks that are close to each other.

Material	JCPDF *d*(Å)	2 θ in ° (Cu, $K\alpha_1$)
Bi_2O_3	3.3100	26.9174
Bi	3.2800	27.1683
Bi_2O_3	2.7530	32.5005
In	2.7150	32.9682
Bi_2O_3	2.3900	37.6082
In_2O_3	2.3850	37.6900
In_2O_3	2.1570	41.8506
Bi_2O_3	2.1540	41.9116
Bi_2O_3	2.0410	44.3514
Bi	2.0300	44.6046
Bi_2O_3	1.8720	48.6008
Bi	1.8680	48.7116
In_2O_3	1.8480	49.2736
Bi_2O_3	1.8409	49.4764

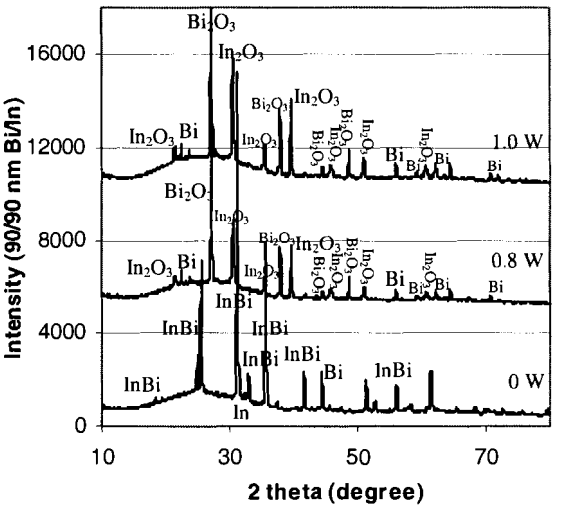

Figure 6.9 X-ray diffraction results of 90/90 nm Bi/In films on glass substrates: as-deposited, 0.8W and 1.0W laser scanned.

Bi/In films were also deposited on silicon (either 100 or 111 oriented) wafers to use Si XRD peaks as the reference. Similar results were obtained, indicating that errors caused by the X-ray instrument were negligible. In summary, XRD θ-2θ scans found Bi-In alloy in the as-

deposited Bi/In films, and indium oxide and bismuth oxide in the laser-exposed films. There were new peaks that could belong to new ternary alloy oxides in the laser-exposed films.

6.3.1.3 TEM Analysis

A great advantage of Transmission Electron Microscopy (TEM) is the capability to observe, by adjusting the electron lenses, both electron microscope images (information in real space) and diffraction patterns (information in reciprocal space) for the same region. Bragg's law is also used to index diffraction patterns. Unfortunately, the preparation of a TEM sample of laser exposed Bi/In films was not successful.

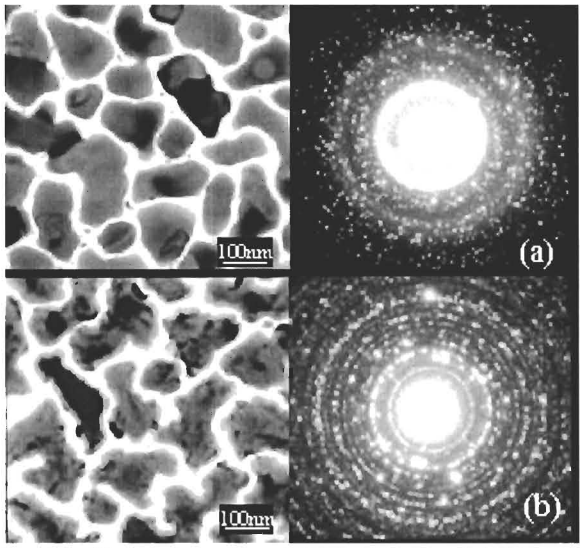

Figure 6.10 Bi/In (12/12 nm) film: plan-view TEM BF (bright field) and SAD (selected area diffraction) patterns of (a) as-deposited on SiO-coated copper grids, and (b) 246°C annealed in air.

As the laser exposure of Bi/In is a thermal process, furnace annealing of Bi/In films were carried out in air at 150, 200 and 246°C for 3 hours in order to compare them to the laser exposed samples. As shown in Figure 6.10 (a), TEM of the same thickness bilayer deposited directly onto SiO-coated Cu grids showed a polycrystalline, island morphology (150 nm average diameter). Analysis of the electron diffraction pattern found that the film was an InBi alloy, in agreement

with XRD results. Figure 6.10 (b) shows a planview TEM results from a similar bilayer deposited onto a SiO-coated copper grids that was furnace-annealed in air at 246°C. The film is still polycrystalline and the grain size is similar to that of as-deposited. Indexing of the SAD patterns by Mahshid Karimi [81] showed the development of Bi and In oxides, as shown in Figure 6.11. It was noted that the Bi/In film turned slightly transparent after annealing at 246°C for 3 hours. However, it was much less transparent than a laser exposed Bi/In film, indicating probably a different process than the laser conversion. Figure 6.12 (a) shows the UV-Vis spectrum test results of 35/35 nm Bi/In films on glass annealed for 25 minutes at different temperatures in the open air. With increasing annealing temperature, the film optical density dropped. However, it saturated at 200°C. One can see that the spectrum curves for 200°C and 246°C overlapped with each other. Figure 6.12 (b) is a re-plot of (a) at the wavelength of 688 nm (as indicated by the double-arrow line).

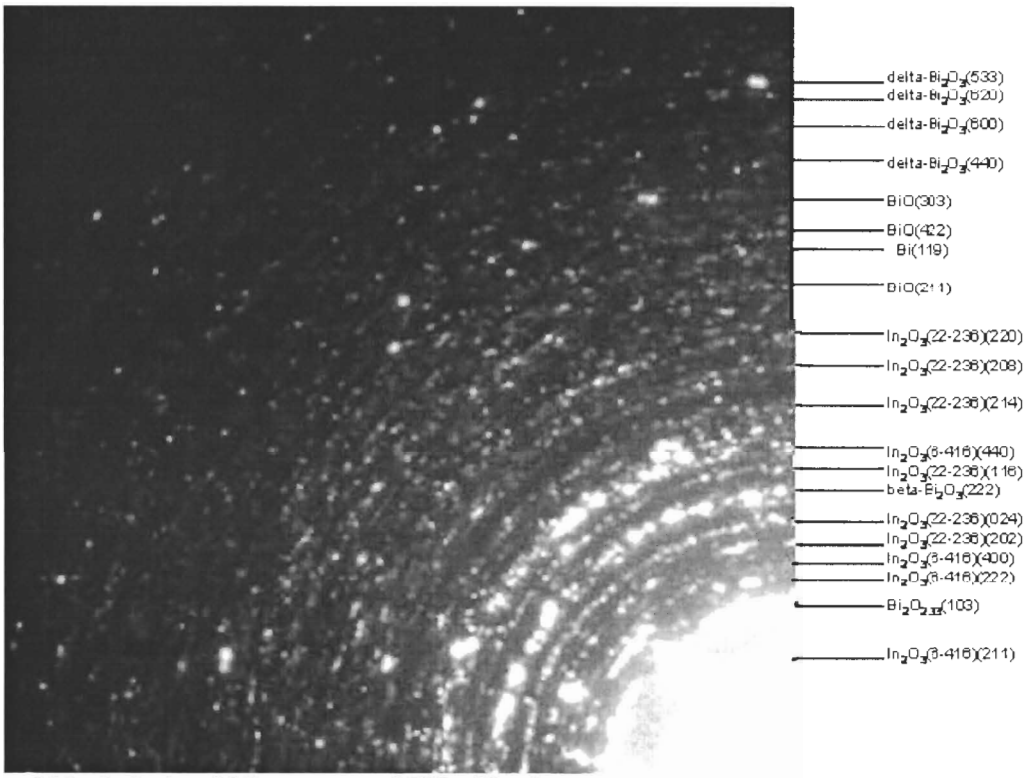

Figure 6.11 Indexing SAD patterns of Bi/In film furnace-annealed at 246°C, shown in Figure 6.10 (b). In and Bi oxides were found.

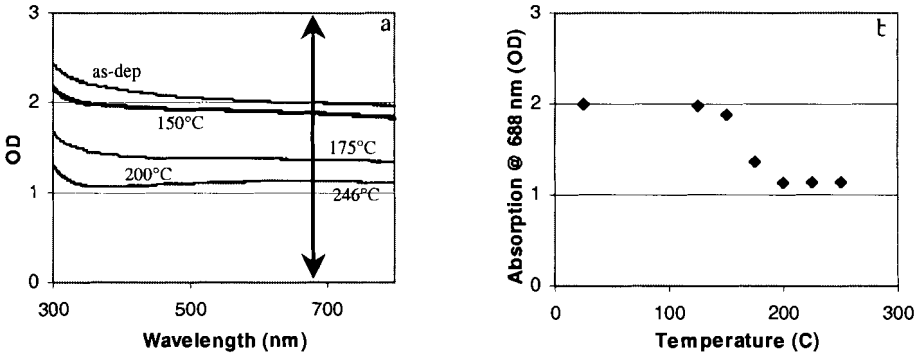

Figure 6.12 Optical density of Bi/In vs. furnace annealing temperature. (a) the UV-Vis spectrum of Bi/In films annealed at difference temperatures for 25 minutes; (b) the Bi/In film absorption vs. the furnace annealing temperature at 688 nm wavelength.

Different preparation methods have been tried out in order to make a good TEM sample of laser-exposed film. We tried to thin down an exposed film on silicon substrate using ion-milling, but later found that the film had been damaged along with the Si substrate. Wet chemical method using HF solution to etch the exposed film away from glass substrates showed that the exposed film reacts with HF to form some new compound. Bimetallic films were also directly DC-sputtered on SiO- and formvar-coated TEM copper grids, followed by argon laser exposure. However, due to the thermal effect (which melts the formvar) and the high heating up rate (2.5×10^6 °C/s, which causes the SiO film to crack), the trial was not successful either. One of the important future works is to continue working on TEM sample preparation. In particular, ways of reducing the grain size of the bimetallic thermal resist films should be explored.

6.3.1.4 RBS (Rutherford Backscattering Spectroscopy)

Rutherford backscattering spectroscopy (RBS) is one of the most powerful techniques for measuring elemental depth profiles. It allows quantitative and non-destructive analysis with a reasonable depth resolution. In conventional RBS (combination of 1 - 4 MeV He ions with a silicon surface-barrier detector), the typical depth resolution is about 10 nm. Sensitivity of

100ppm can be easily obtained for heavy elements in light hosts although analysis of light elements in heavy hosts is difficult.

The RBS analysis (2 and 3 MeV He^{++}), and nuclear reaction analysis (NRA, $^{16}O(d,p)^{17}O$) were done, in collaboration with Prof. K. Kavanagh at Simon Fraser University and Dr. W. Lennard at University of Western Ontario, on as-deposit, laser-exposed, and furnace-annealed Bi/In films at 150, 200 and 246°C. All the samples were 120/120 nm thick on silicon substrates.

The results for the as-deposited films in Figure 6.13 clearly show that In is detected on the surface even though it is deposited first, next to the substrate. This is consistent with the severe roughness observed with the profilometry of In film and the InBi alloy formed from XRD. The simulation results showed that the as-deposited film had a 2.5 nm In_2O_3 surface layer and a 200 nm thick $Bi_1In_{1.4}O_{0.06}$ average film composition beneath it, as shown in Figure 6.14. It is interesting to notice that after furnace-annealing at 150, 200 and 246°C for 3 hours, the film structure does not change (as shown in Figure 6.15, Figure 6.16 and Figure 6.17), except that the top In_2O_3 layer gets a little thicker, which is 18, 15 and 28 nm, respectively. After laser exposure oxidation of the films was detected as seen in Figure 6.18. The simulated spectrum was generated by a target film with a 2.5 nm thick surface layer of In_2O_3 and a $BiIn_{0.6}O_6$ /$Bi_{0.3}InO_6$ bilayer of average thickness 200 - 245 nm below it.

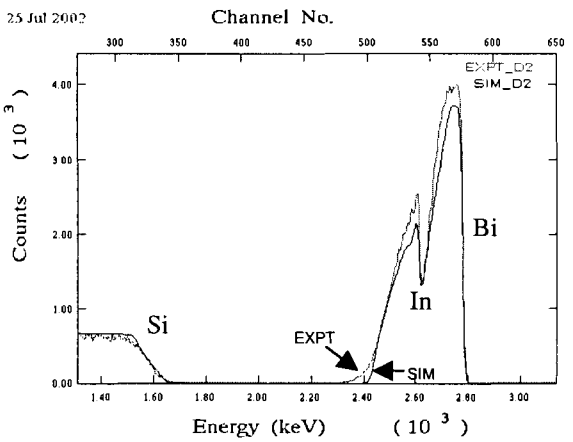

Figure 6.13 The experimental and simulated RBS spectra of as-deposited Bi/In on Si.

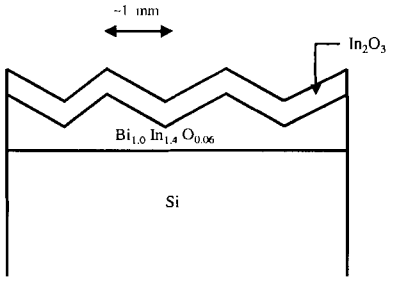

In_2O_3 thickness ≈ 2.5 nm

$Bi_{1.0}In_{1.4}O_{0.06}$ thickness (average) ≈ 200 nm
(ranges from 90-310 nm over ~1 mm distance)

Figure 6.14 A schematic of the as-deposited Bi/In film, with assumed target non-uniformity used in the RBS simulations and the layer compositions.

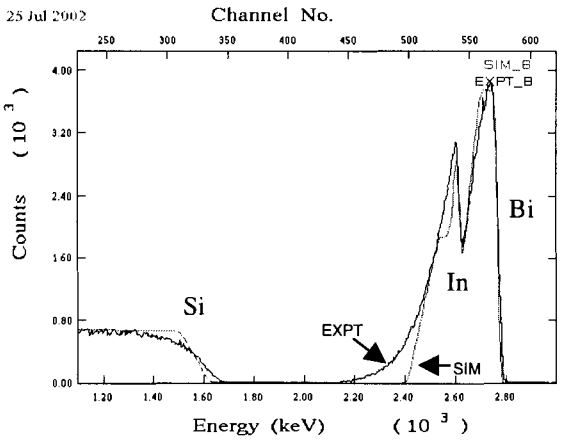

Figure 6.15 The experimental and simulated RBS spectra of Bi/In on Si, furnace–annealed at 150°C.

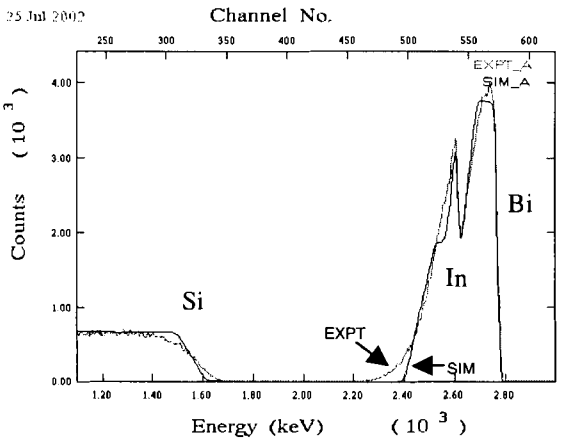

Figure 6.16 The experimental and simulated RBS spectra of Bi/In on Si, furnace–annealed at 200°C.

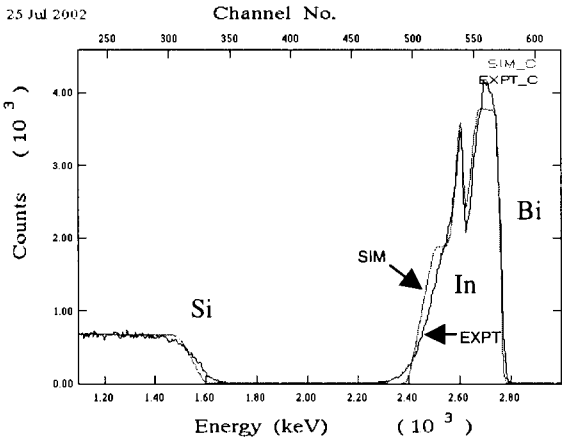

Figure 6.17 The experimental and simulated RBS spectra of Bi/In on Si, furnace–annealed at 246°C.

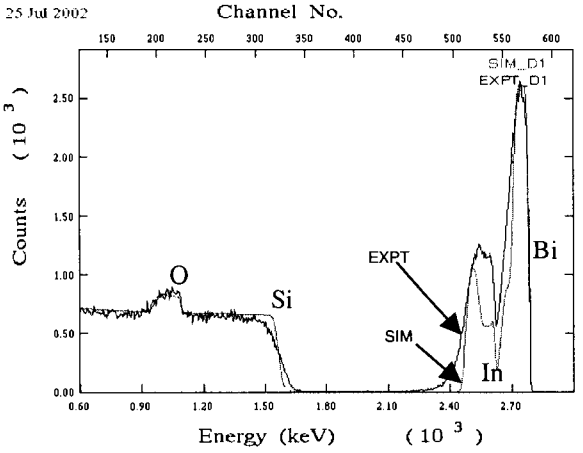

Figure 6.18 The experimental and simulated RBS spectra of Bi/In on Si, laser exposed with 0.95 W power and laser beam focused with a 50× objective lens.

Table 6.2 RBS/NRA results of O concentration.

Sample	[O] NRA (10^{17} at./cm^2)	[O] RBS (10^{17} at./cm^2)
as-deposited	*0.22*	*0.27*
150° furnace anneal	0.87	0.84
200° furnace anneal	0.8	0.7
250° furnace anneal	1.5	1.3
Laser exposed	*9.5*	*13.5*

Table 6.2 summarizes the oxygen content obtained from both the NRA and RBS data. There was considerably more oxygen in the laser-exposed films, almost ten times more than that of furnace-annealed samples. Furnace annealing below 246°C does not cause as much

modification in the thermal resist films as does laser exposure. This was also confirmed by earlier observation on the degree of film transparency of furnace-annealed Bi/in sample. Preliminary furnace-annealing experiments at higher temperature (500°C) were also conducted. UV-Vis spectrometer test showed the 500°C annealed sample was more transparent than those annealed at 246°C, but still far less transparent than laser exposed ones.

These results may indicate that the laser exposure have possibly created a meta-stable film with a high concentration of oxygen, as the laser exposure heats up the film rapidly (~ 2×10^6 K/s, refer to Chapter 9), and the film also cools down quickly after exposure. Such fast thermal cycle cannot be achieved by conventional furnace heat treatments.

6.3.1.5 XPS Analysis

X-ray Photoelectron Spectroscopy (XPS) is a surface analytical technique, which is based upon the photoelectric effect. A core electron can escape from its atom (called photoelectron) when the energy of an incident x-ray photon is large enough. The binding energy of the core electron is give by the Einstein relationship:

$$E_b = h\nu - E_k - \phi \tag{6.3}$$

where $h\nu$ is the x-ray photon energy; E_k is the kinetic energy of the photoelectron, which can be measured by the energy analyzer; and ϕ is the work function induced by the analyzer. Thus, the binding energy of the photoelectron can be determined as all the items on the right side of the equation are known. The photoelectron of an element has a unique binding energy. Thus, almost all elements, except for hydrogen and helium, can be identified via measuring the binding energy of its photoelectron. Furthermore, the binding energy of the photoelectron is very sensitive to its chemical bonding state. The same atom bonded to different chemical species leads to a change in the binding energy of its photoelectron. The variation of binding energy results in the shift of the

corresponding XPS peak, ranging from 0.1 eV to 10 eV. This effect is termed a "chemical shift", which can be applied to studying the chemical status of elements in a surface.

XPS (Mg, Kα @ 54.7°) was used to investigate the chemical state of Bi and In before and after laser exposure in Bi/In films. The penetration depth was 10 ~ 15 Å, without profile sputtering. For the pure metal state (not bonded with other atoms), the Bi photoelectron $4f_{7/2}$ binding energy, as shown in Table 6.3, should be around 156.8 ~ 157 eV. If Bi is bonded with oxygen, the binding energy shifts to around 159.2 ~ 159.8 eV. Similar shifts occur when In becomes oxidized, as shown in Table 6.3. Pure In has the energy of 443.5 ~ 444 eV, and oxidized In has 444.3 ~ 444.8 eV.

Table 6.3 Bi $4f_{7/2}$ and In $3d_{5/2}$ binding energy [84].

Bi $4f_{7/2}$ binding energy (eV)							
Compound Type	156	157	158	159	160	161	162
Bi		■					
Bi_2O_3					■		
BiF_3						■	
In $3d_{5/2}$ binding energy (eV)							
Compound Type	443	444	445	446	447		
In		■					
In_2O_3			■				
$InCl_3$				■			

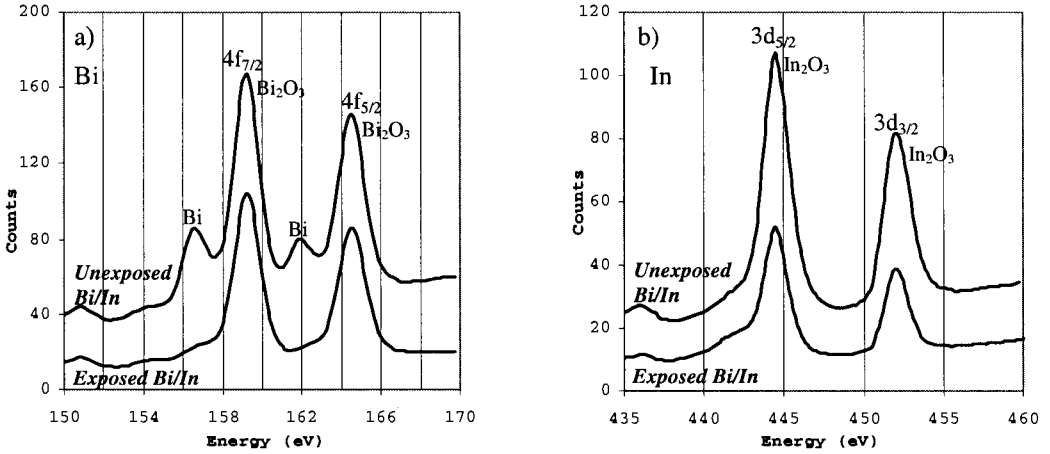

Figure 6.19 XPS analysis results for metals in exposed and unexposed 15/15 nm Bi/In film: (a) Bi and (b) In.

XPS analysis was carried out on a Bi/In film (15/15 nm on glass, laser scanned with 0.2W 50 mm lens focused beam, Y increment = 10 μm). Figure 6.19 (a) shows the binding energy of Bi $4f_{7/2}$ and $4f_{5/2}$ photoelectrons in both unexposed and exposed areas. Both pure Bi and showed up in the unexposed film. This was not unexpected, as the penetration depth was only 10 to 15 Å, and the top 1 or 2 Bi atom layers were oxidized. After laser exposure, all the pure Bi peaks were gone and only Bi_2O_3 peaks were detected, showing an oxidation was associated with the laser exposure process. Figure 6.19 (b) shows the binding energy of In $3d_{5/2}$ and $3d_{3/2}$ photoelectrons in unexposed and exposed Bi/In films. No pure In peaks showed up in the unexposed film. This is in agreement with the RBS result that about 25 Å of the top layer was In_2O_3, which is thicker than the XPS penetration depth. After laser exposure, there was no obvious In peak shift observed, indicating, at least at the top layer, In was in the form of In_2O_3.

XPS depth profile test is very useful for understanding the metal status in the exposed Bi/In films. This result strongly reinforces the concept that oxidation is important for the bimetallic resist process.

6.3.1.6 Auger Analysis

Auger analysis, often called SAM (Scanning Auger Microanalysis), provides elemental and chemical composition for all elements with an atomic number greater than helium. Its sampling depth of 2-3 nm allows films as thin as a few monolayers to be analyzed. Auger also produces images of the distributions of elements along the surface and produces profiles of composition vs. depth from 1 to 2000 nm. In many aspects, XPS and SAM are similar to each other. Table 6.4 shows the comparison of XPS and SAM. The Auger analysis tool used in this research was a semi-customized Scanning Auger Microscope Model 25-120 manufactured by Physical Electronics Industries, which was equipped with a Model 04-303 sputter ion gun.

Table 6.4 Comparison of XPS and SAM

	XPS	SAM
Incident Probe Beam	X-ray Photons	Electrons
Analyzed Signal	Photoelectrons	Auger electrons
Sampling Depths	1 to 5 nm	1 to 5 nm
Detection Limits	~ 0.1 at. %	~ 0.1 at. %
Information obtained	Element, Chemical bond	Element
Spatial Resolution	~150 μm	~ 0.1 μm
Restrictions	Very Few	Best for Conductor
Damage to sample	Non-Destructive	Minor Destruction

Figure 6.20 is the Auger spectrum of the surface of as-deposited 120/120 nm Bi/In film on silicon substrate. After a partial sputter to remove carbon, chlorine and other contaminants, the bimetallic film showed pure Bi and In, and the atomic ration is 1:1.17. Figure 6.21 shows the depth profile of the same Bi/In film after laser exposure with 0.8 W argon laser focused by a 50× objective lens. The Y direction increment was 0.4 μm. The profile shows Bi, In, O, Si, C and Cl concentration changes with the argon ion sputter time, which is directly proportional to the depth. O was present in the exposed film, which is in good agreement with XRD and RBS. The Bi concentration gradually decreased with the sputter time. In, as also found by RBS, already existed on the film surface. No sharp interface between Bi and In layers was observed. What is important is that for laser-exposed samples we see Bi, In and O at all depths, which is consistent with an oxidation process.

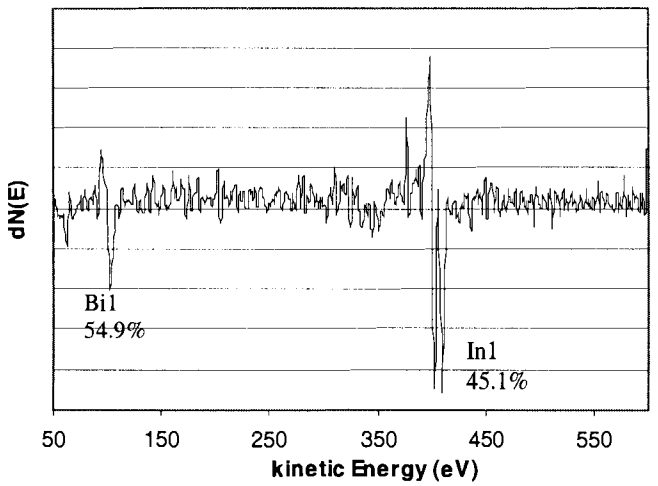

Figure 6.20 Auger spectrum of 120/120 nm as-deposited Bi/In film on silicon substrate.

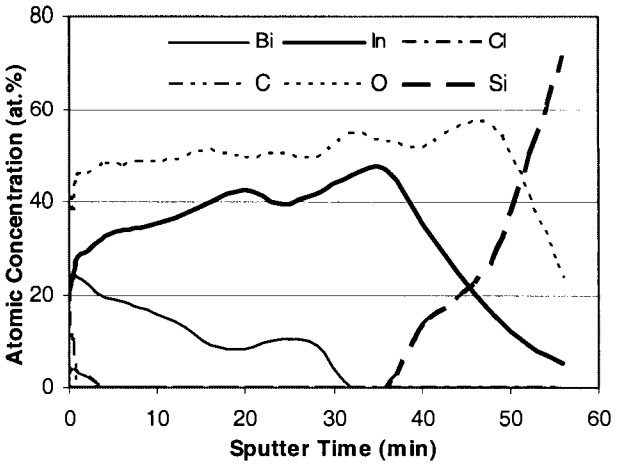

Figure 6.21 Auger spectrum of laser exposed 120/120 nm Bi/In film on silicon substrate.

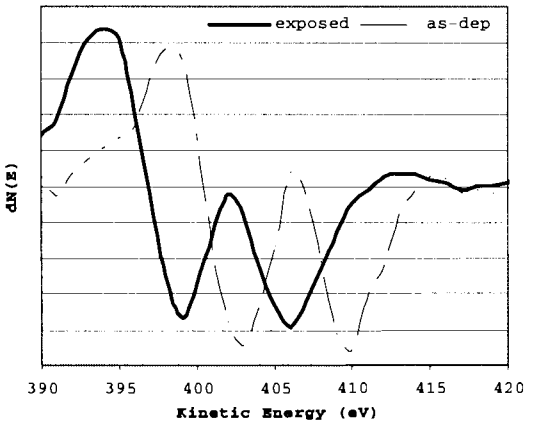

Figure 6.22 In before and after laser exposure: MNN Auger electron kinetic energy comparison.

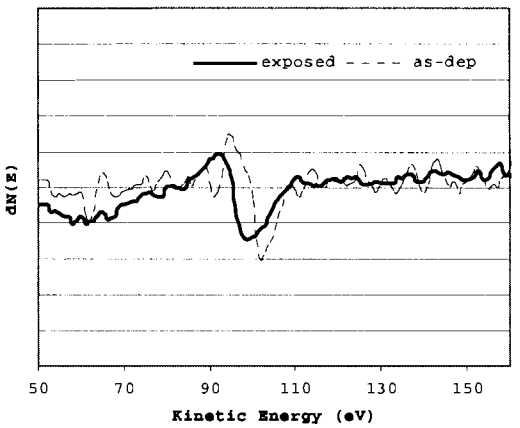

Figure 6.23 Bi before and after laser exposure: NOO Auger electron kinetic energy comparison.

A shift in the kinetic energy of Auger electrons was observed after the argon laser exposure. Figure 6.22 shows that the pure In MNN (410 eV) shifted to 406.4 eV, which is exactly the value for the In MNN in In_2O_3. Here, the MNN Auger electron is created in the following Auger process: when an M-level electron is ejected by the primary beam, an N-level electron drops into the vacancy, and another N-level electron is ejected. Figure 6.23 reveals that pure Bi NOO (101 eV) shifted to 98 eV, which is also the value for the Bi NOO in Bi_2O_3. This again confirms the XPS test result that In and Bi were oxidized in the form of Bi_2O_3 and In_2O_3.

It is also noted that the depth profile, shown in Figure 6.21, has a broad interface region. One scenario is that In had diffused into the silicon substrate after laser exposure, and this was actually what had happened at the interface. However, this may not be the case, as the silicon should have shown a steep concentration increase at the interface, as In does not have high solubility in silicon, or form an alloy with silicon. The other possibility is the interface was sharp, and the broadening of the interface was caused by argon ion sputtering in the Auger microscopy. Kosiba, et al [85], found that the sputtering angle of argon ions played a crucial role in the sputter behaviour of InN, which is similar to In_2O_3, and was very important for the proper sputter depth profiling procedure. The sputtering at 0° and 60° with respect to the surface normal caused the surface to become rougher due to the build-up of indium droplets, and thus the interface was broadened. The sputtering angle of argon ions used in our Bi/In test was 60°. Future work in Auger analysis will be to use higher incident angle, such as 80°, for sputtering. This could alleviate the broadening problem. This Auger work again confirmed that the laser formed Bi/In resist appears to have undergone an oxidation process.

6.3.2 Analysis of Sn/In Laser Conversion

XPS and Auger analyses confirmed that both Bi and In were oxidized after laser exposure. On the other hand, ITO (indium tin oxide) has been widely studied [86-89] for decades.

The extensive materials analysis on ITO can be used as a reference for us to study the laser conversion of Sn/In. In this section, XRD analysis was carried out on bilayer Sn/In films before and after the laser exposure and the results was compared with ITO data.

Figure 6.24 shows the XRD patterns of 120 nm thick, 10*wt.*% Sn/In film, the typical ITO ratio (refer to Appendix C). The diffraction curve of the as-deposited Sn/In film is similar to that of pure In film, as shown in Figure 6.6. No metallic Sn peaks are observed. This is obviously due to the low concentration of Sn. When the film was exposed to 0.1 W argon laser, indium oxide peaks (222) and (400) started to appear. With the increase of the laser power, metal indium peaks retreated and the indium oxide peaks (222) and (400) became stronger. Other oxide peaks also showed up. However, with further increase of the laser power, only a weak In_2O_3 (222) peak was seen, indicating strong orientation along the <111> direction. Figure 6.25 shows the XRD results of 120 nm, 50% Sn/In film. Metal Sn peaks could be seen besides In peaks. When the film was exposed to laser beam, Sn was oxidized first, as shown by the curve at 0.085 W. As the laser power increases, tin oxide peaks disappeared, and indium oxide peaks (222), (400) and (440) appeared, and the intensity increased as well. This is similar to the reports [89-91] that the ITO (222) intensity changes with the oxygen flow rate and the deposition power / deposition rate when ITO films were grown. Figure 6.26 is the typical XRD pattern of an ITO film. Normally, only two peaks (222) and (400) are seen, and the intensity of the two peaks is sensitive to preparation parameters.

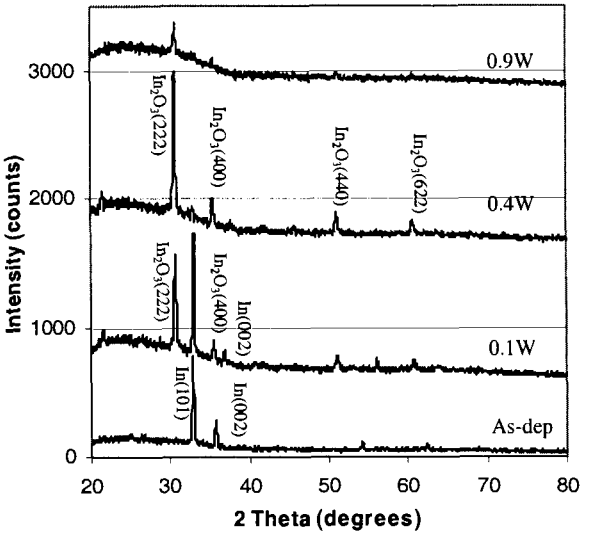

Figure 6.24 XRD results of 10% 120 nm thick Sn/In film exposed with different laser power.

The XRD results imply that the fully laser-converted Sn/In films are similar to ITO films. While ITO films may have different preferred orientation <111> or <100>, laser converted Sn/In films tend to have only one preferred orientation <111>, which is the most densely packed structure. This is probably part of the reason why exposed Sn/In or Bi/In is resistant to plasma and wet chemical etching. X-ray results also indicate that more metal is oxidized when exposed to laser of higher power.

Classic ITO films are prepared by various PVD methods [86-89]. Laser conversion of Sn/In bimetallic films is clearly a new technique for creating ITO films. The biggest advantage it offers is the direct-write patterning feature.

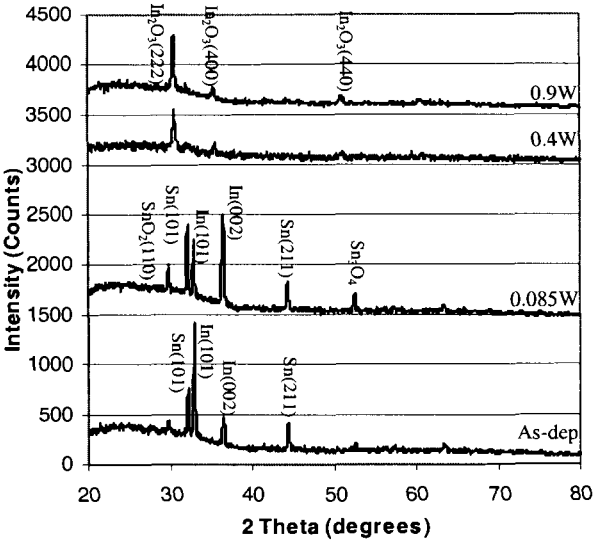

Figure 6.25 XRD results of 50% 120 nm thick Sn/In film exposed with different laser power.

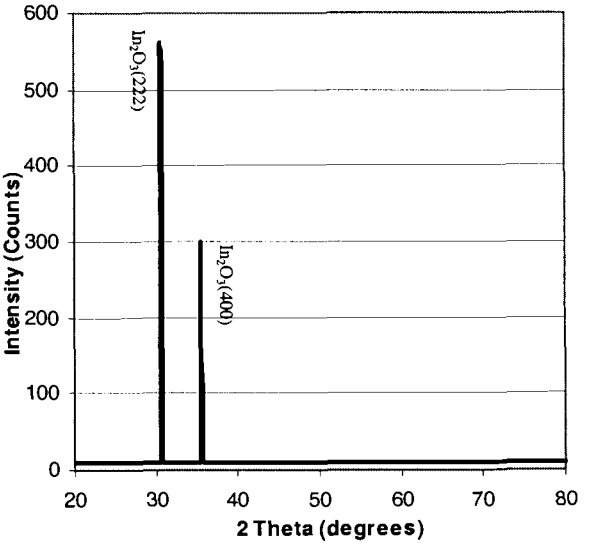

Figure 6.26 The typical XRD pattern for ITO [80,88-91]. The intensity ratio of (222) to (400) varies with processing parameters. Other peaks do not always show up.

6.4 XRD and Auger Analysis of Bimetallic Resist Development

It is the attribute of being developable that makes Bi/In a complete bimetallic thermal resist. Dilute RCA2 and nitric acid solutions can selectively remove the unexposed area and

retain the exposed area, making Bi/In a negative resist. It is interesting to determine if the chemical developing process removes or creates materials, besides removing unexposed metallic layers.

A 60/60 nm Bi/In film was deposited on glass substrate, followed by laser exposure (50mm lens focused, 487.5 mW, argon laser beam). The laser scanning speed was 1cm/s, and the Y direction increment was 10 μm. The exposed pattern was then developed in dilute RCA2 (1:1:48) for 100 seconds at 25°C. Figure 6.27 illustrates the XRD patterns before and after development. As expected, the laser exposed film consisted of In_2O_3 and Bi_2O_3. Due to the fact that Bi was deposited on top of In, and Auger revealed that Bi existed on the top half of the exposed films, one can see much stronger Bi_2O_3 peaks that In_2O_3 ones. After development, it is observed that all the Bi_2O_3 peaks disappeared, showing that bismuth oxide is not resistant to dilute RCA2 etching. All the In_2O_3 peaks remained. Auger analysis of the same developed sample, shown in Figure 6.28, revealed that there was still about 8.9% of Bi in the developed film. This amount of Bi in the In_2O_3 can be considered as a dopant material, as is Sn in ITO films, not detectable by the X-ray detector.

XRD and Auger analysis results indicate: laser exposure of Bi/In alloy film causes phase separation of two oxide phases: one the Bi-doped In oxide, the other Bi oxide. The dilute RCA2 development removes metallic Bi/In on the unexposed area, as well as the Bi_2O_3 on top of the exposed area. We can infer that it is the In_2O_3 possibly doped with Bi that is resistant to dilute RCA2, alkaline solution, and CF_4/CHF_3 plasma etching, and this is in good agreement with single In and single Bi experiment results discussed in Chapter 7.

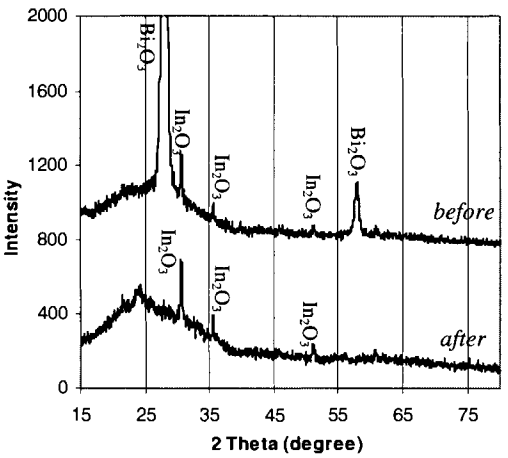

Figure 6.27 XRD patterns before and after dilute RCA2 development.

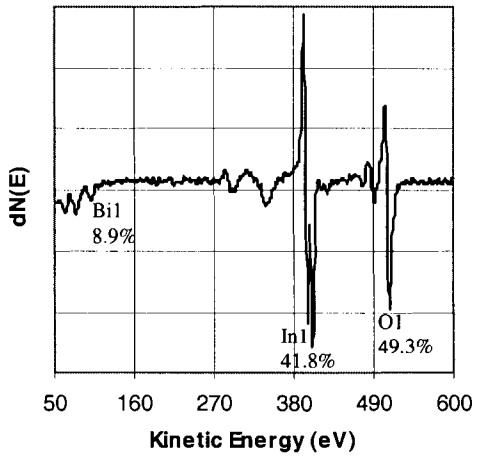

Figure 6.28 Auger analysis of dilute RCA2 developed Bi/In film.

6.5 Oxidation and Bi/In Resist

One puzzling aspect to these oxidation results was that previous experiments [68] had shown that Bi/In resist did convert even under non-oxidizing atmosphere, such as nitrogen, vacuum (10^{-3} Torr) and forming gas (5% H_2 in N_2). Yet the clear evidence in this section shows that oxidation is the important process and that there is only a small amount of oxygen in the film after deposition. What this previous results suggest is that the oxidation is quite aggressive. Only a small amount of oxygen from the residual O in the gases / vacuum or the trapped water molecules in the system are necessary.

6.6 Indium Bismuth Oxide (IBO) as a New Material

For decades, ITO (tin doped indium oxide) film has been widely used for applications such as touch panels, LCD displays, plasma displays, gas sensors, photovoltaics, etc., due to its conductive and transparent properties[86-89]. This research has demonstrated that the laser converted indium bismuth oxide (IBO) is a new type of transparent and conductive material, which is comparable to ITO film. Material analyses show that it has a structure similar to that of ITO. As ITO has been widely studied, this similarity can help us further understand the behaviour of IBO and project the possible conductivity and transparency that it can achieve. Moreover, its value as a transparent conductive oxide should be studied further. The shelf life tests described in Chapter 5 showed IBO was extremely stable. It was noted that no degradation of optical or electrical performance was observed even after long exposure to laser in DI water or saline solutions, while ITO films tend to degrade under these conditions [92].

6.7 Summary

Different analysis tools have been utilized to investigate the changes of film material properties incurred by laser exposure. It was interesting to find that Bi and In form a Bi-In alloy in the as-deposited resist film. XRD and TEM indexing revealed that bimetallic thermal resists were oxidized after laser exposure. Auger, XPS and RBS confirmed that both Bi and In were oxidized, showing that laser exposure is an oxidation process. Analysis of the conversion of Sn/In films revealed that laser converted Sn/In films have identical material structures as do ITO films. The next chapter looks at applications of the bimetallic resists.

Chapter 7
Applications of Bimetallic Thermal Resists

7.1 Introduction

The fundamental task of a photoresist or a thermal resist is to successfully transfer a pattern into the underneath functional layer, and at the same time, offer a shielding mask to the etching of the resist covered areas. That is the reason why these materials are called "resists". Either wet chemical or dry plasma etching is used to "cut" into the layer below. In order to achieve a near-perfect transfer, the masking resist layer should etch or erode at worst at the same rate, and ideally much slower than the substrate material. In other words, the exposed thermal resist should be resistant to the etching. As the bimetallic resists are thin film imaging resists, their full use would involve the addition of a lower thick protection layer patterned by the thinner layer. However, the exploration for direct applications of the bimetallic thermal resists is actually searching for etching processes that bimetallic thermal resists are resistant to. This chapter presents first a proposed thin film imaging process, then the application of Bi/In used as a patterning and masking layer for silicon anisotropic etching for micromachining, application as masking layer for fluorine-base plasma etching for microfabrication, and the novel combination of wet and dry etching to create special structures. As the exposed and developed bimetallic resists are conductive, Bi/In has also been successfully used as a seed layer for metal electroplating.

7.2 Thin Film Imaging Process

As mentioned in Chapter 1, the thickness of the organic photoresists used in conventional lithographic processes is typically from 7000 Å to 1 μm. This thickness serves two purposes. One is for planarization which provides a relatively level, smooth surface for better focusing during the exposure, as shown in Figure 7.1(a). The other is to provide enough mask protection for subsequent plasma etching. Bimetallic thin film thermal resists, however, are much thinner than organic photoresists for lithographic applications. Bi/In resist of 15 – 150 nm thick may not provide enough step coverage for the edges of areas, as shown in Figure 7.1(b). Its resistance to all types of plasma etching is also unknown at this point. Furthermore, it is not clear whether the heat flow and the lasing temperature during the thermal resist exposure can cause a negative impact on the layer underneath. A prototype thermal resist has been devised to address these three issues.

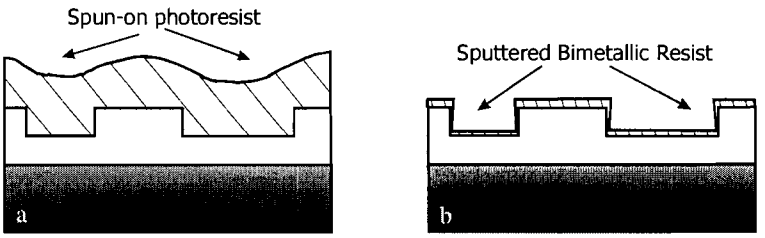

Figure 7.1 Comparison of organic photoresist and thin film bimetallic thermal resist.

The prototype bimetallic thermal resist consists of two layers: the Bi/In imaging layer and a thick protection layer, as shown in Figure 7.2. The bottom layer is a thick 0.5 - 2.5 μm protection layer of amorphous hydrogenated carbon. The bimetallic imaging layer is first patterned with laser exposure. The protection layer provides a thermal insulating boundary to the substrate. After developing the imaging bimetallic resist, the pattern is transferred to the thick protection carbon layer using a reactive ion etch in oxygen (O_2 RIE) which attacks the carbon strongly and minimally affects the metal imaging layers [59]. This will be confirmed by an O_2

plasma test in Section 7.4. The development etch, sketched in Figure 7.2, leaves a high aspect ratio mask on top of the substrate which can be used for various microfabrication processes.

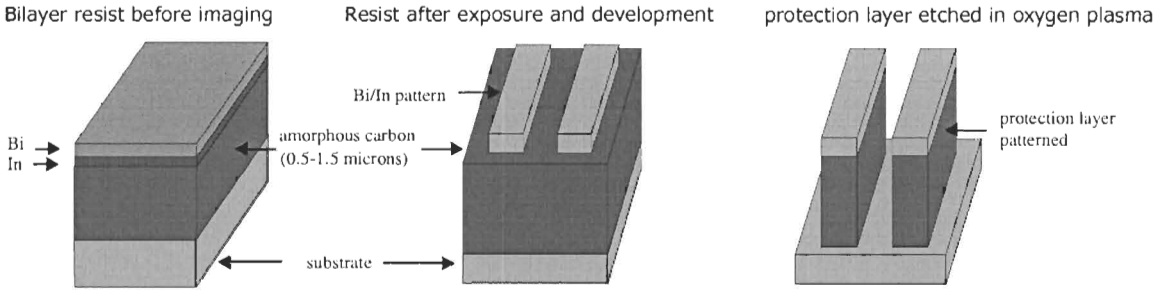

Figure 7.2 The proposed thin film imaging process: Bi/In as imaging resist and amorphous carbon as protection layer. After the resist is exposed, the imaging layer is developed. The pattern is transferred from the imaging layer to the carbon protection layer by using an O_2 RIE.[93]

The prototype thermal resist structure would be applied to tackle lithography on wafers with complex morphology. However, it is still valuable to explore the features of bimetallic thermal resists as a single imaging and masking layer (without carbon protection layer) for planarized surfaces, such as bare silicon wafer and CMP processed oxide film. Furthermore, the unusual characteristics of Bi/In and its class of thermal resists allow us to explore applications not possible with organic resists. This is the primary goal of this thesis. Thus, this protection layer concept was not attempted in this research. The next section describes Bi/In as a patterning and masking layer for Si anisotropic etching.

7.3 Bi/In as a Patterning & Masking Layer for Si Anisotropic Etching

7.3.1 Background

Significant progress has been made in the last decade with micro sensors and micro actuators due to the advances in both bulk and surface micromachining technologies. One of the most important bulk processing techniques is alkaline-based, anisotropic silicon etching on {100}

and {110} orientation wafers, which produces v-shape grooves with {111} sidewall 54.7° to {100} plane, and {111} sidewalls 90° to {110} plane, respectively [94,95,96]. Some reports [97,98] also show that alkaline solutions can be used for "isotropic" etching with porous silicon as the sacrificial layer. Some of the typical applications of this bulk etching technique are the fabrications of fluidic systems [99], sensors [99,100,101], actuators [102] and surface-textured high-efficiency solar cells [103].

The liquid etchants commonly used in current micromachining industry and research are inorganic aqueous KOH (potassium hydroxide), organic TMAH (tetramethyl ammonium hydroxide) and EDP (ethylene diamine pyrocatechol) due to their good etch rate, high selectivity on crystal directions and silicon doping levels, and also the alkaline characteristics [104,105]. Unfortunately, these etchants attack rapidly standard organic photoresists, requiring the creation of a deposited or grown masking layer patterned by regular resists. Despite the etch rate difference for different masking materials, the classic silicon anisotropic etching process has identical masking layer preparation and etching steps, as shown in Figure 7.3,

a) masking material deposition, such as CVD of SiO_2 or Si_3N_4;

b) photo resist coating;

c) exposure to transfer patterns from photomask to the photo resist;

d) resist development;

e) masking layer etching;

f) photoresist stripping;

g) alkaline Si anisotropic etching; and

h) masking layer SiO_2 or Si_3N_4 stripping.

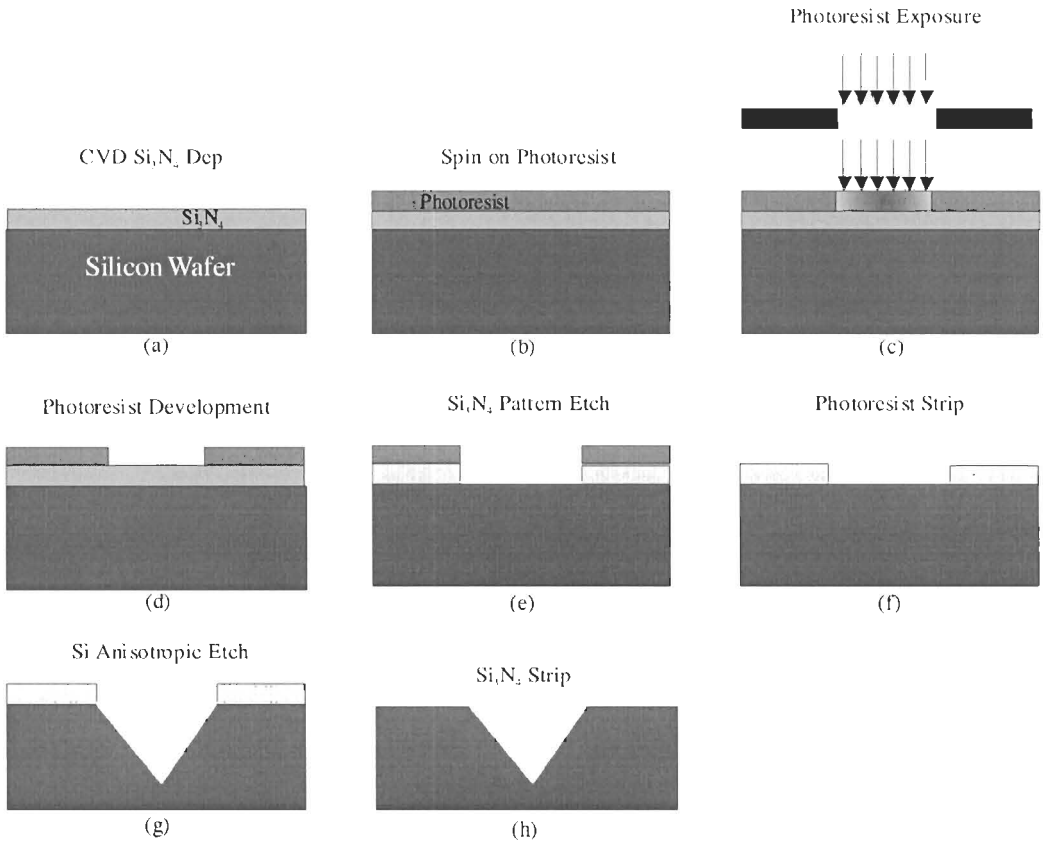

Figure 7.3 Conventional silicon anisotropic etching (bulk micromachining) process

One of the most frequently used masks for silicon anisotropic etching is SiO_2 as it is not only easy to be prepared by thermal oxidation or CVD method, but also easy to be stripped by HF or BOE [105,106]. However, SiO_2 still shows a finite etch rate in these etchants [104,105]. It has been seen that the etch rate for silicon dioxide is about 1.25 nm/min in 35*wt.*% KOH at 60°C, and 7.7 nm/min in 50*wt.*% KOH at 80°C [105,107]. The SiO_2 etch rate is about four orders of magnitude lower than those of {100} and {110} [104]. In order to make a hole through a wafer, silicon dioxide mask layer of 4 to 5 μm thick has to be deposited, which is difficult to do.

By comparison, silicon nitride, which is also widely used in the industry, is etched at an extremely slow rate, making it a good etch masking material [104,105]. Table 7.1 shows the etch rates of silicon, Si_3N_4 and SiO_2 in KOH, TMAH and EDP. Si_3N_4 is difficult to make and etch

itself. Si_3N_4 CVD deposition often produces films with varying stoichiometry and thus etch rate, which is difficult for etch control.

Table 7.1 Comparison of Si anisotropic etchants. [107,108]

Etchant	Etch temperature and *Si etch rate (nm/min)*	Anisotropic <100>/<111> etching ratio	SiO_2 Etch Rate (nm/min)	Si_3N_4 Etch Rate (nm/min)
EDP	50-115 °C *300 - 700*	10-35	1-80 nm/min	Low, <1 Å/min
KOH	50-90 °C *150 - 1500*	100-400	1-10 nm/min	Low, <1 Å/min
TMAH	60-90 °C *150-900*	10-20	1- 5 nm/min	Low, <10 Å/min

The point here is that current anisotropic etch methods involve many steps to implement and use mask materials that have their own disadvantages.

7.3.2 Proposed Bi/In Resist Process for Si Anisotropic Etching

Bi/In bimetallic film as both a thermal resist for patterning and an etch masking material for alkaline-based silicon anisotropic etch has been investigated in this section. This new Bi/In process has fewer steps than conventional SiO_2 or Si_3N_4 processes.

The Bi/In process includes 5 steps as shown in Figure 7.4:

a) The preparation of DC-sputtered Bi/In (30 nm to 90 nm thick for each layer) films on RCA-cleaned (100) silicon wafers (Figure 7.4 (a));

b) Argon laser raster-scan exposure (Figure 7.4 (b));

c) Pattern development (Figure 7.4 (c));

d) Anisotropic etching (Figure 7.4 (d)) and

e) Bi/In stripping (Figure 7.4 (e)).

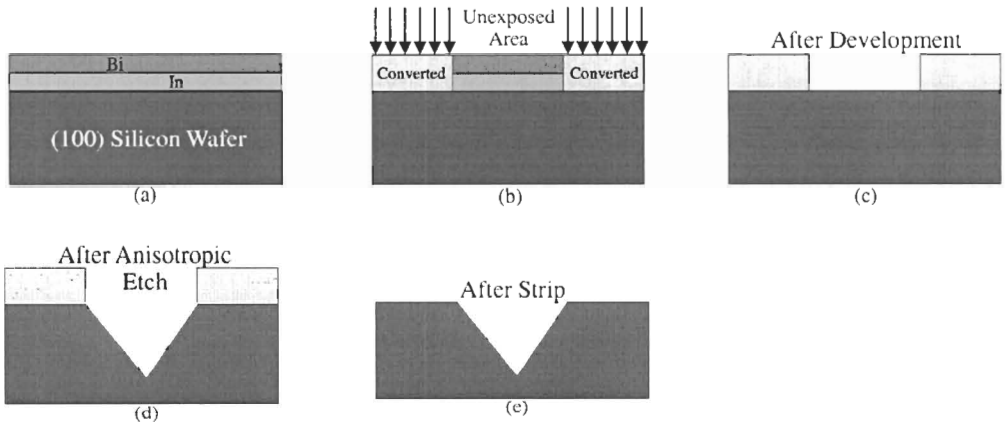

Figure 7.4 Bi/In for anisotropic etch process. (a) Bi and In sputtered on a (100) silicon wafer. (b) Bi/In exposed. (c) Bi/In developed. (d) Developed Bi/In layer as an etch mask in KOH, TMAH or EDP at 80 - 85°C. (e) Bi/In mask stripped off by RCA2 cleaning and HF dipping.

7.3.3 Bi/In Lithography

In order to find out the laser-exposed and developed Bi/In etch rate in KOH, TMAH and EDP, Bi/In was first deposited on glass slides. The glass samples were dipped in the etchant solutions for different durations after laser exposure and development, and the Bi/In pre- and post- thicknesses were measured by a profiler. The glass etch rate was also taken into account when calculating the Bi/In etch rate.

In this Si anisotropic Bi/In lithography DC-sputtering of Bi/In bimetallic film was done on silicon substrates, argon laser exposure to create patterns on the thermal resist, and Bi/In resist development in dilute RCA2 solution, which have been described in previous chapters. The details will not be repeated here. Nevertheless, it was observed that the laser power for exposure of Bi/In films on silicon substrates was higher than that on glass substrates. Obviously, this is due to the fact that silicon has much higher thermal conductivity (149 W/mK) than glass (0.8 W/mK). More heat is lost in silicon during the exposure process, especially for CW or long duration laser exposure. Argon CW laser was used to expose the Bi/In films. The laser beam was focused by different objective lens (5×, 50×, instead of the 50 mm focal length converging lens) before it hit the sample. The waist of the focused beam was from 2 μm to 6 μm. The power of the Argon laser

used for the scanning was from 0.16 W to 0.32 W when using the 50× objective lens. Note that if shorter pulse duration exposures were used, this effect would be much smaller as much less thermal diffusion would occur during the exposure. (refer to Chapter 9 for further discussions)

7.3.4 Exposed Bi/In Etch Rate in Anisotropic Etchants

In order to find out the etch rate of the inorganic resist in KOH, TMAH and EDP, Bi/In (120/120 nm) was DC-sputtered on glass slides. Laser raster-scanning was then carried out to make lines of different width (32 μm – 3 mm) with 1 mm spacing. The slide samples were developed under the same condition, as were the silicon samples. A Tencor AS500 profiler was used to measure the thickness of the lines before and after the etching in different etchants with different durations (20 sec to 10 hours). Figure 7.5 shows the thickness measurement results of the developed Bi/In films on glass slide samples after being etched for different durations in KOH at 85°C. As one can see the Bi/In film thickness reduces with the etching time. However, the etching is very slow: about 120 nm of the developed film was removed after 2 hours of KOH etching. The etch rate is about 1 nm/min (obtained from the slope of the line in Figure 7.5), which is slower than that of the silicon oxide etch rate in 50*wt.*% KOH at 80°C. The silicon etch rate in KOH at 85°C is about 420 nm/min. In comparison, Bi/In etch rate in TMAH is much slower than that in KOH. Figure 7.6 shows that 250 nm Bi/In film was etched away in TMAH in 10 hours time which gives less than 0.5 nm/min etch rate, while the silicon etch rate is about 400 nm/min in 25%TMAH at 85°C. The Bi/In etch rate in EDP is similar to that in KOH, which is 0.9 nm/min, as shown in Figure 7.5. It is noted that TMAH has a much higher silicon to Bi/In etch rate ratio (800:1) than KOH or EDP, making it a better anisotropic etchant for Bi/In process. This means that a Bi/In layer as thin as 630 nm would provide protection for etching through a full wafer. The glass slide substrate etch rate (5 Å/min) in all the three etchants has been compensated when calculating the Bi/In etch rate.

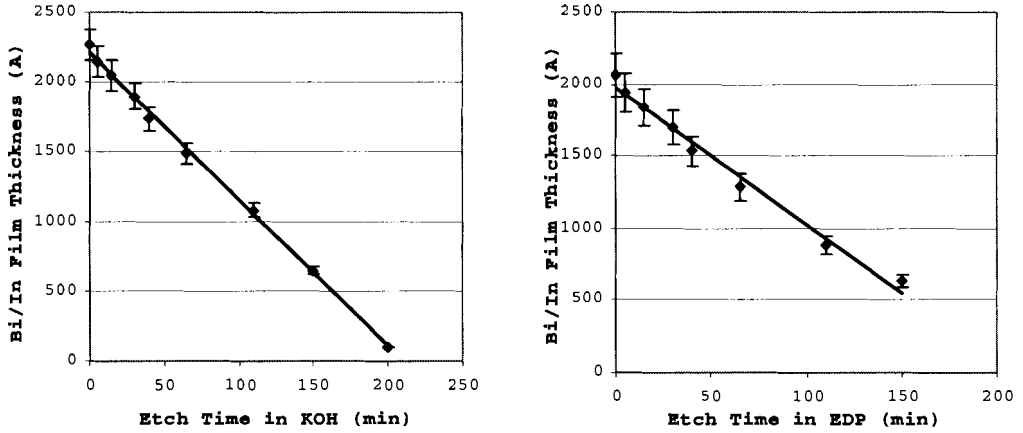

Figure 7.5 Bi/In film thickness with time in KOH and EDP.

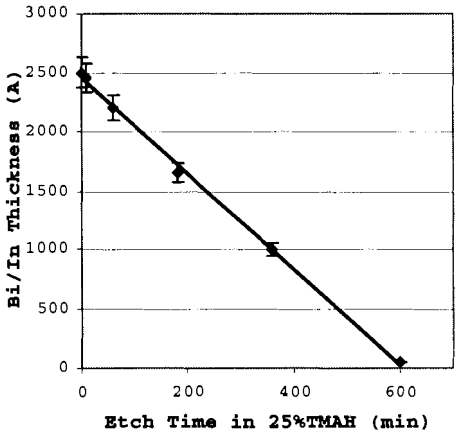

Figure 7.6 Bi/In film thickness with time in TMAH. The etch rate is around 0.5 nm/min.

7.3.5 Bi/In Patterning Alkaline-Based Anisotropic Etching

All three alkaline anisotropic etchants, KOH, EDP and TMAH, were tried in this research. The KOH etchant solution and EDP used for the anisotropic etch were commercial products PSE-200 (33*wt.*% KOH, 1 mil / 3 min @ 100°C, <100>) and PSE-300 (25 μm/hr @100°C, <100>), respectively, from Transene Company. The TMAH (25%) was from Moses Lake Industries Inc. All the etchants were kept at 85°C with mechanical agitation. The etch time tried ranged from 2 minutes to 10 hours. The samples were DI water rinsed for 5 minutes after the etching. These conditions are the same as those used in the traditional oxide mask, anisotropic Si etching processes carried out in our lab.

Different patterns were successfully etched on silicon wafers. Figure 7.7 shows a set of square channels 10 μm wide and 20 μm spacing on a (100) plane after KOH etching, before Bi/In stripping. The Bi/In film was 45/45 nm thick and raster-scanned with 0.32 W laser power and an incremental step of 0.25 μm along the lateral direction. The development time after Bi/In laser exposure was 100 sec in dilute RCA2 and the sample was etched in the KOH solution for 3 minutes at 85°C. The diagonal lines seen on the picture was caused by the laser dwelling when the X-Y-Z table changed its moving direction, which is not related to the etching process.

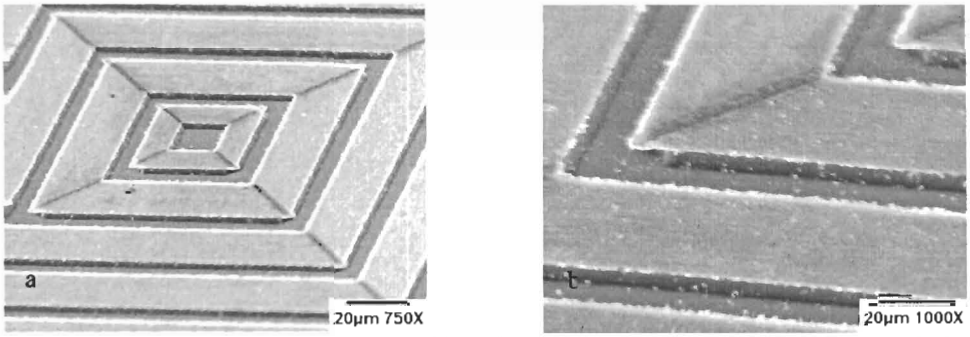

Figure 7.7 Channels were made on (100) Si wafer. The grooves are 3 μm deep and the central square is 20×20 μm. The picture (a) is a higher magnification of (b). A dangling membrane of Bi/In mask can clearly be seen at the corner. (75° tilted SEM images)

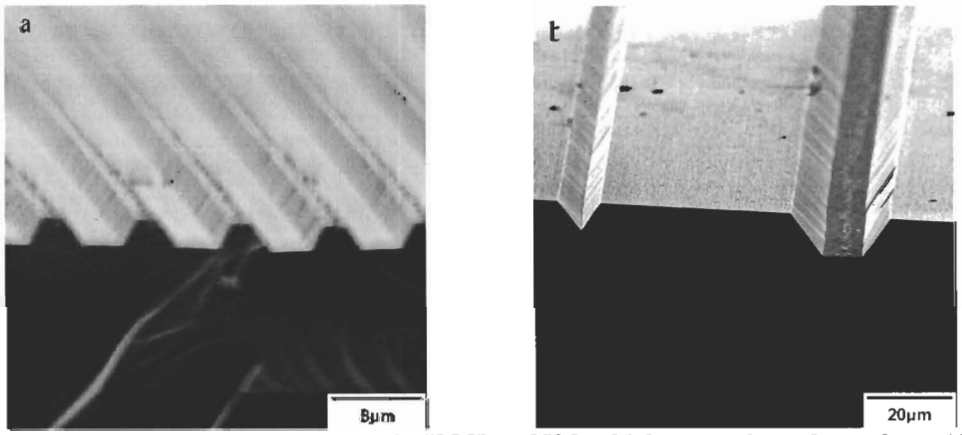

Figure 7.8 (a) V-shape channels etched in KOH at 85°C which were about 3 μm deep. (45° tilted SEM picture). (b) 11 μm deep v-groove was made on (100) silicon wafer after 30 minutes of TMAH etching at 85°C. 45 nm / 45 nm Bi/In was used as the patterning and masking layer.

Figure 7.7 (b) is a higher magnificent SEM image of Figure 7.7 (a). The thin masking layer can be clearly seen at the corner of the square, with an undercut on the (111) silicon plane

underneath which is due to the etchant attack from both sides of the corner. Figure 7.8 (a) is the SEM picture of a set of parallel channels etched in KOH. The (111) plane is clearly seen, showing a typical anisotropic etch. Similar results were also obtained from TMAH and EDP etching. Figure 7.8 (b) shows the patterns etched in TMAH. The profile test of the structures shows a 11 μm deep V-groove and a 20 μm deep trench were created by TMAH etching (Figure 7.9). The stripping of Bi/In masking layer, as mentioned in earlier chapter, can be easily done by RCA2 cleaning. HF dip is needed for stripping SiO_2 and hot H_3PO_4 is needed to strip the Si_3N_4 layer.

Bi/In has proven to be the only known direct resist for anisotropic etching of Si structures with all three etchants (KOH, EDP and TMAH). This also shows that Bi/In is a complete resist with exposure, development and etch mask features. In section 8.7, this process will be used to create V-groove solar cell devices.

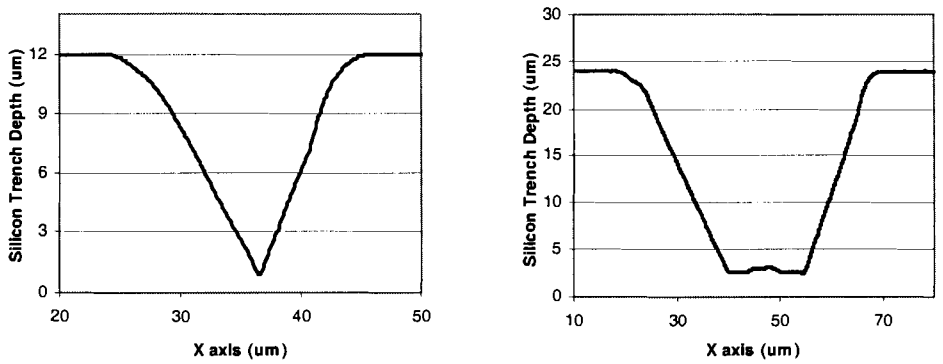

Figure 7.9 Profile of anisotropically etched trenches as shown in Figure 7.8 (b).

7.4 Bi/In as Masking Layer for CF_4 / CHF_3 / O_2 Plasma Etching

7.4.1 Background

Although wet chemical etches are still widely used in micromachining and microfabrication, dry plasma etching is increasingly employed to achieve dimensional control in

etching small geometries, which is necessary for advanced micromachining. Plasma etching has several advantages over other techniques: 1) it can transfer photoresist patterns into the substrates accurately; 2) the etching process is clean and free of contaminants such as K+, and compatible with vacuum processing technologies, 3) it is IC process compatible, and 4) it can achieve etch anisotropy without using the crystal orientation [109]. Since Bi/In resists form oxides (discussed in Chapter 6), their protective capabilities for plasma etching are expected to be vastly different than those of classic organic resists. In this section we investigate their resistance to fluorocarbon and oxygen plasma etches for silicon, silicon dioxide, and organics. Also plasma etching is required for the thin film imaging process discussed in Section 7.2.

7.4.2 Proposed Bi/In Resist Process for Plasma Etching

The plasma etching process with Bi/In as the patterning and masking layer is identical to wet anisotropic etching process, as shown in Figure 7.10. However, we have one more choice of etching after pattern development. The thermal resist deposition, exposure and development processes are the same as those in the wet anisotropic etching.

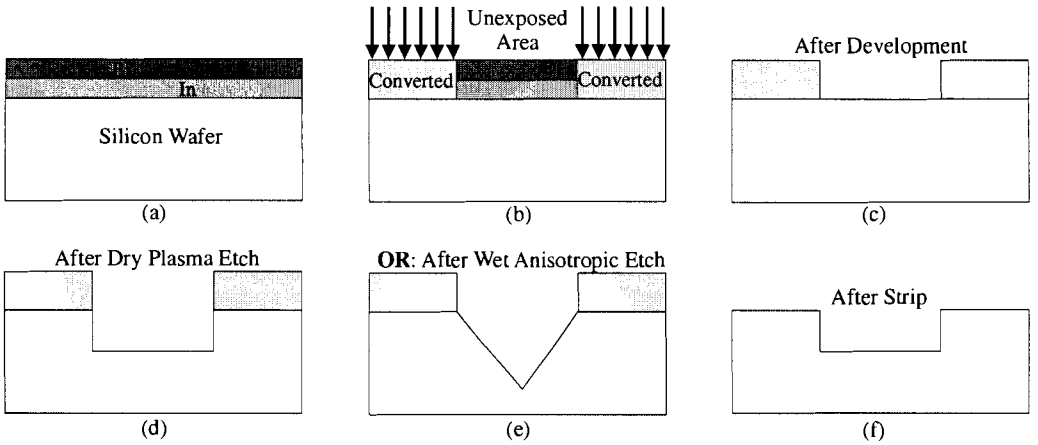

Figure 7.10 The Bi/In microlithography and silicon/silicon dioxide etch process steps. (a) Bi/In is DC-sputtered on a silicon wafer. (b) Bi/In is patterned with a 0.3 W of Argon laser beam focused by a 50× objective lens. (c) Bi/In is developed. (d) The developed Bi/In layer acts as a mask for CF_4 / CHF_3 plasma etching. (e) OR: the developed Bi/In layer can be used for wet chemical anisotropic etch. (f) The Bi/In mask is stripped after RCA clean and/or HF dip.

7.4.3 CF_4 / CHF_3 / O_2 Plasma Etching

Plasma etching was carried out using an Axic Benchmark 800-II PECVD/RIE dual chamber etcher with $CF_4/CHF_3/O_2$ after the wet development of the exposed Bi/In. The substrate chuck is made of stainless steel without heating or cooling system, i.e., the temperature of the substrate cannot be controlled. As most of the plasma etching lasts less than 20 minutes, the chuck temperature is maintained below 30°C. Thus, the substrate temperature is assumed to be kept at room temperature throughout the etching process. After the sample was loaded, the chamber was pumped down to 15 mTorr with a roughing pump. Table 7.2 shows the typical recipes for Si and SiO_2 plasma etch and the O_2 ashing recipe to remove organic photoresists. Plasma etch time was 4 to 15 minutes. The Bi/In etch masking layer was stripped off with RCA2 cleaning after plasma etching.

Table 7.2 Plasma Etch Recipes

Si etch recipe	SiO_2 etch recipe	O_2 ashing recipe
O_2 = 6 sccm	O_2 = 10 sccm	O_2 = 20 sccm
CF_4 = 50 sccm	CF_4 = 75 sccm	CF_4 = 0 sccm
CHF_3 = 0 ~ 5 sccm	CHF_3 = 0 ~ 5 sccm	CHF_3 = 0 sccm
Pressure = 150 mTorr	Pressure = 150 mTorr	Pressure = 100 mTorr
RF Power = 100 ~ 200 W	RF Power = 100 ~ 200 W	RF Power = 200 W
Substrate Temperature = 25 °C	Substrate Temperature = 25 °C	Substrate Temperature = 25 °C

Figure 7.11 shows a tilted cross-section SEM picture of a Si sample etched with a Si etch recipe O_2 = 6 sccm, CF_4 = 50 sccm, Pressure = 150 mTorr, RF Power = 200 W. The trench is 8 μm wide and 2 μm high. Bi/In patterned SiO_2 was also etched with CF_4 plasma. Figure 7.12 shows the cross-section of SiO_2 after 10 minutes of plasma etch. The etch recipe is O_2 = 10 sccm, CF_4 = 75 sccm, Pressure = 150 mTorr, RF Power = 200 W. The 6300 Å SiO_2 layer was grown with wet-ox on a (100) silicon wafer. Profiler and SEM show that the side wall of the Si and SiO_2 trenches is sloped and rounded, not vertical, as shown in Figure 7.13. This is related to the anisotropy of the plasma etching and is not caused by the Bi/In resist. The anisotropy of plasma etching can be improved by adding CHF_3 and argon gas into the etch recipe.

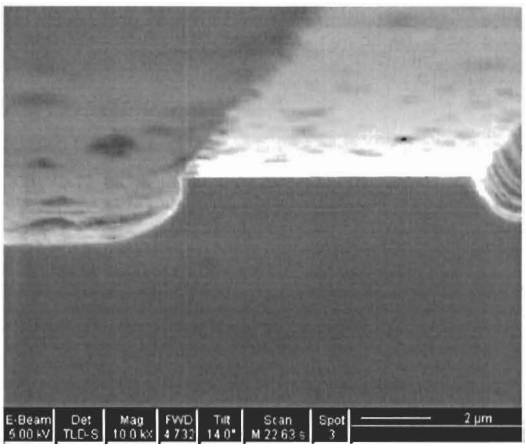

Figure 7.11 Bi/In as the thermal resist and plasma Si etch masking layer to make structures on a (100) Si wafer. The trench shown in this SEM picture is 8 μm wide and 2 μm high and tilted at 14°.

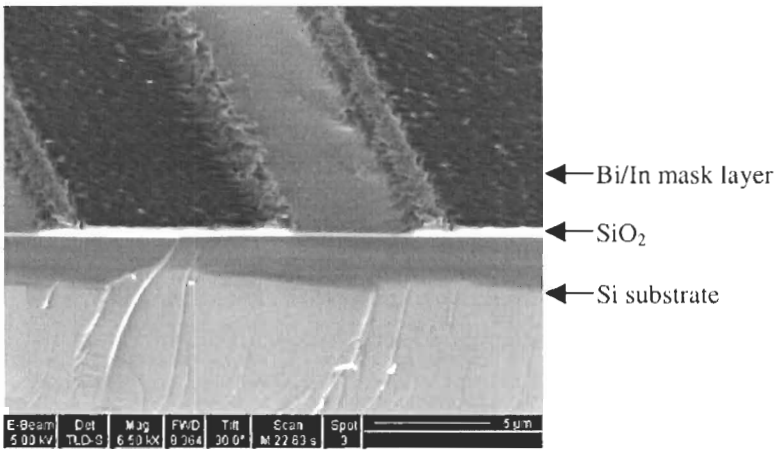

Figure 7.12 90/90 nm Bi/In used as the patterning and etch masking layer for SiO_2 plasma etching. The SEM picture shows the cross-section of SiO_2 after etched with CF_4 plasma for 10 minutes. The etch recipe was O_2 = 10 sccm, CF_4 = 75 sccm, Pressure = 150 mTorr, RF Power = 200 W.

As an argon gas line is not available at this moment in the lab, plasma RIE bombardment is not as directional as in common industrial recipes. However, this anisotropy can be improved by adding CHF_3 into the etching chemistry. Figure 7.14 shows an improved Si profile after etching with a recipe O_2 = 6 sccm, CF_4 = 50 sccm, CHF_3 = 5 sccm, Pressure = 150 mTorr, RF Power = 100 W. The profile can be further improved with the addition of argon gas.

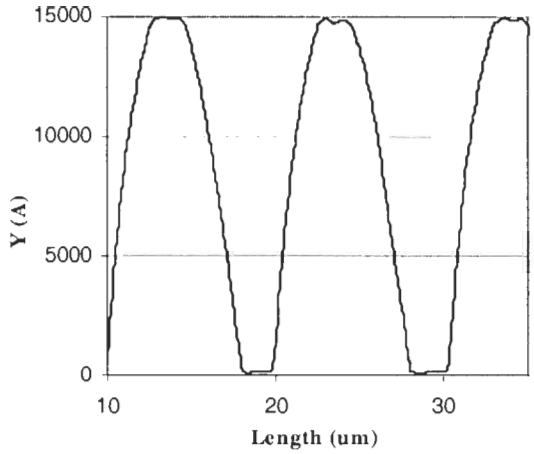

Figure 7.13 Profile of Bi/In patterned, masked and CF_4 plasma-etched Si trenches, showing slightly curved side wall. The anisotropy is due to the plasma chemistry.

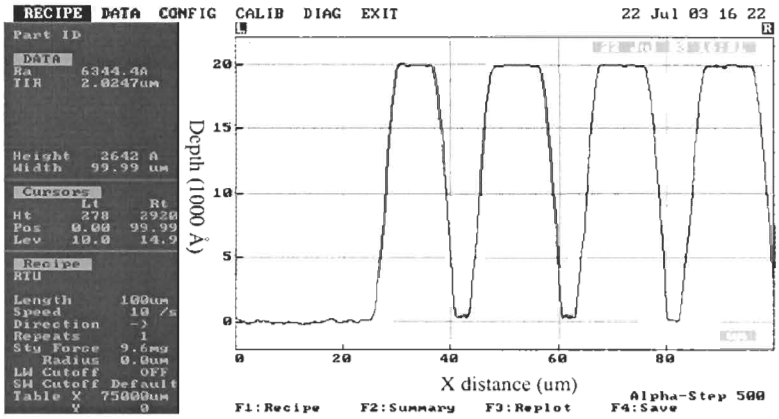

Figure 7.14 Profile of Bi/In (90/90 nm) patterned, masked and $CF_4/CHF_3/O_2$ plasma etched Si trenches, showing improved side wall profile and etching anisotropy after addition of CHF_3.

7.4.4 Exposed Bi/In Etch Rate in Fluorine Plasma

Mass weighing and profiler test results show that normal glass slides are etched away extremely slowly under $CF_4/CHF_3/O_2$ plasma in our system. Etch loss of these glass slides is not detectable even after hours of etching. Hence, glass slides can be used as perfect reference substrates for Bi/In etch rate analysis. Figure 7.15 shows the thickness changes of the exposed Bi/In film and conventional photoresist Shipley SPR2FX-1.3 with plasma etch time. The starting thickness of Bi/In film was 850 Å. After 60 min of plasma etching (Si etch, recipe is O_2 = 6 sccm,

CF_4 = 50 sccm, Pressure = 150 mTorr, RF Power = 100 W), 30 Å was etched away, giving an etch speed of 0.05 nm/min, which Figure 7.15 shows to be nearly linear with time. Under the same etch condition 1μm thick Shipley resist was totally etched away in 22 minutes, and the etch rate is 50 nm/min. This means that the Bi/In resist is 1000 times more resistant to $CF_4/CHF_3/O_2$ plasma etch than regular organic resists. Typical etch rate for Si (100) under this plasma condition is 30 - 50 nm/min and SiO_2 50 - 80 nm/min. This suggests that 30 nm resist patterns are sufficient for typical 0.5 micron layers; ~100 nm Bi/In resist layers would give protection under those conditions for etching 100 μm deep Si patterns, and 500 nm Bi/In for etching the whole wafer. Hence, this suggests an application of Bi/In as a possible resist for Deep RIE etching processes should be considered in future research.

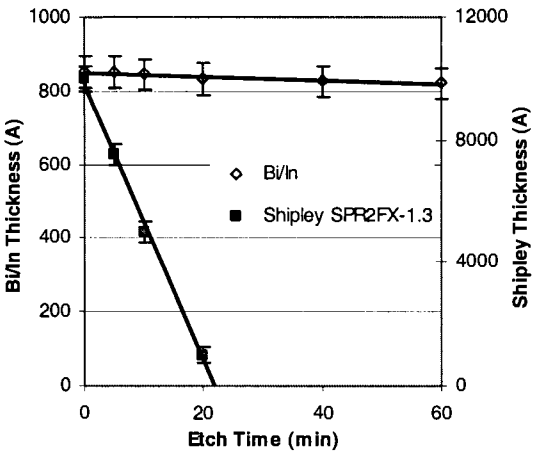

Figure 7.15 Etch rate (Si etch recipe) comparison between exposed Bi/In and conventional Shipley photoresist. The left Y axis is the thickness of exposed Bi/In, and the right Y axis is the thickness of Shipley resist. Note that Bi/In was almost unchanged and the organic resist strongly eroded by the plasma.

It is estimated that, with the SiO_2 plasma etch recipe (O_2 = 10 sccm, CF_4 = 75 sccm, Pressure = 150 mTorr, RF Power = 100 W), the erosion of Bi/In should appear no worse than with the Si etch recipe, while the resist removal is 66% higher due to the higher O levels, thus creating an even higher Bi/In to organic resist etch ratio.

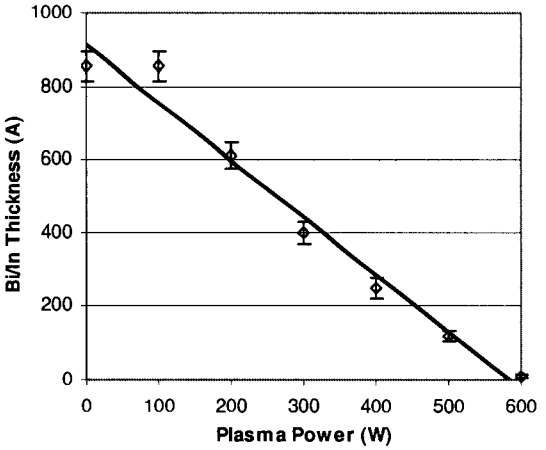

Figure 7.16 Plasma RF power vs. exposed Bi/In thickness after 2 minutes of plasma etch, with O_2, CF_4 and Pressure fixed. O_2 = 6 sccm, CF_4 = 50 sccm, CHF_3 = 0 sccm, Pressure = 150 mTorr. The starting film thickness was 850 Å.

Experiments were also carried out to study the influence of plasma power on the etch rate of exposed Bi/In film. Bi/In was first deposited on glass slides. After laser exposure and wet development, the samples were etched for 2 minutes under the same condition except the RF power was varied. Film thickness was tested before and after the plasma etching. The starting film thickness was 850 Å. Figure 7.16 shows the result after exposed Bi/In was etched under plasma with RF power from 100 W to 600 W. One can see that the etch rate of exposed Bi/In increases almost linearly with RF power. The etch speed is only 0.05 nm/min at 100 W (this is likely due to the re-deposition of sputtered material at a lower sputtering power), and it changes to 12 nm/min at 200 W, and 42 nm/min at 600 W. Other parameters of the recipe were O_2 = 6 sccm, CF_4 = 50 sccm, CHF_3 = 0 sccm, Pressure = 150 mTorr. The etch rate of SiO_2 is 50 – 80nm/min at 100 W, 120 – 200 nm/min at 200 W and ~300 nm/min at 600 W. Si etch rate is 60 – 70% of that of SiO_2.

7.4.5 O_2 Plasma

Test results show that O_2 plasma etching (ashing) has little effect on exposed Bi/In films. The ashing recipe is O_2 = 20 sccm, Pressure = 100 mTorr, RF Power = 200 W. It took just 1 min to remove 1.3 μm Shipley SPR2FX – 1.3 organic photoresist. But no etch loss was observed after 20 minutes of etching an exposed Bi/In films, suggesting an etch rate of less than 0.05 nm/min. This is an etch ratio of greater than 26,000 times that of organic resists. Indeed this is really a lower limit as no resist removal was detected within the measurement limits of the profiler (~1 nm). Figure 7.17 shows the comparison between the ashing rates of exposed Bi/In and Shipley photoresist. This suggests that very thin Bi/In layers can protect and pattern organic material that are susceptible to oxygen plasmas, such as Myler. This lack of response to oxygen plasma is probably due to the Bi/In having been fully oxidized during the laser exposure, and hence no further oxidation happens during the O_2 ashing.

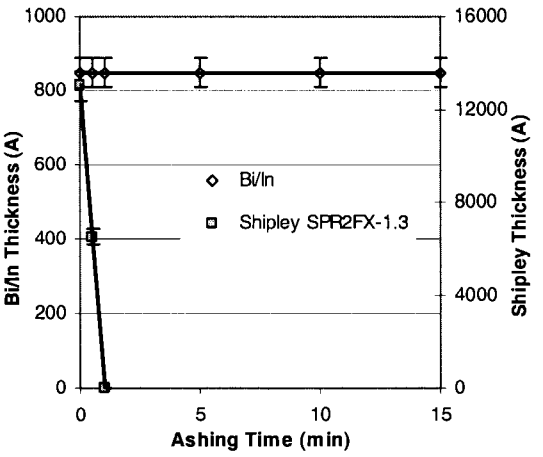

Figure 7.17 Ashing rate (O_2 ashing recipe) comparison between exposed Bi/In and conventional organic photoresist by plasma. O_2 plasma strongly erodes the organic resist.

The strong resistance of exposed Bi/In to O_2 plasma etching makes the thin film imaging method (discussed in Section 7.2) a viable process. This will be further investigated by patterning Bi/In on graphite substrates.

7.4.6 Preliminary Cl_2 Plasma Etching Study

Chlorine-based plasma has been generally used for metal and polysilicon etching in sub- and deep-submicron fabrication. The advantage of chlorine plasma over fluorine plasma is that Cl_2 plasma creates less undercut [110-112]. As we do not have Cl_2 plasma sources in our lab, we did some preliminary studies on Cl_2 plasma with Christina Kaiser at University of British Columbia (UBC).

Bi/In (30/30 nm) was deposited on glass substrates and was raster-scanned with 0.15 - 0.35 W argon laser focused by a 50 mm lens. One group of samples were developed after laser exposure, and the resistance of exposed Bi/In to Cl_2 plasma etching was studied. The other group of samples were not developed after laser exposure, so that we could explore the feasibility of developing Bi/In with dry plasma etching instead of with wet dilute RCA2. The facility we used at UBC is an ECR plasma etcher (electron cyclotron resonance), in which a microwave was used to generate the plasma, and an RF field was applied to the sample chuck to build up a negative DC bias. The etch recipes were as follows:

Total Pressure	10 mTorr
Microwave power	100 W
RF bias power	50 W (-100 volt DC)
Cl_2	2 sccm
BCl_3	2 sccm
Ar	20 sccm
Etch time	30 – 120 seconds

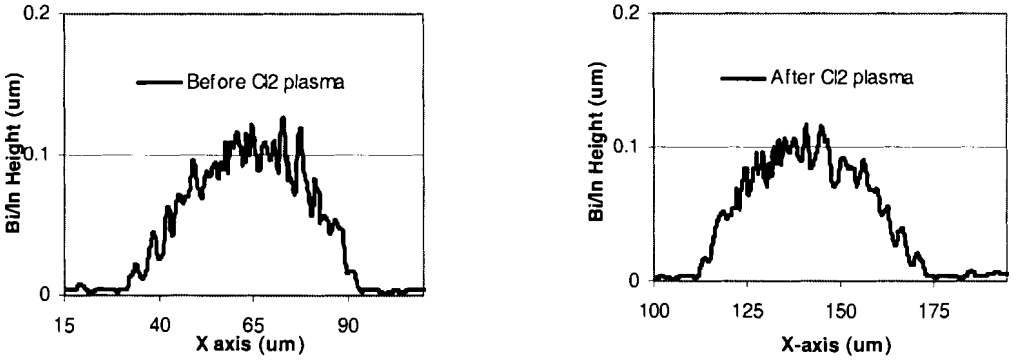

Figure 7.18 Profile of Bi/In lines before and after 120 seconds of Cl_2 plasma etching.

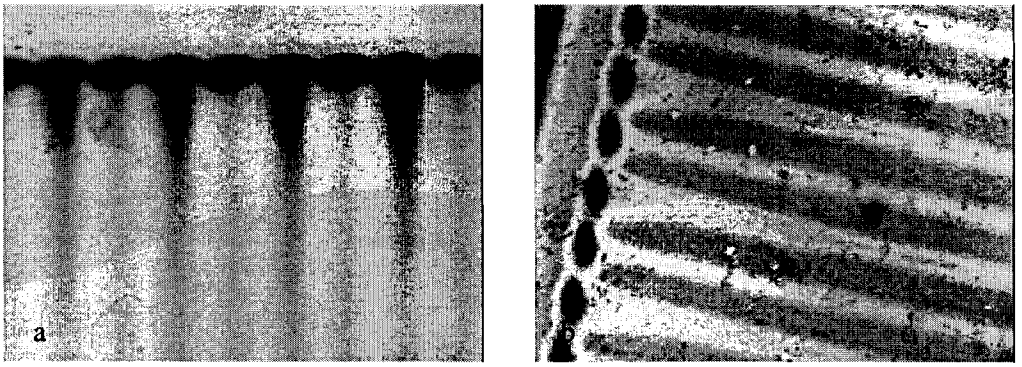

Figure 7.19 Colour change was observed after Cl_2 plasma etching of patterned Bi/In film. (a) before plasma etching and (b) after Cl_2 plasma etching.

Figure 7.18 shows the profile of developed Bi/In lines before and after the Cl_2 dry plasma etching. With this etching recipe, no obvious erosion was observed. However, more experiments with different recipes need to be carried out to confirm the resistance of exposed Bi/In to Cl_2 plasma etching. Figure 7.19 shows optical microscopy images before and after Cl_2 plasma etching. Colour changes were observed after the plasma etching (developing), which could be observed from the change in the contrast of the grayscale image. The unexposed metal part was not removed. However, no concrete conclusion could be drawn from this test yet, as only one Cl_2 plasma etching recipe was tried out. Further study should be conducted to explore the possibility of developing Bi/In with dry plasma etching.

7.4.7 Plasma Etch Summary

The results of this section suggest that bimetallic resists can provide sufficient resist protection for an underlying layer, and may offer some significant advantages over regular organic resists for the plasma etching of silicon, silicon dioxide and organics. These experiments have not answered questions about edge roughness due to the limitations of the exposure system. Furthermore, it is clear that the etch recipes required to achieve the desired sidewall profile will be different for these bimetallic resists than for regular organic resists. The erosion of organic

resists, with its change in the resist pattern edge and the resulting re-deposition of some organic compounds on the sidewalls during the etch, are important factors in obtaining the desired line and hole profiles. The result that Bi/In resists almost do not erode suggests some obvious advantages in maintaining pattern and reducing etch related problems, especially in the case of via or contact cut holes. There the re-deposition of organics creates difficulties in making metal/poly contacts. These results suggest this would probably not occur for the Bi/In resists and hence it may give better results for via/contact cuts. Since Bi/In erosion during the plasma etch is small, the possibility of plasma etch chamber contamination should be low. Future studies will be carried out on this.

7.5 Creating Special Structures with Dry/Wet Etch Processes

Conventional wet, anisotropic etch masking layers, such as Si_3N_4 and SiO_2, are known to be very stable under KOH, TMAH or EDP. However, they cannot be used as CF_4/CHF_3 plasma masking layers as the plasma etch rates of the two layers are very fast. On the other hand, conventional organic photoresists, which are widely used for plasma etching masking layers, cannot work with wet anisotropic etchants. Bi/In thermal resists are unique in being a good resist and masking material for all three alkaline anisotropic etchants, KOH, EDP and TMAH for Si anisotropic etching. In the previous section, we have also shown that Bi/In resists are also good for plasma etching. This enables us to use a single resist layer for both wet and dry etching. Bi/In is the first resist that can be used as both a wet anisotropic etch masking layer and a dry plasma etch masking layer. This unique feature gives Bi/In the capability of patterning and building structures that cannot be made by any other photoresists or masking layers.

Figure 7.20 (f) shows a special structure: a V shape groove with vertical side wall. This structure cannot be created by conventional photoresists or masking layers, but can be made by

utilizing Bi/In as both a wet and dry thermal resist masking layer. First, 120/120 nm Bi/In film is deposited on an RCA-cleaned (100) silicon substrate. Laser exposure makes patterns on the Bi/In film. After development the sample is etched with alkaline-based solutions such as TMAH to create V-groove structure in the silicon, as shown in Figure 7.20 (d). This is followed by a CF_4/CHF_3 plasma dry anisotropic etch shown in (e). After stripping off Bi/In layer, the V shape trench with straight side wall is done.

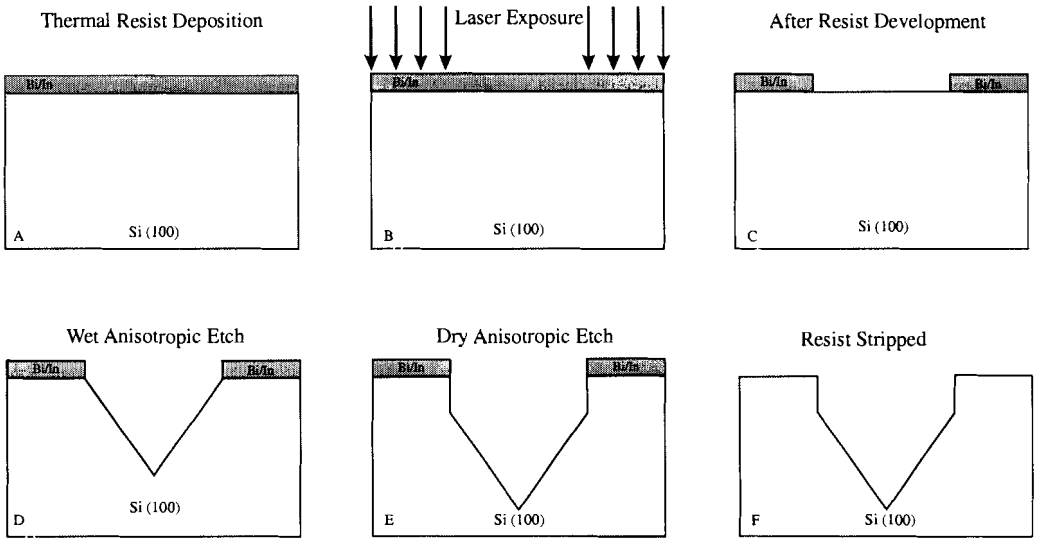

Figure 7.20 Bi/In patterned mask with combined Si anisotropic and plasma etch. Six steps are used. (a) deposit Bi/In, (b) laser expose the film, (c) develop the exposed resist, (d) do wet anisotropic etch, (e) plasma dry anisotropic etch, and (f) Bi/In resist layer is stripped off with RCA2 cleaning.

We have successfully produced this structure on a (100) silicon wafer to prove that this process is feasible. Figure 7.21 shows the profile of the V shape trench right after wet anisotropic etching (thin solid line) in 85°C TMAH for 30 minutes and the profile after CF_4/CHF_3 plasma etching (O_2 = 6 sccm, CF_4 = 50 sccm, Pressure = 150 mTorr, RF Power = 200 W) for 7.5 minutes (thick line). Figure 7.22 is the cross-section view of the double-etched trench, showing straight side walls. About 1 μm deep straight sidewalls can be clearly seen on both sides of the V trench. It is noticed that the top corner of the trench is not straight. Again this anisotropy can be improved by adding argon and CHF_3 gases into the etch recipe.

Important here is that the Bi/In thermal resist has clearly demonstrated a single layer being resistive to both anisotropic Si etch and plasma etching. From the literature it appears that no other photoresists or thermal resists can accomplish this. This opens new potential process combinations for micromachining fabrication.

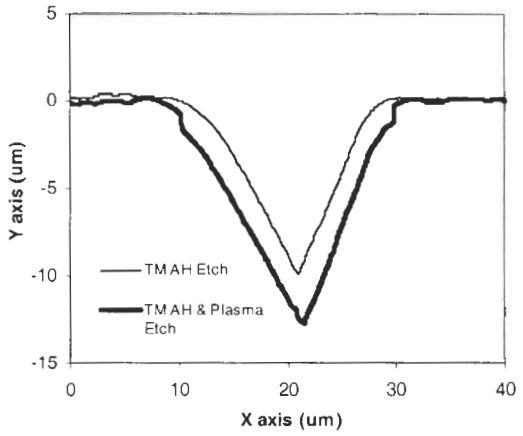

Figure 7.21 Profile of Bi/In masked anisotropic V groove and vertical plasma etched structure. The thin line is the profile after TMAH etching. The thick line is after TMAH etch and CF_4/CHF_3 plasma etching.

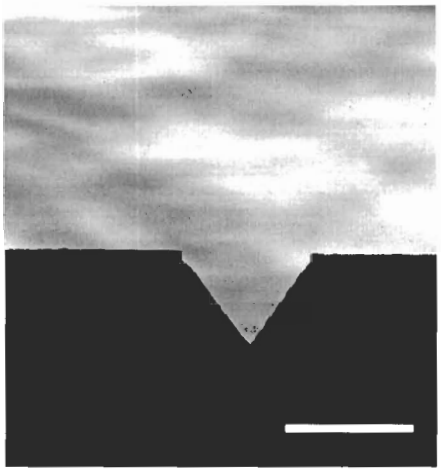

Figure 7.22 The cross-section of a trench masked by Bi/In on (100) Si wafer after a combination of wet anisotropic etch and dry CF_4/CHF_3 plasma etch. The white bar is 20μm.

7.6 Bi/In as an Electroplating Seed Layer

It is amazing to discover that the metallic bilayer thin film thermal resist is conductive both before and after exposure. This special feature opens the door to many potential applications in the micromachining and microfabrication field. The developed film is more conductive than most of the current barrier layer films and silicide films. This indicates that the Bi/In thermal resist can not only be used as a patterning material, but also as a direct-write electroplating resist and as transparent electrodes. By comparison a standard MEMS electroplating process requires deposition of a metal seed layer, spinning on of photoresist, baking, patterning the resist, development, etching, resist and the seed layer stripping and cleaning before electroplating can begin.

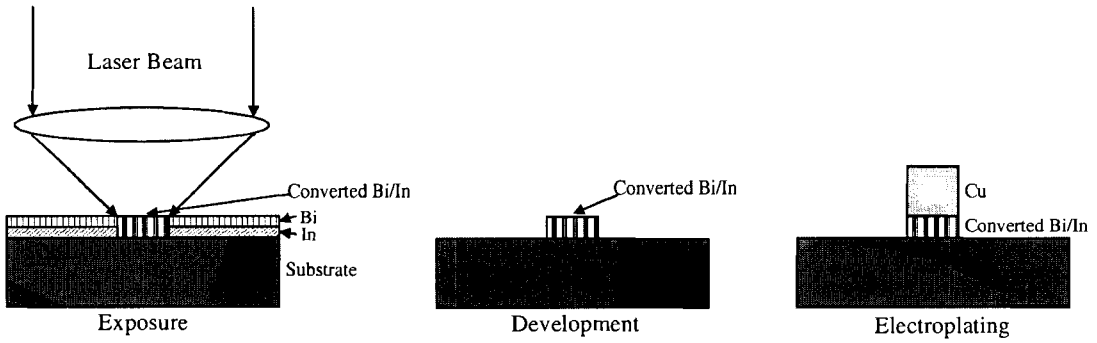

Figure 7.23 Bi/In as both masking and seeding material. Bi/In is first patterned and the exposed area is converted. Resist development removes the unexposed area, and the exposed is retained. It acts as both the patterning and the seed layer for Cu plating.

Conventional metal deposition methods, such as PVD and CVD, have the disadvantage of not being able to deposit thick films (> 1.5 μm) on the substrate due to film stress and the low deposition rate. By comparison, metal electroplating can not only put several microns, even dozens of micron thick films on the substrate, but also fill high aspect ratio vias and contacts. As shown in Figure 7.23, the Bi/In resist can be deposited and directly written on with the laser, and it will act as both a patterning material after development and a seeding layer for electroplating.

By comparison considerable efforts have been made to achieve high-aspect ratio structures in the micromachining area. Using X-ray lithography, standard LIGA (lithographic electroforming and moulding) process can be used to fabricate very thick structures (as thick as 1 mm) with sub-micron lateral accuracy [113]. However, the high cost of using a synchrotron X-ray source prevents it from being a common micromachining process. With Bi/In as both a patterning and seed layer, one can easily plate thick films to achieve high aspect ratio structures. Conductive bimetallic thermal resist offers a new type of LIGA process.

Cu and Ni plating was carried out on developed Bi/In layers on various substrates such as Si wafers, glass slides, wet-oxidized wafers. The Bi/In resist, 15/15 to 60/60 nm thick was first exposed to argon laser by raster-scanning exposure patterns, such as lines and square areas. The advantage of using the laser scanning method is that it allows us to change the exposure patterns easily without having to make photomasks. Laser power varied from 0.05 W to 0.35 W with different lenses (50 mm, 5× objective lens and 50× objective lens). The films were then developed in $HCl:H_2O_2:H_2O$ solutions for 40 to 100 seconds to remove unexposed areas. The conductive pads for plating connections were made during the laser scanning period. Table 7.3 shows the chemical ingredients of the metal solutions that were used for the electroplating experiments [114]. Cu plating was carried out at room temperature and Ni at 55°C. Figure 7.24 shows several Cu lines inside a square Cu window, the space between two Cu lines is 10 μm. To make this pattern on Bi/In, the large window frame was first raster-scanned with argon laser on the X-Y-Z table. Then the lines were made again by Argon laser using a single scan. As shown here, as copper plating continues, a high aspect ratio structure can be achieved. Figure 7.25 (a) is the SEM picture of a Cu square electroplated on Si with an opened window, and (b) is the Cu lines. Depending on the electroplating time, the copper layers range from 3 to 35 μm thick as measured by profilometer. The two SEM pictures in Figure 7.26 are tilted view and cross-section of Cu lines on glass substrate. It is clearly shown in (a) that the Cu lines grow upon the Bi/In

seeding layer. The cross-section of Cu lines in (b) is close to a half moon shape. However, the growth along lateral directions is faster than along the vertical direction, as shown in the copper profile plot in Figure 7.28.

Figure 7.27 (a) is a Ni mesh plated on a Si substrate. Each square is 10×10 μm. (b) shows a densely plated area. The space between two Ni lines is 5 μm. (c) is a small Ni pattern; the thin line is 2 μm wide. The plated nickel layer is 1 - 4 μm thick. The electroplated nickel line has a straighter side wall compared to copper lines, as shown in the nickel profile plot in Figure 7.28.

A potential and unique application of the direct-write metal plating is to apply metal connections to finished chips to provide circuit modifications for rapid design debug or create new devices with thicker metal layers than given by current processes. Compared to the FIB techniques which are widely used by design companies, direct-write metallization is much faster and more cost effective.

Table 7.3 Cu and Ni plating parameters

	1 liter plating solution	Plating Temperature	Typical Plating Current Density
Cu	$CuSO_4.5H_2O$ =100 g, H_2SO_4=10 ml	25°C	10-50 A/m^2
Ni	$NiSO_4.6H_2O$=150 g, $NiCl.6H_2O$=60 g, H_3BO_3=37.5 g	55°C	10-50 A/m^2

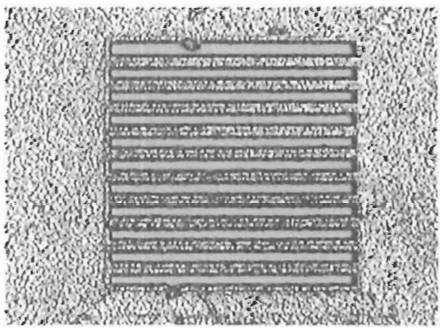

Figure 7.24 An optical picture of plated Cu on SiO_2. The spacing between two lines is 10 μm.

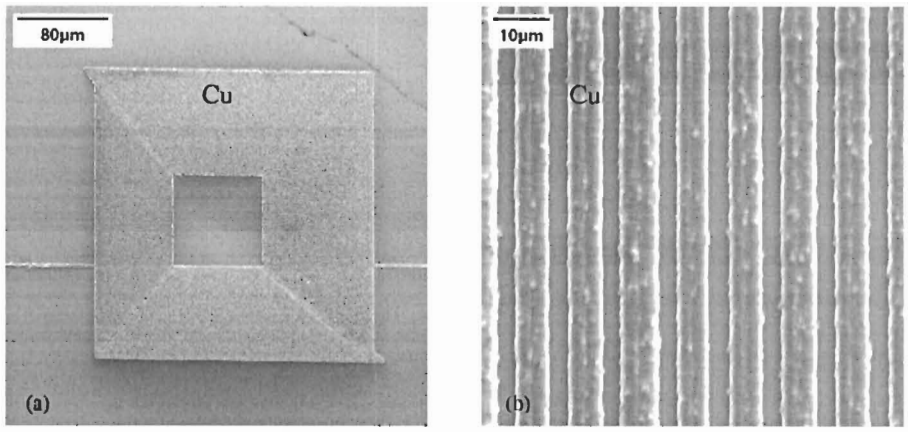

Figure 7.25 (a) SEM picture of a Cu square and (b) SEM picture of Cu lines. The copper layer is 3 μm thick.

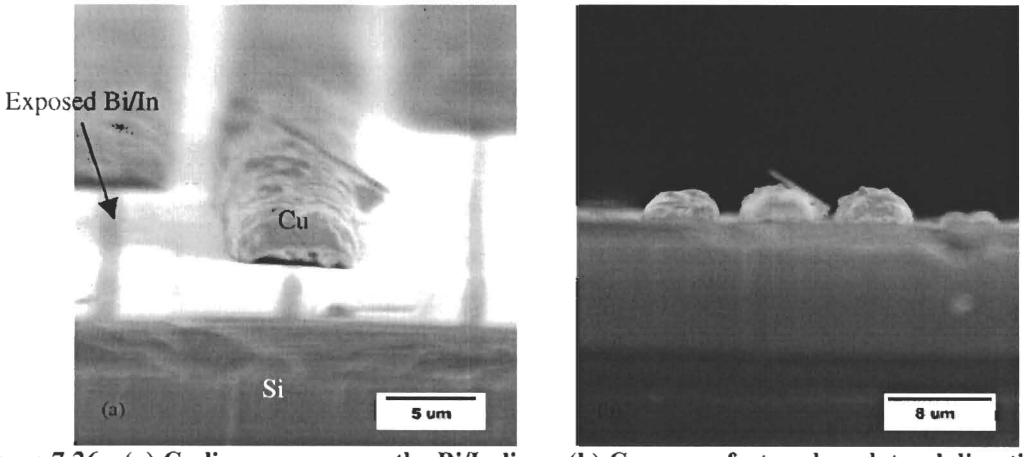

Figure 7.26 (a) Cu lines grow upon the Bi/In lines. (b) Cu grows faster along lateral directions than along the vertical direction.

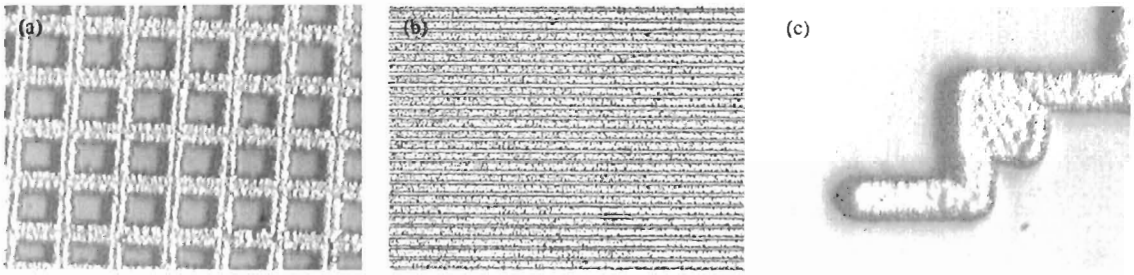

Figure 7.27 Electroplated Ni grown on patterned Bi/In resist on Si wafer. (a) Ni mesh. The spacing between two lines is 10 μm (50× optical). (b) densely plated Ni lines with 5 μm spacing (100× optical) and (c) a small pattern of 4 μm square with 2 μm wide line (800× optical).

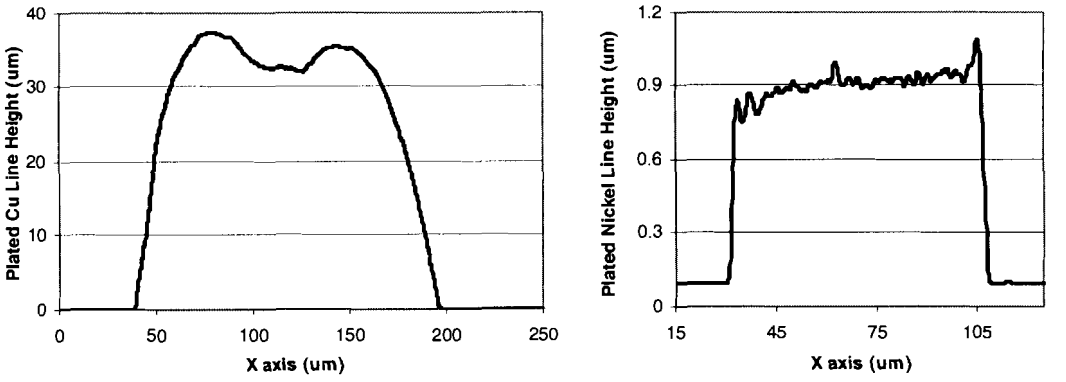

Figure 7.28 Profile of electroplated copper and nickel lines on Bi/In seed layers.

7.7 In and Sn/In as Thermal Resists

Until now, much of the focus of application exploration has been on Bi/In. How about other bimetallic thin films, like Sn/In, and even In single metal film? Since it appears the conversion is an oxidation process, these may work as well. Interestingly, it was found that 48 nm DC-sputtered, In single metal film turned transparent at an argon laser exposure of 225 mW, twice as much power needed to make Bi/In transparent (50 mm lens, 1 cm/s scan rate). This is consistent with a higher melting point for indium compared to the InBi eutectic alloys. Thus, Bi/In films are more sensitive to laser exposure than In films. After laser exposure, an In sample (on a Si substrate) was developed by dilute RCA2 solution. Unexposed In films disappeared in seconds. However, exposed In film remained unchanged even after 15 minutes, as shown in Figure 7.29. This shows that indium films exhibit thermal resist characteristics.

Wet Si anisotropic etching tests showed that exposed In film was also resistant to alkaline-based anisotropic etchants, although KOH and EDP attack exposed In faster than exposed Bi/In. As shown in Figure 7.30, after 40 minutes of etching in 85°C TMAH, exposed In film remained unchanged as an etch masking layer. The SEM cross-section picture shows a 40μm wide trench in a (100) silicon substrate. These test results show that single In film has similar physical and chemical properties as do bimetallic Bi/In films.

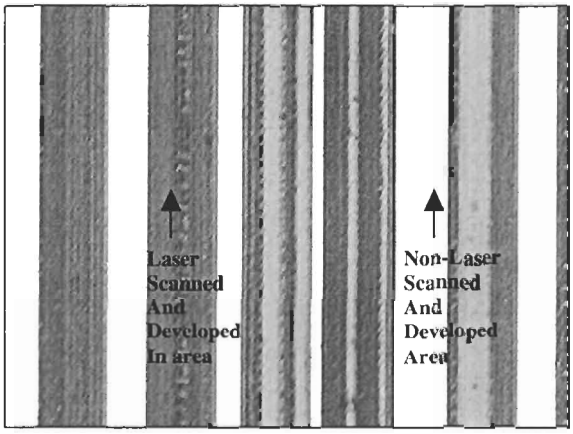

Figure 7.29 Exposed In film (48 nm thick) was developed on Si substrate. The dark lines are In exposed with different laser power. The white area is Si, which had been covered by unexposed In that was removed by dilute RCA2. (50× optical)

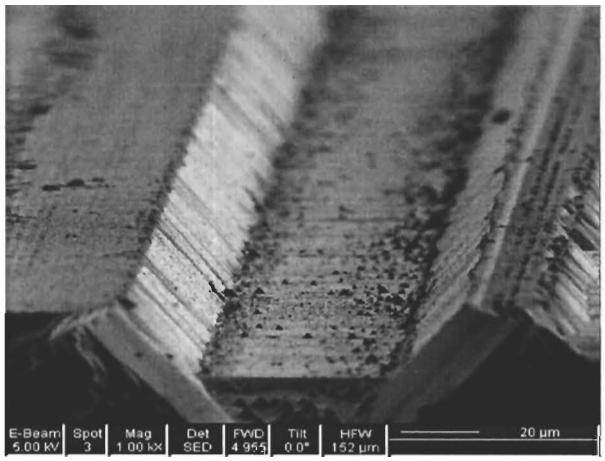

Figure 7.30 48 nm In film used as the patterning and etch masking layer. The cross-section picture shows a trench into (100) silicon wafer after etched in TMAH at 85°C for 40 minutes.

Experiment was also carried out to investigate whether Sn/In bimetallic film has thermal resist properties. As expected, Sn/In can be exposed, developed as Bi/In and In films, and it is also resistant to wet silicon anisotropic etch and dry CF_4 plasma etch. Figure 7.31 shows the profile of a CF_4 plasma etched trench in silicon substrate, with Sn/In as the etching mask layer.

Exposed Sn/In film was etched away faster than exposed Bi/In film with the Si plasma etch recipe, as shown in Figure 7.32 (a). About 30 Å was etched away in 26 minutes, giving the etch rate of 1.2 Å/min. Exposed In film was eroded even faster than Sn/In, with an etch rate of 2.3

Å/min. Identical to exposed Bi/In film, both exposed Sn/In and In films can barely be etched under the O_2 ashing plasma. Figure 7.32 (b) shows the O_2 ashing results for exposed Sn/In and In.

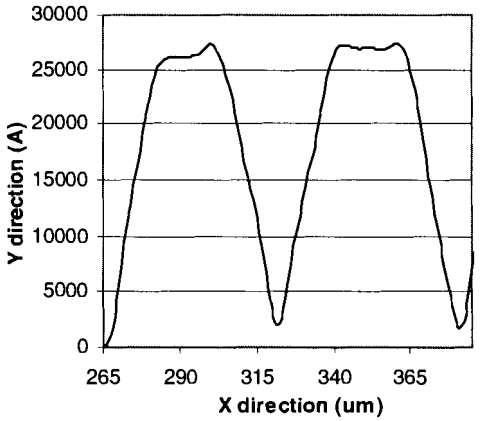

Figure 7.31 A 2.5 μm deep trench etched into silicon substrate with Sn/In as the masking layer for silicon CF_4 plasma etch.

Tests on single Bi film showed that laser exposed Bi film was not continuous (discussed in Chapter 6). Both exposed and unexposed Bi film dissolve within 60 seconds in dilute RCA2 development solution. All these results show that single Bi film is not suitable for thermal resist applications.

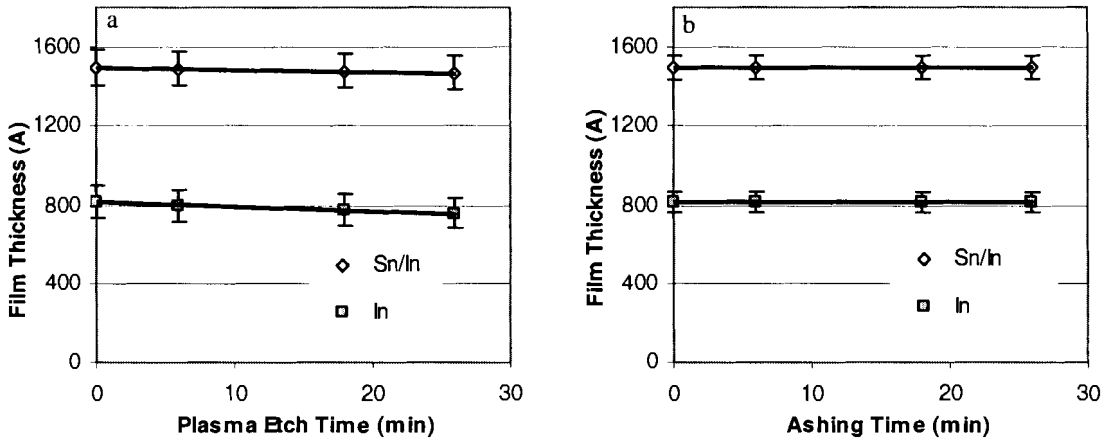

Figure 7.32 (a) Etch rates (Si etch recipe) of exposed Sn/In and exposed single In film. Both Sn/In and In film thickness changes slowly with the plasma etch time. (b) Exposed Sn/In and In ashing rate. The O_2 ashing has little effect on the two films.

7.8 Summary

A prototype thin film imaging process (with a thin imaging layer and a thick carbon protection layer) has been proposed. Bi/In and its class of bimetallic thermal resists are the first reported resists that are resistant to both alkaline-based silicon anisotropic etching and fluorine-based plasma etching. The etch rate of exposed Bi/In film in KOH, EDP and TMAH is slower than that of SiO_2. TMAH etches exposed Bi/In at half of the rate of KOH, making it the best anisotropic solution for Bi/In process. $CF_4/CHF_3/O_2$ plasma etching results show that Bi/In etches 1000 times slower than regular organic resists. With the combination of anisotropic etching and plasma etching into one single process flow, one can create some special features that are not possible by other methods. Unlike organic photoresists, Bi/In thermal resist is conductive even after development, making it a potential material for direct-write electroplating and for transparent electrodes. The combination of anisotropic etch resistance and acting as an electroplating seed layer makes it a very useful MEMS resist. Chapter 8 will discuss applications involving the transparency aspect of films of Bi/In and its class. In the next chapter, we explore bimetallic resists for photomask applications.

Chapter 8
Application of Bimetallic Resist as Direct-write Photomask and Data Storage Materials

8.1 Introduction

The large optical property change between the exposed and unexposed bimetallic thermal resist Bi/In films is attractive since this can be utilized in many fields, such as optical storage and direct-write photomask materials. It was observed that light transmission through converted resist increases rapidly with laser exposure power. This Chapter will focus mainly on photomask applications. A single-step, direct-write photomask making process will be studied using bimetallic thermal resists as the photomask covering or imaging material. The application of bimetallic films for grayscale masks will be examined. It is found that Sn/In exhibits better optical performance for binary and grayscale mask applications than Bi/In does. Finally, to demonstrate the applications of Bi/In as a thermal resist, a Si anisotropic etching mask material, a direct-write photomask material, and its compatibility with conventional CMOS processes, surface-textured, solar cell test device will be fabricated.

8.1.1 Photomasks

Photomasks with smaller features, better line width control, fewer defects, no ESD (electro static damage) issue and lower cost are required by the microfabrication and micromachining industries. A conventional photomask consists of a transparent substrate, and a surface covering and patterning film. Quartz and glass have been extensively used for decades as the mask substrates. Many different kinds of materials have been used as the surface imaging

layer, but the most commonly used is chromium thin film. Emulsion has also been used widely in labs for non-critical applications. However, as we discussed earlier in Chapter 1, Cr/quartz photomasks face a lot of problems.

Direct-write photomask material is attracting more and more attention recently. The initial state of a direct-write material should be either highly transmitting (low OD) or highly absorbing (high OD). The optical density of the material should change significantly when exposed to certain physical (or even chemical) processing. In order to achieve the resolution requirement set by modern microfabrication, electron or laser beams are usually used to write the pattern. As discussed in Chapter 1, HEBS glass darkens (high OD) upon e-beam exposure [2]. *Physical Optics Corporation* proposed a high-resolution laser-beam, mask-pattern-writing technology on a thin layer of ion-exchanged glass medium. The ion-exchanged layer of the special glass plate was pre-darkened and written by laser-induced local heat erasure (making it transparent and low OD). The write beam was a laser beam visible from 400 to 700 nm. It was claimed that high resolution (~ 0.2 μm) was achievable [115]. However, none of the reported direct-write photomask materials can fully satisfy the demands of the microfabrication industry.

8.1.2 Direct-write and Data Storage Materials

In the optics information storage industry, alloying and phase change materials are widely used. Due to the prevalent applications of CD-R (compact disk – recordable) and CD-RW (compact disk – rewritable) both at home and in the office, developing new types of recording media with higher sensitivity and better signal to noise ratio has generated a great deal of interest. Optical recording is achieved by changing the optical properties before and after laser irradiation, and optical reading is achieved by taking the advantage of the contrast difference between the laser exposed and non-laser exposed area. There are 2 types of optical storage media: write-once and write many. The basic requirements of thin film media as optical storage media are high

laser-writing sensitivity, sharp conversion threshold, good optical contrast and stability. The recording mechanism has also been well studied and categorized into the following 6 types [116]: 1) ablation, 2) phase/ microstructure change, 3) chemical reaction, 4) particle coalescence, 5) topography change and 6) magnetization change. Among all of the optical recording materials, Te-based alloys and doped Te oxide films are the most thoroughly studied media [117]. Because of the low melting point (452°C), low thermal diffusivity, and high optical absorption coefficient ($\alpha = \sim 4.9\times10^5$ cm^{-1} at 830 nm for Te), Te and its alloys have been considered to be among the most sensitive materials for ablation optical recording. The typical phase/microstructure change media for storage are $TeO_{1.1}$, Ge and Sn doped $TeO_{1.1}$, Sb_2Se_3 on Bi_2Te_3, and some other chalcogenide films. Watanabe et al [118] reported that the optical characteristics of Sb_2Se_3 and Sb_2Te_3 films were changed due to an amorphous-crystalline phase transition below 200°C. The respective reflectivity of 400 Å Sb_2Se_3 and 300 Å Sb_2Te_3 films, each on a Te reflective layer increased from 10% to 30% and from 45% to 65% by laser radiation. Media in the chemical reaction category are usually composed of 2 thin layers, such as Pd-Si, Pt-Si and Rh-Si bilayer films [116,119,120]. The initial reflectivity was first made low by choosing the proper thickness for each layer so that the antireflection condition was achieved. After laser irradiation the reflectivity became significantly higher due to the detuning of the antireflection condition, and a silicide compound was formed. In some cases ablation also happened during the process. The large optical property changes before and after the laser exposure in this class of bimetallic thermal resist films put them in this same class of optical storage materials.

8.2 Optical Characteristics of Exposed Bi/In and Sn/In

In this section the change in the Bi/In and Sn/In resists and optical characteristics are measured.

8.2.1 Transmission Analysis of Bi/In Films

To characterize the optical properties of Bi/In films before and after laser exposure a Varian CARY 3E spectrometer was used to measure the absorption through the argon CW raster scanned area and the unexposed area of the film. Figure 8.1 shows the Optical Density (OD) versus the transmission light wavelength for a 40 / 40 nm Bi/In film on a glass slide after exposure to argon laser of different powers. The top curve is the as-sputtered 40 / 40 nm Bi/In film, which is around 2.6 – 2.8 OD from 400 nm to 800 nm wavelength. The second, third, fourth and fifth curves are the OD's of films exposed to argon laser of 150, 300, 450, and 600 mW, respectively, with argon laser focused by a 50 mm lens (10 μm spot size) and a raster-scan rate of 1cm/s. As the power of the laser exposure increases, the OD of the exposed area reduces, and saturates at a minimum level where all of the material in the layers is converted. The absorption spectrum for the converted layers in the range from 400 nm to 800 nm reaches a minimum value of less than 0.1 OD at an exposure intensity of 600 mW. This shows a change in the OD of larger than 2.5 orders in terms of transmitted light power. An ideal direct-write photomask for I-line applications should have ~ 3 OD for the unexposed (blocking) area and < 0.25 OD for the exposed (transmitting) area. The OD of unexposed 40/40 nm Bi/In at 365 nm (I-line) is 2.94 and that of area exposed with 600 mW argon laser is 0.43 OD. It is also noticed that the OD rises rapidly at 365 nm. Please note that no heat treatment was carried out on these samples before the laser raster scan.

Before we move on to improving the optical properties, it should be pointed out that the laser powers used for thermal resist and photomask applications are significantly different. It is known that Bi/In thermal resist has a high exposure sensitivity and that a 15/15 nm Bi/In film can be fully exposed for thermal resist application (to successfully develop a relief image in the thermal resist with dilute RCA2 solution) by a single 4 ns pulse with only a 7 mJ/cm^2 energy density. However, in order to achieve maximum transparency in the exposed film, laser exposure

with much higher energy density is required. Using the following argon laser photomask writing condition:

- Argon laser power = 500 mW;
- Focused by 50 mm lens with 10 μm beam spot size;
- X-Y table moving speed = 1 cm/s;

we can estimate that the writing energy density is ~ 500 J/cm^2. On the other hand, thicker films (~40/40 nm) are used for photomask application than for thermal resist applications (15/15 nm). Thus, the starting power for laser conversion is much higher. In addition, the slow speed (CW argon laser) means much higher thermal conduction. Finally, at the slower exposure rates it is clear that during the laser illumination the film is becoming more transparent, which in turn reduces the exposure, and increases the exposure time required.

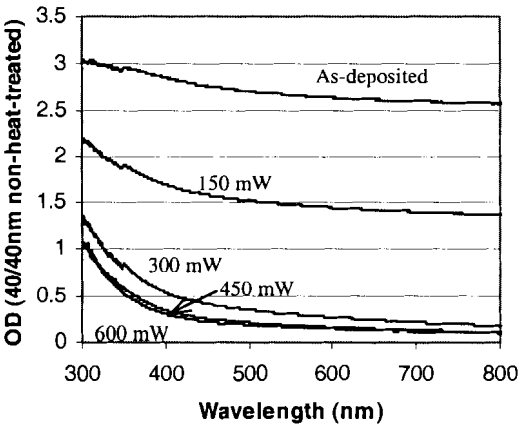

Figure 8.1 Optical absorption (300 nm to 800 nm) through 40/40 nm (non-annealed) Bi/In deposited on glass slide exposed by Ar laser with different power. From top to bottom: 0, 150, 300, 450, and 600 mW. The sample was not heat-treated.

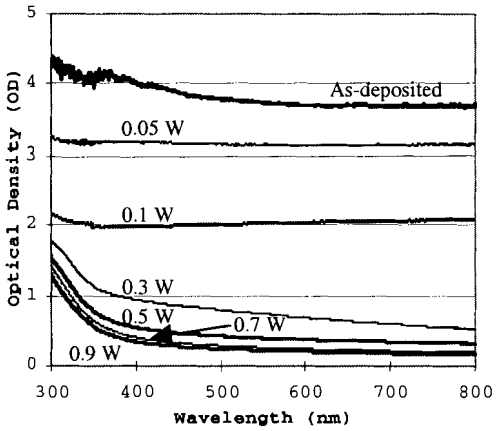

Figure 8.2 Absorption through 50/50 nm Bi/In exposed with the argon laser at different powers. From top to bottom: 0, 50, 100, 300, 500, 700 and 900 mW. The sample was heat-treated for 72 hours at 50°C prior to laser exposure.

8.2.2 Improving Optical Performance

In order to improve the transparency of the exposed area while keeping the high OD of the unexposed area, many methods are under investigation, including adding different gases and elements during film sputtering, varying substrate temperatures during exposure, and finding the optimized film structure (thickness and order of deposition).

It is found that annealing the Bi/In samples at ~90°C for a period of time in air before laser exposure helps reduce the optical density of the subsequent exposed area. Figure 8.2 shows the optical density of a heat-treated 50/50 nm Bi/In film as a function of laser power. Optical transmission was significantly increased when compared to non-heat-treated samples. In order to quantify the improvement, an experiment comparing the OD of the oven-annealed and non-annealed samples was carried out. Two different Bi/In samples were used: one was 40/40 nm and the other was 15/15 nm film, all deposited on glass slides. Each sample was cut into 2 halves for comparison. One half was Ar laser scanned as-deposited and the other half was heat-treated at 90°C for 72 hours before laser scanning. In this way the influence of the fluctuation of film thickness from sample to sample was eliminated. Table 8.1 lists the experiment results measured

at the I-line wavelength. The "Laser Power" column shows the Ar laser power that was used to expose the films. The "OD (Non-annealed)" column shows the OD of the films that were exposed as-deposited with different laser power. The "OD (Annealed)" is the OD of the films that were first heat-treated and then exposed with different laser power. The last column shows the percentage of OD reduction from non-annealed films. One can see that the OD of 40/40 nm film after 600 mW laser exposure dropped 8.42% from 0.435 to 0.398, while the unexposed area only dropped 0.81% and was still above 2.9. Similar results were also found for 15/15 nm films, although the OD drop for unexposed area (23.21%) was much larger than that of 40/40 nm film. The annealing mechanism that brings down the OD of films both before and after exposure is not fully understood at this moment. It could be related to an increase of grain size after annealing.

As its optical absorption starts to increase rapidly below 450 nm, glass slides are no longer suitable substrates for UV and shorter wavelengths. Bi/In was deposited on quartz substrates in order to make photomasks for I-line applications. Tests showed that with quartz as the substrate the OD of exposed area was 0.260 and unexposed area 2.911 at 365 nm wavelength. Figure 8.3 shows the OD of unexposed and 600 mW laser-exposed areas of annealed Bi/In on quartz sample, which is in the wavelength range of 300 nm to 400 nm. It is also seen that the optical absorption of annealed quartz sample at 300 nm is much lower than that of the non-annealed glass sample.

Table 8.1 Comparison of Optical Density (OD @ I-line) between oven-annealed and non-annealed Bi/In films deposited on glass slides.

Film Type	Laser Power (mW)	OD (Non-annealed)	OD (Annealed)	OD Reduction %
40 / 40 nm Bi/In	0	2.936	2.913	0.81%
	300	0.726	0.515	29.13%
	450	0.492	0.431	12.34%
	600	0.435	0.398	8.42%
15 / 15 nm Bi/In	0	1.142	0.877	23.21%
	75	0.504	0.499	0.98%
	150	0.299	0.266	11.18%
	300	0.227	0.155	31.84%
	450	0.170	0.158	7.14%

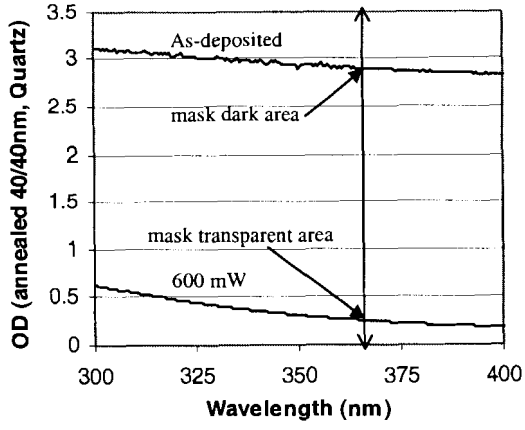

Figure 8.3 Optical absorption through annealed 40/40 nm Bi/In on quartz substrate, in the wavelength range of 300 nm to 400 nm. The top curve is the OD for unexposed, and the bottom is exposed with 600 mW Ar laser.

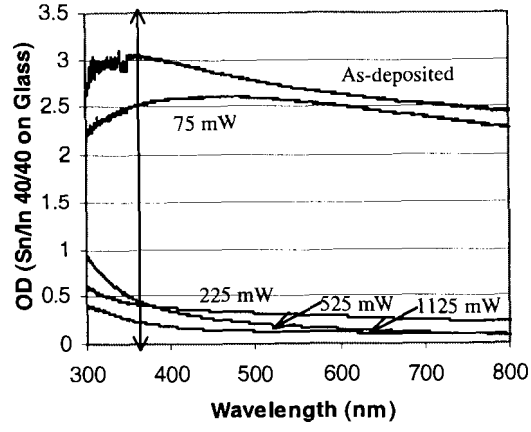

Figure 8.4 40/40 nm Sn/In deposited on glass slides exposed by Ar laser with different power at a 10 mm/s scan rate.

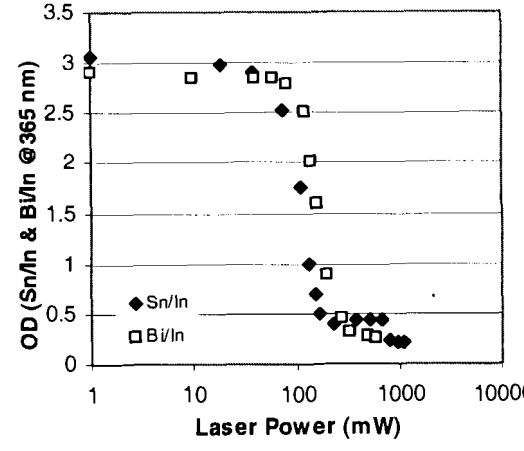

Figure 8.5 40/40 nm Bi/In and Sn/In films optical absorption vs laser power at a wavelength of 365 nm. Absorption drops drastically at around 100 mW laser power and gradually saturates after 300 mW. (laser power in logarithm)

8.2.3 Optical Transmission of Sn/In

Similar spectrum tests were carried out on exposed Sn/In films, and the results were encouraging. Figure 8.4 is the optical transmission data of a heat-treated 40/40 nm Sn/In after exposure to different powers of argon laser. It is noted that while keeping the unexposed film at 3OD at the I-line, we obtain 0.22 OD for exposed films even on glass substrates. As expected, the laser power used to achieve high transmission for Sn/In is nearly twice as much as that for Bi/In, due to the higher melting point and lower absorption for Sn/In (discussed in Chapter 3).

Figure 8.5 shows the curves of optical absorption versus laser writing power at the wavelength of 365 nm, important for determining the direct-write laser power requirements. It is noticed that when the laser is below 50 mW the Optical Density (OD) of the film does not change. The absorption drops sharply around 100 mW writing power and quickly saturates from 300 mW onwards. The optical density stabilizes around 0.26 OD for Bi/In on quartz substrates and 0.22 OD for Sn/In on glass slide.

The substantially higher transmission for Sn/In makes it a better candidate for some photomask processes. The fact that a higher laser power is needed to convert Sn/In films than Bi/In films makes Sn/In mask material more stable under industrial mask exposure conditions.

8.2.4 Stability of Exposed Films

It is important to ensure that both the exposed and unexposed films are optically stable during conventional photomask application, i.e., the laser irradiation from conventional DSW steppers and mask aligners will not change the bimetallic thin film properties. Since the X-Y-Z table moves with a speed of 10 mm/sec and the laser beam is focused to a small spot 10 μm in diameter using a 50 mm lens, 50 mW of Ar laser power will yield a power density of around 50J/cm^2 (for exposure times of milliseconds). Photomasks made from Bi/In and Sn/In are stable

to exposure during mask applications as the mask making powers are much higher than typical industrial DSW exposure system power density at the mask (0.1 – 100 mJ/cm^2) and far below those of mask aligners which have much lower power densities for longer exposures. Note again thermal resists, unlike organic photoresists, do not accumulate exposure energy, so repeated illumination below the threshold power has no conversion effect. Because the organic photoresist exposure time is much shorter, the Bi/In and Sn/In film temperature is raised far less than during the mask making exposures, thus the photomask stability and reliability will be maintained.

A shelf test was also carried out in order to test the stability of the exposed area under normal environments. The Bi/In films raster-scanned with different Ar laser power were kept in an environment of 70°C and ~100% humidity for 7 days. The optical spectrum was measured before and after the shelf test. As shown in Figure 8.6, the spectrum curves before and after the shelf test overlap each other. The transmission barely changed and the optical properties are stable as is required for photomasks.

The shelf tests on both as-deposited (done in Chapter 5) and laser exposed bimetallic films reveal that both areas are very stable. This is important to photomask applications.

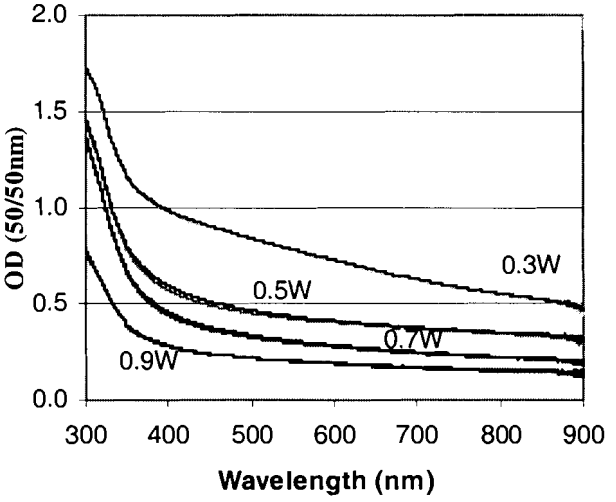

Figure 8.6 Laser converted Bi/In films: optical spectrum before and after the shelf test. The spectrum lines before and after the shelf test overlap with each other, showing that the film optical properties are stable.

8.3 Creating Binary Photomasks with Bimetallic Thermal Resists

The optical density changes due to the laser exposure, shown in the previous section, clearly indicate that bimetallic thermal resists are promising materials for direct-write photomasks for industrial purposes in the I-line or longer wavelength ranges. To demonstrate that the Bi/In and Sn/In bilayer films can be used as a direct-write material for practical fabrication applications, and that the bimetallic films can be written by lasers with a wide range of wavelengths, several photomasks have been made on glass slides and quartz substrates, with the argon laser in our lab and a CREO's flatbed IR thermal-imaging system.

8.3.1 Writing Bimetallic Resists with Argon Laser

The first test mask was a duplicate of a chromium mask pattern containing typical chip exposure test structures. These contain nested L lines and spaces from 30 to 200 μm in size. There are also some 2 μm small test areas. Figure 8.7 - Figure 8.11 show the first mask. It was made with the following conditions:

- A 40 / 40 nm Bi/In or Sn/In deposited on quartz or glass slide;
- Heat treated for 72 hours at 90°C (open air);
- Argon laser raster-scan power = 600 mW for Bi/In and 1125 mW for Sn/In;
- 50 mm lens used to focus Argon laser before hitting the film to a 10μm spot size;
- The X-Y table moving speed (along the x-direction) = 1 cm/sec;
- Raster-scan increment (along Y direction) after each scan = 8 μm.

Figure 8.7 is a front-lit picture of the whole 1×1.6 cm direct-write Bi/In photomask. The laser-scanned areas are darker than the unexposed area from the front-lit picture. Figure 8.8 is a

back-lit image of the mask, showing clearly the patterns. Figure 8.9 is an enlarged front-lit picture showing one of the patterns of a 51 μm line and space exposure structure. Figure 8.10 was taken with both front and back lights on, showing vertical lines in the exposed area that were generated by the laser raster-scan for a 25 μm line and space test structure. However, the raster-scan lines disappeared when only the back-light was on, as shown in Figure 8.11, and are not visible in exposed regular organic resist patterns from this masks (see Figure 8.13). One can also clearly see the smallest feature in the back-lit picture which is a 2 μm wide space. This width is really only the limits of the mask creation program not that of the resists. Although we have not carried out experiments to find out the smallest feature size possible with the Bi/In film, TEM (Transmission Electron Microscopy) analysis showed that the grain size of the Bi/In film is 150 nm, indicating that the smallest feature could be ~ 150 nm (refer to Chapter 6).

Figure 8.12 demonstrates both the direct-write feature of Sn/In film and the powerful pattern drawing capability of our proprietary picture writing software. The argon laser power used was 1125 mW and the y-direction increment was 5 μm. The object is 362 μm × 726 μm. The dark area has an optical density of 3 OD and the transparent area 0.22 OD.

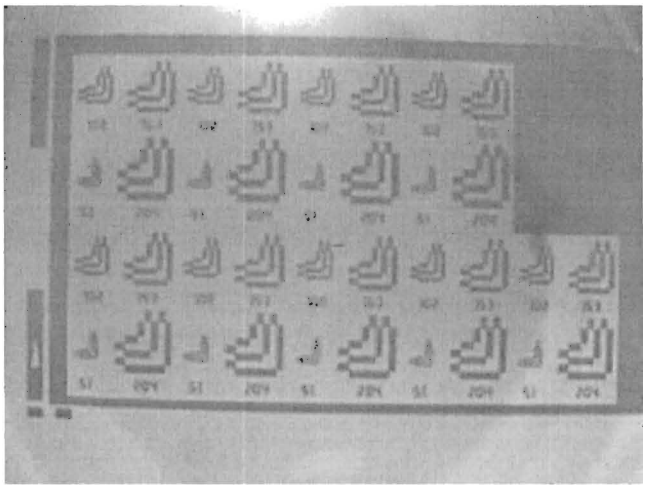

Figure 8.7 40/40 nm Bi/In Direct-write binary photomask made on a quartz plate using an argon laser. The bilayer film was heat-treated for 72 hours at 90°C before laser exposure. (front-lit image, area = 1×1.6 cm)

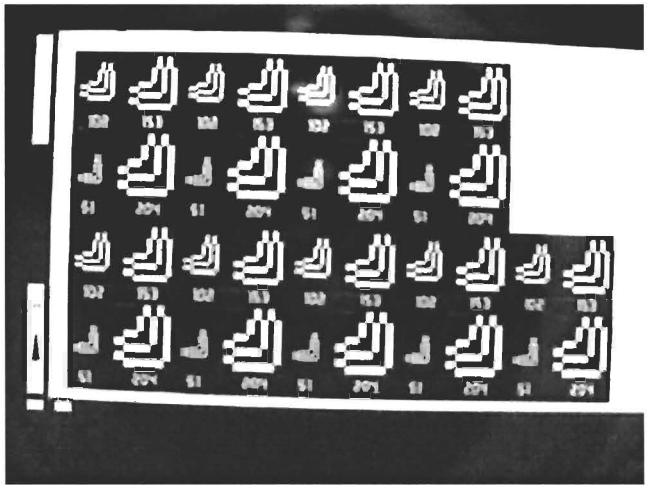

Figure 8.8 Back-lit image of the same Bi/In mask in Figure 8.7.

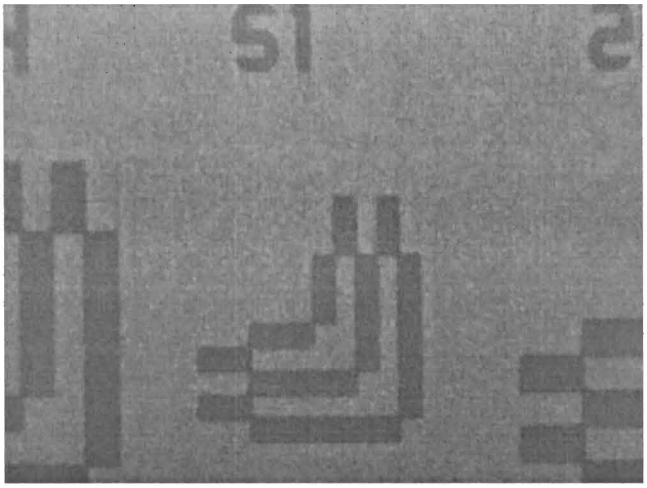

Figure 8.9 Enlarged front-lit picture of the direct-write Bi/In photomask in Figure 8.7. The width of the line at the middle is 51 μm.

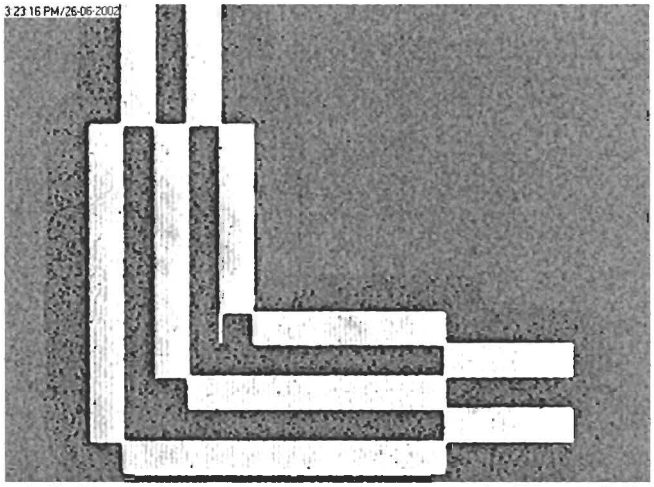

Figure 8.10 Front+back-lit image of a pattern on the Bi/In mask (Figure 8.7) with 25 μm wide lines. Vertical raster-scanned lines can be seen in the exposed areas. However, the scan lines are not seen on exposed photoresist.

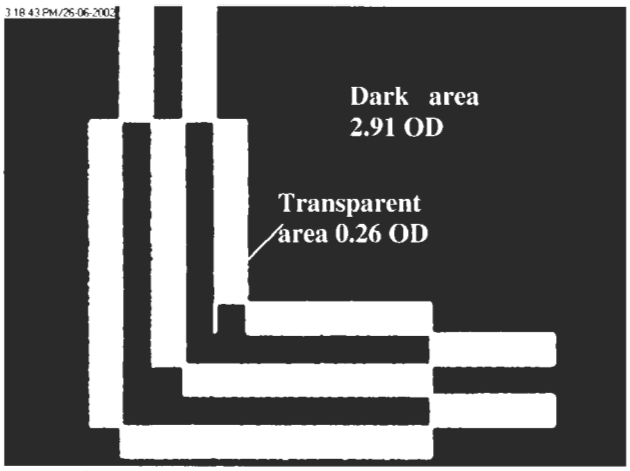

Figure 8.11 Back-lit image of the same pattern on the Bi/In mask in Figure 8.7. No raster-scan lines can be seen in the exposed areas. The thinnest line near the centre is only 2 μm wide.

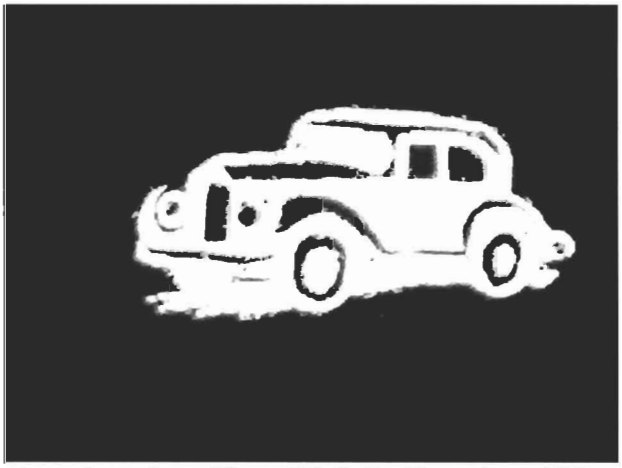

Figure 8.12 Binary photomask made on 80 nm 5% Sn/In film using a 514 nm Ar laser exposure.

8.3.2 Exposing Organic Resist with a Bi/In Direct-write Mask

The true test of a photomask is how it exposes a photoresist. In order to test the direct-write photomask, a Quintel 4" mask aligner with a 365 nm Hg source was used to expose a Shipley SPR2FX-1.3 photoresist coated on a chrome film. With a 15 second exposure time and a 10 mW/cm^2 light intensity, a good pattern was made in the photoresist. These are comparable exposure parameters to those required for processing a chrome mask with the same features. Figure 8.13 shows the pattern on the Shipley photoresist after development in Shipley MF-319 developer for 30 seconds.

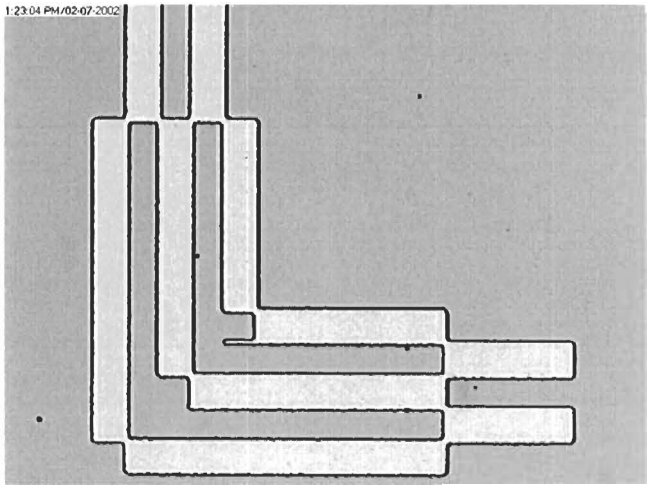

Figure 8.13 Pattern in Shipley SPR2FX-1.3 developed with MF-319. Resist was exposed with the mask of Figure 8.11.

8.3.3 Writing Bimetallic Resists with an Industrial IR Laser

Currently, most photomasks are written using UV laser or e-beam single beam systems. For the maximum resolution these short wavelength sources may be needed for the exposure of resists, but for many other applications larger spot sizes are acceptable. The near wavelength invariance property of these bimetallic thermal resist films suggests that it would be possible to use near Infrared (NIR) laser diodes, which relative to UV lasers have longer lifetime, much lower cost, and are available in laser diode arrays allowing for much faster mask production. As the mask sizes are growing substantially to fit the needs of the LCD and other industrial applications, writing the pattern with parallel beams could substantially speed up mask fabrication times. To test this possibility, we also patterned the Bi/In thermal resist films using a flatbed thermal-imaging tool, a raster-scan system created by CREO Inc [66]. This multi-head system is similar to the laser exposure system we have at Simon Fraser University (X-Y-Z table and argon laser setup, refer to Chapter 4). The CREO system, as shown in Figure 8.14, is equipped with 160 independently controlled light spots using an 830 nm IR laser diode array which writes the pattern in a 0.8 mm wide swath. The spot size for each pixel is 5×5 μm. The

substrate sits on an X table which moves only along the x-direction, and the laser head can move along Y direction. The X and Y movements work in accordance to raster-scan the desired pattern. The X table speed can be set to 0.1 m/s – 1 m/s. The laser head is also equipped with an auto focusing system with a 670 nm laser and focusing speed is 5 m/s. The maximum power of the 830 nm writing laser is 15 W.

The writing parameters were X table speed 0.2 m/s; laser power 14 W; the correspondent energy density was 6573.5 mJ/cm^2. In the initial tests, the Bi/In resists used were both 45/45 nm and 30/30 nm thick. From the results shown in Figure 8.15 and Figure 8.16 an 830 nm IR laser can expose the films. Good patterns were written on Bi/In films with this industrial thermal-imaging equipment for the first trial with resolutions reaching the level that was expected by the writing tool.

While big changes in OD were obtained, maximum transparency was not yet achieved due to the restrictions in the laser power/writing speed of the flatbed thermal-imaging tool, which was not designed for this particular application. The two important results here are first the extension of wavelength invariance for bimetallic thermal resist films to the near IR range. Secondly, the successful writing of patterns with good resolution using the multi-head laser diode concept. Experiments in this area are continuing.

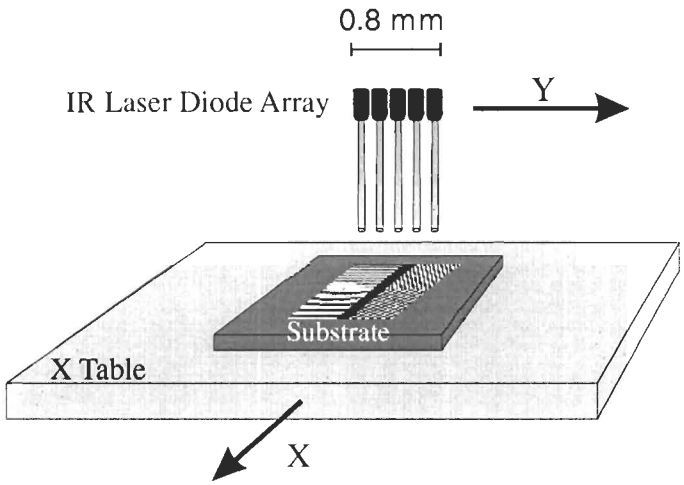

Figure 8.14 CREO Flatbed IR Thermal Imaging System for large area (LCD) masks.

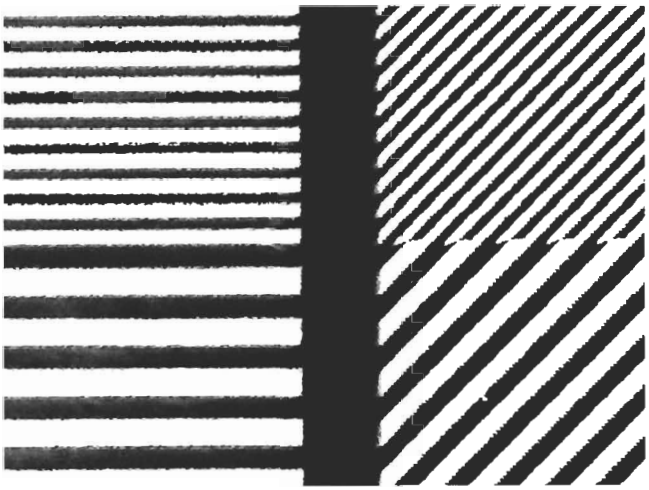

Figure 8.15 Patterns on a 30/30 nm Bi/In film raster-scanned by CREO's flatbed IR thermal-imaging system. The thickest line is 40 μm, the thinnest 15 μm. (Back-lit image)

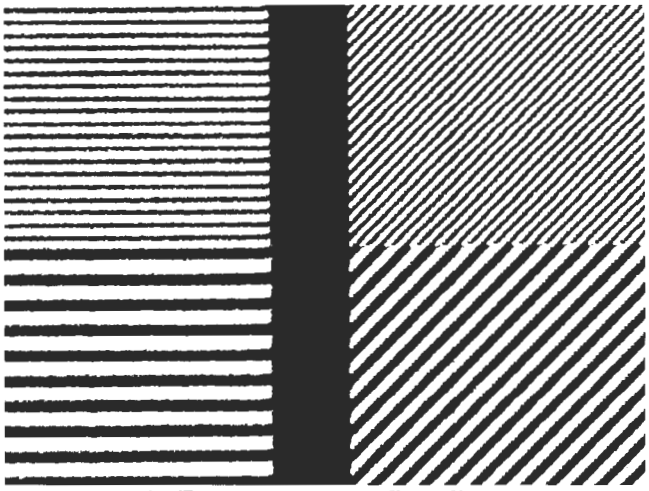

Figure 8.16 The same sample as in Figure 8.15, with finer lines: the thinnest slash lines are 8 μm wide. (Back-lit image)

8.3.4 Results of Bi/In and Sn/In Binary Photomasks

We have demonstrated Bi/In and Sn/In binary masks with the largest OD range (3 OD to 0.22 OD) for a direct-write, no develop mask for I-line applications that have so far been reported. The laser diode writing results showed the feasibility of new ways of creating masks which are not possible with standard resist and Cr mask processes. This is important, since I-line and mask aligners are still widely used. Indeed, current LCD flat panel lithography uses very

large masks of 1 – 5 μm resolution. Hence, large area bimetallic resist (200×200 cm) may have many potential applications in this area.

8.4 Creating Greyscale Photomasks with Bimetallic Thermal Resists

Three-dimensional (3D) microstructures with specified profiles are of great interest for optical, mechanical, fluidic and electronic devices. Various 3D fabrication techniques have been reported to create gradient height structures. However, many of the techniques either require costly, unconventional process equipment, or are not suitable for repeatable batch process [121-125]. On the other hand, grayscale photomasks have attracted much attention recently as they are cost-effective and easy to implement, when used together with a modified, conventional IC manufacturing photolithography and reactive ion etching. As discussed earlier in Chapter 1, grayscale photomasks can be categorized into two groups: binary (or digital) grayscale masks, and analogue grayscale masks, both of which have intrinsic problems.

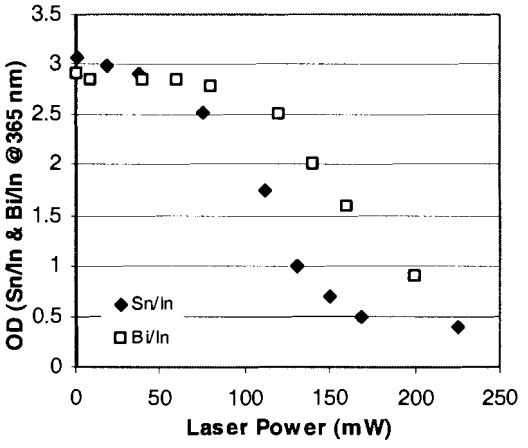

Figure 8.17 Linear plot: Bi/In and Sn/In film optical absorption versus laser power at the wavelength 365 nm. From 50 mW to 200 mW, the behaviour is nearly linear. The slope of both curves is -0.02 OD/mW.

Looking at Figure 8.5, one can note that the optical density (OD) of both Bi/In and Sn/In films drops from ~3 OD to ~0.22 OD over a range of laser power. Figure 8.17 expands the OD vs. laser power curves, showing the curves from 0 to 250 mW plotted with a linear power scale. From about 75 mW to 200 mW the absorption of the films drops nearly linearly with laser power. This indicates that by controlling the laser power one can achieve different absorption in the exposed area and hence different grayscale.

Figure 8.18 shows the setup for making grayscale masks from Bi/In and Sn/In films. It is the same as the setup mentioned in Chapter 4. However, the controller computer this time reads an 8-bit grayscale bitmap file, as shown on the left. According to the grayscale value of each pixel, the computer sends out a signal to the optical shutter which in turn controls the amount of laser light that passes through it. The shutter is fully open when the grayscale value is 0 (black in the bitmap image) and the shutter is fully closed when the value is 255 (white in the bitmap image). The computer also controls the table movement in accordance with the shutter so that the aspect ratio of the bitmap image is maintained.

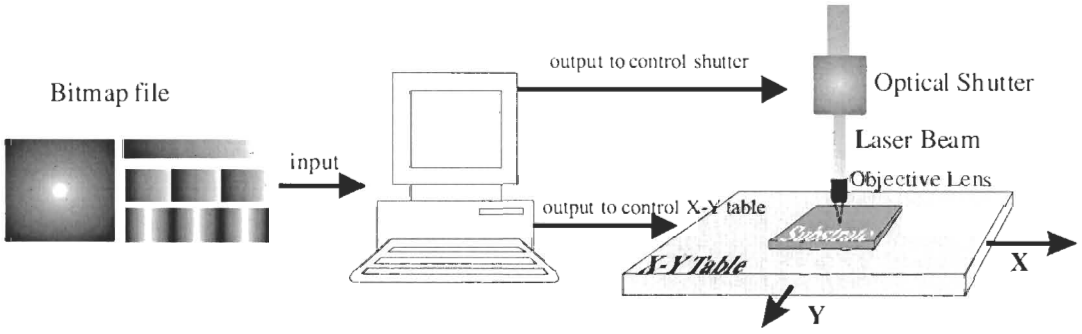

Figure 8.18 The setup for making grayscale masks from Bi/In and Sn/In films.

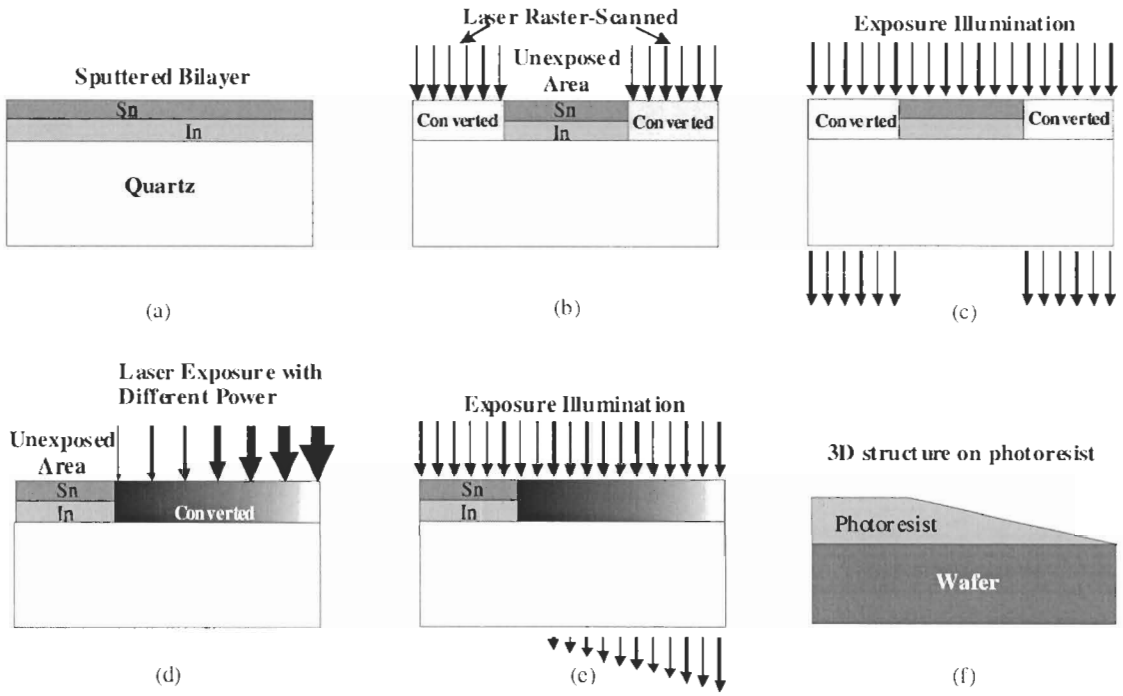

Figure 8.19 Comparison of making binary and grayscale photomasks with bimetallic thermal resists: (a) Thin film deposition on quartz or glass with a bilayer structure. (b) When making binary masks, Sn and In are converted into a new transparent material after exposure to laser with a constant power, and the unexposed area remains opaque. (c) Use as a binary photomask with uniform illumination. (d) When making grayscale masks, the bilayer film is exposed to laser with modulated power, according to the grayscale value. (e) Use as a grayscale mask with uniform illumination. More light goes through the more transparent area. (f) Photoresist is patterned with 3D structures.

Figure 8.19 illustrates the process differences between the preparation of a direct-write binary photomask and a direct-write grayscale photomask using bimetallic thermal resists as the covering material. Sn/In exhibits characteristics similar to Bi/In. It also turns out to be more transparent after laser exposure, as shown in a previous section, compared to Bi/In films. In this section, we will use both Sn/In and Bi/In as the photomask materials. The Sn/In metallic bilayer thermal resist, the same as Bi/In film, is DC-sputtered (15-150 nm) onto the substrate, as shown in (a). The Sn/In binary phase diagram has a eutectic point of 120°C at 46*at.%*. The thickness ratio of the two films is chosen to match these eutectic compositions when preparing the Sn/In thermal resist. When a binary photomask is prepared, the film is exposed to direct laser scan at a constant power level (as in (b)), and the exposed area will absorb the light energy and turn

transparent. The unexposed film will retain the bimetallic structure and remain opaque. Thus, a direct-write binary photomask can be successfully made for photomask application (as in (c)). When a grayscale photomask is manufactured, the laser power is modulated according to the grayscale value in the bitmap file (as in (d)). The optical density of the exposed film changes nearly linearly with the laser power, as depicted in Figure 8.17. Thus, the grayscale is transferred to the film. For an even illumination applied to the grayscale mask during a microlithography process, the intensity of the light that transmits the bimetallic grayscale mask will vary according to the grayscale (optical density) level (as in (e)). Hence, a modulated irradiation is deposited onto the organic photoresist. After development a 3D structure is created in the photoresist (as in (f)).

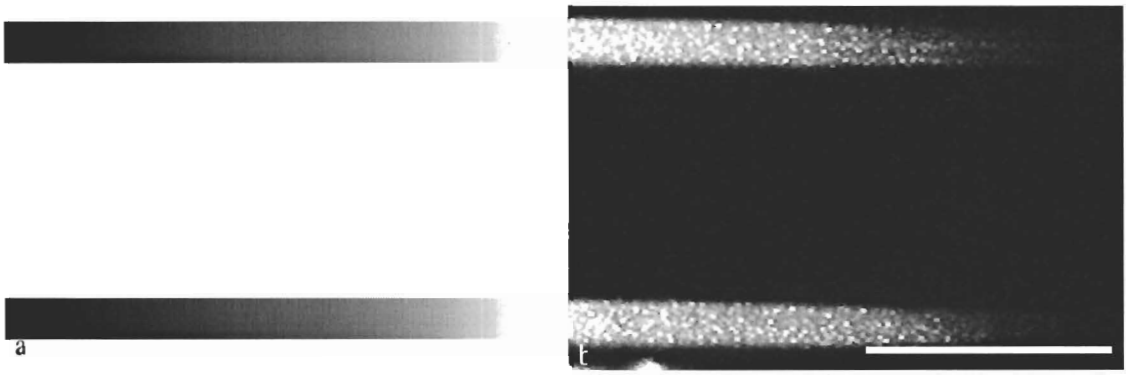

Figure 8.20 (a) An 8-bit grayscale bitmap image as the computer input file. Two grayscale bars are shown here. (b) The back-lit image of the grayscale mask made on Bi/In 40/40 nm according to the bitmap file on the left. The white bar is 200 μm long.

Figure 8.20 shows a successful example of making grayscale masks from Bi/In films. Figure 8.20 (a) is an 8-bit grayscale bitmap file showing two grayscale bars. (b) is a back-lit image of the grayscale mask made according to the bitmap file.

Figure 8.21 More complicated grayscale photo was successfully made on a Sn/In substrate: (a) the original 8-bit grayscale bitmap file; (b) the front-lit image of picture written on Sn/In film; and (c) the back-lit image.

Pictures in Figure 8.21 show a more complex example of making a grayscale image on Sn/In film. Figure (a) is an 8-bit grayscale bitmap file. It was used as an input file for the computer-controlled writing system. The parameters used to make the grayscale picture are listed as follows. Figure (b) is the front-lit and (c) is the back-lit image of the written pattern on Sn/In. Due to the shining surface the front lit image produces a positive while the backlit illumination shows the true negative grayscale image.

- Argon laser power = 155 mW, and 50 mm lens used to focus laser beam;
- Laser writing speed = 500 μm/s;
- Sn/In thickness = 15/15 nm, 5% Sn/In;
- Raster-scan Y direction increment = 5 μm;
- Picture size is 360 μm × 320 μm.

8.5 Creating 3D Structures

Creating 3D structures in substrates is the main goal for grayscale masks. But first a 3D structure has to be produced in the conventional photoresist. In order to test the grayscale

photomasks, a Quintel 4-inch mask aligner was used to expose a Shipley SPR2FX-1.3 photoresist coated on bare silicon wafers and thermally oxidized wafers. With an exposure time of 6 to 10 seconds and a 10 mW/cm^2 light intensity, 3D patterns were successfully made in the photoresist. Shown in Figure 8.22 (a) is an 8-bit grayscale bitmap image for making concave structures. Figure 8.22 (b) is the back-lit image of a mask made on Bi/In film according to (a). Figure 8.23 shows the profile of a concave structure made in the resist with the grayscale mask in Figure 8.22(b).

Figure 8.24 is a back-lit image of a grayscale mask made on Sn/In with 5 different grayscale strips. Each strip is 60 μm wide. Figure 8.25 shows a 2-step structure made on Shipley SPR2FX-1.3 resist with similar grayscale photomask. The resist is 1.1 μm thick and the substrate is SiO_2. One can notice that the Shipley photoresist patterned by the Sn/In mask is much smoother than the one patterned by the Bi/In mask, as illustrated in Figure 8.23 and Figure 8.25. This difference may be because as-deposited Sn/In film is smoother than as-deposited Bi/In film. Work needs to be done to improve the Bi/In film smoothness.

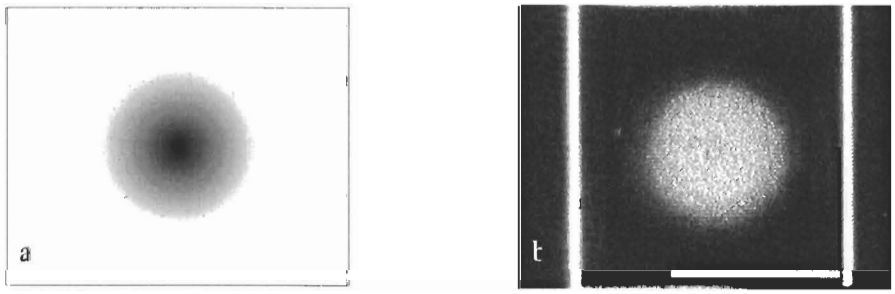

Figure 8.22 (a). An 8-bit grayscale bitmap image of the computer input file in order to make a concave structure. (b). Back-lit image of a grayscale mask made on Bi/In according to the bitmap file shown on the left. The white scale bar is 200 μm.

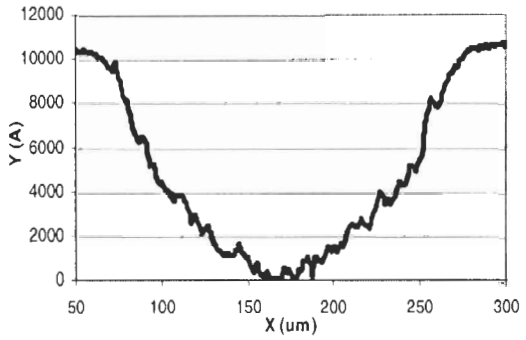

Figure 8.23 The profile of the 3D pattern made on Shipley SPR2FX-1.3 photoresist using the Bi/In grayscale mask with Quintel 4" mask aligner (I-line 365 nm Hg source).

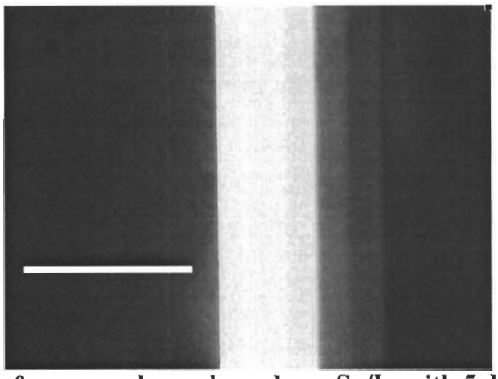

Figure 8.24 Back-lit image of a grayscale mask made on Sn/In with 5 different grayscale strips. The white scale bar is 200μm.

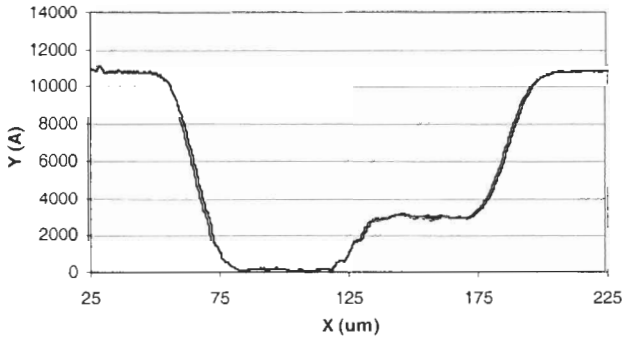

Figure 8.25 The profile of a 2-step structure made on Shipley SPR2FX-1.3 photoresist with a 3 grayscale strip photomask.

Now that a 3D structure has been successfully made in the photoresist through conventional semiconductor lithography, plasma etching process will transfer it into the substrate. We used CF_4 plasma etching to transfer the pattern in Figure 8.25 to the thermally oxidized

silicon wafer substrate. The etch recipe is: O_2 = 10sccm, CF_4 = 50 sccm, Chamber Pressure = 100mT, RF Power = 200W, etch time = 3'30", and SiO_2 etch rate = 750 Å/min. Figure 8.26 shows the profile of the 2-step structure in SiO_2 after stripping the photoresist. One can see that the same 2-step structure was successfully created. In order to transfer the exact 3D profile of the photoresist to the substrate, the plasma etch recipe should be tuned so that both the photoresist and the substrate have the same plasma etch rate.

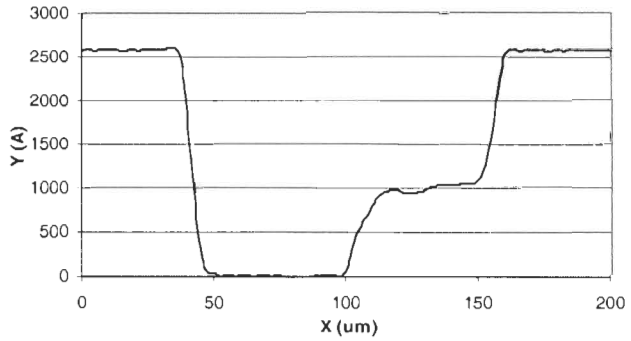

Figure 8.26 The profile of the 2-step structure etched in SiO_2 with CF_4 plasma.

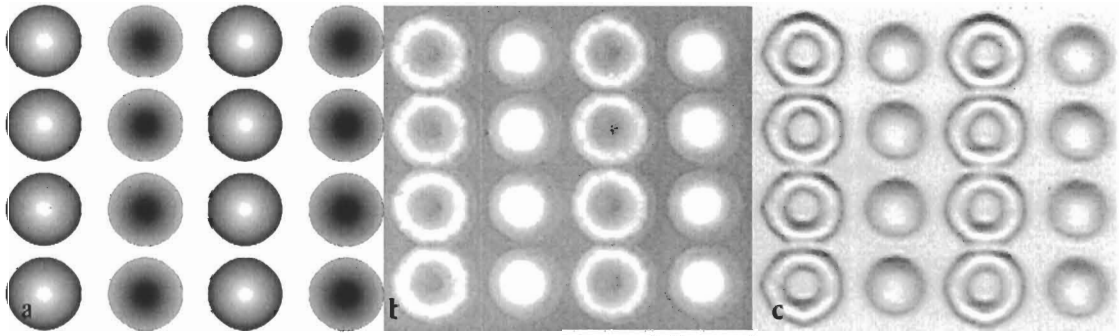

Figure 8.27 Concave and convex structures were successfully made on Shipley photoresist. (a) is the original bmp file; (b) is the back-lit image of the grayscale mask made on 5% Sn/In; and (c) is the concave and convex structures in Shipley photo resist.

The next example is the creation of an array of concave and convex structures. Figure 8.27 (a) shows an 8-bit bitmap image with several arrays of circles, each 65 μm in diameter, with grayscale changing gradually from the centre to the outside. With this bmp image, we intended to make concave and convex mirror-like structures on the photoresist. The writing parameters were the same as for writing the grayscale image in Figure 8.21. Figure 8.27 (b) is the grayscale

photomask. Shipley SPR2FX-1.3 photo resist was spin-coated on a bare silicon wafer at 2500 rpm to a thickness of about 1.3 μm. With a 6 ~ 8 seconds exposure time and a 10 mW/cm^2 light intensity, good patterns were made in the photo resist, as shown in Figure 8.27 (c).

These experiments showed clearly that we could create true grayscale images and 3D structures with the bimetallic grayscale masks.

8.6 Calibrating the Grayscale Mask Writing Process

When creating 3D structures in a photoresist using the bimetallic grayscale photomasks, a question to be answered is whether the profile we obtain in the substrate or photoresist is what we designed? Or, is the grayscale value of each point in the bitmap image translated directly into the height (profile) in the photoresist?

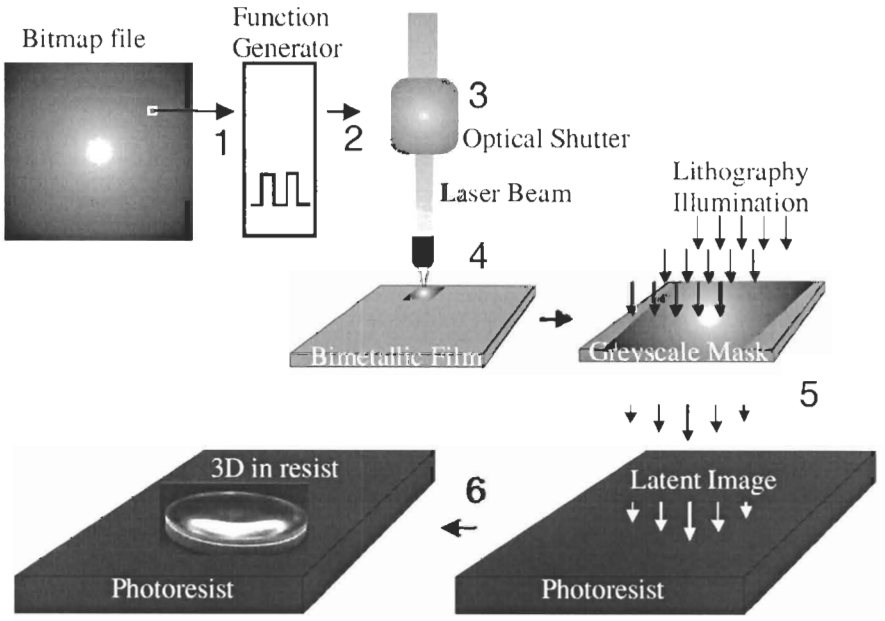

Figure 8.28 From grayscale bitmap image to 3D structure in photoresist.

To answer these questions, let us have a close look at the whole process flow from the grayscale bitmap image to obtaining a 3D structure in a photoresist, as shown in Figure 8.28. There are six process data transfer operations.

Step 1: Grayscale value reading and conversion: the control computer reads the grayscale value of each pixel, converts it into a 12-bit resolution signal and sends it to a function generator.

Step 2: Translation of digital signal into voltage signal: the function generator translates the computer digital signal into a voltage and sends it to the electro-optical shutter.

Step 3: Laser Writing: the electro-optical shutter modulates the power of the laser beam according to the voltage signal received from the function generator. The relationship between the voltage and the laser power through rate can be found out by experiments.

Step 4: Bimetallic Film Conversion: the bimetallic film responds - turning transparent to the laser irradiation. As explained earlier, there is a nearly linear relationship between the film optical density and the laser exposure power within a certain power range.

Step 5: Photoresist Exposure: the photoresist is exposed with the grayscale photomask. This step is expected to be nonlinear. When using the grayscale mask in the photolithography process, transmission is more convenient than OD.

Step 6: Photoresist development: photoresist is developed with a developer. The process of developing a latent image into a relief image is likely a nonlinear process.

The 3D structures created from the first batch of grayscale photomasks prepared without any calibration during the writing process revealed that there was significant discrepancy between the designed grayscale profile and the structure in the photoresist, as shown in Figure 8.29. The desired cone shape with straight walls was rendered into a concave structure. Thus, to create accurate 3D structures, calibrating the grayscale photomask and the whole mask-writing process is required.

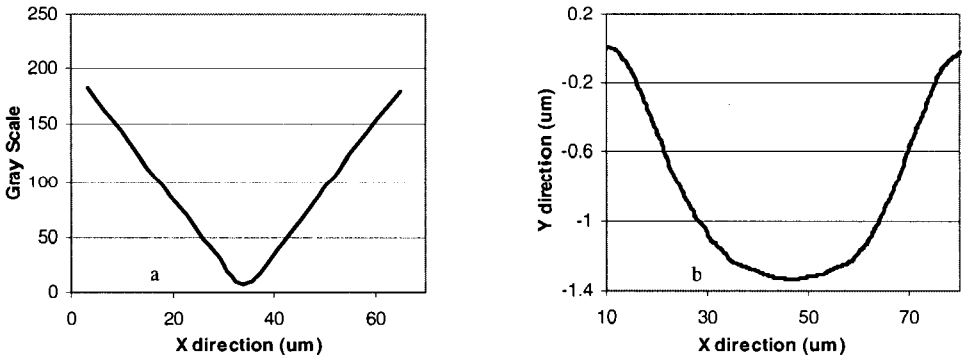

Figure 8.29 From grayscale to 3D structure. (a) Bitmap grayscale profile of a centre-dark circle in Figure 8.27 (a). (b) Profile of the concave mirror structures in the Shipley resist.

As one can see, Step 2 is the best place to carry out the calibration of the whole grayscale photomask writing process. A computer data file can be created that relates each bitmap grayscale value with a specific calibration code for the function generator. The function generator has a 12-bit resolution (2047 to –2048) and typically has its voltage ranging from 0 V to -3.9 V. Thus, a calibration code of 2047 is equivalent to 0 V for the shutter while a value of –2048 is equivalent to –3.9 V. Because the relationship between the laser power and the OD / Transmittance / Photoresist Depth is not always linear, as mentioned earlier, a 12-bit shutter voltage resolution is required to control the laser power. The 12-bit control on the laser power is needed to enable the 8-bit grayscale range to be directly related to the OD / Transmittance / Photoresist Depth. The 12-bit shutter voltage resolution also allows us to make several different calibration files for the same 8-bit bitmap. Each calibration file is unique and designed for a particular mask, laser power, table raster-scan velocity, and photolithographic process. In addition, the resulting relationship between the OD / Transmittance / Photoresist Depth and the 8-bit grayscale will change significantly depending upon the calibration file used.

In order to create a calibration file, each bitmap value must be related to a particular property to be controlled for the mask. This controlled property can be the optical density or transmittance of the mask itself, or the resulting photoresist depth after exposure and

development. Having chosen the property to be controlled, the next step is to identify the relationship between that property and either the laser exposure power or the calibration codes. Interpolation is then used to create the calibration file. Depending on the property being controlled, two different methods were used.

8.6.1 Calibrating for OD/Transmittance

In the case of creating a calibration file to control the mask's optical density or transmittance, we first had to identify the mask's optical density response to laser exposure power. This has been discussed in Section 8.2.1. In the case of controlling a mask's transmittance, using the formula $T = 10^{-OD}$, the bimetallic film transmittance can be easily calculated from the measured optical density. Figure 8.30 presents a typical OD vs. laser exposure power plot for an 80nm thick 10at.% Sn/In film with a table raster-scan velocity of 1 cm/s.

Having identified the relationship between the mask film OD and the laser exposure power, this information can then be used to determine what properties are obtainable for a particular mask. Next step is to decide how the grayscale value will relate to the OD and Transmittance of the mask. To illustrate, let's create a calibration file for a mask where the OD is linearly related to the grayscale value, as shown in Figure 8.31.

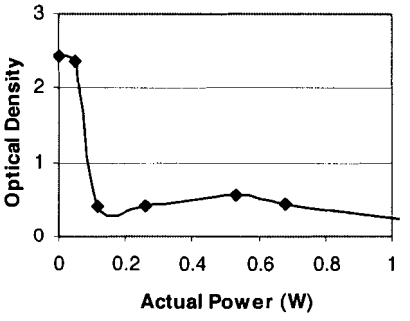

Figure 8.30 OD vs. Laser Exposure Power for an 80 nm, 10at.% Sn/In Thin Film.

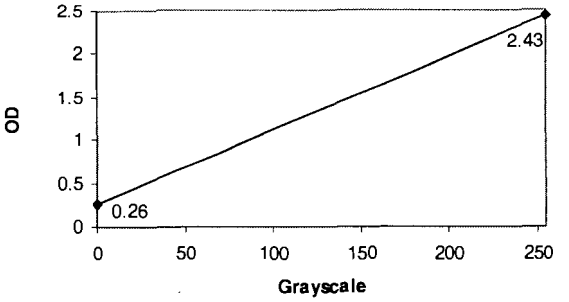

Figure 8.31 OD vs. Grayscale: Desired relationship.

In order to create the calibration file, each grayscale value must be related to the correct shutter voltage. However, the relationship between the laser exposure power and the shutter voltage must first be identified. Using a Coherent FieldMaster GS Power/Energy Analyzer with a thermal detector head, the relationship between the shutter voltage and the laser exposure power was measured for several different commanded laser powers, as shown in Figure 8.32. The commanded laser power is the commanded power output for the laser and will always be higher than the measured laser power.

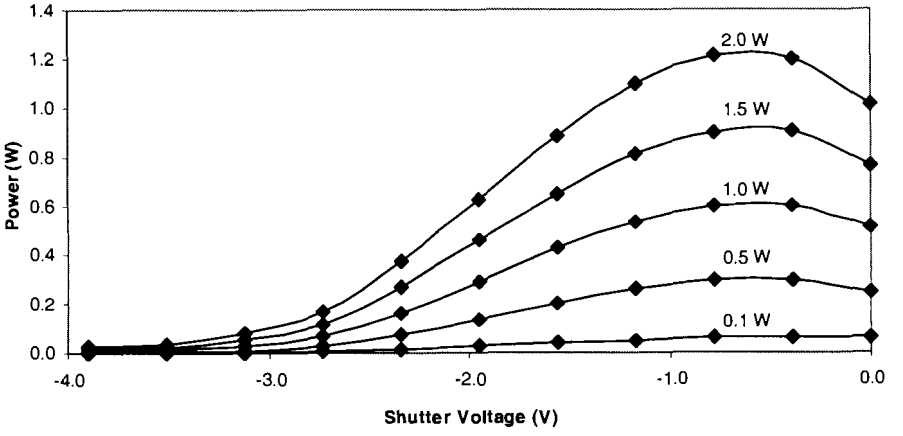

Figure 8.32 Laser Exposure Power vs. Shutter Voltage.

From the OD vs. Laser exposure power results illustrated in Figure 8.30, to achieve the minimum of 0.26 OD from Figure 8.31, the measured laser power must be at least 1 W. Based on

the Laser exposure power vs. shutter voltage results illustrated in Figure 8.32, to achieve 1 W of measured laser power while attempting to get the lowest power at –3.9 V, the commanded laser power should be set to 1.75 to 2 W.

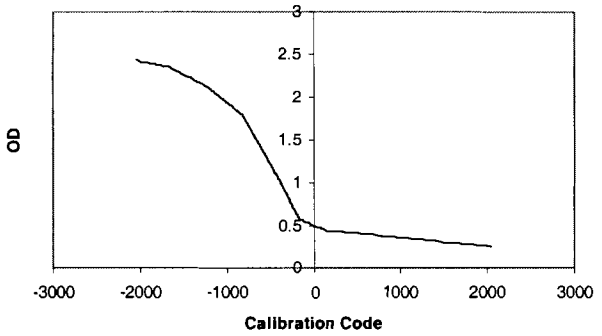

Figure 8.33 OD vs. Calibration Code.

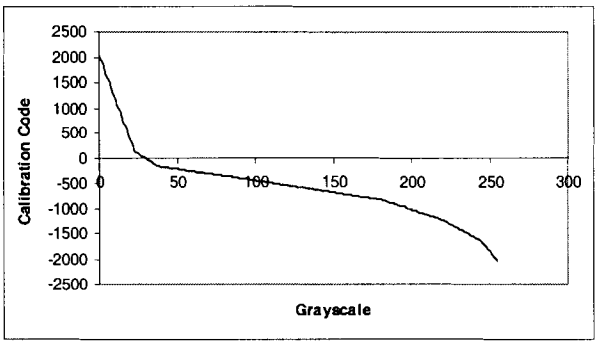

Figure 8.34 Calibration Code vs. Grayscale: Calibration File.

Using a mathematics program such as MatLab, the OD vs. Laser Exposure Power in Figure 8.30 and the 2 W Laser Exposure Power vs. Shutter Voltage curve in Figure 8.32, the relationship between the mask's optical density and the shutter voltage can be interpolated. Since the shutter voltage and calibration codes are linearly related, the shutter voltage values are easily replaced with their equivalent calibration codes to obtain the relationship shown in Figure 8.33.

Having the OD vs. Calibration Code plot, the last step is to use the desired OD vs. Grayscale curve in Figure 8.31 to interpolate the results for the calibration file shown in Figure 8.34.

8.6.2 Calibrating for Photoresist Depth

In the case of creating a calibration file to control the resulting photoresist structure, the relationship between the resulting resist depth and the laser exposure power or more specifically the calibration codes must be identified. As mentioned previously, the calibration codes have a 12-bit resolution from -2047 to 2047. If we were to follow the method described for the OD and Transmittance calibration, we would need to create several square patterns on a test mask at a fixed laser power. We would then need to expose regular photoresist with the mask and measure the depth of each square on the developed photoresist. However, using a profilometer and the 16-step v-groove shown in Figure 8.35, we can obtain more data in less time.

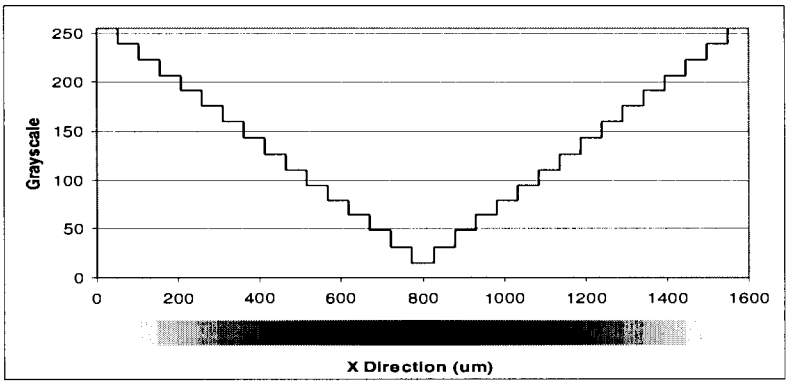

Figure 8.35 16-step V-groove.

First, in order to use the 8-bit grayscale 16-step v-groove bitmap, we need to break-up the 4096 calibration codes into chunks of 256 (8-bit in length). Once broken up, each calibration code is mapped to a single bitmap grayscale value using a test calibration file. This process results in the creation of 16 test calibration files shown in Table 8.2.

Table 8.2 Test Calibration Files: 16 files break-up and map the 12-bit range of the Calibration Codes into the 8-bit grayscale value range of the bitmaps.

Calibration File #1	
Bitmap Grayscale	Calibration Code
0	2047
1	2046
...	...
255	1792

Calibration File #2	
Bitmap Grayscale	Calibration Code
0	1791
1	1790
...	...
255	1536

...

Calibration File #16	
Bitmap Grayscale	Calibration Code
0	-1792
1	-1793
...	...
255	-2047

Choosing a particular commanded laser power, each calibration file is used to write a 16-bit v-groove pattern, resulting in 16 patterns on one mask. After using the mask to expose a photoresist, a profilometer is used to measure the resulting structure for each v-groove pattern. From the measurements, depth values are obtained for 256 (16 patterns by 16-steps) of the calibration codes. Thus, from this method of using the profilometer and the 16 v-groove patterns, we obtained the same results as 256 squares using the OD and Transmittance method. We could have used a 256-step v-groove to get even more data; however, identifying the depth for a specific step becomes much more difficult. Having measured the resulting depth for each step in the v-groove structures, a relationship between the calibration codes and the resulting depth in the photoresist is thus obtained.

The last step is to use the desired Depth vs. Grayscale and the Depth vs. Calibration Code curves to interpolate the final calibration file. Furthermore, knowing the Laser Exposure Power vs. Shutter Voltage shown in Figure 8.32 and the linear relationship between the shutter voltage and the calibration codes, we can also interpolate results relating the photoresist depth to the shutter voltage and laser exposure power.

8.6.3 V-Groove Grayscale Structure

V-groove grayscale structures have been successfully created using Clariant AZ-5214E photoresists. The grayscale photomask is a 80 nm, 5*at.*% Sn/In thin film and raster-scanned using 0.8 W laser power with a 50 mm lens, a scanning speed of 2000 μm/s, and an X-direction step size (laser spot size) of 10 μm. The photoresist is spun onto a RCA-1 cleaned wafer at 4000 rpm for 45 seconds. The expected thickness of the photoresist is ~1 μm. The wafer is soft-baked at 100°C for 60 seconds before exposure. The photoresist is exposed under an I-line mask aligner at 12 mJ/cm^2 for 4 seconds, and developed in Clariant AZ-327 MIF solution. Hard-bake is carried

out at 120°C for 10 minutes after development. Profilometry measurements using the Tencor AlphaStep 500 profilometer were then carried out. Several sizes of a V-shaped groove have been created using the 8-bit gradient bitmap file shown in Figure 8.36.

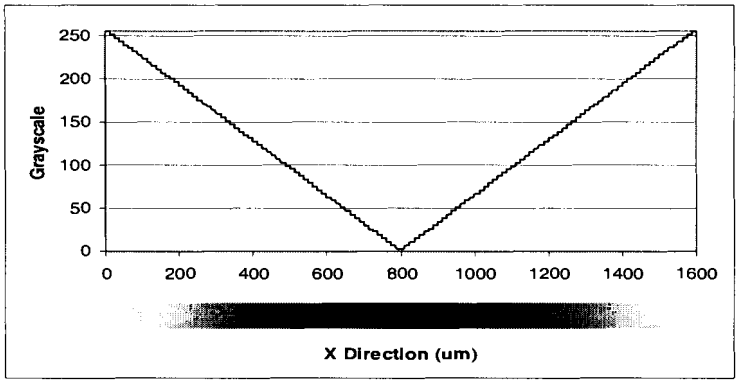

Figure 8.36 256-step V-groove.

The darkest spot of the bitmap image is at the centre and corresponds to the maximum power intensity through the electro-optical shutter. Both the leftmost and rightmost edges contained the brightest spots of the bitmap image, and they correspond to the minimum power intensity through the electro-optical shutter. There are total of 511 pixels created horizontally with the edges starting with a grayscale level of 255 (white) and decreasing by 1 grayscale level for each pixel until the two sides converge at the grayscale level of 0 (black) at the centre. With the appropriate calibration file, the resulting structure will be a v-groove. Figure 8.37 illustrates the profile of a V-groove structure created in Clariant AZ-5214E photoresist. The straight line indicates the desired photoresist profile from the Sn/In grayscale photomask. Figure 8.38 shows the depth of V-groove structure in the photoresist compared to the grayscale curve. Note that with current research, it is not clear how much of the roughness in Figure 8.37 is due to the mask, and how much from the variations in the organic photoresist itself. Recent tests with another type of thicker resist did show much smoother sidewalls in the resist. Nevertheless, it appears these are the best grayscale direct-write mask in terms of OD range and simplicity of fabrication of any reported in the literature.

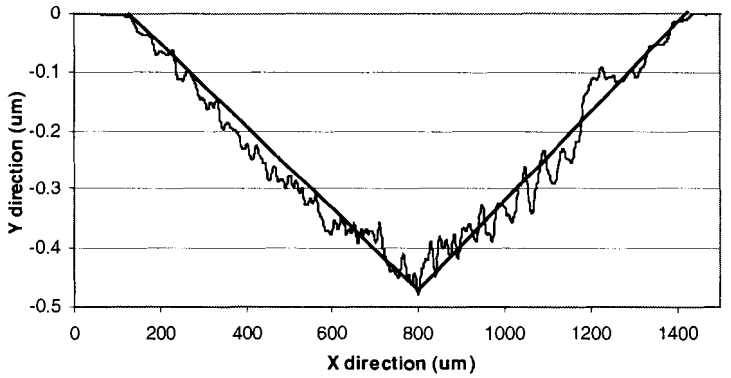

Figure 8.37 Profilometry of the V-groove structure in the photoresist.

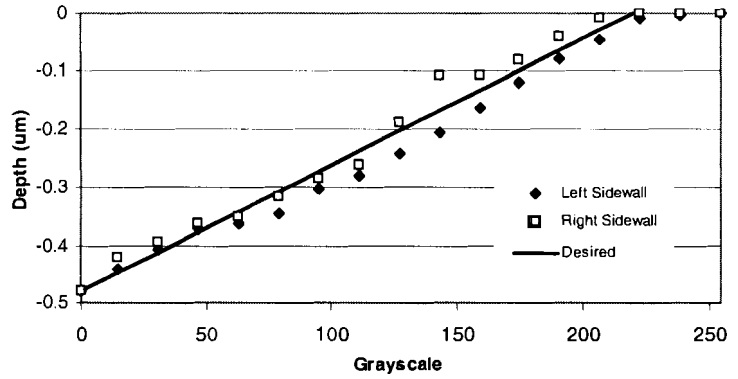

Figure 8.38 Photoresist Depth of the V-groove structure vs. Grayscale Curve.

8.7 Making Solar Cells with a Bimetallic Thermal Resist Process

Making surface-textured silicon solar cells is an example of combining micromachining and microfabrication processes, as it involves silicon bulk etching, thin film deposition, and diffusion. J. Zhao, et al, used silicon anisotropic etching to create reversed pyramids on a silicon surface to enhance the light absorption [103]. Here we make solar cells with a Bi/In process so as to demonstrate its compatibility with conventional silicon processes. It is also an example of combining Bi/In thermal resist application and direct-write photomask application into one device making process. As shown in Figure 8.39, parallel V-grooves were first created by Bi/In patterning and masking process on a (100) n-type 100 mm silicon wafer, followed by standard cleaning and HF dip. Boron diffusion was then carried out after wet oxidation and lithography.

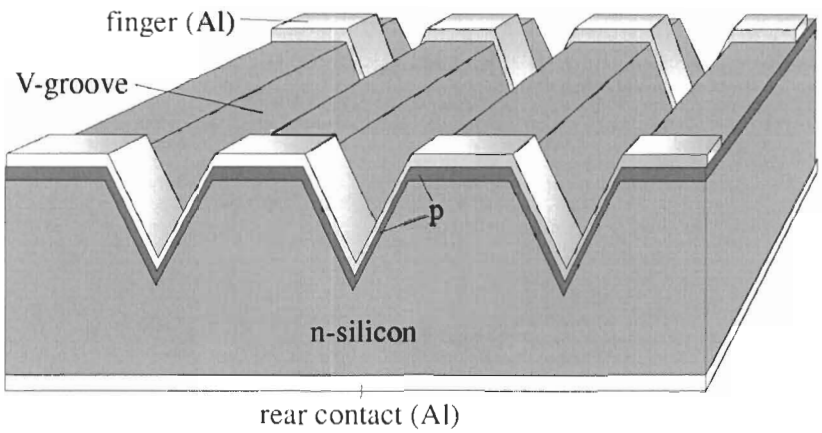

Figure 8.39 V-groove surface textured solar cells are made on a (100) n-type silicon wafer by using Bi/In as the patterning and masking material.

Bi/In was used as the direct-write photomask for the lithography of the oxidation and metallization layers. The masks were created under the same conditions as those in Figure 8.7. Al was deposited on both sides of the wafer as metal contacts. In order to pattern the Al layer, a direct-write dark-field Bi/In mask was used together with a negative photoresist (AZ-5214). The process is as following:

1. Spin-coat 1.4 μm thick AZ-5214 onto the wafer;
2. Soft bake at 120°C for 60 seconds;
3. Exposure Bi/In mask for 30 seconds at P365nm = 10 mW/cm2;
4. Hard bake at 120°C for 45 seconds;
5. Flood exposure (without mask) for 10 seconds at P365nm = 10 mW/cm2;
6. Developed in MIF for 30 seconds.

Table 8.3 Process flow for making V-grooved solar cells with Bi/In as the patterning & masking layer.

No.	Process Name	Purpose	Operation Detail
1	Starting Wafer	Process begins	(100) n-type, Resistivity = 5-15 Ωcm, Thickness = 525 ± 50 μm,
2	Bi/In Deposition	Bi/In as patterning and masking layer for building grooves	120 nm / 120 nm of Bi/In was deposited,
3	Laser Exposure	Make parallel strip patterns on Bi/In	Laser power = 0.8W, 50× objective lens, beam waist = 1 μm, scanning speed = 1cm/sec, lateral scanning step = 0.4 μm, mask width = 6.4 μm, V-groove width = 8 μm,
4	Bi/In Development	Generate groove etch masking layer	Developed in $HCl:H_2O_2:H_2O$=1:1:48 for 18 minutes,
5	Anisotropic Etch	Create anisotropic v-groove with alkaline-based solution	Etched in TMAH @85°C for 30 minutes, mechanical agitation,
6	Pre-oxidation Cleaning	Important cleaning before oxidation to remove metallic and organic contaminants	Processed in the following order 1. Piranha $H_2SO_4:H_2O_2$ = 4:1 @ 100°C for 15 minutes 2. HF dip $HF:H_2O$ = 10:1 for 10 minutes 3. RCA1 $NH_4OH:H_2O_2:H_2O$ = 1:1:5 @ 80°C for 10 minutes 4. HF dip $HF:H_2O$ = 10:1 for 3 minutes 5. RCA2 $HCl:H_2O_2:H_2O$ = 1:1:6 @ 80°C for 20 minutes
7	Oxidation / Litho	This oxidation is for device isolation and diffusion masking	40 minutes of wet-oxidation @ 1100°C to get 0.52 μm of oxide / open diffusion windows,
8	Boron Diffusion Boron Drive-in	Doping	Boron diffusion @ 1000°C for 40 minutes, Drive-in @ 1000°C for 40 minutes,
9	Metallization	Connection	Open contact and deposit 500 nm Al.

Table 8.3 is the detail of the process flow. Figure 8.40 shows the V-groove surface texture of the solar cell. Measurement results show that the 1.5 cm^2 V-grooved solar cell gives 202 mV open circuit output voltage and 8 mA short circuit current under normal florescent tube light at 25°C, which is a fully functioning solar cell. In order to provide a reference to compare with, normal solar cells were also produced on the other half of the same silicon wafer without being patterned with Bi/In films. Measurement results show that the solar cells behave the same in either process.

What is important here is that both Bi/In resist processes and Bi/In mask processes were demonstrated in the same structure and produced devices that work the same as those with other processes.

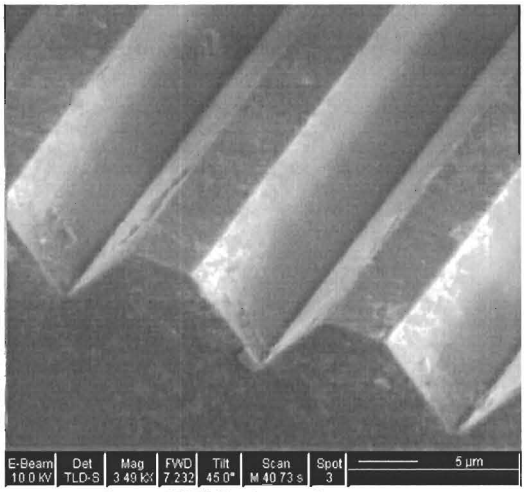

Figure 8.40 Solar cell V-groove surface. (SEM picture)

8.8 Conclusions

Optical properties of bimetallic Bi/In and Sn/In films were studied. It was found that 40/40 nm heat-treated Bi/In and Sn/In could have ~3 OD before laser exposure and 0.26 OD and 0.22 OD, respectively, after high power laser exposure at the I-line wavelength, which are desired for making direct-write binary photomask. Wavelength invariance was proven one more time by writing photomask patterns on Bi/In films with IR (830 nm) wavelength diode laser and a 514 nm argon laser. The transition slope of the OD vs. laser power curve from opaque to transparent allows us to create analogue grayscale photomasks by modulating the laser power. Both binary and grayscale photomasks were successfully produced. Tests showed that a 12-bit resolution function generator is necessary to create an 8-bit grayscale resolution in the photomask and the photoresist. 3D structures were also successfully generated in organic photoresists and various substrates. Effort was made to try to find the relationship between grayscale value in a bitmap

image and the profile of the pattern in the photoresist. Surface-textured solar cells were manufactured successfully with Bi/In as the patterning and etch masking layer and as a direct-write photomask material, exemplifying that the bimetallic thermal resist process is a working process that it is compatible with conventional silicon processes. The next chapter investigates a thermal model of the bimetallic thermal resist exposure process.

Chapter 9
Thermal Modelling of Bimetallic Thermal Resists

9.1 Introduction

Unlike organic photoresists which are transformed by photochemical reactions, thermal resists such as Bi/In and Sn/In are converted by heat that is absorbed from a laser beam. A heat conduction model will help understand how the heat is distributed in the resist film and the substrate, how the substrate affects the exposure, what the conversion temperature of the film is, what the resist profile will be after development, and also the thermal resist exposure behaviour when exposed to long (1 msec) and short laser pulses (<10 nsec). In this chapter, an effort will be made to establish a heat transfer model to describe the laser exposure process. ANSYS 5.7®, a piece of powerful finite element analysis software, will be used as the numerical tool to calculate the temperature in the thermal resist film and in the substrate. Experimental results will be compared with simulation results to verify the model. The influence of various laser exposure parameters (such as laser power density, energy density and pulse duration) on thermal resist heating and the resolution limit of laser imaging will be investigated. The laser-induced interaction at the interface between a thermal resist and a substrate will be discussed. This will help us understand the difference between a thermal resist exposure, a conventional laser-assisted diffusion and a laser-induced annealing after dopant implantation.

9.2 Heat Transfer Model

9.2.1 A Complex Process

When the laser beam hits the thermal resist film, reflection, transmission and absorption occur. Our Airy summation optical model, discussed in Chapter 3, shows that for a 15/15 nm Bi/In film deposited on a glass slide, 35% of the laser light energy is absorbed at 514 nm wavelength, ~60% is reflected and ~5% transmitted through the film. Most of the absorbed energy is transformed into heat and the temperature of the exposed area goes up. According to the Bi/In phase diagram (refer to Chapter 2), a 50*at.*% film melts at a eutectic temperature of 110°C. Thus, when the thermal resist film is heated to or above this threshold, a phase change will occur, and the chemical and physical properties will change. Prokhorov [126] pointed out that two effects should be considered: the modification of the optical properties of the irradiated area, and the additional heat release due to exothermic reactions when metals are exposed to laser exposures in chemically active environments, such as oxygen and air. XRD and RBS (Rutherford Back Scattering) analyses (See Chapter 6) show that large amounts of oxygen was found in the Bi/In film which was laser-exposed in air. Thus, oxidation is occurring under our laser exposure conditions.

Let's first do an estimation of the additional heat release due to the exothermic metal oxidation. The Standard Molar Enthalpy (heat) of Formation $\Delta_f H^o(kJ/mol)$ [58] for In_2O_3 and Bi_2O_3 are -925.8 kJ/mol and -573.9 kJ/mol, respectively. Assuming a 50/50 nm Bi/In film, a laser beam spot size of 1.6 μm in diameter, that the metals under the area exposed to the laser will be fully oxidized to form stoichiometric metal oxides (In_2O_3 and Bi_2O_3), and the total volume of the exposed material being 1×10^{-13} cm^3 for In and Bi, we can calculate that the total heat released from the oxidation of Bi and In is ~ 1×10^{-9} J (Refer to Appendix B for the density and mole weight of Bi and In). For comparison, the lowest power density (using argon CW laser) needed to

heat a 50/50 nm Bi/In film on glass substrate to about 298.5°C is 4×10^{-9} W/m^2 (simulation and experimental results indicate this is the laser conversion temperature, refer to Section 9.3). With a typical exposure time of 1.6×10^{-4} second and a 48.7% film absorption percentage, the heat induced by an argon laser exposure is ~ 1×10^{-6} J. Thus, the heat released by oxidation is negligible. However, when the laser exposure duration is in the nanosecond range, the heat induced by laser exposure and oxidation becomes comparable. For example, a 4 ns, 7mJ/cm^2 Nd:YAG laser pulse on a 1.6 μm spot only transfers ~1×10^{-10} J energy, which is even lower than that created from oxidation process.

9.2.2 ANSYS Model

Our purpose of setting up a thermal model is to find out the conversion temperature of the thermal resist film, or the highest temperature the film reached during the exposure process. It is known that the film gets much more transparent after laser exposure, and the absorption should drop significantly. In order to simplify the model, we will not take into account of the heat generated by metal oxidation, and the optical property changes of the metal films. This enables us to consider the heat transfer process as a conventional transient, nonlinear thermal process (phase change energies will be taken into account).

The heat diffusion equation for an incompressible and non-convectional media is [127]:

$$\nabla \cdot k\nabla T + \dot{q} = \rho c_p \frac{\partial T}{\partial t} \tag{9.1}$$

where k is the thermal conductivity, ρ is the density (g/cm^3), c_p is the specific heat (J/m^3·K), T is temperature, t is time, and $\dot{q}$ is the heat generation rate per unit volume.

Assuming that the thermal resist and its substrate are homogeneous, and isotropic, and that there is no mass transport of heat, we have the following equation:

$$k\nabla^2 T + \dot{q} = \rho c_p \frac{\partial T}{\partial t} \tag{9.2}$$

or in a more familiar form:

$$\frac{\partial}{\partial x}\left(k\frac{\partial T}{\partial x}\right)+\frac{\partial}{\partial y}\left(k\frac{\partial T}{\partial y}\right)+\frac{\partial}{\partial z}\left(k\frac{\partial T}{\partial z}\right)+\dot{q} = \rho c_p \frac{\partial T}{\partial t} \tag{9.3}$$

It is easier to analyze the heat transfer in the laser exposure system in cylindrical coordinates, as shown in Figure 9.1. The following is the differential equation for heat conduction for a homogeneous, isotropic solid:

$$\frac{1}{r}\frac{\partial}{\partial r}\left(kr\frac{\partial T}{\partial r}\right)+\frac{1}{r^2}\frac{\partial}{\partial \varphi}\left(k\frac{\partial T}{\partial \varphi}\right)+\frac{\partial}{\partial z}\left(k\frac{\partial T}{\partial z}\right)+\dot{q} = \rho c_p \frac{\partial T}{\partial t} \tag{9.4}$$

When a laser beam shines on the film, the heat flow is in cylindrical symmetry, thus not dependent on φ. This allows us to simplify the heat-conduction differential equation as follows, and will convert the 3D problem into a much simpler 2D model.

$$\frac{1}{r}\frac{\partial}{\partial r}\left(kr\frac{\partial T}{\partial r}\right)+\frac{\partial}{\partial z}\left(k\frac{\partial T}{\partial z}\right)+\dot{q} = \rho c_p \frac{\partial T}{\partial t} \tag{9.5}$$

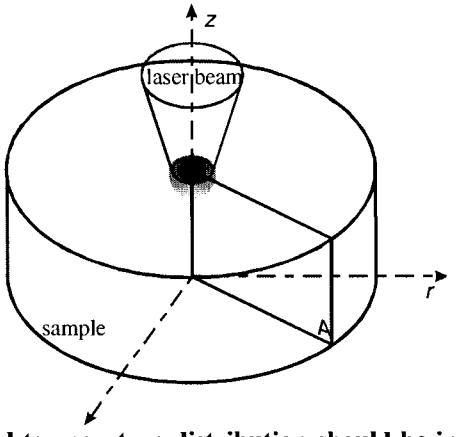

Figure 9.1 The heat flow and temperature distribution should be in cylindrical symmetry when a laser beam shines on a sample.

There are many kinds of finite element analysis software on the market. ANSYS 5.7 was chosen to build the thermal model and to do finite element calculation, as it has a type of axisymetric, harmonic 8-node thermal solid element, which uses 2D models to solve axis-symmetric problem, such as Equation (9.5). The modelling ends up just taking one slice of plane along the radius direction from the cylinder in Figure 9.1. The thermal model was set up with following conditions:

- Both the thermal resists and the substrate are homogeneous and isotropic;
- No convection is considered as exposure duration is 10^{-4} to 10^{-9} second;
- Chemical or other thermodynamic reactions are not taken into account;
- Optical property changes are not taken into account;
- The thermal conductivity of Bi/In and the substrate are constant;
- The laser source is a uniform circular shaped source.

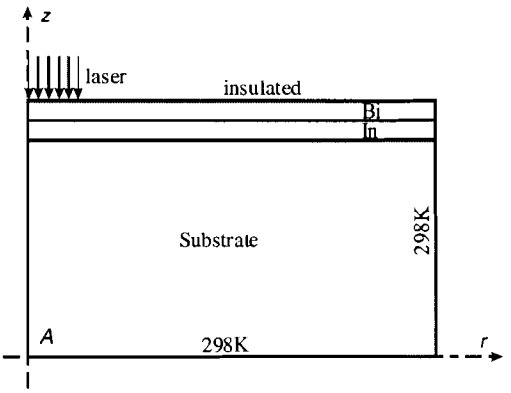

Figure 9.2 Simplified 2D model using ANSYS 5.7 axisymetric harmonic 8-node thermal solid element. It is a slice of area along the radius direction shown in Figure 9.1.

As shown in Figure 9.2, the laser beam was applied on top of the two metal layers, at the axis. The laser beam size was from 1.6 μm to 10 μm in diameter after a 2.4 mm Argon laser was focused by a 50× objective lens or a 50 mm focal length converging lens. Ideally, the dimension

of the substrate and the film in the model should be the actual sample size. But this will generate too many elements for ANSYS5.7 to handle (our academic version of ANSYS57 can handle, at most, 128000 elements), as the substrate (e.g. a glass slide) thickness is 10^4 times thicker than that of the metal films. It was also noticed that the exposure time was short and that the heating only happened in a small local area. Thus, to further simplify the model, a 20 by 12 μm substrate was used. This reduced the calculation time. Analysis showed that if the dimension was doubled to 40 by 24 μm (this simulation time increased by 10 times), the final result changed by <1%. Figure 9.3 shows a typical meshing result of a 20×12 μm thermal model, with 50/50 nm Bi/In on a glass substrate; laser beam is assumed to be 1.6 μm in diameter.

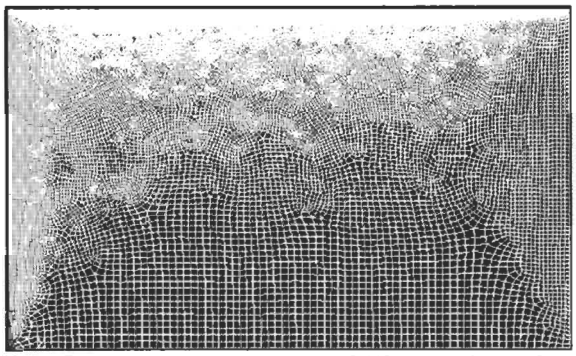

Figure 9.3 50/50 nm Bi/In on glass substrate: ANSYS meshing of a 20×12μm Axisymmetric Harmonic ANSYS model. The laser beam is 1.6 μm in diameter.

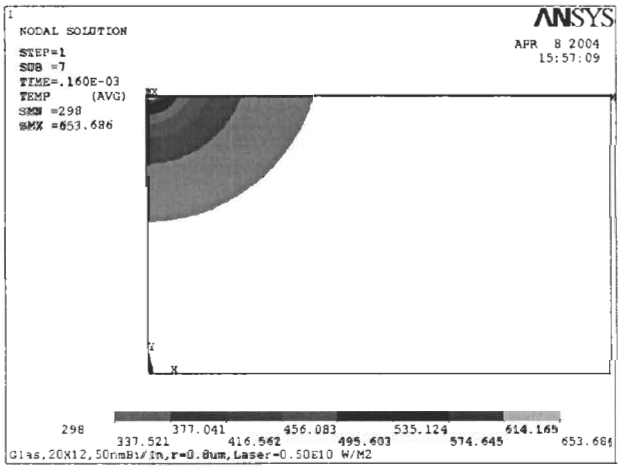

Figure 9.4 ANSYS simulation result showing a temperature profile, with an argon laser beam of typical power (0.5×10^{10} W/m^2, or 10 mW focused down to 1.6 μm spot in diameter) applied at the upper left corner shown in Figure 9.2.

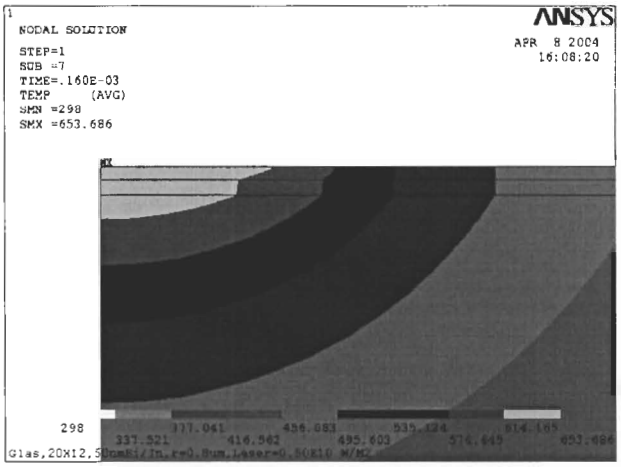

Figure 9.5 An enlarged plot of the laser beam irradiated area in the thermal model shown in Figure 9.4. Temperature at the centre of the top of the bilayer is 653.7K, and the bottom is 638.1K.

Figure 9.4 shows the temperature profile after the 50/50 nm Bi/In on glass sample was exposed to the argon laser power: 0.5×10^{10} W/m^2, or a 10 mW focused to a 1.6 μm spot in diameter. The exposure time was 1.6×10^{-4} second. The hottest spot was at the top of the Bi/In, i.e. the upper-leftmost corner, which was 653.7K, and the bottom of the Bi/In was 638.1K. Figure 9.5 is the enlarged temperature profile plot of the laser beam exposed area, showing the temperature profile in the Bi/In film.

9.3 Simulation Result I: Bi/In Resist Conversion Temperature

Since it is difficult to accurately measure the temperature of the thin film during the laser exposure, without disturbing the temperature distribution, we cannot compare the simulated temperature with the real temperature on the film at this moment. It was experimentally observed that with the same 50/50nm Bi/In film, the optimum exposure power changed when different kinds of substrates were used. Much higher power was needed to expose Bi/In directly on silicon wafers than on glass substrates as silicon has over 100 times more thermal conductivity than does glass (see Appendix B). The power required for samples with 800Å and 4000Å wet oxide on the silicon wafers fell in between.

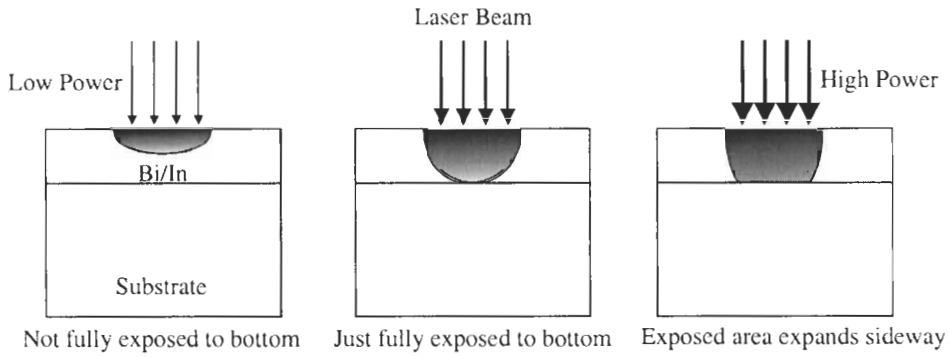

Figure 9.6 The laser exposure power affects the formation of latent and relief images.

Before setting up a critical exposure point as the reference for thermal model simulation, let us have a look at the exposure and development process, as shown in Figure 9.6. If a low power is used to expose the film, the film is not fully exposed to the bottom. Thus, the conversion is not complete, and no relief image will form on the substrate after development since dilute RCA2 will strip away unconverted film. Profilometry tests will not be able to detect a pattern profile. If a high laser power is used, the exposed area is fully converted along the film normal direction. The profilometry of the developed image will show the full height of the converted film. If the threshold laser power is applied, so that the film is just fully converted to the bottom of the film, as shown in Figure 9.6, profilometry will start to show signs of a developed pattern profile. This laser power is the critical laser power to fully expose the film. This power varies with the thickness of the resist film and the type of substrate. However, it is reasonable to assume that the conversion temperature at the bottom of the film under the critical laser power should be a constant which is not dependent on the film thickness or the type of the substrate, and it is the minimum conversion temperature of the thermal resist. If a whole series of exposure is done in single line scan style using different power, and followed by dilute RCA2 development and profilometry test across the lines, one can easily locate the critical laser power.

In order to find the minimum laser power needed to fully expose a 50/50 nm Bi/In film on each substrate, a series of power (Argon laser 0.1 mW ~ 1000 mW, focused by 50× objective

lens, with w_f = 1.6 μm) was used to expose the film. The laser exposure time was 1.6×10^{-4} second. The film was then developed in dilute RCA2 solution and followed by a profilometry test to measure the thickness of the developed film. Figure 9.7 shows the profilometry result from this laser power test on glass substrate. From right to left, the laser exposure power increased gradually from 0.1 mW to 200 mW, and each line had a 180 μm spacing. The 10^{th} line from the left is the first to show the sign of a relief image profile. It was exposed with an 8 mW argon laser beam focused by a 50× objective lens. The corresponding power density is 4×10^{9} W/m^2. Figure 9.8 illustrates the laser power versus thickness of developed Bi/In film on the four different substrates. It is seen that the thickness of the developed Bi/In increases rapidly with the laser power and saturates after the film is fully exposed. Figure 9.9 shows the minimum laser power that is needed to fully expose 50/50 nm Bi/In on four different substrates. With the thermal model, one can easily calculate the temperature at the bottom of the resist film under these minimum laser powers, and it should give similar temperature results for all four substrates.

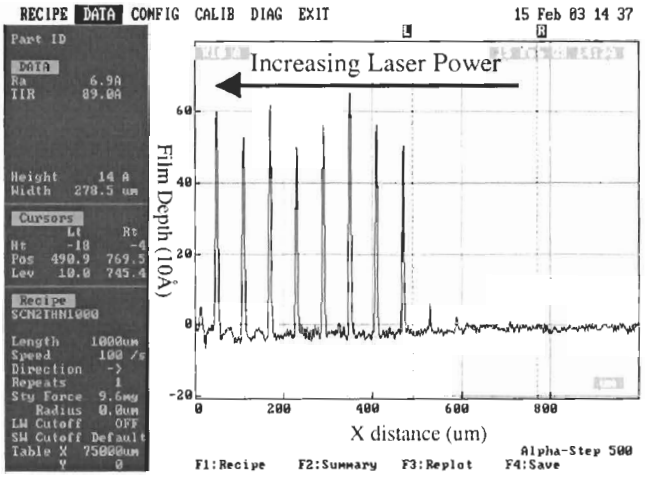

Figure 9.7 Profilometry test across developed, scanned lines exposed with different laser power.

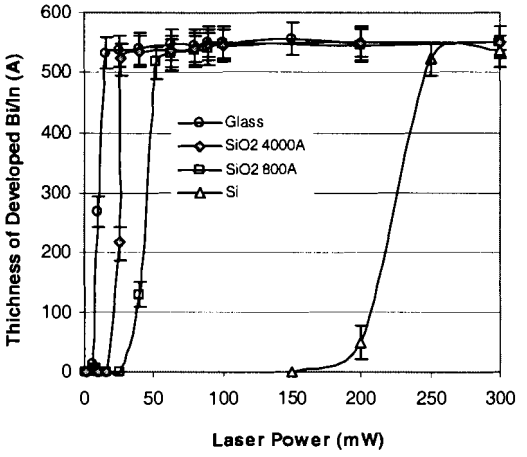

Figure 9.8 Experiment results: laser power vs. thickness of developed Bi/In film.

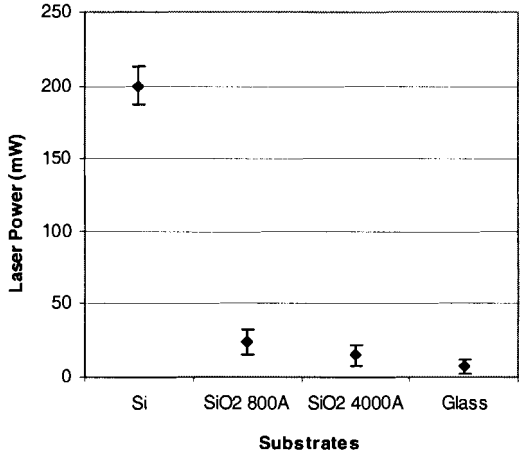

Figure 9.9 Minimum laser power used to fully expose the Bi/In films on four substrates. Data were extracted from Figure 9.8.

Table 9.1 shows the simulation results and the experimental conditions: the film thickness, the laser used to expose the film, the minimum laser power needed to fully expose the film, the laser absorption by Bi/In and the exposure time, that were used to expose the Bi/In on the four different substrates. The simulated temperatures at the bottom of the resist films, which were just fully exposed on all four substrates, fell into a very small range (268.3°C – 315.3°C). This indicates that the model works for the Bi/In thermal resist exposure. Taking the experimental errors into account, we take the average of the four calculated results as the nominal Bi/In laser conversion temperature, which is 287 ± 23°C. This should be considered as a high estimation of

the resist conversion temperature, as the optical property changes during the laser exposure process and other energy losses were not taken into account.

Table 9.1 Experiment conditions and simulation results.

Substrate	Si	Si-SiO_2 800A	Si-SiO_2 4000A	Glass
Bi/In thickness (nm)	50 / 50	50 / 50	50 / 50	50 / 50
Laser wavelength (nm)	514	514	514	514
Laser beam size (μm)	1.6	1.6	1.6	1.6
Laser Power for Full Exposure (W/m^2)	9.95×10^{10}	1.35×10^{10}	0.78×10^{10}	0.40×10^{10}
Laser Absorption by Bi/In Film	48.7%	48.7%	48.7%	48.7%
Exposure Time (second)	1.60×10^{-4}	1.60×10^{-4}	1.60×10^{-4}	1.60×10^{-4}
Simulated Temperature (°C)	268	268	315	298

9.4 Simulation Result II: Influence of Pulse Duration on Exposure

One of the most important performance parameters of a thermal resist is its sensitivity. As noted in Chapter 7, Bi/In has a sensitivity of 6~7 mJ/cm^2 with 4 ns pulses at the Nd:YAG 266nm. Thermal modelling shows that a 15/15 nm Bi/In film can be heated to 340.1°C and 322.2°C at the top and the bottom of the resist film, respectively, with a single 4 ns, ~6 mJ/cm^2 266 nm Nd:YAG short pulse (laser spot size 1.6 μm in diameter, on a glass substrate). It was assumed that Bi/In absorbs 60% of the laser energy. If the same 15/15 nm Bi/In sample is exposed to X-ray (1 nm), a single 16 mJ/cm^2 1 ns pulse can heat it up to 329.8°C and 308.5°C at the top and the bottom of the resist film, assuming a 12% absorption percentage.

Figure 9.10 shows the simulation result of power density versus exposure time that can fully expose a 15/15 nm Bi/In film. It is assumed that the film is fully exposed when heated to over 287.7°C at the bottom of the resist. It is expected that the exposure time increases as the power density drops. However, there is a minimum power density that is required to expose the 15/15 nm Bi/In film which is 8.1×10^4 W/cm^2. Below this level no matter how long the resist is exposed to a light source, it will not be converted. That is why sunlight (0.1 W/cm^2), mask aligner (0.01 W/cm^2) or lamp light cannot expose Bi/In resist. Based on the same simulation result,

Figure 9.11 is the exposure time versus exposure level in mJ/cm^2, showing that the exposure density increases with exposure time. Note that these results agree with the sensitivity of short 4 nsec pulse experimental results of 7 mJ/cm^2.

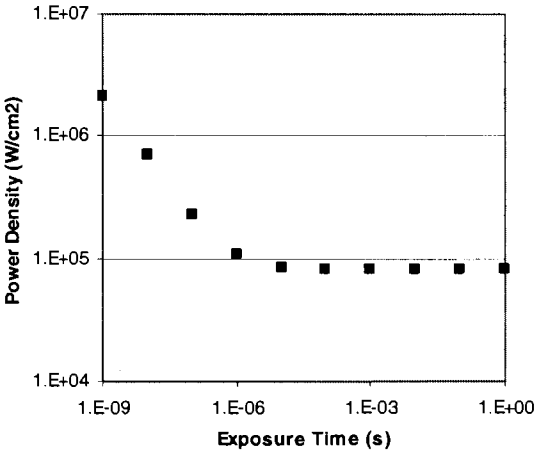

Figure 9.10 Power density vs. exposure time for a 15/15 nm Bi/In.

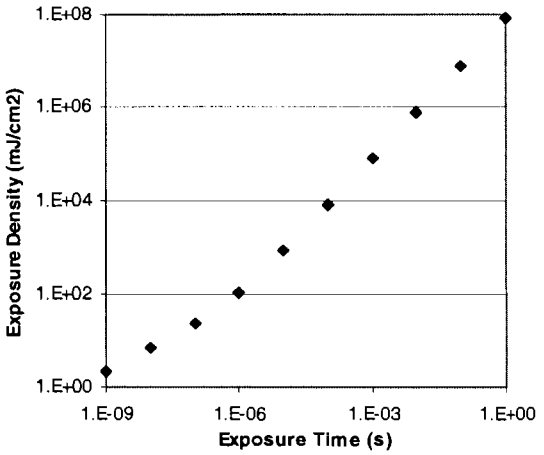

Figure 9.11 Exposure level vs. exposure time for a 15/15 Bi/In.

Due to thermal conduction, laser exposures on thermal resists cause unwanted heating in areas surrounding the exposed features. In order to investigate the influence of laser pulse duration on the lateral heat conduction, simulations were carried out on a 15/15 nm Bi/In film which was exposed with a 266 nm laser beam. Two circular spots were exposed on the film: one is $r = 0.8$ μm and the other $r = 0.05$ μm. Different powers were used to make 0.1 ns to 10 μs

exposures. Figure 9.12 shows the simulation results for a half of the 0.8 μm spot. The X axis is the distance from the spot centre. It shows that with a 1 ns pulse the lateral heat dissipation is the least. The temperature drops quickly within a short range (~0.09 μm). With longer pulse duration one can see that the lateral thermal flow increases and the exposed area gets smaller. Figure 9.13 is the temperature profile of the 0.05 μm spot, showing that even shorter pulses are needed in order to minimize the lateral thermal flow. What is unknown as of yet is how narrow a temperature window is the threshold for the reaction. That would determine how sharp the exposed edge is.

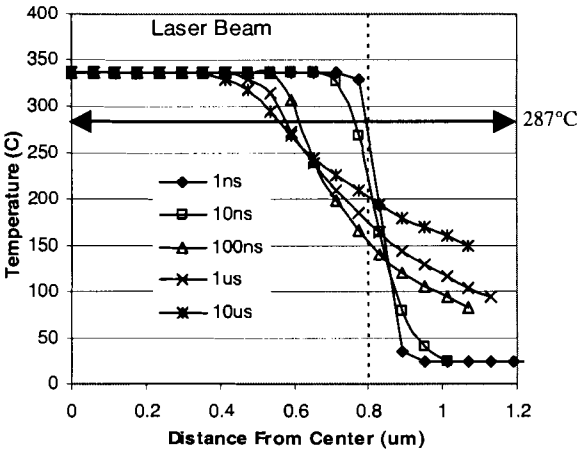

Figure 9.12 Simulated temperature profile of an r = 0.8 μm circular spot, with different pulse durations.

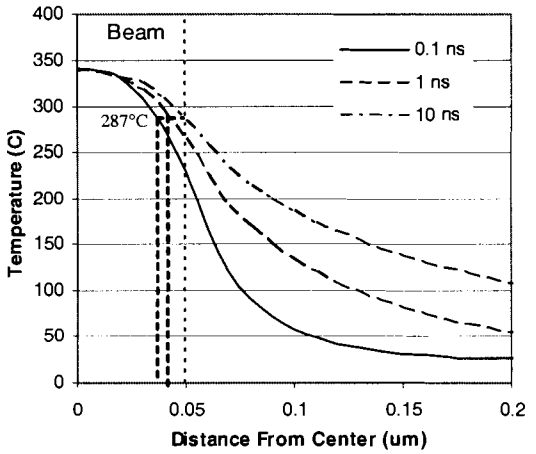

Figure 9.13 Simulated temperature profile of an r = 0.05 μm circular spot, with different pulse durations.

If we take 287°C as the exposure threshold, the 0.1 ns exposure in Figure 9.13 will yield an exposed spot with $r = 0.0375$ μm, 1 ns pulse will give a spot of $r = 0.043$ μm and 10 ns pulse will create a spot of $r = 0.05$ μm. This shows that the feature size will grow with increasing laser pulse duration. The difference caused by a pulse duration variation can be predicted by thermal modelling and can be minimized by feature size compensation. Since this change is small, only 12 nm for a 100 times change in pulse duration, it will be easy to compensate for. It is common in semiconductor industry that a pattern on a photomask is modified to achieve the desired feature size and shape in the photoresist depending on the behaviour of the resist for a given exposure system.

For a few nano-second pulses, an important fact is that the heat contributed by the oxidation of the bimetallic film, as noted previously, is even larger than the energy absorbed from the laser exposure. A 4 ns, 7 mJ/cm^2 pulse transfers 1×10^{-10} J onto a 1.6 μm diameter area, while the oxidation in the same area on a 15/15 nm film creates 1×10^{-9} J. This could be a significant factor in the resolution of the system.

9.5 Summary

A thermal model has been established using the ANSYS5.7 finite element analysis tool. A special axisymetric harmonic element was chosen so that the original 3D model was simplified to a 2D model, which should be more accurate, and more efficient. Simulation results show that the minimum Bi/In laser conversion temperature is 287°C, which is consistent with experimental results. It was found that the laser pulse duration has a great influence on thermal resist exposure. This is due to the heat dissipation along the lateral directions during the laser exposure. Model calculation show that the shorter the pulse duration, the less lateral heat flow, and thus the better

the pattern profile, and the less the exposure energy needed. The next chapter discusses the compatibility of bimetallic thermal resist with silicon processing.

Chapter 10
Evaluation of Substrate Contamination

10.1 Introduction

During the exposure process, bimetallic thermal resists convert into some new materials under raised temperature. Previous chapters discussed the material transformation that happened in the thermal resist films. How about the substrates? Does the metal diffuse into the functional layer? Are there any contamination issues associated with the bimetallic resist exposure process? In this chapter, we will investigate these problems.

Laser irradiation on dopant and metal-coated silicon substrates has been studied for decades [128-135]. Fairfield [128] reported in 1968 that silicon diodes were successfully made by laser irradiation on a phosphorous-coated silicon (111) wafer, using a ruby pulsed laser source (694.3 nm, 5 msec duration). With 10^{-2} J/cm^2 of energy density, the exposed surface area was melted and a *p-n* junction formed to depth of up to 1 μm. Since then many works have been reported on using laser irradiation for doping and annealing or diffusion after implantation. Harper [129] used focused Nd:YAG pulse laser (1.06 μm wavelength, 0.2-3.0 mJ, pulse duration 240 – 500 nsec) to make a *p-n* junction by locally alloying a vacuum-evaporated Al film into *n*-type Si. Kachurin, et al, used a high-power CW argon laser (514 nm, 3-15 W, spot size from 100 to 200 μm in diameter, exposure duration 50 msec) to raster-scan arsenic implantation-doped silicon for annealing purpose [130]. Broutet, et al, did laser-induced diffusion tests on Bi and In. Using a 20 ns pulse ruby laser, he found a dopant distribution profile with a surface disordered layer. A cellular structure was observed in the surface of the treated sample, which was similar to laser-annealed, ion-implanted silicon [131].

These reports show that it is important to investigate the possibility of diffusion or contamination of thermal resist metals into substrates during laser exposure. This subject will be discussed using the experimental data and simulation results.

10.2 Literature Study

Material analysis of laser exposed Bi/In and Sn/In films indicates that this process is an oxidation and that the oxides generated are similar to ITO films. Before moving to the evaluation of contamination by bimetallic thin film processes, we can study some previous research work on In, Bi, Sn and ITO contaminations to silicon substrates.

It was first noticed that the diffusion coefficients of In, Bi and Sn in silicon are quite low, as compared to B and P and many other metals (Table 10.1, calculated from [136-140]). With the exposure conversion threshold around 300°C, none of the thermal resist metals can diffuse into silicon substrate significantly.

Table 10.1 Diffusion coefficients of In, Bi and Sn, compared with B and P.

Diffusion coefficient	In	Bi	Sn	B	P
D (cm^2/s) at 300°C	1×10^{-32}	1×10^{-33}	2×10^{-31}	1×10^{-30}	1×10^{-30}
D (cm^2/s) at 700°C	5×10^{-19}	1×10^{-20}	1×10^{-19}	3×10^{-18}	3×10^{-18}

We can do a standard diffusion calculation to see how far indium can diffuse into a silicon substrate, using the following constant source diffusion for approximation [140], where $N(x,t)$ is the impurity concentration at time t and a distance x from the surface, N_0 is the surface concentration of the impurity, D is the diffusion coefficient of the impurity.

$$N(x,t) = N_0 erfc\left(\frac{x}{2\sqrt{Dt}}\right) \tag{10.1}$$

If an indium film is exposed to an argon laser for 10^{-4} second, and assuming the laser conversion temperature is 300°C, we can estimate the indium diffusion distance as:

$$x = 2\sqrt{Dt} = 2\times\sqrt{10^{-32}\times 10^{-4}} = 2\times 10^{-18} cm = 2\times 10^{-14}\,\mu m$$

This actually means indium cannot diffuse into silicon within such a short period of time at this temperature. A much smaller value is expected if we use an Nd:YAG pulse.

Yang, et al [138], studied the interaction of indium on a silicon surface in a Si molecular beam epitaxy system. Indium was evaporated onto Si at 20°C for 2 min (7 nm thick), and then was annealed at 700°C for 50 min under ultra-high vacuum (5×10^{-10} Torr). It was found that both interstitial and substitutional inter-diffusion occurred at the silicon-indium interface. However, due to its low diffusion coefficient (Table 10.1) at 700°C, diffused indium atoms were restricted to the vicinity of the interface. At the end of the annealing, instead of diffusing into the silicon substrate, indium atoms desorbed from the substrate surface due to its high vapour pressure. Similar results were also reported by H. Li, et al [139]. The authors found that over 90% of indium out-diffusion happens within 1 sec of soak time in the RTA (rapid thermal annealing) process (in N_2 atmosphere) after indium implantation. The indium tends to segregate to the oxide/Si interface or evaporate to the ambient.

H. Ryu, et al [141], proposed using In and Sn as a diffusion barrier layer in a polycrystalline Si, thin film transistor, LCD to reduce the contact resistance. 5 nm thick In and Sn films were thermally evaporated between the ITO film and poly-silicon layer. The samples were then annealed at either 200°C or 250°C in a N_2 atmosphere. It was found that, as a barrier layer, Sn was very stable and no significant diffusion into silicon was noticed. Diffusion of indium into silicon after 5 minutes of annealing at 250°C and a drastic contact resistance increase were noticed. Interestingly, no further resistance increase appeared after annealing longer than 5 minutes. The diffusion depth was not revealed and the oxygen concentration was not reported at

the interface after annealing. It is suspected that this indium diffusion could be caused by indium oxidation at the interface.

Diffusion analysis of bismuth in silicon (111) [142] showed that bismuth has one of the lowest diffusion rates in silicon. The solid solubility limit is only $3\text{-}20\times10^{15}$ cm^{-3}. in the temperature range of 1190 – 1394°C. Hence, it would be much lower at 300°C.

In addition, ITO / silicon solar cell systems have been extensively studied. Goodnick, et al [143], studied the thermal degradation of 400 nm thick ITO / *p*-silicon solar cells. No degradation in cell performance was observed after annealing at 200°C for 2000 hours. No significant changes of I-V curve, open circuit voltage or short circuit current were noticed after 1 hour annealing at 255°C. No open circuit voltage or short circuit current changes were observed, and only a slight degradation of I-V characteristics was noticed after 1 hour of annealing at 420°C. Further analysis indicated that the cause of the degradation was a growth of additional SiO_2 at the ITO/silicon interface which limited the tunnelling current. And the growth of SiO_2 was not caused by the decomposition of ITO, but rather by oxygen diffusion through the ITO film.

Ow-Yang, et al [144], investigated the stability of the interface between an indium tin oxide thin film and a silicon substrate. Capacitors were fabricated in the ITO on *p*-type Si. The structures were then annealed in ultra-high pure N_2 for 30 min at 1058K to obtain a gate oxide of ~5 nm. A typical C-V curve was obtained by scanning the gate bias from -5 to +5 V. The authors concluded from the C-V test results that no significant diffusion of In into the substrate had occurred.

While most papers reporting that no diffusion of In, Bi or Sn into silicon substrates was noticed within the 600 – 1000 K temperature range, and that ITO films are stable at the ITO/silicon interfaces, significant doping was indeed observed for laser exposures of ultra-high

power. Fogarassy, et al [145], claimed that solar cells were made by laser irradiation of 20 – 500Å thick Bi or In film deposited on Si (111) in vacuum. A shallow (<4000 Å) but heavily-doped *P-N* junction was formed. It is important to note that a 20 ns, 1.5 – 2 J/cm^2 high energy ruby laser pulse (1 cm in diameter spot size) was needed to create this junction. This equals to 1×10^{12} W/m^2 laser power, which is ten times higher than what we used to expose Bi/In on silicon substrate using argon laser, and 280 times more than the Nd:YAG exposure values. More importantly, the laser exposure of this solar cell laser doping was carried out in a vacuum environment. No oxidation was involved.

10.3 Experimental Evaluation

10.3.1 Auger Test on Resist Stripped Sample

When developed Bi/In on silicon substrates demonstrated resistance to the 85°C alkaline-based anisotropic etching, it was first suspected that Bi, In or both diffused into the silicon substrates after the laser scanning and that the metal-diffused area formed a high-doping concentration etch stop layer. It has been reported that the etch rate of a high boron concentration (higher than 10^{20}cm^{-3}) area would be 1000 times lower than that of undoped or lightly-doped silicon [146,147]. An Auger surface analysis was carried out to study the surface concentration of bismuth and indium in the silicon substrate after the laser exposure. The sample was exposed with 0.32W Argon laser, focused with a 50× objective lens, and was then cleaned with Piranha (H_2SO_4:H_2O_2=4:1) at 100°C for 15 min, RCA1 (NH_4OH:H_2O_2:H_2O=1:1:5) at 80°C for 10 min, followed by a 25% HF dip for 15 min, and RCA2 (HCl:H_2O_2:H_2O=1:1:6) at 80°C for 10 min. Figure 10.1 shows the Auger result. It is noted that no typical Bi (102 eV) or In (404, 410 eV) could be detected. The same sample was also etched in KOH at 85°C for 2 minutes, and no etched pattern was found. This result implies that a high doping concentration is not the etch-stop

mechanism. The other possible mechanism is that the etching resistance comes from the Bi and In oxides. It is observed that the Bi/In is soft before laser exposure and gets much harder afterwards. Although this result does not disapprove the possibility of Bi or In diffusing into silicon, at least one knows that the doping concentration should be much lower than 10^{20} cm^{-3}, if diffusion did happen. It should be pointed out that the sensitivity of conventional Auger Electron Spectrometry is $0.1 at.\%$, which is $5\times10^{19} cm^{-3}$ when silicon is the substrate.

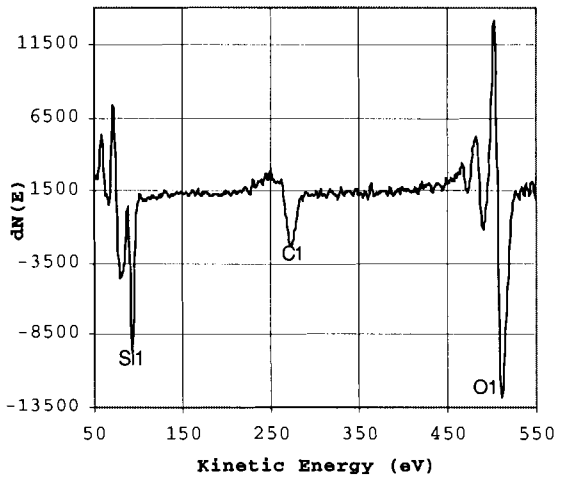

Figure 10.1 Auger surface analysis result. The sample first exposed with argon laser was then cleaned with Piranha, RCA1, HF dip and RCA2 before the test. Bi and In were not detectable.

10.3.2 Solar Cell Test

In Chapter 8, surface-textured silicon solar cells were successfully manufactured by using Bi/In patterning and masking process on a (100) n-type 100 mm silicon wafer. Test results showed that the solar cells worked as well as normally processed solar cells. This is a positive sign that Bi/In bimetallic thermal resist is not deadly poisonous to silicon devices.

10.3.3 Oxidation Process

Structural analysis shows that laser exposure of bimetallic thermal resists is an oxidation process and that the oxidation happens in a very short period of time (~ 4 ns, refer to Chapter 5 and 6). This indicates that most of the metals are oxidized even before they could diffuse significantly into the silicon substrate. Once oxidized, the metals (within the structure similar to ITO) become very stable and no diffusion should be noticed under normal conditions.

10.4 Thermal Model Simulation

It was noticed that, for laser-induced diffusion or annealing purposes, silicon substrates were heated to a high temperature, even to over the melting point, when exposed to lasers of high energy. Fairfield et al. observed surface areas with the appearance of having flowed slightly during localized melting [128]. Harper et al. reported that melt puddles formed after laser exposure, and found that undamaged melt puddles resulted in a comparatively good rectifying junction [129]. However, a melting appearance was not observed on any of the exposed Bi/In and Sn/In thermal resist samples. Figure 10.2 shows the surface condition after high power argon laser exposure and thermal resist strip. This sample was part of the V-groove solar cell. The dark areas were silicon V grooves that were anisotropically etched. The white areas had been exposed to argon laser, and then were Bi/In mask-protected so that no anisotropic etching could occur. No melting or flowing of surface was observed in the white area. Nevertheless, the key point here is the actual surface temperature for laser annealing and for bimetallic thermal resist laser exposure. It is easy to use the heat transfer model to calculate the actual silicon surface temperature according to the laser power, exposure duration and exposed area reported by the authors.

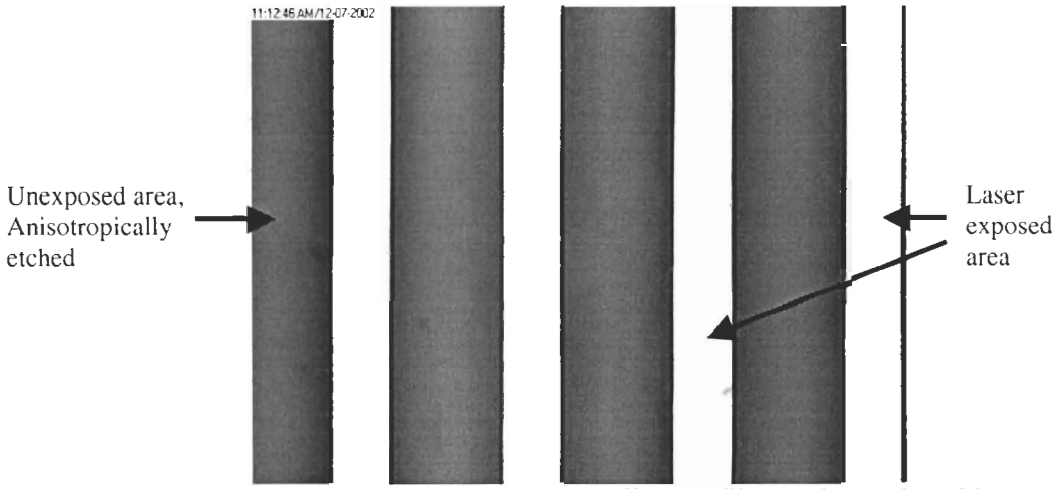

Figure 10.2 Silicon surface after Bi/In was stripped off when silicon anisotropic etching was done.

Using Harper's parameters: laser power density = 5.09×10^{10} W/m^2, exposure duration = 500 ns and spot size 25 – 50 μm in diameter, we get the maximum surface temperature is 1578°C, noting that silicon melting point is 1410.2°C. Kachurin used lasers of different spot sizes to raster scan the sample. With a 15 W argon laser and a 30 μm spot size, a 50 msec exposure can bring the surface temperature up to 1996°C. With a larger spot of 200 μm, the sample surface will still be heated up to 670.3°C, which is 382.6°C higher than the bimetallic film conversion temperature. This temperature is also the surface temperature of the substrate. These results show that the laser annealing or diffusion reported by others happens at a much higher temperature than required for the bimetallic thermal resist exposure.

10.5 A Hypothesis about Indium Contamination

Although the substrate surface temperature is below 300°C under normal thermal resist operation, it still could reach the Si melting point, if high laser power is used. The Auger analysis result shown in Figure 6.21 demonstrates that In was found in the silicon substrate, and that oxygen was present too, indicating that the inter-diffused layer between In and silicon could be a

mixture of In_2O_3 and SiO_2. This assumption is in agreement with some test results that when silicon samples were exposed with higher laser power, the exposed Bi/In could not be stripped off using RCA2 cleaning alone, and HF dip was needed (refer to Chapter 5). This means that silicon oxide had formed.

10.6 Summary

This short chapter is intended to bring attention to possible metallic contaminations in the substrates after laser exposure of bimetallic films. The successful manufacturing of solar cells points out that Bi or In was not poisonous to silicon device. Bi and In were not detectable by AES on samples that were laser exposed first and then cleaned and stripped with standard cleaning. Thermal model computation shows that laser annealing and diffusion on silicon substrates happen at a much higher temperature than thermal resist exposure does. It is suspected that when thermal resist coated samples were exposed to laser of higher power, oxidation and diffusion happened at the same time. Indium existed in silicon in the form of an oxide. The next chapter is the last of the whole thesis: the conclusions and future work.

Chapter 11
Conclusions and Future Work

11.1 Thesis Conclusions

Conventional organic photoresists have started to see many problems as the wavelength of the microlithography laser source moves towards 157 nm and below. The current chromium/quartz binary photomask is subject to ESD, and is becoming too costly due to its complicated and long preparation process. In order to address these issues, this research proposed bimetallic thermal resists as an alternative.

This thesis explored the concept of a bimetallic thermal resist. A sensitive metallic thermal resist should have three properties: a low melting point, optically absorbing and low thermal conductivity. This work showed eutectic alloying is a good choice to further bring down the melting point. The metallic resist should be developable and resistant to wet and / or dry etching. Three metals: Bi, In and Sn were identified as the best metals suitable for thermal resist applications. Bi/In and Sn/In are promising candidates for bimetallic thermal resists with lower eutectic points than each of the single metal.

An optical model based on Airy summation was used to calculate the reflected, transmitted and absorbed light intensity when a laser beam shines on the bilayer thermal resist. With this model, one can calculate the RAT curves vs. film thickness and light wavelength, and compare results of different film structures. It was found that a 2-layer Bi/In film has higher absorption percentage than other film structures, indicating that bilayer metallic thermal resists are more sensitive than single layer co-sputtered Bi-In films. Simulation results show that the

thermal resist film absorption changes slowly as the light wavelength gets shorter, showing the new property of wavelength invariance.

11.2 Thermal Resist Applications

Bimetallic thermal resists were DC- or RF-sputtered onto different substrates. Film density was over 80% of bulk material for Bi and Sn and ~ 74% for In. The thermal resist exposure system used in this thesis research included three major equipment: the X-Y-Z table, the laser sources and the control computer. 8-bit bitmap file or command script text files can be taken as an input for pattern writing. Argon (514 nm) and Nd:YAG (533 nm, 266 nm and 213 nm) lasers were used as the laser sources.

This research developed processes by which bimetallic thermal resists can be exposed, developed and stripped, just like conventional organic photoresists. For short duration exposures the Bi/In thermal resist had a sensitivity of 7 mJ/cm^2. This makes it the first inorganic thermal resist to have organic resist level sensitivity. It was experimentally and theoretically proved that bimetallic thermal resists have a unique feature: wavelength invariance. A wide range of laser sources (argon 514 nm to Nd:YAG 5^{th} HG 213 nm) and different exposure methods (proximity and projection exposures) were successfully utilized to convert the bimetallic thermal resists. Writing patterns on Bi/In with the CREO IR (830 nm) wavelength diode laser array proved once again the wavelength invariance property of bimetallic thermal resists. Exposed bimetallic thermal resist can be developed using one of the two acid solutions which remove the unexposed material with good selectivity, making the resist negative tone. For resist rework, both exposed and unexposed films can be stripped away with an RCA2 clean. As-deposited bimetallic films are stable under ordinary conditions. Exposed bimetallic films are still conductive, which could be employed for some new applications, such as a patterned seed layer for metal electroplating.

Materials analysis showed that Bi and In form Bi-In alloy in the as-deposited resist film. XRD, TEM, Auger, XPS and RBS confirmed that laser exposure is an oxidation process. Study on the conversion of Sn/In films indicated that laser exposed Sn/In films have identical material structures as ITO films do. A new interesting material, indium bismuth oxide (IBO), was created, and is a promising transparent and conductive oxide film.

These inorganic resists proved to have new features in etch resistance. No conventional organic photoresists, no common protective etch masks (such as Si_2O_3 and Si_3N_4) can withstand both wet anisotropic Si etching and dry etching. However, Bi/In and its class of bimetallic thermal resists are the first reported resists that are resistant to both alkaline-based silicon anisotropic etching and fluorine-based plasma etching. Exposed Bi/In film has a slower etch rate in KOH, EDP and TMAH than SiO_2. For plasma dry etching, Bi/In erodes 1000 times slower in $CF_4/CHF_3/O_2$ plasma than regular organic resists. Special structures, not possibly made by other methods, can be created with the combination of anisotropic etching and plasma etching. It was demonstrated that Bi/In thermal resist is a potential material for direct-write electroplating and for transparent electrodes, like ITO, as it is conductive even after development.

11.3 Direct-write Photomask Applications

One of the most important applications of bimetallic thermal resists, making direct-write binary and grayscale photomasks, is based on the optical property changes after laser exposure. The study of optical properties of bimetallic films Bi/In and Sn/In showed that 40/40 nm heat-treated Bi/In and Sn/In could have ~3 OD before laser exposure and 0.26 OD and 0.22 OD after high power laser exposure at the I-line wavelength, desired for making the best reported direct-write binary photomask. Analogue grayscale photomasks can be produced by modulating the laser power, as the optical density of the resist film decreases almost linearly with the increase of

laser power within a certain range. Both binary and grayscale photomasks were successfully produced. Compared to HEBS glass, which is the best direct-write photomask material available on the market, bimetallic thin film direct-write photomask materials have demonstrated much wider OD change range and better transmission rate at the I-line and shorter wavelengths. 3D structures were also successfully generated in organic photoresists and various substrates. Functioning solar cells with surface-texture were prepared successfully with Bi/In as patterning, etch masking layer and as direct-write photomask material, demonstrating that bimetallic thermal resist process is compatible with conventional silicon processes.

A two-dimension ANSYS5.7 finite element model was set up to calculate the conversion temperature of bimetallic thermal resist under different laser exposure conditions. Matching with experimental results, simulation shows that the minimum Bi/In laser conversion temperature is 287.7°C. Model computation shows that laser pulse duration has a great influence on thermal resist exposure: the shorter the pulse duration, the less lateral heat flow, and thus the better the pattern profile, and the less exposure energy needed.

Both the literature and our experimental results showed that the diffusion of In, Bi and Sn into silicon substrates at the laser exposure temperature (600K) and duration (4 ns – 10^{-4} s) range is totally negligible. This is confirmed by Auger surface analysis which found no detectable Bi or In after laser exposure, development and stripping. This indicates that bimetallic thermal resist process is compatible with conventional silicon processing. Furthermore, the fast and aggressive oxidation process during the laser exposure creates metal oxides similar to ITO, which ties up metal atoms and makes diffusion even more difficult. Literature shows that ITO films are widely used transparent and conductive films for solar cells and are very stable under normal conditions. Our successful preparation of solar cells with Bi/In as both the patterning and the etch masking layers demonstrated that the bimetallic thermal resists are not poisonous to silicon devices.

11.4 Suggested Further Work

This research work has explored, for the first time, several aspects of the bimetallic thermal resists. The resist applications for wet and dry etching process are encouraging results that have opened doors for much new research.

11.4.1 Improving As-deposited Film Quality

There are two issues with current films: the need to improve the adhesion of as-deposited film to the substrate (not the exposed film) and the roughness. Adhesion directly affects the applications as a thermal resist and for photomasks. Careful handling is required as scratches can be easily made on the films. Roughness brings negative impact on patterning resolution for both applications. Thus, improving film quality is mandatory. All the metallic films used in this research were DC- or RF-sputtered at room temperature. The following are some suggested methods for possible improvement:

- Try different target materials;
- Cool down or heat up substrates during deposition to get a smaller grain size;
- Try other deposition methods: high vacuum evaporation or electron beam evaporation;
- Try vacuum annealing right after deposition.

The film with improved quality should have a higher film density (closer to bulk density) and much smoother surface (check with profilometry).

11.4.2 Improving Resist Resolution

The thermal resist resolution is determined by two things: the resolution of the optical exposure system and the resist film resolution (film quality such as smoothness and grain size). New optical system and laser exposure methods should be explored. Preliminary exposures using laser diffraction method generated 0.3 μm wide line features. This is one of the directions for us to follow to explore the resolution limit of the thermal resists. The items mentioned in Section 11.4.1 for film quality improvement are also valid for this purpose.

11.4.3 Improving Optical Transparency

The most immediate promising application for micromachining and microfabrication is the direct-write photomask process. We have achieved a 3 OD to 0.22 OD change, at 365 nm wavelength, on 5%, 80 nm Sn/In film, which was deposited on glass substrates and with 1125 mW argon laser exposure. However, while closer than any other materials, it is still a little distant away from the industrial target of 3 OD to 0.1 OD. The immediate improvement that can be made is to use quartz as the substrate for the same Sn/In film. Further improvement is possible by

- improving the quality of as-deposited films;
- modifying the exposure process, such as exposure with different gas atmosphere, exposure under raised temperature environment;
- applying ARC (anti-reflection coating) film underneath the thermal resists.

11.4.4 Further Research on Thin Film Imaging Process

The Thin Film Imaging Process proposed in Section 7.2 is an important and promising resist application that needs to be extensively studied. It is proposed that first graphite substrates

should be used to simulate a thick carbon protection layer. Bimetallic thermal resists will be sputtered on a graphite substrate, patterned with laser exposure and developed with dilute RCA2 developer. O_2 plasma etching will be carried out to pattern the graphite substrate and one can study the feasibility of this process. The second stage of the research will be patterning Si wafers, thick SiO_2 and metal layers with this imaging process.

11.4.5 Further Study on Contamination

As mentioned in earlier chapters, metallic contamination to silicon devices is a concern for microfabrication. Although experiments and calculations have given no indication of contamination, this still needs to be more completely explored. SIMS (secondary ion mass spectroscopy) is a good method to answer this question. Due to the unavailability of this tool, we could not carry out this test during the thesis research. Planning is under way to send samples to other institutes for such analysis. The other good way is silicon device tests. Extensive tests should be carried out to investigate the influence of bimetallic films on I-V characteristics and on carrier life time.

11.4.6 Understanding the Oxidation Process

Materials analyses show that the laser exposure of bimetallic thermal resists is an oxidation process. Optical density change is also observed. Thermal modelling indicates that the oxidation happens around 287°C. However, neither obvious optical changes, nor oxides were observed in the Bi/In film after being furnace-annealed in air at 245°C (this is the highest temperature the oven can reach). It is necessary that the annealing be carried out at higher temperatures for further study. Nevertheless, one should aware that there is a significant difference between furnace annealing and laser exposure, i.e., the heating rate. Taking the argon

raster scanning as an example, a typical Bi/In exposure can achieve > 1.58×10^6 °C/sec heating rate, while conventional furnaces can ramp up only at a speed of 200°C/sec. It will be critical to future research if we understand the difference in structural changes caused be laser exposure and conventional annealing of bimetallic thermal resists. Plan-view TEM analysis of exposed bimetallic films was still not successful due to the difficulty of sample preparation. Argon laser had been used to prepare the sample. Due to the slow exposure process (CW laser), heat dissipation possibly caused the cracking of the supporting films (formvar and SiO). It is worth trying Nd:YAG laser to convert the film on formvar or SiO, as heat dissipation is minimized.

11.4.7 Understanding the Etch Resistance Mechanism

It is still not clear yet why exposed and developed Bi/In and Sn/In are resistant to both wet silicon anisotropic and dry etching. One hypothesis is that In_2O_3 is the material that is resistant to etching. Several experimental results support this. But it needs to be confirmed by doing simple bulk material tests. The results of a first chlorine plasma etching test were promising. Further study needs to be carried out and as chlorine plasma etch is more widely used in the industry than is fluorine plasma etch.

11.4.8 Deep RIE and Cryo-etching Applications

Deep reactive ion etching (RIE) of many materials to depths ranging from 10 μm to more than 100 μm is often required for the fabrication of power electronics and MEMS devices. The common selectivity to the etch mask is from 40:1 to 80:1 [148]. This thesis research has shown that bimetallic thermal resists, under optimized plasma etching recipes, exhibit ~1000:1 selectivity. This is valuable for Deep RIE processes to make features with depths beyond 100 μm.

It has been reported that cryogenic cooling of a substrate during silicon RIE can enhance etching anisotropy by suppressing any thermally initiated etch reactions, particularly on the etched sidewalls [149]. The stress and etching performance of bimetallic films under low temperature should be investigated, and the applications in this area should be explored.

11.4.9 Protection Layer for Mask Applications

As-deposited bimetallic thin films are quite soft, thus scratches can be easily made during the applications, especially for proximity exposures. A thin, hard and transparent layer, e.g., a SiO_2 thin film, is desired to protect the mask from being damaged. Spin-on-glass (SOG) was examined as a protection layer for Bi/In films before and after laser writing. The test was not successful. Due to the low conversion temperature of 40/40 nm Bi/In films, SOG curing was carried out at a temperature (120°C) lower than the product specification (300°C). While cracks were observed in the SOG film during the laser-writing of an SOG-coated Bi/In sample, the transmission dropped significantly for a Bi/In film on which an SOG layer was coated after laser-writing. New materials and processes, such as sputtered SiO_2, should be explored for this protection purpose.

11.5 Summary

At the start of this thesis we set out to see if the bimetallic materials could act as good thermal resists. The Bi/In material has been shown to be capable of the full resist cycle. Moreover, it has important properties that regular organic resists do not have: wavelength invariance, anisotropic etch resistance, high plasma etch resistance, and very easy stripping. In addition, the optical changes give it an application in photomasks and grayscale masks no other materials show. At the I-line (365 nm), it creates the best direct-write material known in the

literature. This means this new resist material and process have many possible applications and are worth further exploration.

REFERENCES

1 Dan Gelbart, Creo Inc., private communication with Professor Chapman, Aug, 2003.

2 Chuck Wu, "High energy beam colored glasses exhibiting insensitivity to actinic radiation" US Patent No. 4567104, issued on Jan 28, 1986; "High energy beam sensitive glasses", US Patent No. 4670366, issued on Jun 2, 1987; "High energy beam-sensitive glasses", US Patent No. 4894303, issued on Jan 16, 1990; "Method of making high energy beam sensitive glasses", US Patent No. 5078771, issued on Jan 7, 1992; and "High energy beam sensitive glasses", US Patent No. 5285517, issued on Feb 8, 1994.

3 "Global Chip Sales Up 1.3% in Recovery Year", Semiconductor Industry Association, Feb, 2003.

4 SEMI, Electronic News, Kline & Company and TechSearch International Inc., December 2002.

5 Marlene Bourne, "MEMS continues upward trek", EE Times, July 25, 2002

6 J. R. Sheats and B. W. Smith, "Microlithography – Science and Technology", Marcel Dekker, Inc., New York, 1998.

7 "Intel® Pentium® 4 Processor Product Information", Intel Corporation, Nov 13, 2003.

8 "TSMC Technology Roadmap", TSMC Ltd., Fall 2003.

9 H. H. Hopkins, "On the Diffraction Theory of Optical Images," Proc. Roy. Soc. (Lond.) A217, 408, 1953.

10 "THE INTERNATIONAL TECHNOLOGY ROADMAP FOR SEMICONDUCTORS: 2002 UPDATE", Semiconductor Industry Association, 2002

11 K. Suzuki, S. Matsui and Y. Ochiai, Sub-Half-Micron Lithography for ULSIs, Cambridge University Press, 2000.

12 "Sailing for new seas in photomask technology", SK-Electronics Co. Ltd., Jan 2004.

13 Newport Corporation, Newport Product Catalogue "Optical Materials", Irvine, CA 92606, 2004.

14 Yamazaki Teruhiko, et al, "Manufacture of photomask", Japan Patent No. 55-143560, issued on Aug.11,1980.

15 Kato Tadao, et al, "Manufacture of photomask", Japan Patent No. 55-144245, issued on Nov. 11, 1980.

16 Erwin Deng, Sylvia Hwang, "Photomask Structure", United States Patent No. 6,440,617, issued on August 27, 2002

17 D. C. O'Shea and W. S. Rockward, "Gray-scale masks for diffractive-optics fabrication: II. Spatially filtered halftone screens", Appl. Opt. 34, pp 7518, 1995.

18 W. Daschner, P. Long, M. Larsson and S. H. Lee, "Fabrication of diffractive optical elements using a single optical exposure with a gray level mask", J. Vac. Sci. Technol. B 13, (6) pp 2729, 1995.

19 B. Wagner, H. J. Quenzer, W. Henke, W. Hoppe and W. Pilz, "Microfabrication of complex surface topographies using grey-tone lithography", Sensors and Actuators A: Physical 46, pp 89, 1995.

20 G. Gal, "Exposure mask for fabricating microlenses", US Patent 5482800, issued on 9 January 1996.

21 K. Hannai, et al, "Comparison of Micro Chrome Patterns in Gray Scale Lithography", Proc. SPIE Vol. 5342, pp221-228, 2004.

22 Barry Block, et al, "Gray scale mask and depth pattern transfer technique using inorganic chalcogenide glass", US Patent No. 6033766, issued on Mar 7, 2000.

23 K. Venkatakrishnan, et al., "Laser writing techniques for photomask fabrication using a femtosecond laser", Appl. Phys. A, 74, pp 493-496, 2002.

24 R. Haight, et al., "MARS: Femtosecond laser mask advanced repair system in manufacturing", J. Vac. Sci. Technol. B, 17, pp 3137-3143, 1999.

25 A. Wagner, R. Haight, and P. Longo, "MARS2: An advanced femtosecond laser mask repair tool", IBM Res. Report, RC 22562, pp 1-12, 2002.

26 Jerome Drexler, "Method for making thermochromic photomasks", United States Patent No. 4,225,659, issued on September 30, 1980.

27 W. S. Ruska, Microelectronic processing: An introduction to the manufacture of integrated circuits, New York : McGraw-Hill, Chapter Four, 1987.

28 O. Süs, Justus Liebigs Ann. Chem., 556, S. 65, p85, 1944.

29 M. K. Crawford, et al, "New Materials for 157 nm Photoresists: Characterization and Properties", Proc. SPIE Vol. 3999, pp 357-364, 2000.

30 J. Hutchinson,V. Rao, G. Zhang, A. Pawloski, C. Fonseca, J. Chambers, S. Holl, S. Das, C. Henderson, D. Wheeler, "Progress in 193 nm top surface imaging process development", Proc. SPIE Vol 3333, pp 165-175, 1998.

31 J. M. Powers, et al, "Intel Benchmarking and Process Integration of 157 nm Resists", Proc. SPIE Vol. 5039, pp 269-276, 2003.

32 Nicholas Pfeiffer, "Process Development for Fabrication of Silicon Semiconductor Devices in a Low Gravity, High Vacuum, Space Environment", Master Thesis, Simon Fraser University, Canada, 2000.

33 "International Technology Roadmap for Semiconductors – Lithography", Semiconductor Industry Association, 2003.

34 M. T. Kostishin, E. V. Michailovskaya, P. F. Romanenko and G. A. Sandul, "About the photographic sensitivity of the thin semiconductor layers" J. Sci. Appl. Photogr. Sinematogr. 10, N6, pp 450-451, 1965.

35 M. T. Kostishin, E. V. Michailovskaya, P. F. Romanenko, "On the effect of photographic sensitivity of the thin semiconductor layers deposited on metal substrates ," Sov.Phys. Solid State 8, N2, pp 571-572, 1966.

36 Y. Mizushima and A. Yoshikava, "Photoprocessing and lithographic applications," in Amorphous Semiconductors Technol. and Devices, Y. Hamakava, Ed., OHM, Tokyo, and North-Holland, Amsterdam, pp277-295, 1982.

37 P. E. Shepeljavi, A. V. Stronski, I. Z. Indutnyi, "Fabrication and properties of vacuum inorganic resists", Proc. of Ukrainian Vacuum Society, Kiev:IMF NASU, v.1, pp 324-327, 1995.

38 J. M. Lavine and M. J. Buliszak, "Ag2Te/As2S3: A high-contrast, top-surface imaging resist for 193 nm lithography", J. Vac. Sci. & Technol. B, Vol. 14, No. 6, pp 3489-3491, Nov/Dec 1996.

39 M. S. Chang, T. W. Hou, J. T. Chen, K. D. Kolwicz, and J. N. Zemel, "Inorganic resist for dry processing and dopant applications", J. Vac. Sci. & Technol. B, Vol. 16, No. 6, pp 1973-76, Nov/Dec 1979.

40 Akira Yoshikawa, Osamu Ochi, and Yoshihiko Mizushima, "Dry development of Se-Ge inorganic photoresist", J. Vac. Sci. & Technol. B, Vol. 17, No. 5, pp 1169-76, Sept/Oct 1980.

41 K. L. Tai, R. G. Vadimsky, C. T. Kemmerer, J. S. Wagner, V. E. Lamberti, and A. G. Timko, "Submicron optical lithography using an inorganic resist/polymer bilevel scheme", J. Vac. Sci. & Technol. B, Vol. 36, No. 1, pp 107-109, Jan/Feb 1980.

42 S. A. Kostioukevitch, P. E. Shepelyavi, A. V. Stronski and I. Z. Indutnyi, "Investigations and modeling of physical processes in high-density information recording with the help of inorganic resists", SPIE Proceeding Vol 2647, pp 166-173, 1995.

43 W. S. Ruska, Microelectronic Processing : An Introduction to the Manufacture of Integrated Circuits, New York : McGraw-Hill, p34, 1987.

44 A.R. Janus, "Rapid conversion of an iron oxide film", US Patent No. 3,873,341, issued on March 25, 1975.

45 C. Bozler, et al., "Solid-transformation thermal resist", US Patent, No. 4,619,894, issued on October 28, 1986.

46 S. W. Pang, R. R. Kunz, M. Rothschild, R. B. Goodman, and M. W. Horn, "Aluminum oxides as imaging materials for 193nm excimer laser lithography", J. Vac. Sci. & Technol. B, Vol. 7, No. 6, pp 1624-1628, Nov/Dec 1989.

47 Dan Gelbart and Valentin A. Karasyuk, "UV thermoresists: sub-100-nm imaging without proximity effects", Proc. SPIE Vol. 3676, p. 786-793, March 1999.

48 Erwin Deng, Sylvia Hwang, "Photomask Structure", United States Patent No. 6,440,617, issued on August 27, 2002.

49 Hiroyuki Miyashita, et al., "Halftone phase shift photomask comprising a single layer of halftone light blocking and phase shifting", United States Patent No. 5,604,060, issued on February 18, 1997.

50 "International Technology Roadmap of Semiconductor 2001, Lithography", International SEMATECH, 2001.

51 Jung-Min Sohn, et al, "Process Technology for Next Generation Photomask", Jpn. J. Appl. Phys. Vol. 37 Pt. 1, No. 12B pp 6669-6674, 1998.

52 Robert N. Castellano, "The photomask industry: minimizing a crisis in escalating costs", Solid State Technology, pp 44 – 48, Aug 2002.

53 Kazuchiyo Takaoka, et al, "Photomask material, photomask and methods for the production thereof", Unite State Patent No. 6,303,262, issued on October 16, 2001.

54 J. R. Lankard Sr. and G. Wolbold, "Excimer Laser Ablation of Polyimide in a Manufacturing Facility", Appl. Phys. A 54, pp355-359, 1992.

55 G. Beheim and C.S. Salupo, "Deep RIE Process for Silicon Carbide Power Electronics and MEMS", Mat. Res. Soc. Symp. V. 622, pp. T8.9.1- T8.9.6., 2000.

56 Marinko V. Sarunic, "BiIn: A prototype Bimetallic Laser Activated Thermal Inorganic Resist for Microlithography", Master Thesis, Simon Fraser University, 2001.

57 William G. Moffatt, The handbook of binary phase diagrams, Schenectady, N. Y. : General Electric Co., Corporate Research and Development, Business Growth Services, 1976.

58 D. R. Lide, CRC Handbook of Chemistry and Physics, 82nd Edition, CRC Press, 2001/2002.

59 S. W. Pang and M. W. Horn, "Plasma-deposited amorphous carbon films as planarization layers", J. Vac. Sci. Technol. B, Vol. 8, No. 6, Nov/Dec 1990.

60 O.S. Heavens, Optical Properties of Thin Solid Films, Dover Publications Inc., New York, 1965.

61 Z. Knittl, Optics of Thin Films, John Wiley & Sons, Czechoslovakia, 1976.

62 M. V. Sarunic, G. H. Chapman and Y. Tu, "A Prototype Laser Activated Bimetallic Thermal Resist For Microfabrication", SPIE Proc., Vol 4274, pp 183 – 193, 2001.

63 H. J. Hagemann, W. Gudat and C. Kunz, "Optical Constants from the Far Infrared to the X-Ray Region: Mg, Al, Cu, Ag, Au, Bi, C and Al_2O_3", Deutsches Electronen-Synchrotron, May 1974.

64 E. D. Palik, "Handbook of Optical Constants of Solids III", Orlando, Academic Press, 1998.

65 G. Chapman , Y. Tu, J. Dykes, M. Mio and J. Peng, "Creating Direct-write Gray-scale Photomasks with Bimetallic Thin Film Thermal Resists", Proc. SPIE Vol. 5256, pp 400-411, 2003.

66 E. Elizur and D. Gelbart, "Thermal transfer for flat-panel-display manufacturing", Journal of the Society for Information Display, Vol 11, No. 1, pp 199-202, 2003.

67 G. Chapman, Y. Tu and M. V. Sarunic, "Bi/In Bimetallic Thermal Resists for Microfabrication, Photomasks and Micromachining Applications", Proc. SPIE Vol. 4690, pp 465-476, 2002.

68 G. Chapman , Y. Tu and J. Peng, "Wavelength Invariant Bi/In Thermal Resist As A Si Anisotropic Etch Masking Layer And Direct-write Photomask Material", SPIE Proc. Vol. 5039, pp 472-483, 2003.

69 M. A. Ali, K. E. Gonsalves, N. Batina, V. Golovkina and F. Cerrina, "High-sensitivity nanocomposite resist materials for x-ray and EUV lithography", SPIE Proc. Vol. 5039, pp 1173-1180, 2003.

70 H.K. Pulker, Coatings on Glass, Elsevier, Amsterdam, pp. 356, 1984.

71 K. Gürtler, K. Bange, W. Wagner, F. Rauch and H. Hantsche, "Characterization of Ta_2O_5 layers by electron spectroscopy for chemical analysis rutherford backscattering spectrometry, nuclear reaction analysis and optical methods", Thin Solid Films, Vol. 175, pp185-189, 1989.

72 M. Hüppauff, K. Bange and B. Lengeler, "Density, thickness and interface roughness of SiO_2, TiO_2 and Ta_2O_5 films on BK-7 glasses analyzed by x-ray reflection", Thin Solid Films, Vol. 230, pp 191-198, 1993.

73 W. E. Wallace and W. L. Wu, "A novel method for determining thin film density by energy-dispersive x-ray reflectivity", Appl. Phys. Lett. 67 (9), 28 August 1995.

74 Andrew McPherson, "Development of a Control Program for Advanced Laser Micromachining", Master Thesis, Simon Fraser University, 2002.

75 Operator's Manual: the Coherent Infinity™ Nd:YAG Laser System, Coherent Laser Group, Santa Clara, 2000.

76 Jagjot Dhaliwal, "Research and Development of Binary Metal Alloy Thermal Resists to Develop Sub 0.1μm Structures", Bachelor Thesis, Simon Fraser University, 2000.

77 Gary S. May and Simon M. Sze, Fundamentals of Semiconductor Fabrication, Chapter 5.1, New York : Wiley Publishers, 2004.

78 D. Gelbart and V. A. Karasyuk, "UV thermoresists: sub-100-nm imaging without proximity effects", Proc. SPIE Vol. 3676, p. 786-793, March 1999.

79 G.S. Chen and S.T. Chen, "Diffusion Barrier Properties of Single- and Multilayered Quasi-amorphous Tantalum Nitride Thin Films against Copper Penetration", J. Appl. Phys. Vol. 87, Issue 12, pp 8473-8482, 2000.

80 JCPDS cards, The Joint Committee on Powder Diffraction Standards, 2601 Park Lane, Swarthmore, PA 19081, USA.

81 Mahshid Karimi, Simon Fraser University, private communication, Nov, 2004.

82 Bi_2O_3 and In_2O_3 product specifications, Nanostructured & Amorphous Materials, Inc., 820 Kristi Lane, Los Alamos, New Mexico 87544, USA, 2004.

83 D. J. You, et al, "Effect of the deposition geometry on the electrical properties within Tin-doped indium oxide film deposited under a given RF magnetron sputtering condition", Thin Solid Films 401, pp. 229-234, 2001.

84 Handbook of X-ray Photoelectron Spectroscopy, Perkin-Elmer Corporation, Physical Electronics Division, 1979.

85 R. Kosiba, G. Ecke, V. Cimalla, L. Spieß, S. Krischok, J.A. Schaefer, O. Ambacher, and W.J. Schaff, "Sputter depth profiling of InN layers", Nuclear Instruments and Methods in Physics Research B, 215, pp 486–494, 2004.

86 Lynn Davis, "Properties of transparent conducting oxides deposited at room temperature", Thin Solid Films, Vol. 236, Issues 1-2, Pages 1-5, 15 December 1993.

87 D. V. Morgan, Y. H. Aliyu, R. W. Bunce and A. Salehi, "Annealing effects on opto–electronic properties of sputtered and thermally evaporated indium–tin-oxide films", Thin Solid Films, Vol. 312, Issues 1-2, Pages 268-272, 14 January 1998.

88 A. Salehi, "The effects of deposition rate and substrate temperature of ITO thin films on electrical and optical properties", Thin Solid Films, Vol. 324, Issues 1-2, Pages 214-218, 1 July 1998.

89 Yeon Sik Jung and Sung Soo Lee, "Development of indium tin oxide film texture during DC magnetron sputtering deposition", Journal of Crystal Growth, Vol. 259, Issue 4, Pages 343-351, December 2003.

90 Young-Chul Park, Young-Soon Kim, Hyung-Kee Seo, S.G. Ansari and Hyung-Shik Shin, "ITO thin films deposited at different oxygen flow rates on Si(100) using the PEMOCVD method", Surface and Coatings Technology 161, pp 62-69, 2002.

91 E. Terzini, P. Thilakan and C. Minarini, "Properties of ITO thin films deposited by RF magnetron sputtering at elevated substrate temperature", Materials Science and Engineering, B77, pp 110–114, 2000.

92 Joseph Ford, Karen Kavanagh and Glenn Chapman, private communication, May 6, 2003.

93 G. Chapman, Y. Tu, M. Sarunic and J. Dhaliwal, "BiIn: a Sensitive Bimetallic Thermal Resist", SPIE Proc. Vol. 4345, pp 557-568, 2001.

94 D. B. Lee, "Anisotropic Etching of Silicon", J. Appl. Phys, Vol. 40, No. 11, pp. 4569-4575, Oct 1969.

95 K. E. Bean, "Anisotropic Etching of Silicon", IEEE Transactions on Electron Devices, Vol. ED-25, No. 10, pp. 1185-1193,Oct 1978.

96 G. Kovacs, N. Maluf, K. Petersen, "Bulk Micromachining of Silicon", Proc. IEEE 86, pp. 1536-1551, 1998.

97 T.E. Bell, P.T.J. Gennissen, M. Kuhl, "Porous silicon as a sacrificial material", J. Micromech. Microeng. 6, pp. 361–369, 1996.

98 F. Hedrich, S. Billat, W. Lang, "Structuring of membrane sensors using sacrificial porous silicon", Sensors and Actuators 84, pp.315–323, 2000.

99 Nicolas Szita, Ruben Sutter, Jürg Dual and Rudolf A. Buser, "A micropipettor with integrated sensors", Sensors and Actuators A: Physical 89 (1-2), pp. 112-118, 2001.

100 K. E. Petersen, "Silicon as Mechanical Material", Proc. IEEE, vol. 70, no. 5, pp. 420-457, May 1982.

101 J. Thomas, R. Kühnhold, R. Schnupp and H. Ryssel, "A silicon vibration sensor for tool state monitoring working in the high acceleration range", Sensors and Actuators A: Physical 85 (1-3), pp. 194-201, 2000.

102 H. Sehr, A. G. R. Evans, A. Brunnschweiler, G. J. Ensell, T. E. G. Niblock, "Fabrication and Test of Thermal Vertical Bimorph Actuators for Movement in the Wafer Plane", MME 00 Micromechanics Europe, Uppsala, A4, October 1-3, 2000.

103 J. Zhao, A. Wang, P. Altermatt, and M. A. Green, "Twenty-four percent efficient silicon solar cells with double layer antireflection coatings and reduced resistance loss", Appl. Phys. Lett. 66 (26), 26 June 1995.

104 O. Tabata, R Asahi, H. Funabashi, K. Shimaoka and S. Sugiyama, "Anisotropic Etching of Silicon in TMAH Solutions", Sensors and Actuators A, 34, pp. 51-57, 1992.

105 H.Seidel,L.Csepregi, A.Heuberger and H.Baumgärtel, "Anisotropic Etching of Crystalline Silicon in Alkaline Solution – I. Orientation Dependence and Behavior of Passivation Layers", J. Electrochem. Soc., 137, pp. 3612-3626, 1990.

106 L. Ristic, "Sensor Technoloy and Devices", Artech House, Boston, pp.49-89, 1994.

107 K. R. Williams and R. S. Muller, "Etch Rates for Micromachining Processing", J. Microelectromechanical Systems, Vol. 5, NO. 4, pp. 256-268, Dec 1996.

108 G. T. A. Kovacs, N. I. Maluf and K. E. Petersen, "Bulk Micromachining of Silicon", Proc. IEEE, Vol 86, No 8, pp. 1536-1551, 1998.

109 M. Elwenspoek and H. V. Jansen, "Silicon Micromachining", Cambridge University Press, pp. 200, 1998.

110 G. C. Schwartz and P. M. Schaible, "Reactive ion etching of silicon", J. Vac. Sci. Technol. 16, Issue 2, pp. 410-413, 1979.

111 P. Czuprynski, O. Joubert and L. Vallier, "X-ray photoelectron spectroscopy analyses of metal stacks etched in Cl_2/BCl_3 high density plasmas", J. Vac. Sci. Technol B. Vol 16, Issue 1, pp. 147-158, 1998.

112 M. H. Khater and L. J. Overzet, "Chlorine plasma and polysilicon etch characterization in an inductively coupled plasma etch reactor", Plasma Source Science and Technology, Vol 13, pp466-483, 2004.

113 W. Ehrfeld, F. Gotz, D. Munchmeyer, W. Schelb, and D. Schmidt, "LIGA Process: Sensor Construction Techniques Via Xray Lithography," Tech. Digest of Solid-State Sensor and Actuator Workshop, Hilton Head, SC, pp. 1-4, June 1998.

114 A. K. Graham, Electroplating Engineering Handbook, Van Nostrand Reinhold Co., 1971.

115 Michael Wang, "Rewritable Direct-Write Photomask for Microcircuit Lithography", Physical Optics Corporation, Topic #: AF 95-248, Small Business Innovation Research (SBIR) Phase 1 Selections, Department of Defense, USA, 1995.

116 Wen-yaung Lee, "Thin Films for Optical Data Storage", J. Vac. Sci. Technol. A3(3), pp 640-646, May/Jun 1985.

117 W.Y. Lee, et al, "Nanosecond Pulsed Laser-Induced Segregation of Te in TeO_x Films", J. Vac. Sci. Technol. A 4 (6), pp 2988-2992, Nov/Dec 1986.

118 K. Watanabe, N. Sato and S. Miyaoka, "New optical recording material for video disc system", J. Appl. Phys, 54, pp1256, 1983.

119 P. Arun, A.G. Vedeshwar, "Potential of Sb_2Se_3 Films for Photo-Thermal Phase Change Optical Storage", Thin Solid Films, Vol 335, pp. 270-278, 1998.

120 Toshihisa Nonaka, et al, "Crystal Structure of GeTe and $Ge_2Sb_2Te_5$ Meta-stable Phase", Thin Solid Films, Vol 370, pp. 258-261, 2000.

121 T. Bourouina, et al, "The MEMSNAS process: microloading effect for micromachining of 3D structures with nearly arbitrary shape", IEEE/LEOS Optical MEMS, pp 25–28, 2001.

122 T-K A. Chou and K. Najafi, "Fabrication of out-of-plane curved surfaces in Si by utilizing RIE lag", IEEE Int. Conf. on Micro Electro Mechanical Systems (MEMS 2002) pp 145–148, 2002.

123 A. A. Ayon, et al, "Tailoring etch directionality in a deep reactive ion etching tool", J. Vac. Sci. Technol. 18 pp 1412–1416, 2000.

124 C. Beuret, et al, "Microfabrication of 3D multidirectional inclined structures by UV lithography and electroplating", Proc. IEEE Int. Conf. on Micro Electro Mechanical Syst. (MEMS 1994), pp 81–85, 1994.

125 A. Bertsch A, H. Lorenz and P. Renaud, "Combining microstereolithography and thick resist UV lithography for 3D microfabrication", IEEE 11th Annual Int. Workshop on Micro Electro Mechanical Systems (MEMS 1998) pp 18–23, 1998.

126 A. M. Prokhorov, et al, Laser Heating of Metals, Adam Hilger, 1990.

127 John H. Lienhard, A Heat Transfer Textbook, Prentice-Hall, 1981.

128 J.M. Fairfield, G.H. Schwuttke, "Silicon diodes made by laser irradiation", Solid-State Electronics, Vol 11, pp 1175 – 1176, 1968.

129 F. E. Harper, M. I. Cohen, "Properties of Si diodes prepared by alloying Al into n-type Si with heat pulses from a Nd:YAG laser", Solid-State Electronics, Vol. 13, pp 1103-1109, 1970.

130 G. A. Kachurin, et al, "Annealing of implanted layers by a scanning laser beam", Sov. Phys. Semicond., Vol. 10, No. 10, pp 1128 – 1130, 1976.

131 F. Broutet, et al, "Etude par microscopie electronique de la diffusion induite par laser", Journal de Physique, Colloque C5, supplement au n° 10, Tome 44, pp C5-215 ~ C5-221,Octobre 1983.

132 E. I. Shtyrkov, et al, "Local laser annealing of implantation doped semiconductor layers", Sov. Phys. Semicond., Vol. 9, No. 10, pp 1309-1310, 1976.

133 O. G. Kutukova, et al, "Laser annealing of implanted silicon", Sov. Phys. Semicond., Vol. 10, No. 3, pp 265-267, 1976.

134 J. Krynicki, et al, "Laser annealing of arsenic implanted silicon", Physics Letters, Vol. 61A, No. 3, pp 181-182, May, 1977.

135 I. B. Khaibullin, et al, "Utilization coefficient of implanted impurities in silicon layers subjected to subsequent laser annealing", Sov. Phys. Semicond., Vol. 11, No. 2, pp 190-192, Feb 1977.

136 W. S. Ruska, Microelectronic Processing: An introduction to the manufacture of integrated circuits, New York : McGraw-Hill, p 77, 1987.

137 Y. Akasaka, K. Horie, K. Tsukamoto, G. Nakamura and Y. Yukimoto, "Study of tin diffusion into silicon by backscattering analysis", Japanese Journal of Applied Physics, Vol 13, Issue 10, pp 1533-1540, 1974.

138 H. T. Yang and W. S. Berry, "Interaction of indium on Si surface in Si molecular beam epitaxy (MBE)", J. Vac. Sci. Technol. B2 (2), pp 206-208, 1984.

139 H. Li, J. Bennett, P. Zeitzoff, T. A. Kirichenko, S. K. Banerjee and D. Henke, "Indium Out-Diffusion From Silicon During Rapid Thermal Annealing", IEEE Electron Device Letters, Vol. 24, No. 4, pp 221-223, April, 2003.

140 Glenn Chapman, Introduction to Microelectronic Fabrication Course Note, Diffusion Constants in Si, Simon Fraser University, 2004.

141 H. Ryu, et al, "Indium-Tin Oxide/Si contacts with In- and Sn-diffusion barriers in polycrystalline Si thin-film transistor liquid-crystal displays", Journal of Electronic Materials, Vol. 32, No. 9, pp 919 -924, 2003.

142 R. N. Ghoshtagore, "Donor Diffusion Dynamics in Silicon", Physics Review B, Vol 3, No. 2, pp 397-403, 1971.

143 S. M. Goodnick, J. F. Wager and C. W. Wilmsen, "Thermal degradation of indium-tin-oxide / p-silicon solar cells", J. Appl. Phys. 51 (1), Jan, 1980.

144 C. W. Ow-Yang, Y. Shigesato, and D. C. Paine, "Interfacial stability of an indium tin oxide thin film deposited on Si and Si0.85Ge0.15", J. Appl. Phys., Vol 88, No. 6, pp 3717-3724, 2000.

145 E. Fogarassy, R. Stuck, J. J. Grob and P. Siffert, "Silicon solar cells realized by laser induced diffusion of vacuum-deposited dopants", J. Appl. Phys. 52(2), pp 1076-1082, Feb, 1981.

146 L. Ristic, "Sensor Technoloy and Devices", Artech House, Boston, pp.69-70, 1994.

147 H.Seidel, L.Csepregi, A.Heuberger and H.Baumgärtel, "Anisotropic Etching of Crystalline Silicon in Alkaline Solution – II. Influence of Dopants", J.Electrochem.Soc., 137, pp. 3626-3632, 1990.

148 G. Beheim and C.S. Salupo, "Deep RIE Process for Silicon Carbide Power Electronics and MEMS", Mat. Res. Soc. Symp. V. 622, pp. T8.9.1- T8.9.6., 2000.

149 S. Tachi, K. Tsujimoto, and S. Okuddaira, Appl. Phys. Lett. Vol 52, pp 616-618, 1988.

Appendix A. Optical Properties of Bi, In and Sn [63,64]

	Bi		In		Sn	
λ (nm)	n	k	n	k	n	k
1.0	0.999000	0.000329	0.999192	0.000343	0.999403	0.000262
13.4	0.937500	0.048650	0.935200	0.045000	0.953100	0.067000
248.0	1.482000	1.520000	0.280000	2.350000	0.630000	2.300000
514.0	1.920000	2.732000	0.790000	5.080000	1.500000	4.200000
830.0	2.861000	3.890000	1.850000	8.000000	2.700000	6.500000

Appendix B. Material Parameters for Thermal Modelling [58]

Bi: Thermal conductivity = 7.92 W/m·K
Specific Heat (solid) = 0.123 J/g·K = 123 J/kg·K
Specific Heat (liquid)= 0.152 J/g·K = 152 J/kg·K
Density = 9.80 g/cm^3 = 9800 kg/m^3
Enthalpy = 11.30 KJ/mol = 5.29906E-10 J/um^3
1 mol = 208.9804 g
melting piont = 544.5 K

In: Thermal conductivity = 81.8 W/m·K
Specific Heat (solid) = 0.233 J/g·K = 233 J/kg·K
Specific Heat (liquid)= 0.275 J/g·K = 275 J/kg·K
Density = 7.31 g/cm^3 = 7310 kg/m^3
Enthalpy = 3.263 kJ/mol = 2.07738E-10 J/um^3
1 mol = 114.82 g
melting point = 429.81 K

Glass:Thermal cond. = 1.4 W/m·K (0.546 - 1.6 W/m·K)
Specific Heat (solid) = 0.84 J/g·K = 840 J/kg·K
Density = 2.5 g/cm^3 = 2500 kg/m^3 (varies)

Si: Thermal Conductivity = 149 W/m·K
Specific Heat (solid) = 0.71 J/g·K = 710 J/kg·K
Density = 2.33 g/cm^3 = 2330 kg/m^3

50%BiIn: Thermal cond. = 45 W/m·K
Specific Heat (solid) = 180 J/kg·K
Density = 8600 kg/m^3
Enthalpy = 4.21E-10 J/um^3 (according to 66%Bi vs 34%In)

Heat Flux = 6.366E8 W/m^2 (0.2W focused down to φ=20 um beam)
Heat Flux = 9.947E10 W/m^2 (0.2W focused down to φ=1.6 um beam)

50/50 nm Bi/In on glass, silicon and silicon dioxide substrates has 48.7% absorption at 514 nm wavelength.

Standard Molar Enthalpy (heat) of Formation: $\Delta_f H^\circ(kJ/mol)$ [58]

In_2O_3 = -925.8
Bi_2O_3 = -573.9

Appendix C. Typical ITO Composition [88-91]

Typical ITO composition is 10wt.% SnO_2. Knowing the atomic weights as follows: In = 114.82 gm; O = 16 gm and Sn = 118.69 gm, we can calculate the atomic weights of In_2O_3 = 277.64 gm and SnO_2 = 150.69 gm. Thus, assuming ITO is composed of stoichiometric SnO_2 and In_2O_3, 10wt.% SnO_2 is equal to 9.3at.% Sn or 9.6wt.% Sn in a Sn:In ratio.